

**REPORT DOCUMENTATION PAGE**Form Approved  
OMB No. 0704-0188

Public reporting burden for this collection of information is estimated to average 1 hour per response, including the time for reviewing instructions, searching existing data sources, gathering and maintaining the data needed, and completing and reviewing the collection of information. Send comments regarding this burden estimate or any other aspect of this collection of information, including suggestions for reducing this burden, to Washington Headquarters Services, Directorate for Information Operations and Reports, 1215 Jefferson Davis Highway, Suite 1204, Arlington, VA 22202-4302, and to the Office of Management and Budget, Paperwork Reduction Project (0704-0188), Washington, DC 20503.

1. AGENCY USE ONLY (Leave blank)	2. REPORT DATE June 15, 2001	3. REPORT TYPE AND DATES COVERED Technical 03/16/99 to 06/15/01
4. TITLE AND SUBTITLE Unsteady Skin-friction Measurements on a Maneuvering DARPA2 Suboff Model	5. FUNDING NUMBERS N00014-99-1-0428 N00014-01-1-0420	
6. AUTHORS  Serhat Hosder and Roger L. Simpson		
7. PERFORMING ORGANIZATION NAME(S) AND ADDRESS(ES)  Department of Aerospace and Ocean Engineering Virginia Polytechnic Institute and State University Blacksburg, Virginia 24061-0203	8. PERFORMING ORGANIZATION REPORT NUMBER  VPI-AOE-272	
9. SPONSORING/MONITORING AGENCY NAME(S) AND ADDRESS(ES)  Office of Naval Research 800 N. Quincy Street Arlington, Virginia 22217	10. SPONSORING/MONITORING AGENCY REPORT NUMBER	
11. SUPPLEMENTARY NOTES		

## 12a. DISTRIBUTION/AVAILABILITY STATEMENT

**DISTRIBUTION STATEMENT A**  
Unlimited Approved for Public Release  
Distribution Unlimited

**20011031 135**

13. ABSTRACT (Maximum 200 words) The skin-friction magnitude was measured for steady and unsteady flow over a Suboff submarine model by surface hot-film constant temperature sensors. The locations of the local spatial minima in the skin-friction magnitudes are used to obtain the separation locations. Steady surface static pressures were measured at 10° and 20° angles of attack. The dynamic plunge-pitch-roll model mount (DyPPiR) in the Stability Wind Tunnel was used to simulate rapid pitch-up maneuvers, which are a linear ramp from 1° to 27° in 0.33 seconds, for the bare-body and sail-on-side cases at  $Re_L = 5.5 \times 10^6$  and a wind speed of  $42.7 \pm 1$  m/s. Steady results show a cross-flow separation structure on the leeward side of the bare-body. In the sail-on-side case, the separation pattern of the non-sail region follows the bare-body separation trends; on the sail side it is strongly affected by the presence of the sail-body junction and its horseshoe-vortex type separation. Unsteady results of the bare-body and the non-sail region of the sail-on-side case show a different separation topology from the steady flow separation structure and significant time lags, which are described by a first-order time lag model. The unsteady separation pattern of the sail side does not follow the quasi-steady data with a time lag.

14. SUBJECT TERMS Unsteady flow, separation, three-dimensional flow, turbulent boundary layers		15. NUMBER OF PAGES 226
		16. PRICE CODE
17. SECURITY CLASSIFICATION OF REPORT UNCLASSIFIED	18. SECURITY CLASSIFICATION OF THIS PAGE UNCLASSIFIED	19. SECURITY CLASSIFICATION OF ABSTRACT UNCLASSIFIED
20. LIMITATION OF ABSTRACT UNLIMITED		

# Contents

<b>Acknowledgements</b>	<b>i</b>
<b>Table of Contents</b>	<b>ii</b>
<b>List of Figures</b>	<b>v</b>
<b>List of Tables</b>	<b>xx</b>
<b>1 Introduction</b>	<b>1</b>
1.1 Unsteady Aerodynamics . . . . .	1
1.2 Three-Dimensional Separations . . . . .	3
1.3 Previous Studies . . . . .	4
1.4 Present Work . . . . .	6
<b>2 Experimental Facilities, Equipment and Apparatus</b>	<b>10</b>
2.1 Stability Wind Tunnel . . . . .	10
2.2 DyPPiR . . . . .	11
2.3 Data Acquisition System . . . . .	12
2.4 Skin-Friction Measurement System . . . . .	12
2.4.1 Hot-film Sensors . . . . .	13

2.4.2	Constant Temperature Anemometers . . . . .	17
2.5	Wind Tunnel Model . . . . .	18
2.5.1	Sensor Configuration and the Locations . . . . .	18
2.5.2	Sensor Mounting Strategy . . . . .	19
2.5.3	Rotatable Ring . . . . .	20
2.5.4	Boundary Layer Trips . . . . .	21
2.6	Pressure Measurement System . . . . .	21
<b>3</b>	<b>Steady Measurements and the DyPPiR Maneuvers</b>	<b>29</b>
3.1	Skin-Friction Measurements . . . . .	29
3.1.1	Steady Hot-film Measurements . . . . .	30
3.1.2	DyPPiR Maneuvers . . . . .	31
3.2	Pressure Measurements . . . . .	32
<b>4</b>	<b>Calibration of the Hot-film Sensors</b>	<b>35</b>
4.1	Description of the Experimental Apparatus . . . . .	35
4.2	Boundary Layer Velocity Profile Measurements . . . . .	37
4.2.1	Boundary Layer Thickness Determination . . . . .	37
4.2.2	Calculation of the Boundary Layer Properties . . . . .	38
4.3	Calculation of the Skin-Friction Values . . . . .	40
4.4	Calculation of the Calibration Coefficients . . . . .	41
<b>5</b>	<b>Results and Discussion for Steady Measurements</b>	<b>48</b>
5.1	Steady Skin-Friction Measurements . . . . .	48
5.1.1	Data Acquisition and Reduction . . . . .	48
5.1.2	Results and Discussion for the Barebody Case . . . . .	50

5.1.3	Results and Discussion for the Sail-on-side Case . . . . .	52
5.2	Steady Pressure Measurements . . . . .	55
5.2.1	Data Reduction . . . . .	55
5.2.2	Results and Discussion . . . . .	56
<b>6</b>	<b>Results and Discussion for Unsteady Measurements</b>	<b>123</b>
6.1	Data Acquisition and Reduction . . . . .	123
6.1.1	Determination of the unsteady separation locations . . . . .	126
6.2	Unsteady Flow Topology . . . . .	127
6.3	Time-Lag Models . . . . .	131
6.3.1	Algebraic Time-lag Models . . . . .	131
6.3.2	First-Order Differential Time-Lag Model . . . . .	133
<b>7</b>	<b>Conclusions</b>	<b>192</b>
	<b>References</b>	<b>196</b>
<b>A</b>	<b>Uncertainty Analysis for the Skin-friction Measurements</b>	<b>200</b>
A.1	Classification of the Uncertainties . . . . .	200
A.2	Uncertainty Calculations . . . . .	200
<b>B</b>	<b>Robust Locally Weighted Regression and Smoothing <i>LOESS</i></b>	<b>203</b>
B.1	Mathematical Description . . . . .	203
B.2	Selection of the Loess Parameters . . . . .	204
	<b>Vita</b>	<b>207</b>



# List of Figures

1.1	Limiting streamline pattern and surfaces of separation for three types of 3-D separation:(a) horseshoe type separation; (b) Werle type separation (the view of the surface separation is rotated $90^\circ$ from the view of the limiting streamline pattern); (c) cross flow separation. Taken from Yates and Chapman [1]. . . . .	8
1.2	On-axis cross sectional view of secondary flow streamlines from a cross-flow separation. P1: primary separation, P2: secondary separation, R1: Primary reattachment, R2: secondary reattachment. . . . .	9
2.1	Top view of the Virginia Tech Stability Wind Tunnel . . . . .	24
2.2	Dynamic Plunge-Pitch-Roll(DyPPiR) Model Mount installed in the wind tunnel.(taken from Wetzel [2]) . . . . .	24
2.3	Coordinate nomenclature for the DyPPiR and the model. (taken from Wetzel [2]) . . . . .	25
2.4	Hot-film sensor. All dimensions are in mm, and the figure is not drawn to scale. . . . .	25
2.5	Sensor plug with a hot-film sensor mounted . . . . .	26
2.6	Schematic of the sensor mounting strategy . . . . .	26
2.7	Computer generated 3-D view of the Suboff model with the sail . . . . .	27
2.8	Top and side view of the model and the hot-film sensor locations . . . . .	27
2.9	Barebody and sail-on-side configurations of the model . . . . .	28

3.1	Regions for Darpa2 Skin Friction and Pressure Measurements. . . . .	34
3.2	DyPPiR plunge and pitch feedback for pitchup maneuvers. Filled symbols show the $\alpha$ locations for the steady measurements. . . . .	34
4.1	Cross-sectional view of the model and support assembly in the Y-Z plane	43
4.2	Measurement stations for the flow symmetry check . . . . .	43
4.3	Results of the velocity measurements at the flow symmetry check points .	44
4.4	Planform view of the sensor configuration, boundary layer traverse and streamwise velocity measurement stations (all dimensions are measured in inches and the figure is not drawn to scale). . . . .	44
4.5	Boundary layer velocity profiles for $U_e = 80$ ft/s. . . . .	45
4.6	Boundary layer velocity profiles for $U_e = 95$ ft/s. . . . .	45
4.7	Boundary layer velocity profiles for $U_e = 110$ ft/s. . . . .	46
4.8	Streamwise Velocity Distributions for all calibration speeds. . . . .	46
4.9	$C_f$ vs. $x/L$ at $0^\circ$ angle of attack (For the measurements at Virginia Tech $Re_L = 5.5 \times 10^6$ , for the measurements at David Taylor Model Basin (DTMB) $Re_L = 1.2 \times 10^7$ ) . . . . .	47
5.1	Oil flow visualization showing the cross flow separation topology on the constant diameter region of the model for the barebody case at $\alpha = 20^\circ$ , $Re = 4.5 \times 10^6$ . Flow is from left to right. . . . .	60
5.2	Oil flow visualization showing the low speed fluid region on the stern of the model for the barebody case at $\alpha = 15^\circ$ , $Re = 4.5 \times 10^6$ . Flow is from left to right. . . . .	60
5.3	Oil flow pattern showing the separation in the vicinity of the sail at $\alpha =$ $15^\circ$ , $Re = 4.5 \times 10^6$ . Flow is from right to left. . . . .	61
5.4	Oil flow visualization of the sail side showing the low speed fluid region on the stern of the model for the sail-on-side case at $\alpha = 10^\circ$ , $Re = 4.5 \times 10^6$ . Flow is from right to left. . . . .	61

- 5.5  $C_f$  vs.  $\phi$  for all  $x/L$  locations at  $\alpha = 0.9^\circ$  for steady barebody and sail-on-side cases. Sail side on the right of the figure starting from  $\phi = 180^\circ$ . 62
- 5.6  $C_f$  vs.  $\phi$  for all  $x/L$  locations at  $\alpha = 3.1^\circ$  for steady barebody and sail-on-side cases. Sail side on the right of the figure starting from  $\phi = 180^\circ$ . 63
- 5.7  $C_f$  vs.  $\phi$  for all  $x/L$  locations at  $\alpha = 5.1^\circ$  for steady barebody and sail-on-side cases. Sail side on the right of the figure starting from  $\phi = 180^\circ$ . 64
- 5.8  $C_f$  vs.  $\phi$  for all  $x/L$  locations at  $\alpha = 7.2^\circ$  for steady barebody and sail-on-side cases. Sail side on the right of the figure starting from  $\phi = 180^\circ$ . 65
- 5.9  $C_f$  vs.  $\phi$  for all  $x/L$  locations at  $\alpha = 9.3^\circ$  for steady barebody and sail-on-side cases. Sail side on the right of the figure starting from  $\phi = 180^\circ$ . 66
- 5.10  $C_f$  vs.  $\phi$  for all  $x/L$  locations at  $\alpha = 11.3^\circ$  for steady barebody and sail-on-side cases. Sail side on the right of the figure starting from  $\phi = 180^\circ$ . 67
- 5.11  $C_f$  vs.  $\phi$  for all  $x/L$  locations at  $\alpha = 13.2^\circ$  for steady barebody and sail-on-side cases. Sail side on the right of the figure starting from  $\phi = 180^\circ$ . 68
- 5.12  $C_f$  vs.  $\phi$  for all  $x/L$  locations at  $\alpha = 15.3^\circ$  for steady barebody and sail-on-side cases. Sail side on the right of the figure starting from  $\phi = 180^\circ$ . 69
- 5.13  $C_f$  vs.  $\phi$  for all  $x/L$  locations at  $\alpha = 17.4^\circ$  for steady barebody and sail-on-side cases. Sail side on the right of the figure starting from  $\phi = 180^\circ$ . 70
- 5.14  $C_f$  vs.  $\phi$  for all  $x/L$  locations at  $\alpha = 19.4^\circ$  for steady barebody and sail-on-side cases. Sail side on the right of the figure starting from  $\phi = 180^\circ$ . 71
- 5.15  $C_f$  vs.  $\phi$  for all  $x/L$  locations at  $\alpha = 21.4^\circ$  for steady barebody and sail-on-side cases. Sail side on the right of the figure starting from  $\phi = 180^\circ$ . 72
- 5.16  $C_f$  vs.  $\phi$  for all  $x/L$  locations at  $\alpha = 23.4^\circ$  for steady barebody and sail-on-side cases. Sail side on the right of the figure starting from  $\phi = 180^\circ$ . 73
- 5.17  $C_f$  vs.  $\phi$  for all  $x/L$  locations at  $\alpha = 25.5^\circ$  for steady barebody and sail-on-side cases. Sail side on the right of the figure starting from  $\phi = 180^\circ$ . 74
- 5.18  $C_f$  vs.  $\phi$  for all  $x/L$  locations at  $\alpha = 27.6^\circ$  for steady barebody and sail-on-side cases. Sail side on the right of the figure starting from  $\phi = 180^\circ$ . 75

5.19 $C_f$ vs. $\phi$ for all $\alpha$ at $x/L = 0.110$ for steady barebody and sail-on-side cases. Sail side on the right of the figure starting from $\phi = 180^\circ$ . . . . .	76
5.20 $C_f$ vs. $\phi$ for all $\alpha$ at $x/L = 0.131$ for steady barebody and sail-on-side cases. Sail side on the right of the figure starting from $\phi = 180^\circ$ . . . . .	77
5.21 $C_f$ vs. $\phi$ for all $\alpha$ at $x/L = 0.170$ for steady barebody and sail-on-side cases. Sail side on the right of the figure starting from $\phi = 180^\circ$ . . . . .	78
5.22 $C_f$ vs. $\phi$ for all $\alpha$ at $x/L = 0.266$ for steady barebody and sail-on-side cases. Sail side on the right of the figure starting from $\phi = 180^\circ$ . . . . .	79
5.23 $C_f$ vs. $\phi$ for all $\alpha$ at $x/L = 0.306$ for steady barebody and sail-on-side cases. Sail side on the right of the figure starting from $\phi = 180^\circ$ . . . . .	80
5.24 $C_f$ vs. $\phi$ for all $\alpha$ at $x/L = 0.345$ for steady barebody and sail-on-side cases. Sail side on the right of the figure starting from $\phi = 180^\circ$ . . . . .	81
5.25 $C_f$ vs. $\phi$ for all $\alpha$ at $x/L = 0.434$ for steady barebody and sail-on-side cases. Sail side on the right of the figure starting from $\phi = 180^\circ$ . . . . .	82
5.26 $C_f$ vs. $\phi$ for all $\alpha$ at $x/L = 0.501$ for steady barebody and sail-on-side cases. Sail side on the right of the figure starting from $\phi = 180^\circ$ . . . . .	83
5.27 $C_f$ vs. $\phi$ for all $\alpha$ at $x/L = 0.570$ for steady barebody and sail-on-side cases. Sail side on the right of the figure starting from $\phi = 180^\circ$ . . . . .	84
5.28 $C_f$ vs. $\phi$ for all $\alpha$ at $x/L = 0.638$ for steady barebody and sail-on-side cases. Sail side on the right of the figure starting from $\phi = 180^\circ$ . . . . .	85
5.29 $C_f$ vs. $\phi$ for all $\alpha$ at $x/L = 0.706$ for steady barebody and sail-on-side cases. Sail side on the right of the figure starting from $\phi = 180^\circ$ . . . . .	86
5.30 $C_f$ vs. $\phi$ for all $\alpha$ at $x/L = 0.774$ for steady barebody and sail-on-side cases. Sail side on the right of the figure starting from $\phi = 180^\circ$ . . . . .	87
5.31 $C_f$ vs. $\phi$ for all $\alpha$ at $x/L = 0.819$ for steady barebody and sail-on-side cases. Sail side on the right of the figure starting from $\phi = 180^\circ$ . . . . .	88
5.32 $C_f$ vs. $\phi$ for all $\alpha$ at $x/L = 0.863$ for steady barebody and sail-on-side cases. Sail side on the right of the figure starting from $\phi = 180^\circ$ . . . . .	89

5.33	Steady primary separation locations vs. $\alpha$ for the barebody case. . . . .	90
5.34	Steady primary separation locations vs. $\alpha$ for the barebody case (continued). . . . .	90
5.35	Steady secondary separation locations vs. $\alpha$ for the barebody case. . . . .	91
5.36	Steady secondary separation locations vs. $\alpha$ for the barebody case (continued). . . . .	91
5.37	Comparison of the oil-flow primary separation locations with the hot-film primary separation locations for the barebody case. For the hot-film measurements $\alpha = 15.3^\circ$ and for the oil-flow results $\alpha = 15^\circ$ . . . . .	92
5.38	Comparison of the oil-flow primary separation locations with the hot-film primary separation locations for the barebody case. For the hot-film measurements $\alpha = 19.4^\circ$ and for the oil-flow results $\alpha = 20^\circ$ . . . . .	92
5.39	Solid vs. slotted wall comparison for the barebody $C_f$ vs $\phi$ distribution at $x/L = 0.345$ . $\alpha = 10^\circ$ for the solid wall case, and $\alpha = 9.3^\circ$ for the slotted wall case. . . . .	93
5.40	Solid vs. slotted wall comparison for the barebody $C_f$ vs $\phi$ distribution at $x/L = 0.345$ . $\alpha = 20^\circ$ for the solid wall case, and $\alpha = 19.4^\circ$ for the slotted wall case. . . . .	93
5.41	Solid vs. slotted wall comparison for the barebody $C_f$ vs $\phi$ distribution at $x/L = 0.570$ . $\alpha = 10^\circ$ for the solid wall case, and $\alpha = 9.3^\circ$ for the slotted wall case. . . . .	94
5.42	Solid vs. slotted wall comparison for the barebody $C_f$ vs $\phi$ distribution at $x/L = 0.570$ . $\alpha = 20^\circ$ for the solid wall case, and $\alpha = 19.4^\circ$ for the slotted wall case. . . . .	94
5.43	Solid vs. slotted wall comparison for the barebody $C_f$ vs $\phi$ distribution at $x/L = 0.819$ . $\alpha = 10^\circ$ for the solid wall case, and $\alpha = 9.3^\circ$ for the slotted wall case. . . . .	95
5.44	Solid vs. slotted wall comparison for the barebody $C_f$ vs $\phi$ distribution at $x/L = 0.819$ . $\alpha = 20^\circ$ for the solid wall case, and $\alpha = 19.4^\circ$ for the slotted wall case. . . . .	95

5.45 Steady primary separation locations vs. $\alpha$ for the sail-on-side (region without sail) case. . . . .	96
5.46 Steady primary separation locations vs. $\alpha$ for the sail-on-side (region without sail) case (continued). . . . .	96
5.47 Steady secondary separation locations vs. $\alpha$ for the sail-on-side (region without sail) case. . . . .	97
5.48 Steady secondary separation locations vs. $\alpha$ for the sail-on-side (region without sail) case (continued). . . . .	97
5.49 Comparison for steady primary separation locations vs. $\alpha$ for barebody and the sail-on-side (region without sail) case at $x/L = 0.501, 0.638$ and $0.774$ . . . . .	98
5.50 Comparison for steady secondary separation locations vs. $\alpha$ for barebody and the sail-on-side (region without sail) case at $x/L = 0.501, 0.638$ and $0.774$ . . . . .	98
5.51 Steady 1 <sup>st</sup> separation locations vs. $\alpha$ for the sail-on-side (region with sail) case. . . . .	99
5.52 Steady 1 <sup>st</sup> separation locations vs. $\alpha$ for the sail-on-side (region with sail) case (continued). . . . .	99
5.53 Steady 2 <sup>nd</sup> separation locations vs. $\alpha$ for the sail-on-side (region with sail) case. . . . .	100
5.54 Steady 2 <sup>nd</sup> separation locations vs. $\alpha$ for the sail-on-side (region with sail) case (continued) . . . . .	100
5.55 Steady $C_f$ contours in the vicinity of sail at $\alpha = 0.9^\circ$ . . . . .	101
5.56 Steady $C_f$ contours in the vicinity of sail at $\alpha = 3.1^\circ$ . . . . .	101
5.57 Steady $C_f$ contours in the vicinity of sail at $\alpha = 5.1^\circ$ . . . . .	102
5.58 Steady $C_f$ contours in the vicinity of sail at $\alpha = 7.2^\circ$ . . . . .	102
5.59 Steady $C_f$ contours in the vicinity of sail at $\alpha = 9.3^\circ$ . . . . .	103
5.60 Steady $C_f$ contours in the vicinity of sail at $\alpha = 11.3^\circ$ . . . . .	103

5.61 Steady $C_f$ contours in the vicinity of sail at $\alpha = 13.2^\circ$ .	104
5.62 Steady $C_f$ contours in the vicinity of sail at $\alpha = 15.3^\circ$ .	104
5.63 Steady $C_f$ contours in the vicinity of sail at $\alpha = 17.4^\circ$ .	105
5.64 Steady $C_f$ contours in the vicinity of sail at $\alpha = 19.4^\circ$ .	105
5.65 Steady $C_f$ contours in the vicinity of sail at $\alpha = 21.4^\circ$ .	106
5.66 Steady $C_f$ contours in the vicinity of sail at $\alpha = 23.4^\circ$ .	106
5.67 Steady $C_f$ contours in the vicinity of sail at $\alpha = 25.5^\circ$ .	107
5.68 Steady $C_f$ contours in the vicinity of sail at $\alpha = 27.6^\circ$ .	107
5.69 $C_p$ vs. $x/L$ distribution obtained from RANS code at $0^\circ$ angle of attack.	108
5.70 $C_p$ vs. $\phi$ for the stations between $x/L = 0.112$ and $x/L = 0.327$ at $\alpha = 10.0^\circ$ for the barebody case. Solid and slotted wind tunnel wall configurations.	109
5.71 $C_p$ vs. $\phi$ for the stations between $x/L = 0.348$ and $x/L = 0.865$ at $\alpha = 10.0^\circ$ for the barebody case. Solid and slotted wind tunnel wall configurations.	110
5.72 $C_p$ vs. $\phi$ for the stations between $x/L = 0.112$ and $x/L = 0.327$ at $\alpha = 20.0^\circ$ for the barebody case. Solid and slotted wind tunnel wall configurations.	111
5.73 $C_p$ vs. $\phi$ for the stations between $x/L = 0.348$ and $x/L = 0.865$ at $\alpha = 20.0^\circ$ for the barebody case. Solid and slotted wind tunnel wall configurations.	112
5.74 $C_p$ vs. $\phi$ for the stations between $x/L = 0.112$ and $x/L = 0.327$ at $\alpha = 10.0^\circ$ for the barebody case and sail-on-side cases. Sail side on the right of the figure starting from $\phi = 180^\circ$ . Slotted wind tunnel wall configuration.	113

5.75 $C_p$ vs. $\phi$ for the stations between $x/L = 0.348$ and $x/L = 0.865$ at $\alpha = 10.0^\circ$ for the barebody case and sail-on-side cases. Sail side on the right of the figure starting from $\phi = 180^\circ$ . Slotted wind tunnel wall configuration. . . . .	114
5.76 $C_p$ vs. $\phi$ for the stations between $x/L = 0.112$ and $x/L = 0.327$ at $\alpha = 20.0^\circ$ for the barebody case and sail-on-side cases. Sail side on the right of the figure starting from $\phi = 180^\circ$ . Slotted wind tunnel wall configuration. . . . .	115
5.77 $C_p$ vs. $\phi$ for the stations between $x/L = 0.348$ and $x/L = 0.865$ at $\alpha = 20.0^\circ$ for the barebody case and sail-on-side cases. Sail side on the right of the figure starting from $\phi = 180^\circ$ . Slotted wind tunnel wall configuration. . . . .	116
5.78 Barebody $C_p$ vs. $x/L$ distributions for different $\phi$ locations at $\alpha = 10^\circ$ . .	117
5.79 Barebody $C_p$ vs. $x/L$ distributions for different $\phi$ locations at $\alpha = 20^\circ$ . .	117
5.80 Sail-on-side $C_p$ vs. $x/L$ distributions for different $\phi$ locations at $\alpha = 10^\circ$ . .	118
5.81 Sail-on-side $C_p$ vs. $x/L$ distributions for different $\phi$ locations at $\alpha = 20^\circ$ . .	118
5.82 Steady $C_p$ and $C_f$ vs. $\phi$ for the barebody case. For $C_p$ measurements $\alpha = 10.0^\circ$ and $x/L = 0.503$ . For $C_f$ measurements $\alpha = 11.3^\circ$ and $x/L = 0.501$ . . . . .	119
5.83 Steady $C_p$ and $C_f$ vs. $\phi$ for the barebody case. For $C_p$ measurements $\alpha = 20.0^\circ$ and $x/L = 0.503$ . For $C_f$ measurements $\alpha = 21.4^\circ$ and $x/L = 0.501$ . . . . .	119
5.84 Steady $C_p$ and $C_f$ vs. $\phi$ for the barebody case. For $C_p$ measurements $\alpha = 10.0^\circ$ and $x/L = 0.777$ . For $C_f$ measurements $\alpha = 11.3^\circ$ and $x/L = 0.774$ . . . . .	120
5.85 Steady $C_p$ and $C_f$ vs. $\phi$ for the barebody case. For $C_p$ measurements $\alpha = 20.0^\circ$ and $x/L = 0.777$ . For $C_f$ measurements $\alpha = 21.4^\circ$ and $x/L = 0.774$ . . . . .	120



5.86	Steady $C_p$ and $C_f$ vs. $\phi$ for the sail-on-side case. For $C_p$ measurements $\alpha = 10.0^\circ$ and $x/L = 0.503$ . For $C_f$ measurements $\alpha = 11.3^\circ$ and $x/L = 0.501$ .	121
5.87	Steady $C_p$ and $C_f$ vs. $\phi$ for the sail-on-side case. For $C_p$ measurements $\alpha = 20.0^\circ$ and $x/L = 0.503$ . For $C_f$ measurements $\alpha = 21.4^\circ$ and $x/L = 0.501$ .	121
5.88	Steady $C_p$ and $C_f$ vs. $\phi$ for the sail-on-side case. For $C_p$ measurements $\alpha = 10.0^\circ$ and $x/L = 0.777$ . For $C_f$ measurements $\alpha = 11.3^\circ$ and $x/L = 0.774$ .	122
5.89	Steady $C_p$ and $C_f$ vs. $\phi$ for the sail-on-side case. For $C_p$ measurements $\alpha = 20.0^\circ$ and $x/L = 0.777$ . For $C_f$ measurements $\alpha = 21.4^\circ$ and $x/L = 0.774$ .	122
6.1	Comparison of barebody $C_f$ vs. $\phi$ distribution for steady and unsteady data at all $x/L$ locations. $\alpha = 3.1^\circ$ , $t' = 3.417$ , $\alpha(t') = 3.1^\circ$ .	138
6.2	Comparison of barebody $C_f$ vs. $\phi$ distribution for steady and unsteady data at all $x/L$ locations. $\alpha = 5.1^\circ$ , $t' = 3.818$ , $\alpha(t') = 5.1^\circ$ .	139
6.3	Comparison of barebody $C_f$ vs. $\phi$ distribution for steady and unsteady data at all $x/L$ locations. $\alpha = 7.2^\circ$ , $t' = 4.238$ , $\alpha(t') = 7.2^\circ$ .	140
6.4	Comparison of barebody $C_f$ vs. $\phi$ distribution for steady and unsteady data at all $x/L$ locations. $\alpha = 9.3^\circ$ , $t' = 4.696$ , $\alpha(t') = 9.3^\circ$ .	141
6.5	Comparison of barebody $C_f$ vs. $\phi$ distribution for steady and unsteady data at all $x/L$ locations. $\alpha = 11.3^\circ$ , $t' = 5.307$ , $\alpha(t') = 11.3^\circ$ .	142
6.6	Comparison of barebody $C_f$ vs. $\phi$ distribution for steady and unsteady data at all $x/L$ locations. $\alpha = 13.2^\circ$ , $t' = 5.785$ , $\alpha(t') = 13.2^\circ$ .	143
6.7	Comparison of barebody $C_f$ vs. $\phi$ distribution for steady and unsteady data at all $x/L$ locations. $\alpha = 15.3^\circ$ , $t' = 6.128$ , $\alpha(t') = 15.3^\circ$ .	144
6.8	Comparison of barebody $C_f$ vs. $\phi$ distribution for steady and unsteady data at all $x/L$ locations. $\alpha = 17.4^\circ$ , $t' = 6.472$ , $\alpha(t') = 17.4^\circ$ .	145

6.9	Comparison of barebody $C_f$ vs. $\phi$ distribution for steady and unsteady data at all $x/L$ locations. $\alpha = 19.4^\circ$ , $t' = 6.815$ , $\alpha(t') = 19.4^\circ$ . . . . .	146
6.10	Comparison of barebody $C_f$ vs. $\phi$ distribution for steady and unsteady data at all $x/L$ locations. $\alpha = 21.4^\circ$ , $t' = 7.235$ , $\alpha(t') = 21.4^\circ$ . . . . .	147
6.11	Comparison of barebody $C_f$ vs. $\phi$ distribution for steady and unsteady data at all $x/L$ locations. $\alpha = 23.4^\circ$ , $t' = 7.655$ , $\alpha(t') = 23.4^\circ$ . . . . .	148
6.12	Comparison of barebody $C_f$ vs. $\phi$ distribution for steady and unsteady data at all $x/L$ locations. $\alpha = 25.5^\circ$ , $t' = 8.175$ , $\alpha(t') = 25.5^\circ$ . . . . .	149
6.13	Comparison of barebody $C_f$ vs. $\phi$ distribution for steady and unsteady data at all $x/L$ locations. $\alpha = 27.6^\circ$ , $t' = 10.290$ , $\alpha(t') = 27.6^\circ$ . . . . .	150
6.14	Comparison of sail-on-side (region without the sail) $C_f$ vs. $\phi$ distribution for steady and unsteady data at all $x/L$ locations. $\alpha = 3.1^\circ$ , $t' = 3.293$ , $\alpha(t') = 3.1^\circ$ . . . . .	151
6.15	Comparison of sail-on-side (region without the sail) $C_f$ vs. $\phi$ distribution for steady and unsteady data at all $x/L$ locations. $\alpha = 5.1^\circ$ , $t' = 3.742$ , $\alpha(t') = 5.1^\circ$ . . . . .	152
6.16	Comparison of sail-on-side (region without the sail) $C_f$ vs. $\phi$ distribution for steady and unsteady data at all $x/L$ locations. $\alpha = 7.2^\circ$ , $t' = 4.261$ , $\alpha(t') = 7.2^\circ$ . . . . .	153
6.17	Comparison of sail-on-side (region without the sail) $C_f$ vs. $\phi$ distribution for steady and unsteady data at all $x/L$ locations. $\alpha = 9.3^\circ$ , $t' = 4.7123$ , $\alpha(t') = 9.3^\circ$ . . . . .	154
6.18	Comparison of sail-on-side (region without the sail) $C_f$ vs. $\phi$ distribution for steady and unsteady data at all $x/L$ locations. $\alpha = 11.3^\circ$ , $t' = 5.197$ , $\alpha(t') = 11.3^\circ$ . . . . .	155
6.19	Comparison of sail-on-side (region without the sail) $C_f$ vs. $\phi$ distribution for steady and unsteady data at all $x/L$ locations. $\alpha = 13.2^\circ$ , $t' = 5.663$ , $\alpha(t') = 13.2^\circ$ . . . . .	156

6.20	Comparison of sail-on-side (region without the sail) $C_f$ vs. $\phi$ distribution for steady and unsteady data at all $x/L$ locations. $\alpha = 15.3^\circ$ , $t' = 6.070$ , $\alpha(t') = 15.3^\circ$ . . . . .	157
6.21	Comparison of sail-on-side (region without the sail) $C_f$ vs. $\phi$ distribution for steady and unsteady data at all $x/L$ locations. $\alpha = 17.4^\circ$ , $t' = 6.449$ , $\alpha(t') = 17.4^\circ$ . . . . .	158
6.22	Comparison of sail-on-side (region without the sail) $C_f$ vs. $\phi$ distribution for steady and unsteady data at all $x/L$ locations. $\alpha = 19.4^\circ$ , $t' = 6.827$ , $\alpha(t') = 19.4^\circ$ . . . . .	159
6.23	Comparison of sail-on-side (region without the sail) $C_f$ vs. $\phi$ distribution for steady and unsteady data at all $x/L$ locations. $\alpha = 21.4^\circ$ , $t' = 7.215$ , $\alpha(t') = 21.4^\circ$ . . . . .	160
6.24	Comparison of sail-on-side (region without the sail) $C_f$ vs. $\phi$ distribution for steady and unsteady data at all $x/L$ locations. $\alpha = 23.4^\circ$ , $t' = 7.626$ , $\alpha(t') = 23.4^\circ$ . . . . .	161
6.25	Comparison of sail-on-side (region without the sail) $C_f$ vs. $\phi$ distribution for steady and unsteady data at all $x/L$ locations. $\alpha = 25.5^\circ$ , $t' = 8.266$ , $\alpha(t') = 25.5^\circ$ . . . . .	162
6.26	Comparison of sail-on-side (region without the sail) $C_f$ vs. $\phi$ distribution for steady and unsteady data at all $x/L$ locations. $\alpha = 27.6^\circ$ , $t' = 10.290$ , $\alpha(t') = 27.6^\circ$ . . . . .	163
6.27	Comparison of sail-on-side (region with the sail) $C_f$ vs. $\phi$ distribution for steady and unsteady data at all $x/L$ locations. $\alpha = 3.1^\circ$ , $t' = 3.293$ , $\alpha(t') = 3.1^\circ$ . . . . .	164
6.28	Comparison of sail-on-side (region with the sail) $C_f$ vs. $\phi$ distribution for steady and unsteady data at all $x/L$ locations. $\alpha = 5.1^\circ$ , $t' = 3.742$ , $\alpha(t') = 5.1^\circ$ . . . . .	165
6.29	Comparison of sail-on-side (region with the sail) $C_f$ vs. $\phi$ distribution for steady and unsteady data at all $x/L$ locations. $\alpha = 7.2^\circ$ , $t' = 4.261$ , $\alpha(t') = 7.2^\circ$ . . . . .	166

6.30 Comparison of sail-on-side (region with the sail) $C_f$ vs. $\phi$ distribution for steady and unsteady data at all $x/L$ locations. $\alpha = 9.3^\circ$ , $t' = 4.7123$ , $\alpha(t') = 9.3^\circ$ . . . . .	167
6.31 Comparison of sail-on-side (region with the sail) $C_f$ vs. $\phi$ distribution for steady and unsteady data at all $x/L$ locations. $\alpha = 11.3^\circ$ , $t' = 5.197$ , $\alpha(t') = 11.3^\circ$ . . . . .	168
6.32 Comparison of sail-on-side (region with the sail) $C_f$ vs. $\phi$ distribution for steady and unsteady data at all $x/L$ locations. $\alpha = 13.2^\circ$ , $t' = 5.663$ , $\alpha(t') = 13.2^\circ$ . . . . .	169
6.33 Comparison of sail-on-side (region with the sail) $C_f$ vs. $\phi$ distribution for steady and unsteady data at all $x/L$ locations. $\alpha = 15.3^\circ$ , $t' = 6.070$ , $\alpha(t') = 15.3^\circ$ . . . . .	170
6.34 Comparison of sail-on-side (region with the sail) $C_f$ vs. $\phi$ distribution for steady and unsteady data at all $x/L$ locations. $\alpha = 17.4^\circ$ , $t' = 6.449$ , $\alpha(t') = 17.4^\circ$ . . . . .	171
6.35 Comparison of sail-on-side (region with the sail) $C_f$ vs. $\phi$ distribution for steady and unsteady data at all $x/L$ locations. $\alpha = 19.4^\circ$ , $t' = 6.827$ , $\alpha(t') = 19.4^\circ$ . . . . .	172
6.36 Comparison of sail-on-side (region with the sail) $C_f$ vs. $\phi$ distribution for steady and unsteady data at all $x/L$ locations. $\alpha = 21.4^\circ$ , $t' = 7.215$ , $\alpha(t') = 21.4^\circ$ . . . . .	173
6.37 Comparison of sail-on-side (region with the sail) $C_f$ vs. $\phi$ distribution for steady and unsteady data at all $x/L$ locations. $\alpha = 23.4^\circ$ , $t' = 7.626$ , $\alpha(t') = 23.4^\circ$ . . . . .	174
6.38 Comparison of sail-on-side (region with the sail) $C_f$ vs. $\phi$ distribution for steady and unsteady data at all $x/L$ locations. $\alpha = 25.5^\circ$ , $t' = 8.266$ , $\alpha(t') = 25.5^\circ$ . . . . .	175
6.39 Comparison of sail-on-side (region with the sail) $C_f$ vs. $\phi$ distribution for steady and unsteady data at all $x/L$ locations. $\alpha = 27.6^\circ$ , $t' = 10.290$ , $\alpha(t') = 27.6^\circ$ . . . . .	176

6.40	First-order differential lag approximation to the unsteady separation data at $x/L = 0.266$ for the barebody case. . . . .	177
6.41	First-order differential lag approximation to the unsteady separation data at $x/L = 0.306$ for the barebody case. . . . .	177
6.42	First-order differential lag approximation to the unsteady separation data at $x/L = 0.345$ for the barebody case. . . . .	178
6.43	First-order differential lag approximation to the unsteady separation data at $x/L = 0.434$ for the barebody case. . . . .	178
6.44	First-order differential lag approximation to the unsteady separation data at $x/L = 0.501$ for the barebody case. . . . .	179
6.45	First-order differential lag approximation to the unsteady separation data at $x/L = 0.570$ for the barebody case. . . . .	179
6.46	First-order differential lag approximation to the unsteady separation data at $x/L = 0.638$ for the barebody case. . . . .	180
6.47	First-order differential lag approximation to the unsteady separation data at $x/L = 0.706$ for the barebody case. . . . .	180
6.48	First-order differential lag approximation to the unsteady separation data at $x/L = 0.774$ for the barebody case. . . . .	181
6.49	First-order differential lag approximation to the unsteady separation data at $x/L = 0.819$ for the barebody case. . . . .	181
6.50	First-order differential lag approximation to the unsteady separation data at $x/L = 0.266$ for the non-sail region of the sail-on-side case. . . . .	182
6.51	First-order differential lag approximation to the unsteady separation data at $x/L = 0.306$ for the non-sail region of the sail-on-side case. . . . .	182
6.52	First-order differential lag approximation to the unsteady separation data at $x/L = 0.345$ for the non-sail region of the sail-on-side case. . . . .	183
6.53	First-order differential lag approximation to the unsteady separation data at $x/L = 0.434$ for the non-sail region of the sail-on-side case. . . . .	183

6.54	First-order differential lag approximation to the unsteady separation data at $x/L = 0.501$ for the non-sail region of the sail-on-side case. . . . .	184
6.55	First-order differential lag approximation to the unsteady separation data at $x/L = 0.570$ for the non-sail region of the sail-on-side case. . . . .	184
6.56	First-order differential lag approximation to the unsteady separation data at $x/L = 0.638$ for the non-sail region of the sail-on-side case. . . . .	185
6.57	First-order differential lag approximation to the unsteady separation data at $x/L = 0.706$ for the non-sail region of the sail-on-side case. . . . .	185
6.58	First-order differential lag approximation to the unsteady separation data at $x/L = 0.774$ for the non-sail region of the sail-on-side case. . . . .	186
6.59	First-order differential lag approximation to the unsteady separation data at $x/L = 0.819$ for the non-sail region of the sail-on-side case. . . . .	186
6.60	Steady and unsteady separation locations (second minima in $C_f$ measured from $\phi = 180^\circ$ ) vs $t'$ at $x/L = 0.434$ for the sail region of the sail-on-side case. . . . .	187
6.61	Steady and unsteady separation locations (second minima in $C_f$ measured from $\phi = 180^\circ$ ) vs $t'$ at $x/L = 0.501$ for the sail region of the sail-on-side case. . . . .	187
6.62	Steady and unsteady separation locations (second minima in $C_f$ measured from $\phi = 180^\circ$ ) vs $t'$ at $x/L = 0.570$ for the sail region of the sail-on-side case. . . . .	188
6.63	Steady and unsteady separation locations (second minima in $C_f$ measured from $\phi = 180^\circ$ ) vs $t'$ at $x/L = 0.638$ for the sail region of the sail-on-side case. . . . .	188
6.64	Steady and unsteady separation locations (second minima in $C_f$ measured from $\phi = 180^\circ$ ) vs $t'$ at $x/L = 0.706$ for the sail region of the sail-on-side case. . . . .	189

6.65	Steady and unsteady separation locations (second minima in $C_f$ measured from $\phi = 180^\circ$ ) vs $t'$ at $x/L = 0.774$ for the sail region of the sail-on-side case. . . . .	189
6.66	Steady and unsteady separation locations (second minima in $C_f$ measured from $\phi = 180^\circ$ ) vs $t'$ at $x/L = 0.819$ for the sail region of the sail-on-side case. . . . .	190
6.67	Incremental effective angle of attack $\Delta\alpha_{eff}$ for the barebody pitch-up maneuver at four $x/L$ stations as a function of instantaneous angle of attack $\alpha(t')$ . Open symbols show the $\Delta\alpha_{eff}$ given by the equation 6.17.(Both angles are in degrees) . . . . .	190
6.68	Computed time lags as a function of $x/L$ for the barebody and the non-sail region of the sail-on-side case. . . . .	191
B.1	Loess smoothing for unsteady barebody data at $\alpha(t') = 11.3^\circ$ and $x/L = 0.819$ . . . . .	206
B.2	Loess smoothing for unsteady barebody data at $\alpha(t') = 21.5^\circ$ and $x/L = 0.638$ . . . . .	206

# List of Tables

1.1	Summary of the test conditions from some unsteady aero/hydrodynamic experiments (modified from Wetzels and Simpson [3]) . . . . .	5
2.1	Hot-film sensor locations (port number is the order of the sensors in $x/L$ direction starting from the nose). . . . .	23
3.1	Darpa2 steady skin-friction measurements . . . . .	30
3.2	Darpa2 unsteady skin-friction measurements . . . . .	31
3.3	Darpa2 pressure measurements . . . . .	32
4.1	Boundary layer properties at $U_e = 80, 95$ and $110$ ft/s. . . . .	40



# Chapter 1

## Introduction

### 1.1 Unsteady Aerodynamics

The study of truly unsteady, high-excursion and high-Reynolds Number separated flows over submarines, aircraft or missiles has become of great importance in the analysis and the improvement of the dynamic performance. Because of highly complex, three-dimensional, turbulent and separated nature, standard stability derivative techniques fail to capture the nonlinearities in these flows and Computational Fluid Dynamics (CFD) techniques need physical models that can resolve the complexities of such flow fields in order to get accurate and more reliable results. Suitable simulation of the time-dependent maneuvers in the wind tunnels is not only important for understanding the physics of complex flow phenomena, but also supplies the necessary information required for developing the realistic unsteady physical flow models. The DyPPiR (Dynamic plunge-pitch-roll) model mount, a computer controlled, three degrees of freedom robotic arm at the Stability Wind Tunnel of Virginia Tech, provides the unique capability of performing pre-programmed general, high-excursion, large scale, high-Reynolds Number unsteady maneuvers [4].

Dynamic testing has been an important part of design and validation of various types of craft for decades. Typically these techniques are only *quasi-steady*, relying on very small amplitude sinusoidal oscillations that can describe small-excursion maneuvers reasonably well [2]. As discussed by Wetzel and Simpson [3], there is a significant difference between

quasi-steady and unsteady aerodynamics. In a quasi-steady approach, the aerodynamics of a maneuvering body are dependent only on the instantaneous state of the model ( $\alpha$  angle of attack,  $\beta$  sideslip angle, control surface deflections, etc.), whereas in fully general unsteady aerodynamics, explicit time dependency, or history effects are also included. Mathematically the distinction between quasi-steady and unsteady aerodynamics can be shown as follows: steady,  $\mathbf{F}(\alpha, \beta, \dots)$ ; quasi-steady,  $\mathbf{F}[\alpha(t'), \beta(t'), \dots]$ ; and fully unsteady  $\mathbf{G}[t', \alpha(t'), \dot{\alpha}(t'), \beta(t'), \dot{\beta}(t'), \dots]$  where  $\mathbf{F}$  and  $\mathbf{G}$  can be a dominant flow feature such as separation location. Here  $t'$  is the non-dimensional time defined by Etkin [5]:

$$t' = \frac{t}{t_{ref}} = \frac{tU_\infty}{L} \quad (1.1)$$

$t_{ref}$  represents the time for the flow to pass over a model:  $L/U_\infty$ . The non-dimensional time  $t'$  relates the unsteady wind tunnel tests to the real-time maneuvers. This non-dimensionalization follows the approach that is used to non-dimensionalize the variables in the equations of motion of aircraft dynamics [5] and it does not include any viscous terms. However the onset and the propagation of the three-dimensional unsteady flow separation, which is a frequent flow phenomena seen over a vehicle undergoing a typical, high-excursion, and truly unsteady maneuver, are strongly influenced by the viscous effects. Reynolds number based on the model length (or any other appropriate characteristic length)  $Re_L = \rho U_\infty L / \mu$  representing the ratio of the inertial forces to the viscous forces, is another important parameter to be considered during the unsteady wind tunnel testing. The type of the flow separation (laminar or turbulent), and the transition location on the model surface are strong functions of the Reynolds number until a *critical* value is reached. Beyond this critical value of  $Re_L$ , the separation type and locations become less sensitive to the Reynolds number effects. In some experiments, it may be impossible to simulate the real flow Reynolds number (such as  $Re_L$  for submarines, big transport airplanes etc.) due the model size or the wind tunnel speed limitations. In this study and some of the previous unsteady experiments done at Virginia Tech, specially designed boundary layer trips are used to simulate higher Reynolds number flows and to fix the transition location that will produce a less Reynolds-number-sensitive separation.

Besides quantitative differences between the steady and the unsteady aerodynamic parameters such as the skin-friction, force and moment coefficients, the qualitative nature of the unsteady flow fields also differ from the steady ones. In fact, the quantitative variations are the results that originate from flow topology differences between the steady and

the unsteady flow fields. As an example, in the crossflow separation phenomena discussed in this study and previous prolate spheroid work [2], the history effects mainly cause time lags between the unsteady and the corresponding quasi-steady flow fields, which can be quantified by measuring the flow separation locations. Approximating these time lags by the models that can explain the *real physics* of the three-dimensional, turbulent, unsteady flow separation is a big challenge in the field of aerodynamics as well as acquiring unsteady data. One of the main purposes of this study is to apply such an approximation to the unsteady separation locations measured on the DARPA2 model.

## 1.2 Three-Dimensional Separations

Both the steady and the unsteady flow fields over the DARPA2 model used in this study are dominated by the three-dimensional flow separation after a certain angle of attack. As described by Simpson [6], separation is the entire process of *departure* or *breakaway*, or the breakdown of the boundary layer flow. An abrupt thickening of the rotational-flow region next to a wall and significant values of the normal-to-wall velocity component  $V$  must accompany breakaway, or otherwise this region will not have significant interaction with the inviscid free-stream flow. As can be seen from figure 1.1, surface skin-friction lines converge on each side of the separation line. Along this separation line, there exists a stream surface across which no flow from one side of the separation line can pass to the other side.

Three-dimensional (3-D) separations can be classified in three groups with respect to their topology and kinematics (figure 1.1): (a) horseshoe type; (b) Werle type; and (c) crossflow separations. In Yates and Chapman [1], horseshoe and Werle type separations are defined as *global separations* (or *closed separations*). These always have a saddle point of separation on the surface. Figure 1.1 (c) shows the local or the crossflow separation topology. No 3-D critical points on the surface or in the flow can be observed in such type of flows and the center of a separated vortex structure has minimum streamline curvature.

The horseshoe type and the crossflow separation are of particular interest in this study: the flow field in the vicinity and the downstream of the sail is dominated by the horseshoe type separation and the crossflow separation is the main flow characteristic on the leeward

of the DARPA2 model at an angle of attack for steady and the unsteady measurements. The circumferential pressure gradient is the dominant factor in the crossflow separation process. Figure 1.2 shows the on-axis cross sectional view of the secondary flow streamlines from a crossflow separation: S1 is the primary separation location and S2 stands for the secondary separation location. R1 and R2 locate the primary and the secondary reattachment positions. At low angles of attack, only the primary separation is observed on the leeward side of the model and as the angle of attack increases the primary separation line moves towards the windward side. After a certain angle of attack, the secondary separation line on the leeward side of the model can be observed.

Besides qualitative verification of the crossflow separation, one is also interested in finding the actual values of the separation locations. Simpson [6] shows that the wall shear provides lower order information about the separation location than the pressure by analyzing the continuity and the momentum equations near the wall:

$$V = -\frac{1}{2\mu} (\nabla \cdot \vec{\tau}_w) y^2 + \frac{1}{6\mu} (\nabla^2 p) y^3 + \dots \quad (1.2)$$

Time-averaged wall pressure measurements are relatively insensitive to the flow separation and only *massive* separations are detected from time-averaged wall pressure measurements [6]. In order to use equation 1.2 rigorously, the entire wall shear direction and the magnitude fields should be known to perform the divergence operation on the right hand side for finding normal-to-wall velocity  $V$  at all points on the body and to determine the separation location. This approach is impractical due to the large number of sensors that should be used. As an alternative, Simpson et al. [7] showed that the local minimum of the circumferential skin-friction distribution is a good approximation of separation location. By using this fact, directionally insensitive hot-film sensors are used to measure the magnitudes of the skin-friction on the model surface in this study. The local minima are used for the determination of the steady and the unsteady separation locations.

## 1.3 Previous Studies

Table 1.1 gives a summary of the test conditions from some previous unsteady three-dimensional aero/hydrodynamic experiments relevant to this study. In the last row of

Table 1.1: Summary of the test conditions from some unsteady aero/hydrodynamic experiments (modified from Wetzel and Simpson [3])

<i>Authors</i>	<i>Model</i>	<i>Tunnel</i>	$Re_L$	$\bar{\alpha} = \dot{\alpha} \frac{L}{U_\infty}$	$\alpha$ range	<i>Measurements</i>
Gad-el-hak and Ho [8]	ogive cylinder	water	40,000	1.05	0 ° to 30 °	flow vis.
Montividas et al. [9]	cone cylinder	wind	56,650	0.7	0 ° to 90 °	flow vis., wake LDV
Smith and Nunn [10]	ogive cylinder	wind	1,200,000	0.0405	-15 ° to 105 °	flow vis., force & moments
Panzer et al. [11]	hemisphere cylinder	wind	229,000	0.0065	15 ° to 30 °	wake LDV
Panzer et al. [11]	hemisphere cylinder	water	75,000	0.1	15 ° to 30 °	wake LDV
Brandon and Shah [12]	F-18	wind	1,600,000	0.0364	-10 ° to 80 °	flow vis., force, & moments
Wetzel and Simpson [3]	6:1 prolate spheroid	wind	4,200,000	0.047	0 ° to 30 °	hot-film
Whitfield [13]	DARPA2 Suboff	wind	5,500,000	0.076	0 ° to 25 °	force & moments
<b>Hosder (current study)</b>	<b>DARPA2 Suboff</b>	<b>wind</b>	<b>5,500,000</b>	<b>0.071</b>	<b>1 ° to 27 °</b>	<b>hot-film</b>

this table, information about the current work is presented. The maneuvers performed for all the experiments shown are the pitchup motions. The model geometry, experimental facility, Reynolds number  $Re_L$ , non-dimensional pitch rate  $\bar{\alpha}$ ,  $\alpha$  range, and the measurement technique of each study can be compared by using table 1.1. In terms of  $Re_L$ , the prolate spheroid study of Wetzel and Simpson [3], DARPA2 Suboff study of Whitfield [13] and the present study can be considered as the only experiments that have high Reynolds number well above the critical value. Therefore the separation locations in these experiments are least likely to be sensitive to the Reynolds number effect. These three studies are performed at Virginia Tech Stability Wind Tunnel with the DyPPiR

and the boundary layer tripping are used for all three. The current study uses the same model geometry and the maneuver type as the ones in Whitfield's force and moment study [13]. In fact these two experiments are complementary in the sense that different measurement techniques are used to describe the whole picture of the same unsteady phenomena over the same geometry.

Among the previous studies, the unsteady crossflow separation location measurements on a maneuvering 6:1 prolate spheroid model by Wetzel and Simpson [3] can be considered as the most similar work to the one presented here in terms of the experimental measurement technique and the unsteady high-excursion maneuvers performed. In that study, they have determined significant lags in the unsteady flow separation locations on the prolate spheroid undergoing pitch-up and turning maneuvers compared with the steady data. Wetzel and Simpson [3] also found that a first-order lag model fits the unsteady data. Present work and the prolate spheroid study are the only experiments that utilize fine spatial resolution surface hot-film measurements to determine the unsteady skin-friction magnitudes and the separation locations on a maneuvering body. Most of the previous work uses different techniques and focuses on flow features other than separation, such as vortex location and breakdown [3].

## 1.4 Present Work

In the present work, unsteady turbulent surface flow on a maneuvering DARPA2 submarine model is studied. Hot-film sensors are used to measure the steady and the unsteady skin-friction magnitudes over the body surface. Local minima of the skin-friction magnitude are used to determine the separation locations. Steady skin-friction measurements are obtained at fourteen steady angles of attack. Unsteady maneuvers include the ramp pitchup maneuvers simulated by the DyPPiR. Mean wall static pressures are measured at  $10^\circ$  and  $20^\circ$  angles of attack. Surface oil flow visualizations are also used in order to examine the steady surface flow topology and the separation locations qualitatively. Both steady and unsteady tests are performed for two model configurations: The barebody (axisymmetric case) and the body with the sail (sail-on-side case).

Steady and the unsteady results obtained in this study give valuable information about the complex surface flow structure over the DARPA2 submarine model. The steady skin-

friction values and mean pressure measurements are used to describe the steady flow-field topology. Unsteady data show the difference between the steady and the unsteady flow-fields, especially in the separation topology. In this study, a first-order time lag model is used to approximate the unsteady data. The results of this approximation as well as the unsteady data may supply important information to the development of the realistic flow models to be used in calculating the unsteady 3-D flows over complex geometries.

The organization of the chapters here can be summarized as follows. In chapter 2, the experimental apparatus, facilities and techniques are described. This chapter gives the details about the DyPPiR, hot-film sensors, constant temperature anemometers and the pressure measurement system used in the experiments. The wind tunnel model including the geometry, different configurations and integration of the sensors is also described. Chapter 3 gives the test conditions and describes the steady measurements and the unsteady maneuvers performed in this study. Calibration of the hot-film sensors is explained in chapter 4. Chapter 5 includes the results obtained from the steady skin-friction and pressure measurements. The discussion about the data and conclusions based on the steady results are presented. The steady data reduction procedure both for the hot-film and the pressure measurements is also described in this chapter. The unsteady results and the data reduction procedure are presented in chapter 6. The unsteady flow topology and the differences between the steady and the unsteady flow fields are discussed. This chapter also includes the algebraic and the first-order time lag model approximations to the unsteady separation location data. Discussion about the unsteady data and the time lag approximation results are given. The last chapter presents the overall conclusions obtained from this study. Uncertainties in the measured skin-friction values and the related uncertainty calculations are included in the appendices.

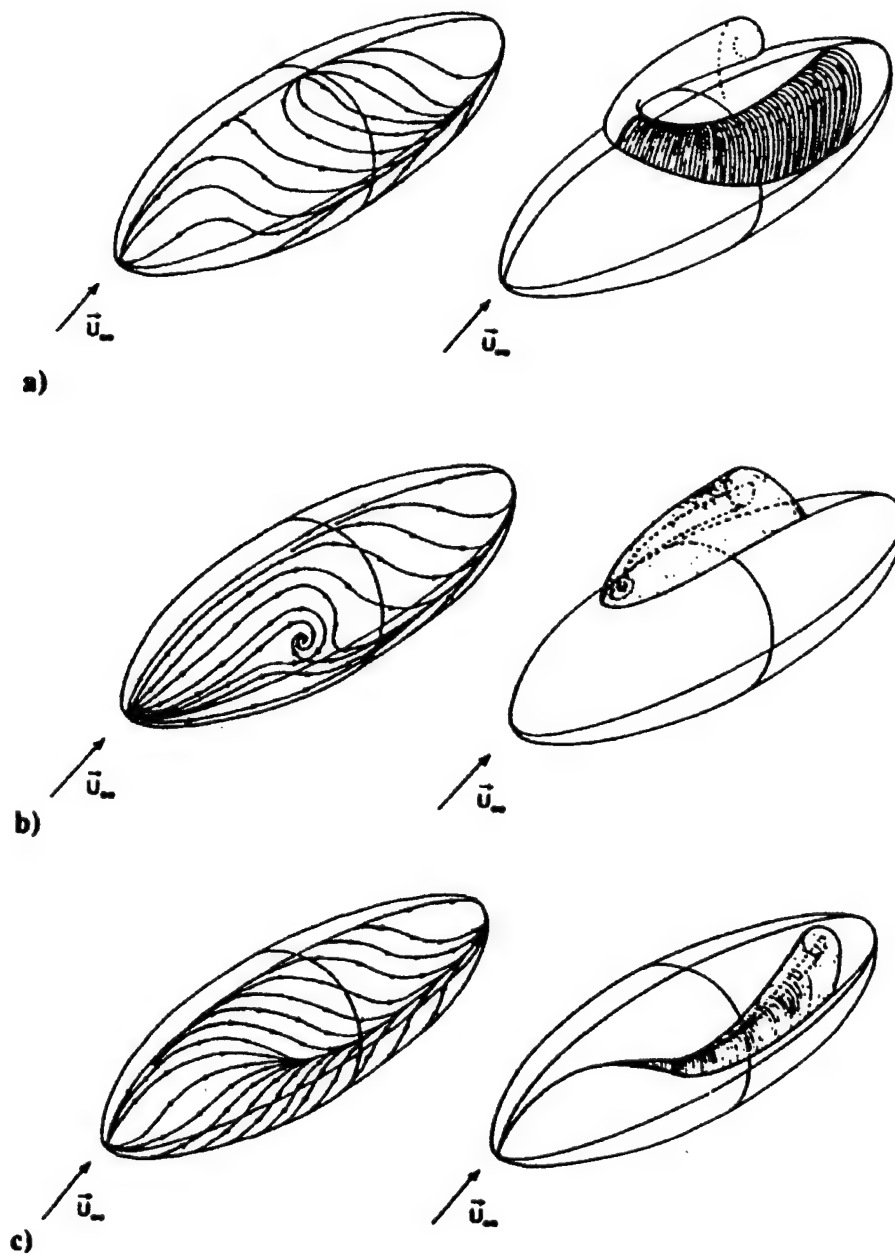


Figure 1.1: Limiting streamline pattern and surfaces of separation for three types of 3-D separation: (a) horseshoe type separation; (b) Werle type separation (the view of the surface separation is rotated  $90^\circ$  from the view of the limiting streamline pattern); (c) cross flow separation. Taken from Yates and Chapman [1].



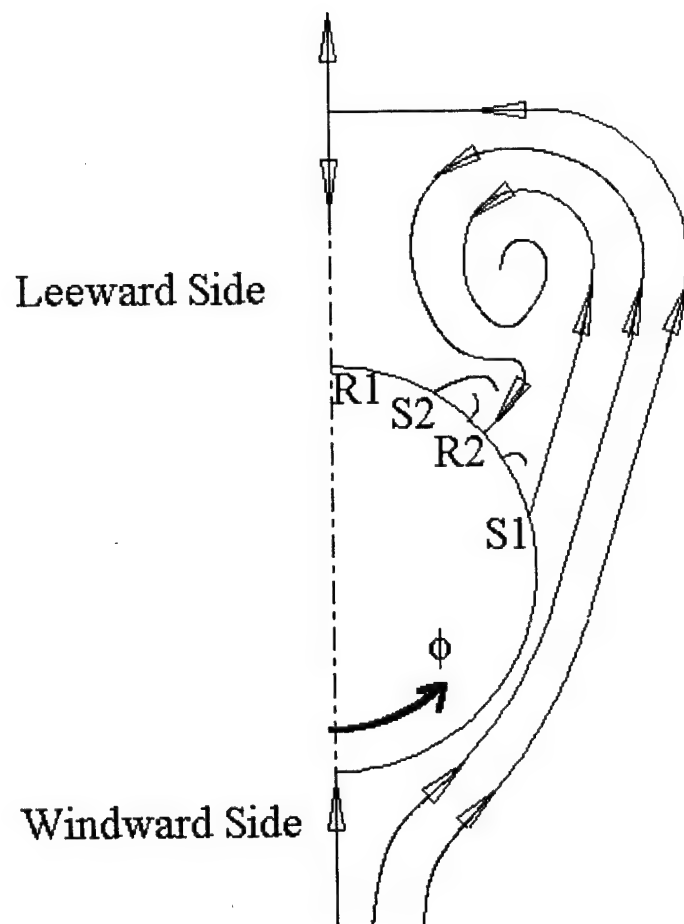


Figure 1.2: On-axis cross sectional view of secondary flow streamlines from a crossflow separation. P1: primary separation, P2: secondary separation, R1: Primary reattachment, R2: secondary reattachment.

## Chapter 2

# Experimental Facilities, Equipment and Apparatus

### 2.1 Stability Wind Tunnel

The Virginia Tech Stability Wind tunnel is a continuous, closed jet, single return, subsonic wind tunnel with six foot cross section interchangeable test sections. Each test section is 24 feet long. The tunnel is powered by a 600 HP D.C. motor driving a 14 foot propeller [4]. Surface flow experiments on DARPA2 model has been performed in  $6' \times 6'$  square test section. In this configuration, a maximum speed of  $275 \text{ ft/s}$  and a Reynolds number up to  $1.66 \times 10^6$  per foot can be obtained.

Tunnel speed is regulated by a custom designed Emerson VIP ES-6600 SCR Drive. This drive system eliminates all the cyclic unsteadiness in tunnel velocities and turbulence inducing vibrations inherent with older systems. The Stability Tunnel has a low turbulence intensity. The small-scale turbulence intensity is on the order of 0.03% or less depending on the tunnel speed. The unsteadiness due to large-scale pulsation of the fan was also found to be on the order of 0.03% [4].

The tunnel temperature is stabilized by the use of an air exchange tower. After a certain amount of operation time, tunnel temperature becomes equal to the outside temperature. Therefore the changes in the outside temperature directly effects the tunnel temperature. Since the hot-film sensors are sensitive to the ambient flow temperature as well as the

local skin-friction value, the changes in the free-stream temperature should be taken into account in the data acquisition and the reduction process.

Surface hot-film measurements on DARPA2 model have been performed in a slotted-wall test section with 38% open air ratio. The main purpose for using the slotted-wall configuration in the experiments is to reduce the blockage effects typically encountered during testing at high angles of attack with large models. More information about the slotted wall configuration in the stability tunnel can be found in [14]. Figure 2.1 shows the top view of the Stability Wind Tunnel.

## 2.2 DyPPiR

Unsteady maneuvers have been performed by using the **D**ynamic **P**lunge, **P**itch and **R**oll actuator of the Virginia Tech Stability Wind Tunnel, also known as the *DyPPiR*. The DyPPiR was designed to provide the unique capability of performing general, high excursion, large scale, high Reynolds number, unsteady maneuvers [4]. The DyPPiR has three degrees of freedom: plunge with a range of  $\pm 0.64$  m measured from the tunnel centerline, pitch with a motion range of  $\pm 45^\circ$  and roll with a range of  $\pm 140^\circ$ . For each degree of freedom, there is an independent 3000 psi hydraulic actuator which can move a maximum model load of 45 kg and 250 kg of hardware load at rates approaching 9 m/s in plunge and 120  $^\circ$ /s in pitch. The DyPPiR has also the capability of performing maneuvers around an arbitrary model center of rotation, which is important for obtaining the correct lateral velocities across the aircraft, missiles and submarines. The DyPPiR is computer controlled and in addition to traditional sinusoidal, ramp and snaking maneuvers, any pre-programmed *real* maneuver can be simulated, including time history effects. Previous tests have confirmed that the sting mount places the model far enough from the main DyPPiR strut to make strut interference negligible [3]. Figure 2.2 shows the DyPPiR installed in the stability wind tunnel. For DARPA2 experiments, besides unsteady maneuvers, the DyPPiR has also been used as a computer controlled model mount for the steady skin friction measurements. Due to a technical problem in the hydraulically powered roll actuator, a manually controlled dummy roll actuator has been built and used to change the roll angle of the model. This enabled a full 360 $^\circ$  coverage of the model roll orientation. The coordinate nomenclature for the DyPPiR and the model

is shown in figure 2.3:  $x$  is measured from the nose,  $\phi$  is the circumferential location measured from the windward line of symmetry,  $z$  is the plunge ordinate, and  $\alpha$  is the pitch angle and equivalently the model center of rotation angle of attack.

## 2.3 Data Acquisition System

The tunnel data acquisition system has been used for sampling the analog signals from each hot-film anemometer as well as recording tunnel dynamic pressure, static pressure and the tunnel temperature in steady and unsteady skin friction measurements. Since the tunnel data acquisition system is incorporated and synchronized with the DyPPiR control system, it has also been used for recording the plunge, pitch and roll command and feedback signals (voltage values). These values were converted to proper dimensional units by using a linear calibration routine which gave the location and the orientation of the model as a function of time.

The centerpiece of the system is an SCXI-1001 Mainframe from National Instruments. The mainframe allows for the installation of up to 12 SCXI modules which may perform any desired signal conditioning and sampling of the input signals. Currently four SCXI-1120D isolation modules are installed in the mainframe. Each of these modules allows isolation and amplification of 8 differential analog voltages with an input range of  $-10$  to  $+10$  volts. Each module multiplexes the 8 inputs which are read by a National Instruments AT-MIO-16-XE-10 Data Acquisition Card installed in the tunnel computer. This results in a total of 32 isolated differential analog input channels with an Analog to Digital conversion resolution of 16 bits. The software used for data acquisition is written using LabView 4.0 under the Windows NT environment.

## 2.4 Skin-Friction Measurement System

Hot-film sensors mounted on the surface of the DARPA2 model were used to measure steady and unsteady skin friction magnitudes in the experiments. Each hot-film sensor was connected to a constant temperature type anemometer. Hot-film sensors and the constant temperature anemometers were the same as the ones used by Wetzel [2] in his prolate spheroid study.

### 2.4.1 Hot-film Sensors

#### Theory of Operation

The thermal or hot-film sensor benefits from the fact that the heat transfer from a sufficiently small heated surface depends only on the flow characteristics in the viscous region of the boundary layer [15]. Due to the similarity between gradient transport of momentum and scalars (heat), the amount of heat transfer into the fluid gives a measure of the wall shear stress  $\tau_w$ . The hot-film gauge consists of a thin metallic film positioned into a substrate. Usually the gauge forms one part of a Wheatstone bridge in the anemometer circuit and an electric current is passed through the film in order to maintain it at constant temperature (if a constant temperature anemometer is used) as heat is continuously being transferred from the film to the moving fluid as well as to the film's substrate.

The ohmic (joule) heating in the device  $Q_j$  is transferred both to the fluid and to the surrounding substrate. This can be expressed as:

$$Q_j = Q_s + Q_f \quad (2.1)$$

where  $Q_f$  represents the average heat transferred to the fluid directly from the heated surface and indirectly through the heated portion of the substrate.  $Q_s$  represents the average heat lost irretrievably to the substrate.

The relationship between the heat transfer  $Q_f$  and the wall shear stress  $\tau_w$  can be obtained by making an unheated starting length forced convection analysis from a single heated sensor [7]. It is assumed that the thermal boundary layer developed on the sensor is within the viscous sublayer of a pre-existing momentum boundary layer.

We start our derivation for the relationship between  $Q_f$  and  $\tau_w$  with the thermal energy transport equation near the wall for locally two dimensional flow:

$$U \frac{\partial T}{\partial x} = \alpha \frac{\partial^2 T}{\partial y^2} \quad (2.2)$$

Here  $x$  is the streamwise coordinate and  $y$  represents the normal-to-wall coordinate. The temperature is  $T$ ,  $U$  is the velocity in the  $x$  direction, and  $\alpha$  is the thermal diffusivity. Since the flow upstream of the sensor is unheated, the incoming flow temperature is the same as the free-stream temperature  $T_\infty$ . We assume the sensor length in the streamwise

direction is short enough so that the thermal boundary layer grows from the upstream edge of the sensor, but remains entirely within the near wall region. In the viscous sublayer, we can approximate  $U$  as:

$$U = \left( \frac{\partial U}{\partial y} \right)_w y \quad (2.3)$$

where  $\left( \frac{\partial U}{\partial y} \right)_w$  is the mean velocity gradient at the wall and the shear stress at the wall is given by:

$$\tau_w = \mu \left( \frac{\partial U}{\partial y} \right)_w \quad (2.4)$$

Here  $\mu$  is the dynamic viscosity of the fluid. By putting non-dimensional temperature  $\tilde{T}$

$$\tilde{T} = \frac{T - T_w}{T_\infty - T_w} \quad (2.5)$$

into equation 2.2 and using equation 2.3, we will have:

$$\left( \frac{\partial U}{\partial y} \right)_w y \frac{\partial \tilde{T}}{\partial x} = \alpha \frac{\partial^2 \tilde{T}}{\partial y^2} \quad (2.6)$$

The boundary conditions for this problem in terms of  $\tilde{T}$  would be:

$$\tilde{T} = 0 \quad \text{at} \quad y = 0 \quad (2.7)$$

$$\tilde{T} = 1 \quad \text{as} \quad y \rightarrow \infty \quad (2.8)$$

$$\tilde{T} = 1 \quad \text{at} \quad x = 0 \quad (2.9)$$

To reduce the partial differential equation given by 2.6 to an ordinary differential equation, we introduce the similarity parameter  $\eta$  defined as:

$$\eta = \frac{y \left( \frac{\partial U}{\partial y} \right)_w^{1/3}}{(3\alpha x)^{1/3}} \quad (2.10)$$

And the resulting ordinary differential equation would be:

$$\tilde{T}'' + \eta^2 \tilde{T}' = 0 \quad (2.11)$$

Boundary conditions for equation 2.11 in terms of  $\eta$  become:

$$\tilde{T} = 0 \quad \text{at} \quad \eta = 0 \quad (2.12)$$

$$\tilde{T} = 1 \quad \text{as} \quad \eta \rightarrow \infty \quad (2.13)$$

The solution of the ordinary differential equation can be obtained as:

$$\tilde{T} = M \int_0^\eta e^{-\eta^3/3} d\eta \quad (2.14)$$

where

$$M^{-1} = \int_0^\infty e^{-\eta^3/3} d\eta = \frac{1}{3} \Gamma\left(\frac{1}{3}\right) = 0.893 \quad (2.15)$$

The heat flux at the surface is given by:

$$q_w = -k \left( \frac{\partial T}{\partial y} \right)_w = -k(T_\infty - T_w) \left( \frac{\partial \tilde{T}}{\partial y} \right)_w \quad (2.16)$$

Here  $k$  is the thermal conductivity. By using equation 2.14 and the chain rule;

$$\frac{\partial \tilde{T}}{\partial y} = \frac{\partial \tilde{T}}{\partial \eta} \frac{\partial \eta}{\partial y} \quad (2.17)$$

we obtain  $q_w$  as:

$$q_w = Mk(T_\infty - T_w) \frac{\left( \frac{\partial U}{\partial y} \right)_w^{1/3}}{(3\alpha x)^{1/3}} \quad (2.18)$$

Assuming that we have a rectangular sensor of constant width  $w$  in the spanwise direction and length of  $l$  in the streamwise direction, we can obtain the average heat transfer rate  $Q_f$  by integrating  $q_w$  over  $w$  and  $l$ :

$$Q_f = w \int_0^l q_w dx = \frac{3}{2} Mk(T_w - T_\infty) \frac{\left( \frac{\partial U}{\partial y} \right)_w^{1/3}}{(3\alpha)^{1/3}} l^{2/3} \quad (2.19)$$

Then by definition mean film coefficient  $\bar{h}$  would be equal to:

$$\bar{h} = \frac{Q_f}{(T_w - T_\infty)} = \frac{3}{2} Mklw \frac{\left( \frac{\partial U}{\partial y} \right)_w^{1/3}}{(3\alpha l)^{1/3}} \quad (2.20)$$

As can be seen from equation 2.20,  $\bar{h}$  is directly proportional to  $\left( \frac{\partial U}{\partial y} \right)_w^{1/3}$ , thus the wall shear stress  $\tau_w$ . All the other parameters are properties of the fluid and the sensor.  $T_w$  represents the temperature of the hot-film sensor and in case a constant temperature anemometer circuit is used, this temperature remains constant. In the ideal case, the free-stream temperature  $T_\infty$  can also be considered as constant although in most cases, especially in long experimental run periods, there may be considerable changes in the

flow temperature. (This issue and the effects of free-stream temperature change to the calibration of the hot-film sensors will be discussed in chapter 4).

If we assume that the heat transfer to the substrate is minimized by using isolation methods and negligible, then in equation 2.1, the joule heating  $Q_j$  will be equal to the heat transfer to the fluid  $Q_f$ . For the hot-film sensor, we can write the joule heating term as:

$$Q_j = Q_f = \frac{E^2}{R_w} \quad (2.21)$$

where  $E$  is the voltage value across the hot-film sensor, and  $R_w$  is the resistance of the hot-film sensor at its operating temperature  $T_w$ . Since  $T_w$  is constant for a constant temperature anemometer, then  $R_w$  will also be constant by considering the well-known equation:

$$R_w = R_c [1 + \alpha_R (T_w - T_c)] \quad (2.22)$$

In the above equation,  $R_c$  is the resistance of the hot-film in a known temperature  $T_c$  and  $\alpha_R$  is the temperature coefficient of resistivity. By using equation 2.20 in accordance with the equation 2.21;

$$\frac{E^2}{T_w - T_\infty} \propto \tau_w^{1/3} \quad (2.23)$$

Therefore, after a proper calibration, one can determine the shear stress value  $\tau_w$  by measuring  $E$ .

### Specifications of the Hot-film Sensors used in the Experiments

To measure the skin-friction, hot-film sensors designed and documented by Simpson et al. [7] were used. Figure 2.4 shows the top view of a typical sensor. The hot-film sensors are made of Balco foil (70% nickel, 30% iron) with a nominal temperature coefficient of resistivity of  $0.0051/^\circ C$  and are manufactured by the MINCO, Inc. The main sensing part of the sensor is a spiral of 5.1 mm in diameter which is approximately 0.23% of the model length. At the constant diameter section of the model, the sensor occupies  $2.184^\circ$  of the model surface along the circumference. The foil sensor is bonded to a kapton substrate and the total sensor thickness is 0.0635 mm. Sensors are connected to the constant temperature anemometers by 22 AWG wires, which are soldered on the two tabs of the foil.



It should be noted that the hot-film sensors have been designed to measure only the magnitude of the skin-friction as described in Simpson et al. [7]. However, in his prolate spheroid study, Wetzel [2] detected a directional sensitivity of as much as  $\pm 5\%$ . He reduced the directional sensitivity effects to less than 3% by mounting the sensors at  $65^\circ$  off the longitudinal line on the model surface. In this study, the sensors were placed parallel to the longitudinal line on the model surface. Wetzel [2] also showed that the sensors are incapable of resolving small scale turbulence structures due to the relatively large sensor size. The skin-friction magnitudes measured by the hot-film sensors are actually the values spatially-averaged over the sensing spiral part.

### 2.4.2 Constant Temperature Anemometers

The hot-film sensors were operated with Miller-type non-linearized constant temperature anemometers [16]. The original boards were modified by Wetzel [2] in the prolate spheroid study. For the Suboff tests, some further adjustments were made in order to increase the stability of the anemometers and to reduce the noise associated with the electronics. The main power supply was replaced with a new one that can supply sufficient amount of current to each anemometer at long run periods and at relatively high speeds. This change enabled the use of fifteen anemometers simultaneously during the tests without any power loss. Some of the op-amps in the anemometer circuits that were not functioning properly were replaced with the new ones and this reduced the noise level significantly. All the channels were grounded properly. Some of the current knobs were replaced with the new ones in order to increase the accuracy of setting the overheat ratio. Constant temperature anemometers had a bridge ratio of 60 and the hot-film sensors were operated at a nominal, but imprecisely set, overheat ratio of 1.10.

The frequency response of the Miller-type anemometers with the present hot-film sensors was determined to be approximately 200 Hz by Wetzel [2]. He used the method described in Wood [17] for finding the frequency response. While this frequency response is too low to measure the fluctuating turbulence quantities, it is high enough to resolve the time-history of the spatially-averaged skin-friction values in the unsteady maneuvers.

## 2.5 Wind Tunnel Model

The light weight Darpa2 model used in the experiments has a generic Suboff undersea vehicle geometry with a scaled length ( $L$ ) of 2.24 m. The model has a bow region for  $0.0 \leq (x/L) \leq 0.23$ , a constant diameter region for  $0.23 \leq (x/L) \leq 0.75$  and an afterbody (stern) region for  $0.75 \leq (x/L) \leq 1.0$ . The sail can be detached, resulting in the axi-symmetric configuration of the model which can be thought as a missile or to a certain extent an aircraft fuselage geometry. Geometric equations defining the shape of the model body and the sail are given in a DTRC (David Taylor Research Center) report [18]. The same equations are also included in Whitfield [13]. Figure 2.7 shows the computer generated image of the Suboff model by using these equations.

The geometry and the structural components of the model (except the ring assembly integrated to the model structure for moving the sail) are exactly the same as that of the Darpa2 model used in the force and moment measurements. Whitfield [13] gives an extensive description of the steps followed during the construction of the model and the structural details. The model is mainly made of composite materials. Between the inner and the outer carbon fiber layer, the vinyl foam and the aluminum bars having hollow square cross sections were placed on the constant diameter region of the model. On the nose and the stern regions, the honeycomb material was used to maintain the required curvature between the inner and the outer skin. The model weighs approximately 10 lbs. and has a high strength to weight ratio. This is an important property required in the unsteady maneuvers both for the structural integrity of the model and the performance of the DyPPiR.

The model is mounted to the DyPPiR with a light-weight composite sting which was also built for the Darpa2 force and moment measurements [13]. The last 15 cm of the stern region of the model was removed in order leave enough space for the sting and the wires coming from the sensors. The overall weight of the model with the composite sting is approximately 30 lbs.

### 2.5.1 Sensor Configuration and the Locations

Figure 2.8 shows the model geometry with the hot-film sensor locations. More sensors have been used near the body-sail junction region to resolve the complex structure of the

separated flow. Oil flow visualization pictures also have been used in order to determine the optimum sensor locations. A total number of 29 sensors were used on the Darpa2 Suboff body. Since only 15 anemometers could be run simultaneously, the sensors were separated into two groups each having 14 sensors. These sensor sets were labeled as *Sensor Set A* and *Sensor Set B*. Two ribbon cables, each carrying the wires connected to the sensors of each set, were used. These ribbon cables were lead outside of the model, to the carriage part of the DyPPiR where they were connected to the 15 BNC cables coming from the anemometers via gold plated pin-connectors. BNC cables were connected to a single female connector. Switching from one set of sensors to the other was simply done by connecting the pin-connector of the ribbon cable to be used to the single female connector. One sensor was individually connected directly to an anemometer and used as a *control sensor*. The data from this sensor were taken during all the runs regardless of the sensor set used in order to check the consistency of the measurements taken with different sensor groups in each model position and the orientation. The barebody measurements were performed by using the sensors of Set B and the individual control sensor located at certain positions on the long row (figure 2.8). The same sensors were used in the sail-on-side case throughout the whole circumferential locations. The remaining sensors (set A) were used near the sail region in order to resolve the flow structure. The nominal circumferential distance between the long and the short sensor row is  $\Delta\phi = 11^\circ$ . At some sensor locations, this distance vary by  $\pm 1^\circ$ . The uncertainty in the measurement of the peripheral distances is  $\pm 0.44^\circ$ . Table 2.1 gives the  $x/L$  location of each sensor. Wetzel [2] determined that to avoid the heating interference between adjacent and upstream sensors, they must be spaced at least 1.25 inches apart from each other. The minimum distance between the sensors used in the DARPA2 experiments is 1.32 inches which indicates the lack of any heating interface. For the sail-on-side configuration, the chordline of the sail is aligned with the circumferential location  $\phi = 270^\circ$ . At its maximum thickness location, the sail extends from  $\phi = 262^\circ$  to  $278^\circ$  and is placed between  $x/L = 0.21$  and  $x/L = 0.31$ .

### 2.5.2 Sensor Mounting Strategy

Instead of directly mounting the sensors on the model surface, the hot-film sensors were first glued onto the cylindrical plugs made up of epoxy and the hardener as shown in

figure 2.5. The upper surface of the plugs (where the sensors were mounted) were shaped so that they match with the contour of model surface. The plugs have circular holes just beneath of the sensing spiral part of the sensors. These holes were filled with insulating foam to minimize the amount of the heat transfer into the model skin. Behind these, additional holes for the pressure taps were drilled in the plugs. At the sensor locations, hollow circular plastic cylinders were integrated to the model structure (figure 2.9). The sensor plugs were inserted into these holes (that had approximately the same diameters as the plugs) and were secured by using the hot-glue. This sensor installation strategy shown in figure 2.6 not only improves the surface quality in the vicinity of the sensors but also keeps the structural integrity of the model. The plug region where the sensor tabs were glued is inclined to the inner part of the model so that the wires that were soldered to the sensor tabs remain under the surface level. The resulting gap was filled with clay which was shaped to be levelled with the model surface.

### 2.5.3 Rotatable Ring

The sail was mounted on a movable ring integrated into the model structure and can be rotated and fixed to any desired circumferential location with  $2^\circ$  increments (figure 2.9). The ring is secured at the desired position by a set screw. Both in steady and unsteady testing, the skin friction magnitude distribution on the whole surface of the model with desired circumferential spacing can be obtained by using only one row of sensors on the model surface (note that the purpose of the second short sensor row shown in figure 2.8 is to resolve the skin-friction distribution around the sail in the x direction). The model is rotated with a certain roll angle in one direction while the sail is rotated in the opposite direction with the same amount. By this action, while changing the circumferential location of the row of sensors, the model geometry and the alignment relative to the free-stream for a specific pitch angle and sail location is kept constant. A small gap between the model and the sail has been kept in order the sail to be moved on top of the sensors without any contact. This gap has been sealed properly by using scotch tape and without giving any fillet effect for every roll angle before the data were taken.

### 2.5.4 Boundary Layer Trips

In order fix the transition location on the model and further guarantee a less Reynolds-number sensitive separation, trip posts of 0.76 mm high cylinders with 1.28 mm diameter, 2.5 mm spaced apart, were placed on the model nose part at  $x/L = 0.10$ . Two rows of the same trip posts were put on the lower and the upper surfaces of the sail in the spanwise direction. The rows were located 0.64 cm (measured on the surface) away from the leading edge of the sail. The same trips were used in the prolate spheroid study of Wetzel [2] and in the DARPA2 force and moment study of Whitfield [13].

## 2.6 Pressure Measurement System

Mean static pressures on the model surface were measured at 29 port locations listed in table 2.1. Each location is behind a hot-film sensor on the same sensor plug, and the distance between the pressure port and the hot-film sensor (measured from the center of the sensing spiral part) is approximately 0.2% of the overall model length (figure 2.5). Each pressure tap of each station was connected to a Scanivalve diaphragm (having 48 ports) through tygon tubing. These diaphragms were connected to a Scanivalve system (CTLR2P/S2-S6 Scanivalve Corp.) that has a 48 to 1 multiplexing. In order to reduce the length of the tygon tubing that connects each pressure tap with the scanivalve system, the housing of the scanivalve was placed inside the model and mounted on the sting by using cable tie-wraps. The pressures were sensed by two pressure transducers: a Setra 239 pressure transducer with a calibrated range of 0.0 to 15.0 inches of water was used to measure the free-stream dynamic pressure ( $P_{0,\infty} - P_\infty$ ), and another Setra 239 pressure transducer with a calibrated range of -2.5 to 2.5 inches of water was used to measure the static pressure relative to the free-stream static pressure ( $P - P_\infty$ ) at the pressure taps. Olcmen et al. [19] used an inclined manometer with a resolution of 0.01 inches to verify the calibration of the two pressure transducers. The total pressure  $P_{0,\infty}$  and the free-stream static pressure  $P_\infty$  were measured by using the tunnel Pitot-static tube. The pressure coefficient  $C_p$  at each port is calculated by:

$$C_p = \frac{P - P_\infty}{P_{0,\infty} - P_\infty} \quad (2.24)$$

A data acquisition board (DT2801) installed in a PC-AT386 computer was used to acquire data from the pressure transducers at a sampling frequency of 1000 Hz. The data were sampled continuously for 3.0 seconds after a settling time of 10.0 seconds.

For the same pressure measurement system, the net uncertainty in  $C_p$  was reported as  $\pm 0.018$  by Olcmen et al. [19].

Table 2.1: Hot-film sensor locations (port number is the order of the sensors in  $x/L$  direction starting from the nose).

Port number	Sensor Number	Sensor Set	$x/L$
1	1	B	0.110
2	2	B	0.131
3	1	A	0.151
4	4	B	0.170
5	2	A	0.180
6	3	A	0.189
7	4	A	0.199
8	8	B	0.208
9	5	A	0.218
10	6	A	0.256
11	control	-	0.266
12	7	A	0.276
13	8	A	0.285
14	10	A	0.295
15	5	B	0.306
16	9	A	0.316
17	11	A	0.325
18	12	A	0.336
19	6	B	0.345
20	14	A	0.356
21	15	A	0.366
22	7	B	0.434
23	3	B	0.501
24	9	B	0.570
25	10	B	0.638
26	12	B	0.706
27	11	B	0.774
28	14	B	0.819
29	13	B	0.863

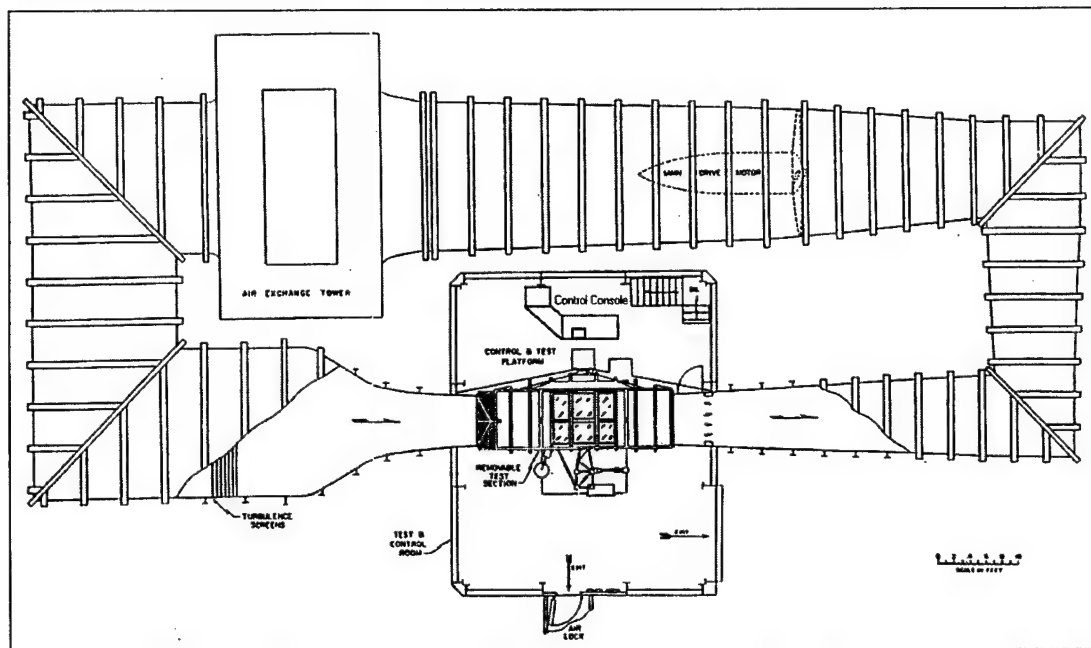


Figure 2.1: Top view of the Virginia Tech Stability Wind Tunnel

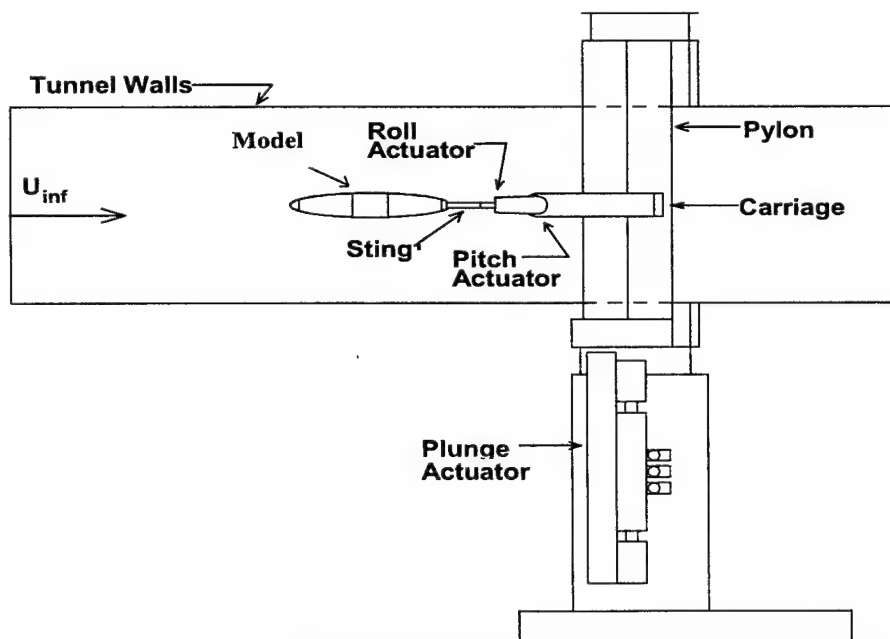


Figure 2.2: Dynamic Plunge-Pitch-Roll(DyPPiR) Model Mount installed in the wind tunnel.(taken from Wetzel [2])



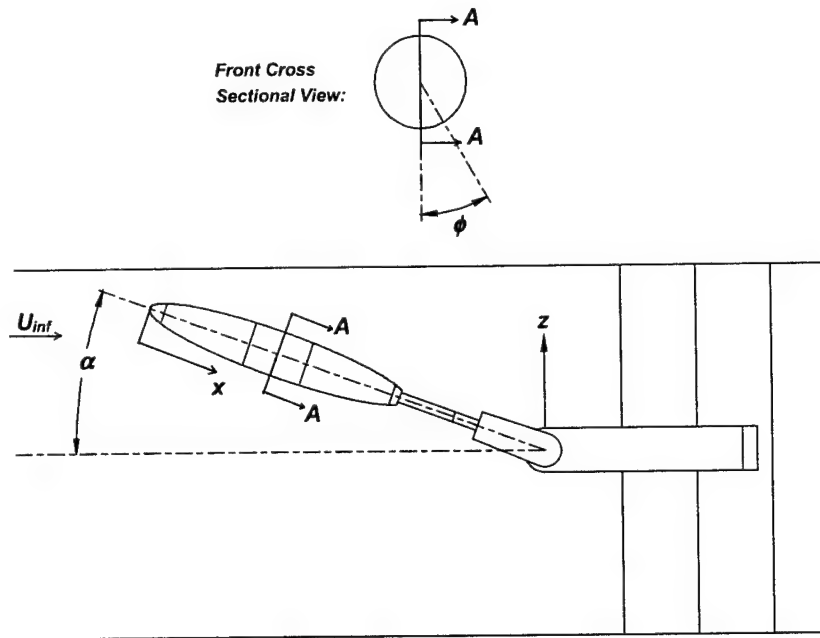


Figure 2.3: Coordinate nomenclature for the DyPPiR and the model. (taken from Wetzel [2])

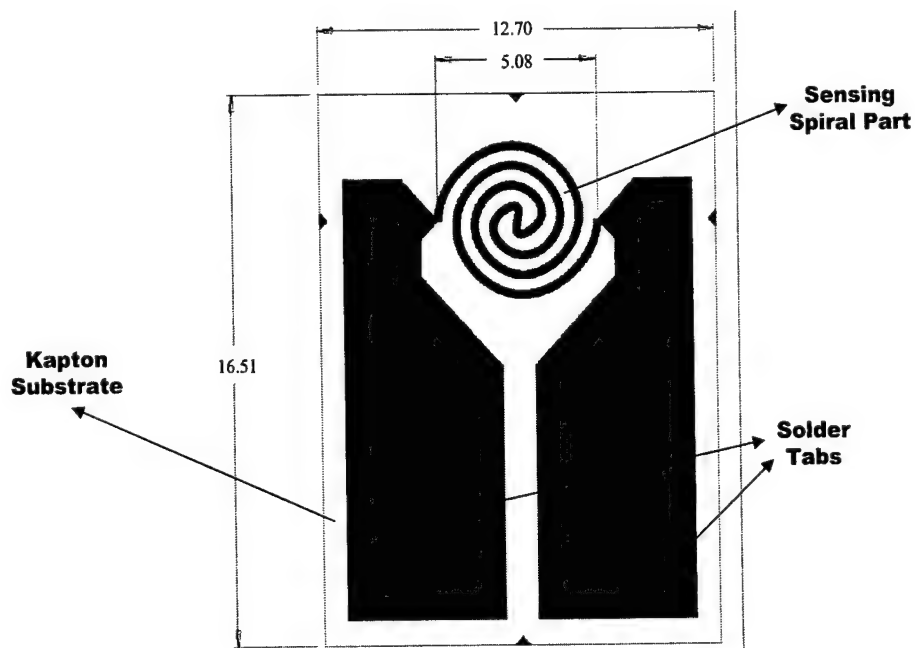


Figure 2.4: Hot-film sensor. All dimensions are in mm, and the figure is not drawn to scale.

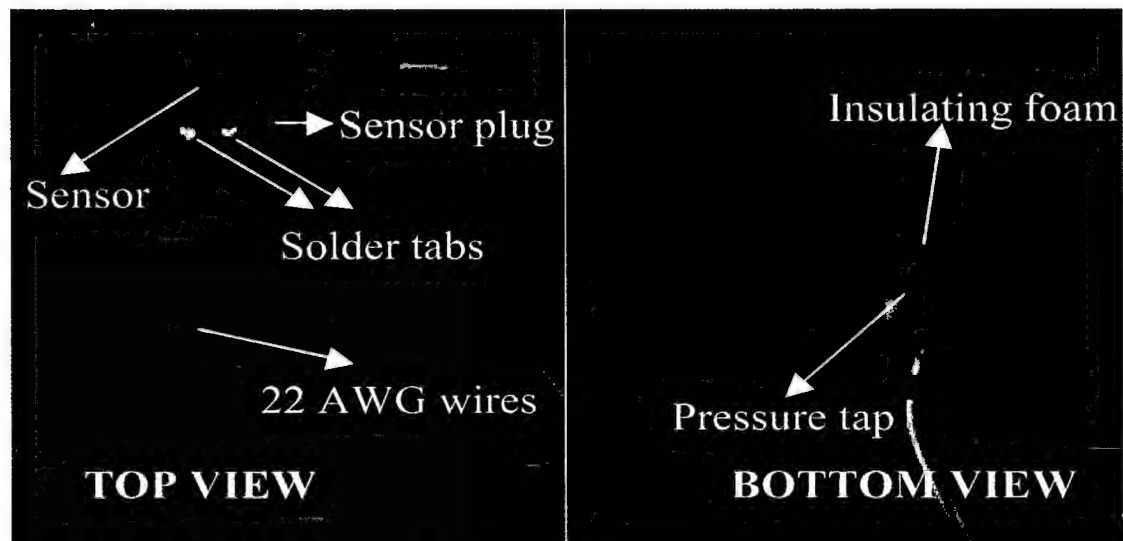


Figure 2.5: Sensor plug with a hot-film sensor mounted

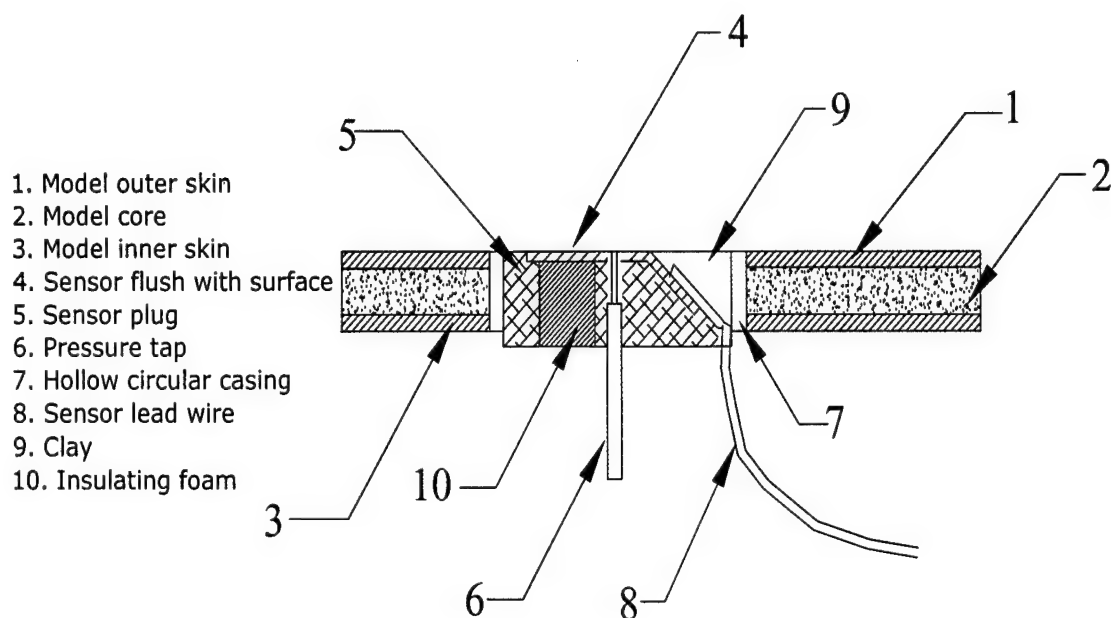


Figure 2.6: Schematic of the sensor mounting strategy

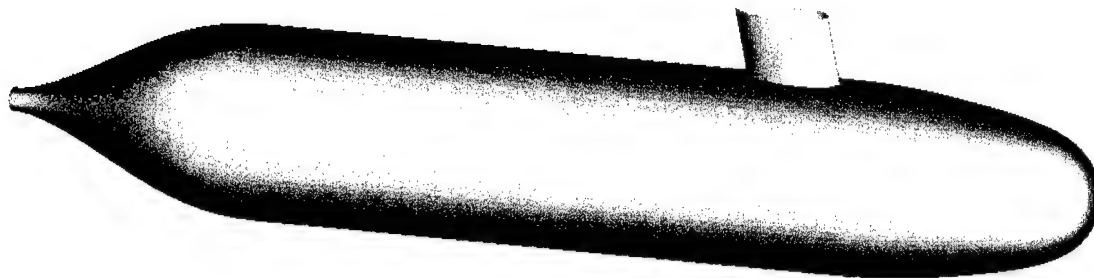


Figure 2.7: Computer generated 3-D view of the Suboff model with the sail

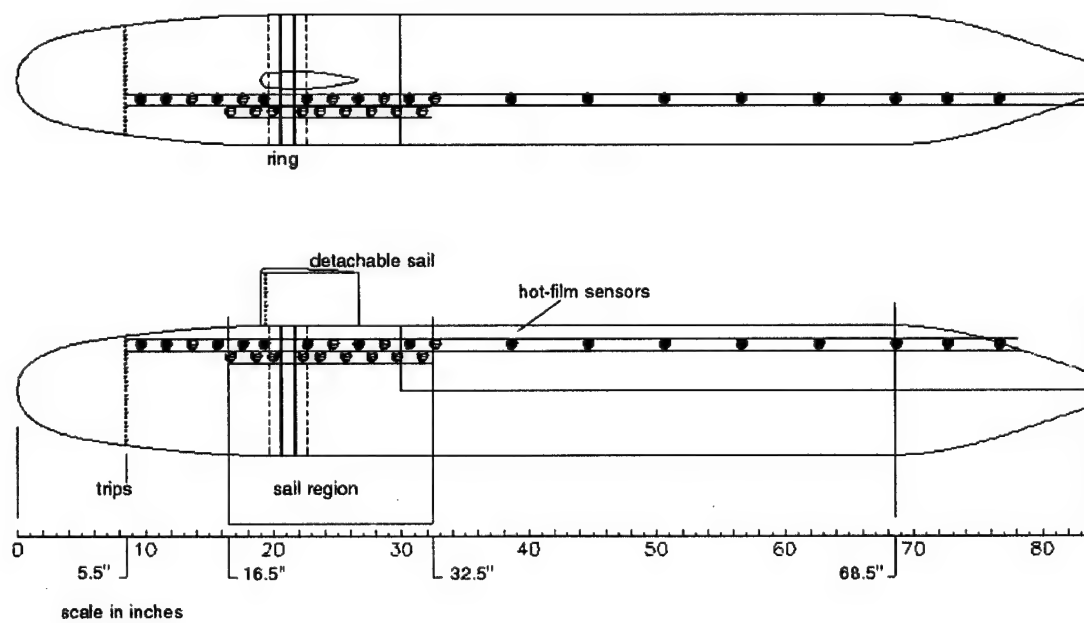


Figure 2.8: Top and side view of the model and the hot-film sensor locations

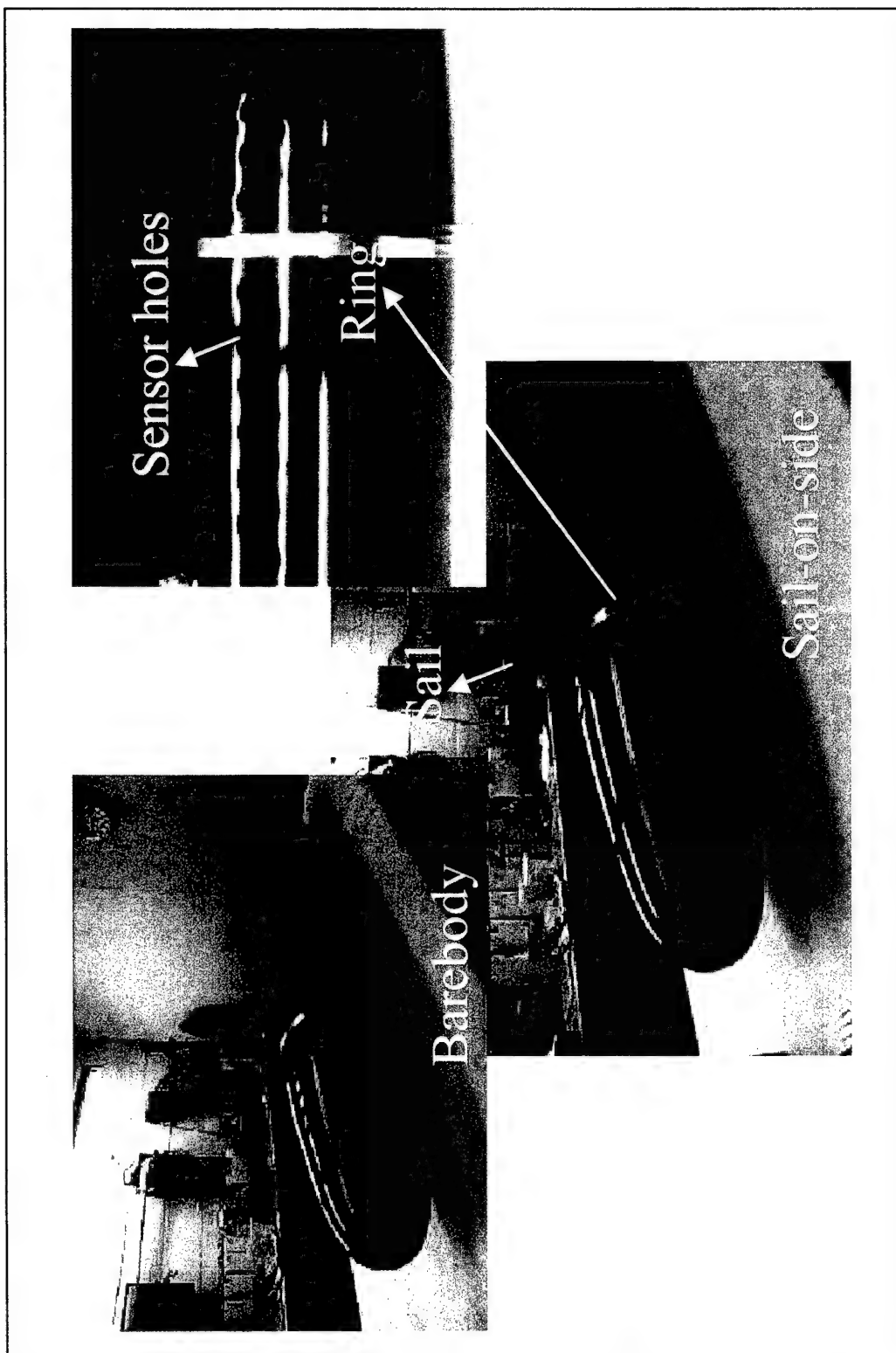


Figure 2.9: Barebody and sail-on-side configurations of the model

## Chapter 3

# Steady Measurements and the DyPPiR Maneuvers

All the skin friction and the pressure measurements were done with a tunnel speed of  $42.7 \pm 1\%$  m/s. For these experiments, the Reynolds number based on the model length  $Re_L$  was  $5.5 \times 10^6$ . The oil flow visualizations were taken at  $Re_L = 4.5 \times 10^6$  by Wetzel [20]. Figure 3.1 shows different circumferential regions of the Darpa2 model where the skin-friction and pressure measurements were performed. The angle range of each region was determined by examining the oil-flow visualization pictures of the sail-on-side case taken at  $10^\circ$  and  $20^\circ$  angles of attack. Since only 15 anemometers could be used simultaneously, hot-film measurements for each roll angle were done by using one set of 15 sensors. For the barebody and sail-on-side case, except regions IV and V in figure 3.1, both steady and unsteady hot-film data were acquired by using sensor set B. In order to resolve the surface flow spatial structure near the sail, all the steady and unsteady measurements were repeated in regions IV and V by using sensor set A for the sail-on-side case.

### 3.1 Skin-Friction Measurements

Measurement of the skin friction in steady experiments and unsteady maneuvers has been performed for two model configurations: barebody and sail-on-side cases. In the barebody case, both steady and unsteady skin friction data were acquired between  $\phi = 0^\circ$

and  $180^\circ$  in the circumferential direction with  $10^\circ$  increments on the windward side and for every  $2^\circ$  on the leeward side. For the sail-on-side case, measurements were made between  $\phi = 0^\circ$  and  $360^\circ$ . The  $\phi$  increment was again  $2^\circ$  on the leeward side in order to locate the crossflow separation locations with low uncertainty. On the windward side, measurements were made with  $10^\circ$  increments except the region between  $\phi = 270^\circ$  and  $292^\circ$  where  $C_f$  was measured every  $2^\circ$  so as to resolve the surface flow structure in the vicinity of the sail.

### 3.1.1 Steady Hot-film Measurements

The steady skin-friction measurements were done using the DyPPiR as the model mount. Slotted walls were used as the wind tunnel wall configuration. Table 3.1 outlines the steady hot-film measurements.

Table 3.1: Darpa2 steady skin-friction measurements

Body Configuration	Pitch Angles ( $^\circ$ )	Sensor Set	Region #	Roll Angle Incr. ( $^\circ$ )
barebody	$10^\circ$ & $20^\circ$ (w/ solid walls)	B	I	10.0
barebody	$10^\circ$ & $20^\circ$ (w/ solid walls)	B	II	2.0
barebody	$0.9$ to $27.6^\circ$ w/ $2^\circ$ incr.	B	I	10.0
barebody	$0.9$ to $27.6^\circ$ w/ $2^\circ$ incr.	B	II	2.0
sail-on-side	$0.9$ to $27.6^\circ$ w/ $2^\circ$ incr.	B	I	10.0
sail-on-side	$0.9$ to $27.6^\circ$ w/ $2^\circ$ incr.	B	II	2.0
sail-on-side	$0.9$ to $27.6^\circ$ w/ $2^\circ$ incr.	B	III	2.0
sail-on-side	$0.9$ to $27.6^\circ$ w/ $2^\circ$ incr.	A, B	IV	2.0
sail-on-side	$0.9$ to $27.6^\circ$ w/ $2^\circ$ incr.	A, B	V	2.0
sail-on-side	$0.9$ to $27.6^\circ$ w/ $2^\circ$ incr.	B	VI	10.0

Before the actual tests with the DyPPiR, the steady barebody  $C_f$  data were also taken at  $10^\circ$  and  $20^\circ$  angles of attack with the solid walls. The NACA Strut of the Stability Wind Tunnel was used as for the model mount in these experiments. Steady hot-film measurements with the DyPPiR were taken at 14 angles of attack starting from  $0.9^\circ$ . The angle of attack increment was about  $2^\circ$  and the last angle covered was  $27.6^\circ$ . These

angles are shown by solid square symbols in figure 3.2. Besides obtaining the steady surface flow structure over the model, the results of the steady data at these angles of attack were also used to construct the quasi-steady data to be used in a first-order lag model.

### 3.1.2 DyPPiR Maneuvers

Unsteady maneuvers were performed by using the DyPPiR. Slotted walls were used as the wind tunnel wall configuration. Table 3.2 summarizes the unsteady skin-friction measurements.

Table 3.2: Darpa2 unsteady skin-friction measurements

Body Configuration	Maneuver	Sensor Set	Region #	Roll Angle Incr. (°)
barebody	0.33 s. pitch-up	B	I	10.0
barebody	0.33 s. pitch-up	B	II	2.0
sail-on-side	0.33 s. pitch-up	B	I	10.0
sail-on-side	0.33 s. pitch-up	B	II	2.0
sail-on-side	0.33 s. pitch-up	B	III	2.0
sail-on-side	0.33 s. pitch-up	A, B	IV	2.0
sail-on-side	0.33 s. pitch-up	A, B	V	2.0
sail-on-side	0.33 s. pitch-up	B	VI	10.0

Unsteady results were obtained for the pitchup maneuvers. The pitchup maneuver performed for the present work is a simple linear ramp from  $1^\circ$  to  $27^\circ$  in 0.33 seconds. The maneuvers were performed with a constant pitch rate of  $78^\circ/s$  and the model center of rotation was at  $x_{cg}/L = 0.24$ . Figure 3.2 shows the DyPPiR pitch angle and plunge location feedback for the pitchup maneuvers. The DyPPiR pitch angle is also the instantaneous angle attack measured at the model center of rotation. Because of the angular motion of the model, the instantaneous local angle of attack varies linearly from the nose to the stern of the model, with the nose being at a lower angle of attack than the model center of rotation, and the stern at a higher angle of attack compared to the model center of rotation. The magnitude of the local induced increment in angle of attack is only a

function of the distance from the model center of rotation since the pitch rate is constant. For the pitch-up maneuvers performed, at  $x/L = 0.0$  the induced angle of attack increment is approximately  $-0.5^\circ$ , while at  $x/L = 1.0$  this angle increment is approximately equal to  $1.5^\circ$ . Although it is possible to keep the model center from moving vertically by using the plunge actuator during a maneuver, it is inevitable that the model center of rotation translates downstream during a maneuver. This downstream movement is approximately 0.18 m and the induced velocity in the downstream direction is around 1.2% of the free-stream velocity which can be considered as insignificant. The objective while performing the pitch-up maneuver is to get as abrupt a start and stop as possible. However, the DyPPiR has a finite acceleration and deceleration capability. Note that the actual maneuver starts at  $t' = 3.00$  in figure 3.2. For each  $\phi$  orientation of the model, the pitchup maneuver was executed for 10 times. In his prolate spheroid work, Wetzel [2] has reported that 10 repetitions for a given maneuver at each roll angle position of the model are enough for ensemble averages that have a low uncertainty level. Unsteady skin friction values at each  $x/L$  measurement station has been calculated for each repetition and the final value was obtained by ensemble averaging the skin friction values as will be described in the data reduction section in more detailed.

## 3.2 Pressure Measurements

Table 3.3: Darpa2 pressure measurements

Body Configuration	Pitch Angles ( $^\circ$ )	Region #	Roll Angle Incr. ( $^\circ$ )
barebody	10 & 20	I	10.0
barebody	10 & 20	II	6.0
sail-on-side	10 & 20	I	10.0
sail-on-side	10 & 20	II	6.0
sail-on-side	10 & 20	III	6.0
sail-on-side	0, 10 & 20	IV	2.0
sail-on-side	0, 10 & 20	V	2.0
sail-on-side	10 & 20	VI	10.0



Steady mean surface static pressures on the Darpa2 model were measured both for the barebody and the sail-on-side cases. The NACA Strut of the Stability Wind Tunnel was used as for the model mount. The information about the pressure measurements are outlined in table 3.3. For the barebody case, measurements were performed at two angles of attack:  $\alpha = 10^\circ$  and  $\alpha = 20^\circ$ . In order to check the symmetry of the flow, pressure data were also taken on four circumferential locations of the model ( $\phi = 0^\circ$ ,  $90^\circ$ ,  $180^\circ$ , and  $270^\circ$ ) at  $0^\circ$  angle of attack. Barebody results were obtained both for the solid and slotted wall configuration, whereas the sail-on-side data were acquired with the slotted walls. Sail-on-side pressure measurements were done at  $10^\circ$  and  $20^\circ$  angles of attack. In regions IV and V, data were also obtained for  $\alpha = 0^\circ$ .

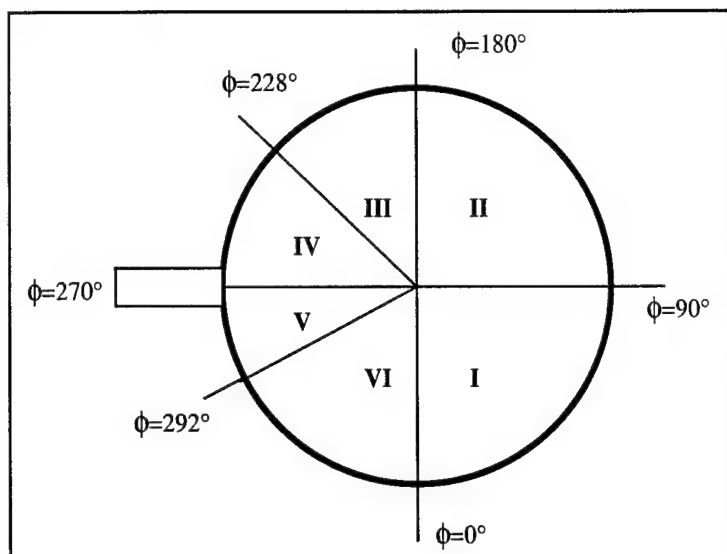
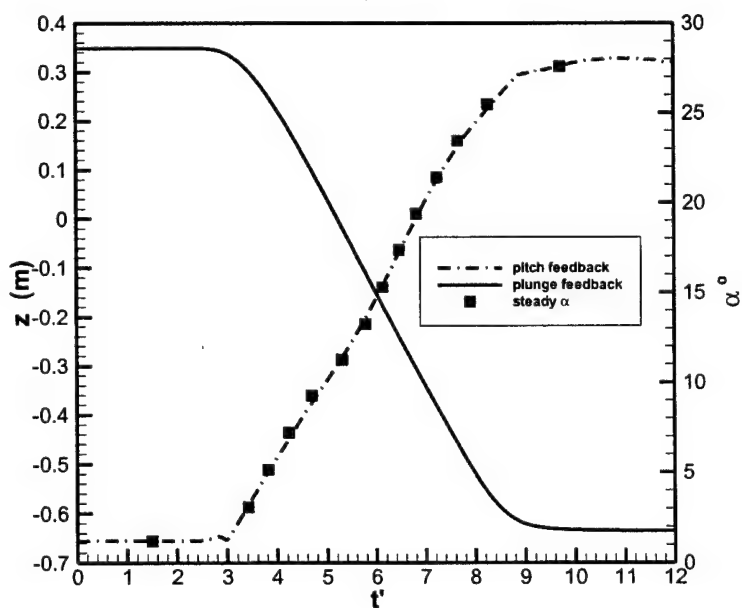


Figure 3.1: Regions for Darpa2 Skin Friction and Pressure Measurements.

Figure 3.2: DyPPiR plunge and pitch feedback for pitchup maneuvers. Filled symbols show the  $\alpha$  locations for the steady measurements.

## Chapter 4

# Calibration of the Hot-film Sensors

The hot-film sensors that are used in the actual tests have been calibrated for each roll angle position of the model at zero angle of attack in the Stability Wind Tunnel. During the calibrations, for the sail-on-side case, axis-symmetric flow around the model was maintained by removing the sail. The boundary layer velocity profiles were obtained on the constant diameter region of the model at  $0^\circ$  angle of attack in the Open-throat tunnel of Virginia Tech. Boundary layer properties calculated from these velocity profiles were used in the calibration procedure. The details about the calibration process are presented in this chapter.

### 4.1 Description of the Experimental Apparatus

Boundary Layer velocity profile measurements were performed in the Open-throat tunnel of the Virginia Tech Aerospace and Ocean Engineering Department. The Open-throat wind tunnel is a wooden, circular, return type tunnel with an open test section. Detailed description of the tunnel can be found on the AOE Web page. In recent years, flow quality of the tunnel has been improved by installing a screen to make the flow exit the nozzle more uniform and by building a vent to bleed the same amount of air that is entrained at the test section [21]. The valve on the top of the vent box was kept open during all the runs in order to make use of this improvement. One disadvantage of the tunnel is the temperature control. It has been seen that it was difficult to keep the temperature

constant, however temperature change was not high enough to effect the velocity profile measurements.

A support assembly, as shown in figure 4.1, was build in order to place the model in the Open-throat tunnel. This assembly consists of two wooden supports each connected to the lower tunnel walls through two steel legs. The model was placed on the wooden supports in such a way that the whole part of the constant diameter region could be remained in the test section. The centerline of the model and the support assembly in the Y-direction was aligned with the centerline of the tunnel in the Y direction. However, center of symmetry of the model was shifted up from the center of the tunnel with a certain distance in order to minimize the blockage effects and keep the flow axis-symmetric around the constant diameter part of the model. Keeping the flow axis-symmetric is an important task, since all the theoretical calculations used to determine the skin-friction distribution are based upon this assumption. To find the magnitude of the shift distance in the Y-direction, center of the cross-sectional area of the model with the wooden block and the legs in the Y-Z plane has been calculated and this center is aligned with the center of the tunnel. As a result, a shift distance of 3.22 inches in the Y-direction has been found.

After the model was placed on the supports, velocity measurements were made with a Pitot tube in eight stations to check the symmetry of the flow. These eight stations were taken on a circle of radius 30 inches and each station was  $45^\circ$  apart from the next station in the circumferential direction as shown in figure 4.2. (Note that streamwise direction X is into the page in figures 4.1 and 4.2). The results are plotted in figure 4.3. As can be seen from this plot, the velocity difference in each station is in acceptable limits and flow can be regarded as axis-symmetric.

Boundary layer velocity profiles were obtained by using a boundary layer type pitot probe with a tip diameter of 0.035 inches. The boundary layer probe was moved in the normal direction to the wall by using an electrically driven traverse mechanism. One revolution of the barrel in the traverse mechanism was equivalent to a 0.025-inch vertical move. The probe was moved in the streamwise direction by hand on an aluminum bar placed over the test section and secured in two ends on the upper tunnel walls. The pitot probe was attached to a water manometer with a resolution of 0.02 inches.

## 4.2 Boundary Layer Velocity Profile Measurements

Boundary layer velocity profiles on the constant diameter region of the model were taken in four different speeds: 60 ft/s (18.3 m/s), 80 ft/s (24.4 m/s), 95 ft/s (28.9 m/s) and 110 ft/s (33.5 m/s). Measurements were made in two stations located on the first sensor row for each speed. As can be seen from figure 4.4, the first station is at the upstream location of the constant diameter region ( $x/L = 0.25$ ) and the second station at the downstream part ( $x/L = 0.59$ ). Boundary layer properties obtained from the second station were used as the initial value for the theoretical calculations.

To resolve the typical regions of the turbulent velocity profiles, (semi-logarithmic region, wake region etc.) the pitot probe was moved with logarithmic increments from the wall. The readings were assumed to be started from the half of the diameter of the probe, 0.0175 inches from the wall. Therefore the data from the viscous sublayer and some part of the logarithmic region couldn't be obtained. In fact, as will be discussed in the next section, the data obtained in the vicinity of the wall weren't used in the calculation of the boundary layer properties because of the possible errors originating from the wall-probe interference.

Streamwise velocity measurements were made in 29 stations to determine the boundary layer edge velocity  $U_e$  distribution for each speed. First and the last stations are the same as the first and the second stations used in the boundary layer traverses. From station 0 to station 27, the distance between the stations are 1 inches. The results obtained from these measurements are given in figure 4.8. As can be seen from these plots, for all the speeds, the change in  $U_e$  in the streamwise direction is negligible and can be regarded as constant. The temperature of the tunnel and the atmospheric pressure have been recorded regularly during all the runs in order to update the dynamic viscosity  $\mu$ , and the density  $\rho$  of the air which were used in the theoretical calculations.

### 4.2.1 Boundary Layer Thickness Determination

The boundary layer thickness  $\delta$  is defined as the normal distance  $y$  from the wall where  $U = 0.99 \times U_e$ . Here  $U$  is the streamwise velocity component and  $U_e$  is the boundary layer edge velocity. The  $U$  vs.  $y$  values have been recorded for all the profile measurements and the value of the boundary layer edge has been determined by making linear interpolation

between the appropriate values. Values of  $\delta$  at the first and the second stations for each speed are given in Table 4.1.

Boundary layer thickness determination, both in experimental and numerical studies, is a difficult issue, since near the edge of the turbulent boundary layer velocity change is rather small and the uncertainties associated with the measurement technique (e.g. resolution of the anemometer or reading errors) may cause significant deviations in the determination of the  $\delta$  values. Therefore, the characterization of the boundary layer profiles with the integral properties like displacement thickness  $\delta^*$  and momentum thickness  $\theta$  would be more appropriate.

### 4.2.2 Calculation of the Boundary Layer Properties

In order to calculate the boundary layer properties like  $\delta^*$  and  $\theta$ , the complete velocity profile should be used. However, as previously discussed, the profiles obtained experimentally didn't contain the viscous sublayer and some part of the logarithmic layer. Contributions to the calculation of the integral properties from these regions is not negligible, thus a proper method to complete the profile data should be sought. The first step is to find the friction velocity  $U_\tau$  for that particular profile.

$U_\tau$  can be obtained by using the logarithmic region in a turbulent profile. In the literature one may see many ways of finding  $U_\tau$ . All these methods make use of the logarithmic region. In this study curvature effects are also considered. In White [22], the logarithmic region for a turbulent profile with curvature effect is given by the equation:

$$U^+ = \frac{1}{K} \ln(r^+) + A \quad (4.1)$$

where

$$U^+ = \frac{U}{U_\tau} \quad \text{and} \quad r^+ = \frac{a U_\tau}{\nu} \ln \left( 1 + \frac{y}{a} \right) \quad (4.2)$$

Also for the coefficients,  $K=0.41$  and  $A=5.0$  have been used (Coles and Hirst [23]). At  $r^+ = 100$ , equation 4.1 gives  $U^+ = 16.23$ . In equation 4.2,  $a$  is the radius of curvature and for our case in the constant diameter region of the model this value is 5.25 inches. For finding  $U_\tau$ , the point in the velocity profile where both  $U$  and  $y$  values are satisfied is sought for  $U^+ = 16.23$  and  $r^+ = 100$  by changing the value of  $U_\tau$ . Once the point is found, the corresponding value of  $U_\tau$  is taken as the actual friction velocity for that particular

profile. Two equations used in this iteration process are derived from equations 4.1 and 4.2 and given as:

$$y_{r^+=100} = 5.25 \left( e^{\frac{C\nu}{U_\tau}} \right) \quad (4.3)$$

$$U = 16.23U_\tau \quad (4.4)$$

In equation 4.3,  $C = 750.0 \text{ m}^{-1}$ . Once the friction velocity is obtained, the viscous sublayer can be approximated up to  $r^+ = 10$  by the equation:

$$U^+ = r^+ \quad (4.5)$$

To eliminate the bad points in the vicinity of the wall, actual experiment data with  $r^+$  value equal to or greater than 100 are used and the region between  $r^+ = 10$  and  $r^+ = 100$  is approximated by the equation:

$$U^+ = 7.5333 (r^+)^{1/6} \quad (4.6)$$

In Kays and Crawford [24], this equation is given with  $(1/7)$  as the exponent and with a different constant as well. However for the profiles obtained in this study, it has been seen that  $(1/6)$  exponent form fits the data better than  $(1/7)$  exponent form for all the cases. The constant in equation 4.6 was obtained by making  $U^+$  equal to 16.23 for  $r^+ = 100$ , which agrees with equation 4.1 using the Coles and Hirst [23] constants.

The above procedure has been used for obtaining the complete profile for each station and speed. The results are given in figures 4.5 to 4.7. The logarithmic region gets larger as the speed increases and particularly for a given speed the logarithmic region of the profile obtained in the second station is again larger with respect to the one obtained in the first station.

After the complete profile data for each case were obtained, boundary layer properties  $\delta^*$ ,  $\theta$  and the shape factor  $H$  have been calculated. These properties and  $Re_\theta$ , the Reynolds Number based on  $\theta$  for each case are presented in table 4.1.

Although all the calibration steps described to this point have been applied to  $U_e = 60$  ft/s case besides 80, 95 and 110 ft/s, boundary layer properties obtained at this particular speed were not used in the remaining calibration procedure. The velocity profiles at 60 ft/s showed transitional character. Since all the theoretical calculations in the calibration procedure were based on fully turbulent axis-symmetric flow assumption over the model, the results of the 60 ft/s case were not used in the skin-friction determination. Therefore

Table 4.1: Boundary layer properties at  $U_e = 80, 95$  and  $110$  ft/s.

$U_e$ , ft/s	Station #	$U_\tau$ , ft/s	$\delta$ , inches	$\delta^*/\delta$	$\theta/\delta$	H	$Re_\theta$
80.0	1	1.11	0.26	0.17	0.12	1.44	1114
80.0	2	0.98	0.96	0.15	0.11	1.35	3840
95.0	1	1.33	0.22	0.17	0.12	1.43	1127
95.0	2	1.13	0.96	0.15	0.11	1.34	4752
110.0	1	1.44	0.25	0.16	0.11	1.44	1470
110.0	2	1.30	0.85	0.15	0.11	1.36	4920

actual experimental data used in the calibration procedure consist of boundary layer velocity profile measurements acquired at 80, 95 and 110 ft/s. As can be seen from table 4.1, experimental calibration  $C_f$  values were obtained for  $1010 \leq Re_\theta \leq 4900$ . The extension of the calibration range to 140 ft/s was achieved by using a theoretical approach described in section 3.3.

For 80, 95 and 110 ft/s, to determine the  $\theta$  distribution between two measurement stations, the following momentum integral equation has been used:

$$0.03138 \left[ Re_a \ln \left( 1 + 9.337 \frac{\theta}{a} \right) \right]^{-0.2857} = \frac{d\theta}{dx} \quad (4.7)$$

This equation has been obtained by using the approach in Kays and Crawford [24] and making necessary modifications to include the transverse curvature effects. Equation 4.7 which represents an initial value problem, has been solved numerically by using *Modified Euler's Method* in order to determine the momentum thickness distribution. As the initial value for the momentum thickness, the  $\theta$  value measured at the second station has been used.

### 4.3 Calculation of the Skin-Friction Values

After obtaining the  $\theta$  distribution at 80, 95 and, 110 ft/s, the skin friction coefficient at each sensor location has been calculated by using the *Ludwig-Tillmann equation* [25]:

$$\frac{C_f}{2} = 0.123 \times 10^{-0.678H} \left( \frac{U_e \theta}{\nu} \right)^{-0.268} \quad (4.8)$$



Steady and unsteady experiments over the DARPA2 model have been performed at a nominal wind tunnel speed of 140 ft/s. The wall shear stress at this speed, especially on the windward side of the model at an angle of attack, would be significantly high compared to the values obtained at the experimental calibration speeds. Since the highest calibration speed that can be reached at the open throat tunnel was 110 ft/s, the calculation of the actual shear stress in the experiments would require to approximate the values well above the skin-friction magnitudes obtained from the experimental velocity profile measurements. In order to reduce the error in the extrapolation, the skin-friction distribution at the constant diameter region of the model at 140 ft/s was approximated by using the equation given in White [26]:

$$C_f = 0.0015 + \left[ 0.20 + 0.016 \left( \frac{x}{a} \right)^{0.4} \right] Re_x^{-1/3} \quad (4.9)$$

In the same work, White [26] showed that equation 4.9 had an rms error of  $\pm 9\%$  compared with the available data, which was the lowest of any theory known to the author at that time.

## 4.4 Calculation of the Calibration Coefficients

In order to relate the voltage values acquired from the constant temperature anemometers with the wall shear values, the surface hot-film version of King's Law has been used (Bruun [27]):

$$\frac{E^2}{(T_w - T_\infty)} = A + B(\tau_w)^{1/3} \quad (4.10)$$

Here,  $E$  is the time-averaged voltage value obtained from a surface hot-film sensor connected to a constant temperature anemometer,  $T_w$  stands for the sensor temperature and  $T_\infty$  for free-stream temperature of the flow in the tunnel. The purpose of the calibration is to determine the coefficients  $A$  and  $B$  in equation 4.10. For finding these coefficients,  $E$  and the corresponding  $\tau_w$  value obtained at 80, 95, 110 and 140 ft/s have been used to make a linear regression.

In equation 4.10, the change in the free-stream temperature will also cause a change in the calibration coefficients  $A$  and  $B$ . Since the temperature of the stability tunnel is ambient and cannot be controlled, the calibration procedure was repeated as the tunnel

temperature changed. In order to minimize the uncertainty in the skin friction measurements due to the free-stream temperature change for the barebody case, the calibration coefficients for each sensor have been re-calculated for every roll angle position of the model before taking steady data and performing unsteady maneuvers for that specific roll angle. At each roll position of the model, the voltage values  $E$  from each sensor were acquired at  $0^\circ$  angle of attack for the speeds 80, 95, 110 and 140 ft/s. Since the  $\tau_w$  value corresponding to each speed at all the sensor locations were known, the calibration coefficients  $A$  and  $B$  for each sensor and roll angle position could be obtained by using equation 4.10. The free-stream temperature change was at most  $\pm 0.5^\circ \text{C}$  between the start of the steady measurements and the end of the unsteady maneuvers for each roll angle and this was included in the overall uncertainty calculations. For the measurements with the sail, calibration coefficients for each sensor were re-calculated approximately in every 10 roll angle by simply detaching the sail from the body and applying the calibration procedure to the barebody. Between each calibration runs, the same values of  $A$  and  $B$  coefficients were used for each sensor.

Figure 4.9 shows the skin-friction vs.  $x/L$  distribution obtained as the result of the calibration procedure at the actual experiments in the Stability Wind Tunnel at  $0^\circ$  angle of attack. The Reynolds number based on the model length  $Re_L$  is  $5.5 \times 10^6$ . In the same figure, the data are compared with the  $C_f$  values obtained at David Taylor Model Basin (DTMB) for  $Re_L = 1.2 \times 10^7$  (Huang et al. [28]). Skin-friction measurements at DTMB were based on the principle that shear stress on a body in a flow can be measured with using small obstacles that stagnate the velocity field near the surface to produce a pressure rise that is approximately proportional to the shear stress. Huang et al. [28] placed small blocks with certain dimensions on the model surface near to the pressure tap locations. The pressure was measured at the tap with and without these obstacles and the measurement differences were used to compute the shear stress at that location. They reported an uncertainty of  $\pm 0.0002$  in their skin-friction measurements. Skin friction  $C_f$  vs.  $x/L$  distributions of Virginia Tech and DTMB follow the same trend. However, the magnitudes of the  $C_f$  obtained at Virginia Tech are bigger than that of DTMB. This is likely due to the difference between the Reynolds numbers and the uncertainty of the both measurements.

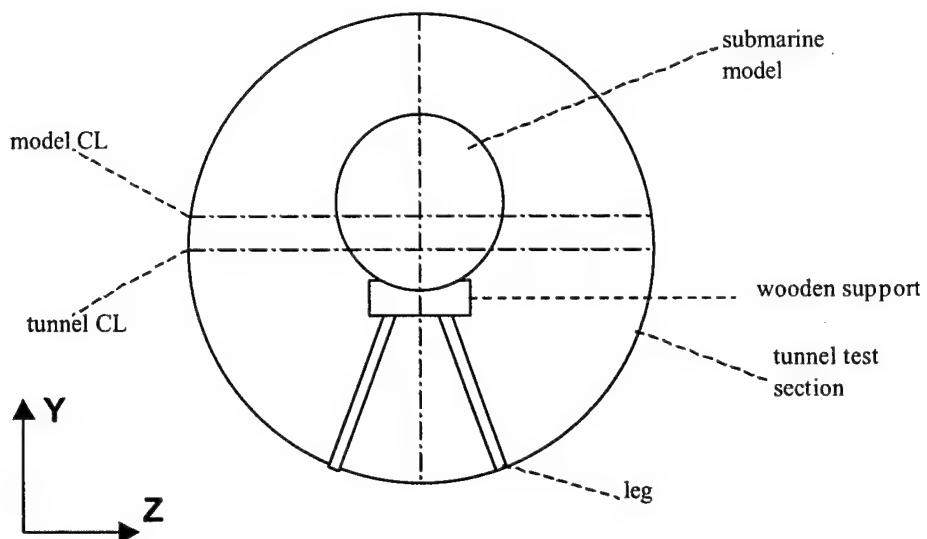


Figure 4.1: Cross-sectional view of the model and support assembly in the Y-Z plane

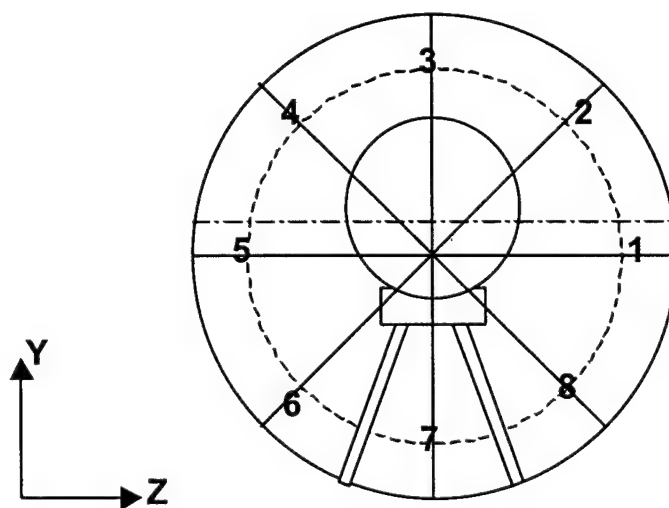


Figure 4.2: Measurement stations for the flow symmetry check

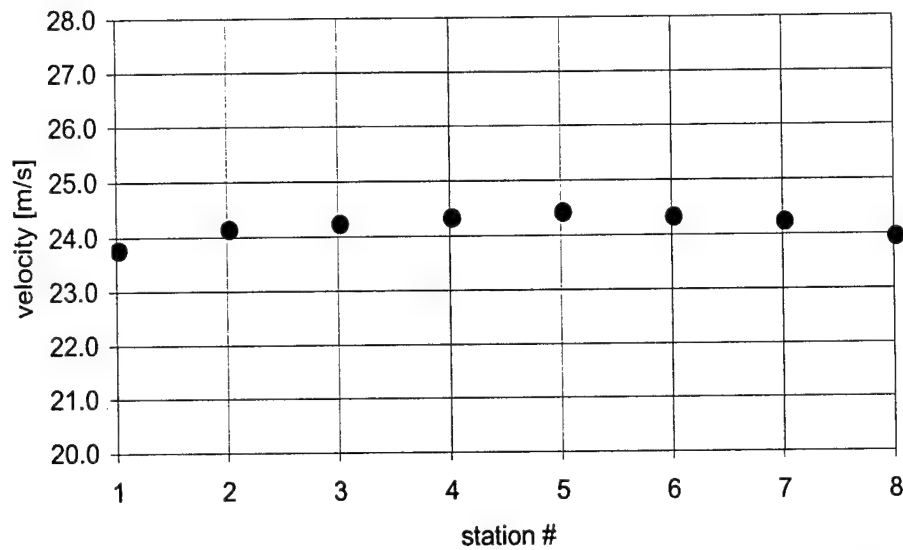


Figure 4.3: Results of the velocity measurements at the flow symmetry check points

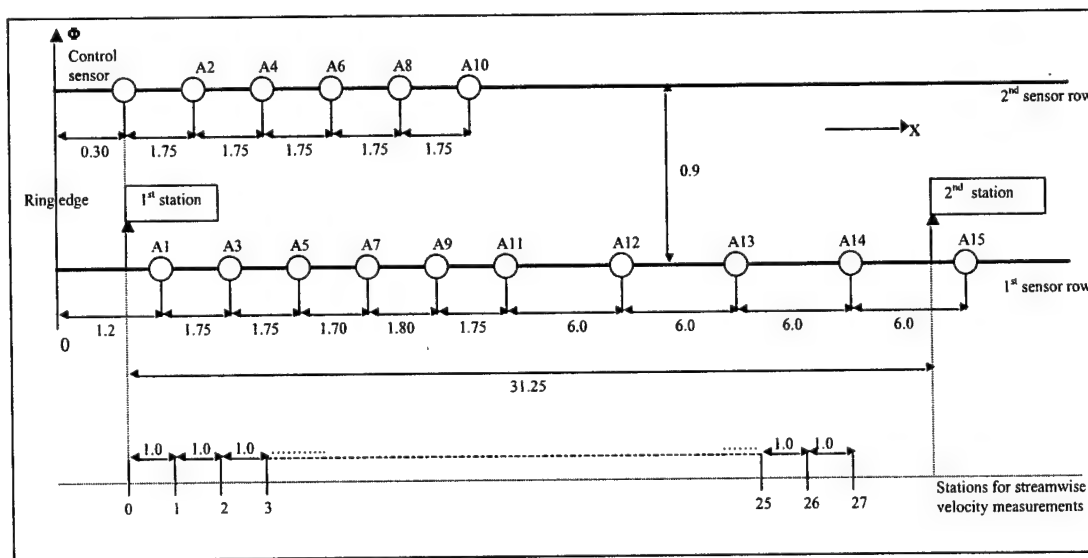
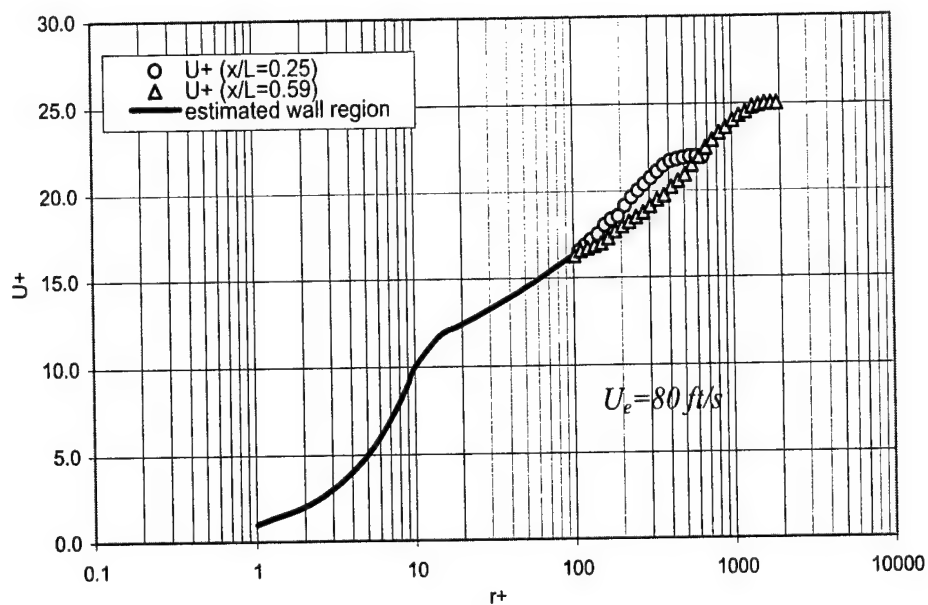
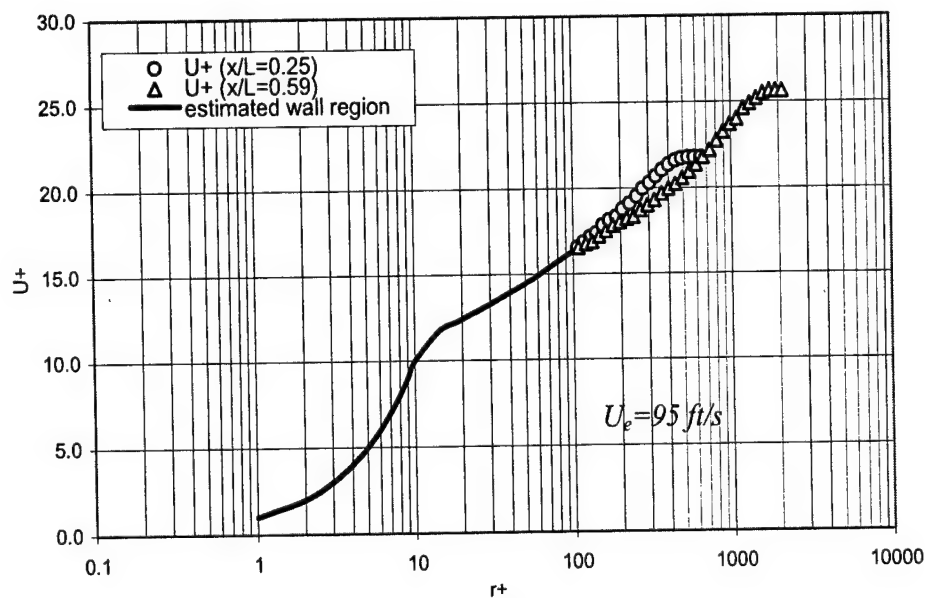


Figure 4.4: Planform view of the sensor configuration, boundary layer traverse and streamwise velocity measurement stations (all dimensions are measured in inches and the figure is not drawn to scale).

Figure 4.5: Boundary layer velocity profiles for  $U_e = 80 \text{ ft/s}$ .Figure 4.6: Boundary layer velocity profiles for  $U_e = 95 \text{ ft/s}$ .

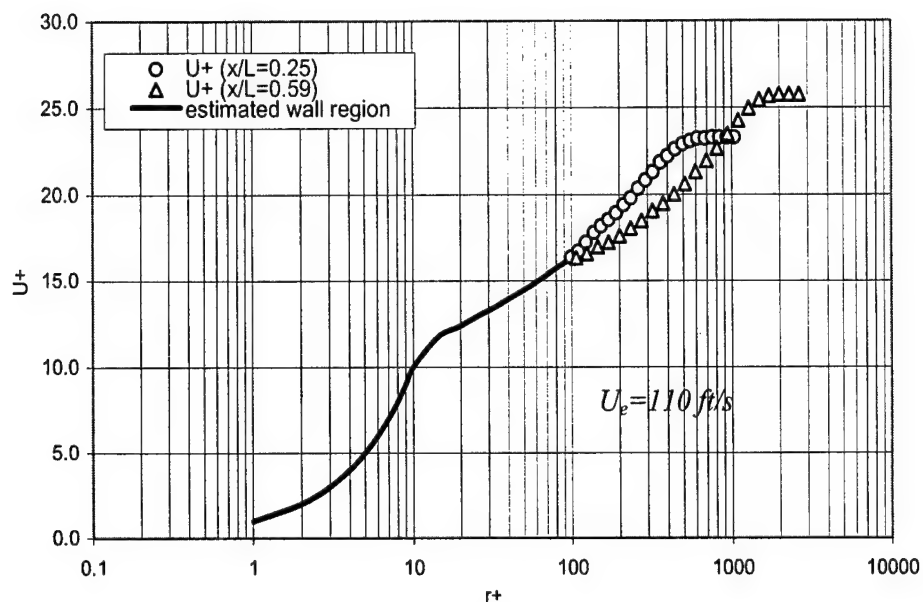
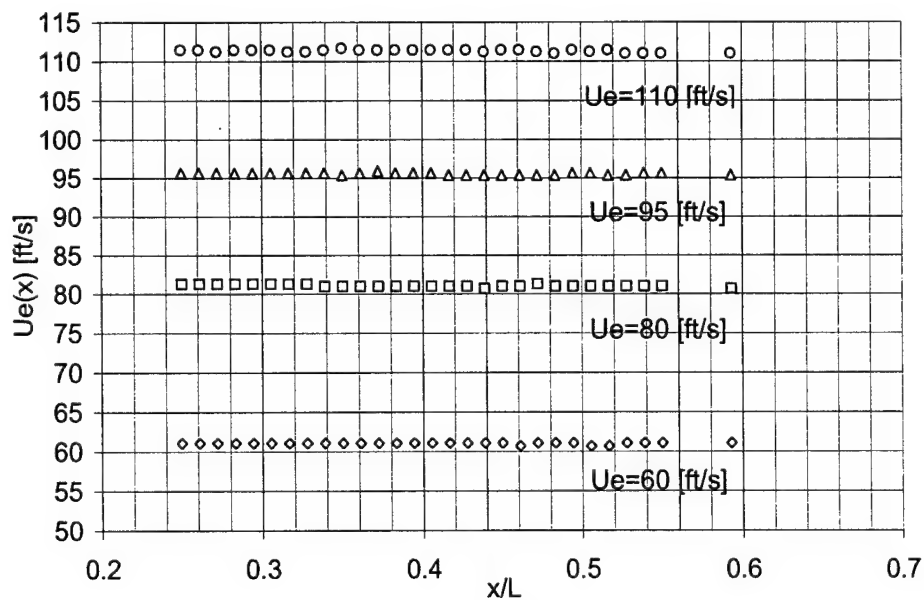
Figure 4.7: Boundary layer velocity profiles for  $U_e = 110$  ft/s.

Figure 4.8: Streamwise Velocity Distributions for all calibration speeds.

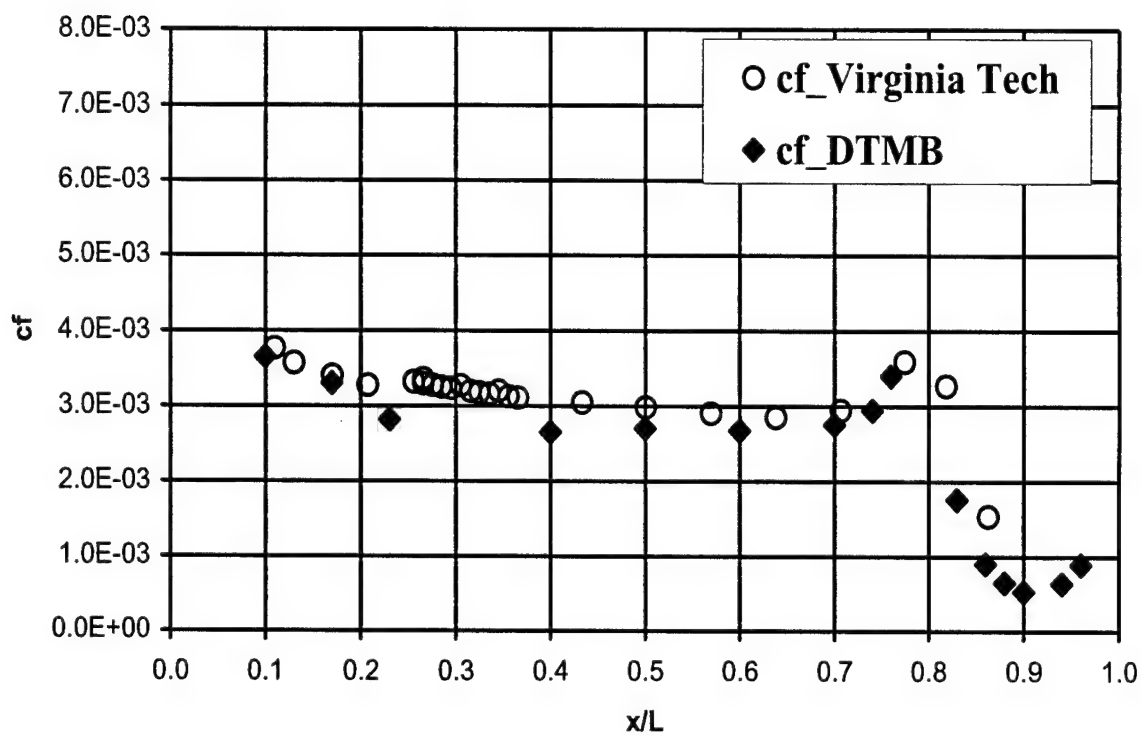


Figure 4.9:  $C_f$  vs.  $x/L$  at  $0^\circ$  angle of attack (For the measurements at Virginia Tech  $Re_L = 5.5 \times 10^6$ , for the measurements at David Taylor Model Basin (DTMB)  $Re_L = 1.2 \times 10^7$ )

# Chapter 5

## Results and Discussion for Steady Measurements

### 5.1 Steady Skin-Friction Measurements

#### 5.1.1 Data Acquisition and Reduction

A Labview software program was developed for the acquisition of the steady skin-friction data. This software program was used to obtain the raw voltage values from the constant temperature anemometers, each connected to a hot-film sensor mounted on the model surface. In order get a single steady skin-friction  $C_f$  value, 10 seconds of voltage data were acquired at a sampling rate of 500 Hz. This gave a total number of 5000 samples per one skin-friction value.

The steady values that were measured or calculated can be defined as arrays of indexed variables for the description of the steady data reduction process. For instance, the voltage value acquired from each anemometer can be written as:

$$E = E(\alpha_j, s_k, \phi_m) \quad (5.1)$$

$$j = 1, \dots, 14 \quad k = 1, \dots, 15 \quad \text{and} \quad m = 1, \dots, nroll \quad (5.2)$$

where  $\alpha_j$  corresponds to each steady angle of attack;  $s_k$  to the sensor number or location; and  $\phi_m$  to the roll angle position of the model. The total number of roll angles  $nroll$  is



56 for the barebody case and 117 for the sail-on-side case.

The steps followed during the steady skin-friction data reduction process can be described in the items below:

1. For each roll position and angle of attack, the voltage data of the free-stream temperature  $T(\alpha_j, \phi_m)$ , the dynamic pressure  $q(\alpha_j, \phi_m)$ , and the atmospheric pressure  $p(\alpha_j, \phi_m)$  are converted to actual values by using the calibration factors.
2. The wall shear stress  $\tau_w(\alpha_j, s_k, \phi_m)$  is calculated by using King's Law (equation 4.10) for each sensor, at each angle of attack and model roll position:

$$\tau_w(\alpha_j, s_k, \phi_m) = \left[ \frac{E^2(\alpha_j, s_k, \phi_m) - A(s_k, \phi_m)}{B(s_k, \phi_m)} \right]^3 \quad (5.3)$$

$A(s_k, \phi_m)$  and  $B(s_k, \phi_m)$  are the calibration coefficients obtained for each sensor at each roll angle position of the model. The skin-friction coefficient  $C_f(\alpha_j, s_k, \phi_m)$  can be calculated simply by dividing the wall shear stress by the dynamic pressure:

$$C_f(\alpha_j, s_k, \phi_m) = \frac{\tau_w(\alpha_j, s_k, \phi_m)}{q(\alpha_j, \phi_m)} \quad (5.4)$$

3. Before the determination of the separation locations,  $C_f = C_f(\alpha_j, s_k, \phi_m)$  vs.  $\phi = \phi_m$  distributions for each sensor are obtained at each angle of attack. In order to filter out some deviant points in the  $C_f$  vs.  $\phi$  distributions of the sail-on-side case, a robust locally weighted regression technique called *loess method* (Cleveland [29]) is used. This smoothing technique uses pre-determined windows of  $\phi$  values in the regression process and gives higher weights to the points near to the location where the smoothed  $C_f$  value is sought. Outliers in the data set are detected during the fitting process and not used in the regression. These features enable to smooth the data without changing the original pattern. A mathematical description of the *loess method* and important parameters to be considered in the smoothing process is given in Appendix A. For further details about the method, see Cleveland [30].
4. The separation locations at each sensor location are determined from the graphs of circumferential skin-friction distributions. The local minima in  $C_f$  is used to locate the separation.

### 5.1.2 Results and Discussion for the Barebody Case

For the range of test conditions mentioned in chapter 4, steady results over the barebody show typical characteristics of the crossflow separation. Figure 5.1 shows the oil flow visualization of the near-wall fluid over the constant diameter region of the model at  $\alpha = 20^\circ$  in the barebody case (Wetzel [20]) and qualitatively describes the crossflow separation topology. Skin-friction lines converge along the separation lines and from this figure two separation lines can be identified on the leeward side of the model. The one closer to the windward side is defined as the primary separation and the other as the secondary separation line.

Figures 5.5 to 5.18 give the skin-friction  $C_f$  distribution vs. circumferential location on the model surface  $\phi$  for different  $x/L$  stations each at a steady angle of attack  $\alpha$ . They show the change of the circumferential  $C_f$  distribution as a function of  $x/L$  at each  $\alpha$  value. Figures 5.19 to 5.32 give the  $C_f$  distribution vs.  $\phi$  for all steady angles of attack at each sensor location. From these figures, the change of circumferential  $C_f$  distribution as a function of  $\alpha$  at each  $x/L$  location can be observed. Barebody results are represented by the filled symbols. In these figures, primary separation locations can be detected as the most windward minima of the  $C_f$  distribution and the secondary separation location can be obtained by finding the second minimum. Figures 5.33 and 5.34 show the primary separation locations as a function of  $\alpha$  for each sensor location. The primary separation locations can be first detected at the last five stations  $x/L = 0.638, 0.706, 0.774, 0.819,$  and  $0.863$  for  $\alpha = 3.1^\circ$ . However, the primary separation locations can be seen more clearly at angles of attack starting from  $\alpha = 5.1^\circ$ . From figures 5.33 and 5.34, it can be seen that as  $x/L$  increases, the primary separation location moves towards the windward side at a specific angle of attack. The same behavior can also be seen as the angle of attack increases: the primary separation location moves towards the windward side at a specific  $x/L$  location. At  $x/L = 0.266$ ,  $\phi = 150^\circ$  can be located as the first primary separation at  $\alpha = 11.3^\circ$ . For this station, the primary separation location moves to  $\phi = 134^\circ$  at  $\alpha = 27.6^\circ$ . At  $x/L = 0.819$ , the primary separation location starts from  $\phi = 147^\circ$  at  $\alpha = 3.1^\circ$  and moves to  $\phi = 111^\circ$  at  $\alpha = 27.6^\circ$ . Figures 5.35 and 5.36 show the secondary separation locations vs.  $\alpha$  for different  $x/L$  stations. The secondary separation can be first detected at  $\alpha = 11.3^\circ$ . For this angle of attack, the secondary separation location is  $\phi = 141^\circ$  at  $x/L = 0.774$  and  $\phi = 143^\circ$  at  $x/L = 0.819$ . In general, at a certain angle of attack, the secondary separation location moves leeward as

$x/L$  increases. Although no data between the measurement stations are available, the separation location at each  $x/L$  location can be used to interpolate the values in-between and this may give an estimate of the primary and secondary separation lines on the model surface.

From the circumferential skin-friction distributions, a nearly flat profile can be seen (figure 5.31) at the vicinity of the minimum point for the last station,  $x/L = 0.863$  located on the stern region. The flat profile extends from  $\phi = 100^\circ$  to  $\phi = 124^\circ$  at  $\alpha = 15.3^\circ$ . This profile indicates separated low speed fluid in this complex flow region that makes the identification of the true minimum difficult. The result is consistent with the oil-flow visualization pictures of this region. Figure 5.2 shows the low speed fluid pattern on the stern region at  $\alpha = 15^\circ$ .

Figure 5.19 shows a bump in the  $C_f$  distribution on the leeward side of the model at the first station  $x/L = 0.110$  starting from  $\alpha = 15.3^\circ$ . In this region, at  $\alpha = 27.6^\circ$ , the increase in  $C_f$  starts approximately from  $\phi = 124^\circ$  and reaches the peak value at around  $\phi = 136^\circ$  and returns back to regular trend at  $\phi = 144^\circ$ . A similar pattern can be observed also for the stations  $x/L = 0.131$  and  $0.170$ . These three stations are located on the nose region of the model. Therefore, this  $C_f$  pattern may imply a weak separation and reattachment of the flow on the nose region of the model at relatively high angles of attack.

Figures 5.37 and 5.38 show the comparison of the barebody primary separation locations obtained with the hot-film sensors and the oil-flow visualizations. The angle of attack is approximately  $15^\circ$  for figure 5.37 and  $20^\circ$  for the other. In both figures, the oil-flow predicts the separations locations more windward compared to the hot-film results with a difference of approximately  $20^\circ$ . As described in Wetzel et al. [32], the errors associated with the separation locations of the oil-flow visualization can be attributed to the gravity effects or direct interactions between the flowfield and the oil mixture, which tends to pool near separations. As in this study, these errors can be very significant, therefore oil-flows should be used for qualitative interpretations of the flow only.

Steady barebody  $C_f$  data obtained with the solid walls are compared with the slotted wall results in figures 5.39 through 5.44 at three  $x/L$  stations: 0.345, 0.570, and 0.819. The results are presented for two angles of attack: for the solid wall case,  $\alpha = 10^\circ$  and  $\alpha = 20^\circ$  and for the slotted wall case  $\alpha = 9.3^\circ$  and  $\alpha = 19.4^\circ$ . For all the stations,

the difference between the solid wall and the slotted wall data can be observed on the windward side and on the last part of leeward side starting approximately from  $\phi = 150^\circ$ . On these regions, the skin-friction values of the slotted wall case are higher than the ones obtained in the solid wall case. This difference is more significant at  $\alpha = 20^\circ$  due to the increased blockage effect of the model. At both angles of attack, the difference in  $C_f$  decreases as  $x/L$  increases. In other words, the blockage effect in  $C_f$  values is more obvious on the upstream constant diameter part of the model as compared to the stern region. The primary and the secondary separation locations are the same in both wall configurations, thus the separation locations are less sensitive to the blockage effect.

### 5.1.3 Results and Discussion for the Sail-on-side Case

In figures 5.5 to 5.32, open symbols stand for the  $C_f$  vs.  $\phi$  distributions of the sail-on-side case. It is more appropriate to evaluate the results of the sail-on-side case in two separate regions: the region with no sail (between  $\phi = 0^\circ$  and  $180^\circ$ ) and the region with the sail (between  $\phi = 180^\circ$  and  $360^\circ$ ). In the first region, the origin and the variation of the primary and the secondary separation lines as a function of  $x/L$  and  $\alpha$  show the same characteristics as defined for the barebody case. This implies that the main flow feature on the non-sail region is the cross flow separation. Figures 5.45 and 5.46 give the primary separation locations vs.  $\alpha$  for each  $x/L$  stations on the non-sail side. The same distribution for the secondary separation locations are presented in figures 5.47 and 5.48. Although the general trend is the same, the locations of the primary and the secondary separations are slightly different from the barebody separation locations. They are more leeward compared to the barebody locations. This difference can be observed in figures 5.49 and 5.50. Figure 5.49 shows the variation of the primary separation location with  $\alpha$  for three different  $x/L$  stations. As can be seen from this figure, the primary separation locations of the barebody case and the non-sail region of the sail-on-side case are approximately the same within uncertainties up to  $\alpha = 15.3^\circ$ . Beyond this angle, the separation locations of the sail-on-side case start to deviate from the barebody results having an offset in the leeward direction. This difference is obvious for  $\alpha = 21.4^\circ, 23.4^\circ$  and  $25.5^\circ$ . Figure 5.50 shows the variation of the secondary separation location with  $\alpha$  for the same  $x/L$  locations. In this figure, for all angles of attack, the secondary separation locations on the non-sail region of the sail-on-side case are shifted in the leeward direction

compared to the secondary separation locations of the barebody case.

The skin-friction distribution trend of the sail region on the nose part of model is approximately the same as the one obtained for the barebody case. At stations  $x/L = 0.110$ ,  $0.131$  and  $0.170$ , the same flow separation and reattachment pattern can be seen starting from  $\alpha = 15.3^\circ$ . As can be seen from the figures 5.19, 5.20, and 5.21,  $C_f$  vs.  $\phi$  distributions for all angles of attack are symmetric with respect to  $\phi = 180^\circ$ . The low speed separated flow region on the stern of the model can be seen again from figure 5.4 which shows the oil flow pattern of this region for the sail-on-side case at  $\alpha = 10^\circ$ .

Downstream of the sail, the flow structure on the sail side of the model is much different than the one observed for the non-sail side. The flow field in this region is strongly affected by the presence of the sail. Compared to the separation topology of the barebody and the non-sail region of the sail-on-side case, the separation location trend as a function of  $x/L$  and  $\alpha$  shows significant differences. Two minima in  $C_f$  vs.  $\phi$  distributions on the leeward side of the sail region can be observed for certain angles of attack and  $x/L$  locations.

Figures 5.51 and 5.52 show the first (measured from  $\phi = 180^\circ$ ) of these separation locations as a function of  $\alpha$  for different streamwise measurement stations starting from  $x/L = 0.434$ . At the stations upstream of  $x/L = 0.434$ , this separation pattern is not observed. For the other stations, first measured separation location on the leeward side does not follow a certain pattern as the angle of attack or  $x/L$  are increased. It changes between  $\phi = 207^\circ$  and  $\phi = 216^\circ$  in an irregular fashion. This separation pattern can be observed at different angles of attack for different sensor locations. The first angle of attack at which this separation can be detected is  $\alpha = 5.1^\circ$  for all sensor locations, while the highest angle of attack changes for different  $x/L$ . Among all the sensor locations, the highest angle of attack is  $17.4^\circ$  and observed at  $x/L = 0.434$ . Beyond this angle of attack, the minimum associated with the first separation location on the leeward side of the sail region vanishes at all  $x/L$  locations.

A second minima in  $C_f$  distribution can be located on the leeward side of the sail region. Figures 5.53 and 5.54 show these separation locations at angles of attack between  $\alpha = 3.1^\circ$  and  $\alpha = 27.6^\circ$  for the sensor stations starting from  $x/L = 0.434$ . For the stations  $x/L = 0.434$ ,  $0.501$ ,  $0.570$ , and  $0.638$ , the separation locations move leeward as the angle of attack is increased up to  $15.3^\circ$ . After this particular angle of attack, the separation

location for each sensor remains approximately the same. For the stations downstream of  $x/L = 0.638$ , the separation locations move leeward until  $\alpha = 9.3^\circ$  is reached. At the remaining angles of attack, the separation location remains approximately at the same  $\phi$  location for each sensor station. The results on the sail side indicate that the flow field does differ from the crossflow separation structure observed for the barebody and non-sail region of the sail-on-side case. Therefore the categorization of the separation locations as the primary or the secondary is not clear and may not reflect the real flow structure of this region.

The flow in the vicinity of the sail-body junction is dominated by the horseshoe type separation. This can be clearly seen from figure 5.3 which shows the oil-flow pattern in the leeward side of the sail region at  $\alpha = 15^\circ$ . The separation line emanating from a three-dimensional stagnation point upstream of the sail extends from both leeward and windward side of the sail and travels downstream. The separation line on the leeward side of the sail can be seen along the converging skin friction lines in figure 5.3. Although the flow topology near the onset of the horseshoe separation is different from that of the crossflow separation as described in Yates and Chapman [1], both show similar characteristics of separated flows downstream: there is a strong convergence of the limiting streamlines on the surface and there are concentrated regions of vorticity in the flow. This may raise the ambiguity about the identification of the separation pattern downstream of the sail. However, the first and second separation locations on the leeward side of the sail region described in the previous paragraph may represent the separation lines emanating from the leeward and windward side of the sail respectively. At high angles of attack, only one separation line (described by the second minimum in the previous paragraph) can be detected. This may imply that leeward and windward separation lines emerge just at the downstream of the sail forming a single separation line.

Figures 5.55 to 5.68, show the  $C_f$  contours around the sail region at steady angles of attack. Note that the blank areas are the regions where no data were acquired. The vertical blank between  $x/L \simeq 0.22$  and  $x/L \simeq 0.26$  designates the ring area where the sail is mounted. These contour plots are generated by using the  $C_f$  measurements obtained from both sensor sets A and B. From figure 5.55, the symmetry in the  $C_f$  distribution with respect to the sail chord line at  $\alpha = 0.9^\circ$  can be observed. This symmetry disappears as the angle of attack is increased. In figure 5.62, at  $\alpha = 15.3^\circ$ , a low velocity region can be noticed at around  $x/L = 0.27$  and  $\phi = 245^\circ$  which also

matches with the oil flow visualization results at that location given by figure 5.3.  $C_f$  on the hull takes relatively large values at regions closer to the sail. At higher angles of attack starting from  $\alpha = 21.4^\circ$ , the increase in the  $C_f$  magnitude on the leeward side of the sail leading edge where the flow is most accelerated can also be seen.

## 5.2 Steady Pressure Measurements

### 5.2.1 Data Reduction

Pressure data reduction was straight forward, however some corrections to the data had to be made. As described in chapter 2, the pressure taps were on the sensor plugs located just behind each hot-film sensor. Although the sensor plugs were levelled with the surface of the model as much as possible, there were slight surface irregularities in the vicinity of the pressure holes which effected the pressure distribution. These irregularities were minimized before the final measurements. However, there were still some oscillations in the data. In order to get rid of these oscillations, the following approach has been developed: the local irregularities on the pressure ports effect the shape of the local streamlines (make more convex or concave) changing the local static pressure measured. By using the normal-to-wall momentum equation, this change in the pressure coefficient  $\Delta C_p$  can be approximated as:

$$\frac{dC_p}{dr} \sim \frac{U^2}{r} \quad (5.5)$$

where  $U$  is the velocity in the local streamwise direction and  $r$  is the normal-to-wall coordinate. Assuming that the local streamline curvature due to the surface irregularity will be approximately the same at all angles of attack and roll position of the model;

$$\Delta C_p = A \left( \frac{U^2}{U_\infty^2} \right) \quad (5.6)$$

Here  $A$  is the unknown coefficient which is different for each port position. With a simple approach,  $C_p$  can be written as:

$$C_p = 1 - \frac{U^2}{U_\infty^2} \quad (5.7)$$

By using the above result in equation 5.6;

$$\Delta C_p = A(1 - C_p) \quad (5.8)$$

If we define  $\Delta C_p$  as the correction to be made to each port location, then we can write

$$C_{pc} = C_{pm} + \Delta C_p \quad (5.9)$$

where  $C_{pm}$  is the measured  $C_p$  value and  $C_{pc}$  is the corrected  $C_p$  value. By using the expression for  $\Delta C_p$  given by equation 5.8, we can obtain the final form of the correction equation as:

$$C_{pc} = A + (1 - A)C_{pm} \quad (5.10)$$

In order to find the  $A$  value for each port position, the  $C_p$  results of the barebody at  $0^\circ$  angle of attack obtained from a RANS code were used (figure 5.69). These CFD results were supplied by Dr. D. L. Whitfield, Mississippi State University. At each port position, the  $C_{pc}$  was taken as the  $C_p$  value of the CFD and the  $C_p$  values of the barebody pressure measurements at  $0^\circ$  angle of attack with slotted walls were taken as the  $C_{pm}$ . The  $A$  values obtained as the result of this procedure were used for the correction of the rest of the data that were taken at  $10^\circ$  and  $20^\circ$  angles of attack.

### 5.2.2 Results and Discussion

Figures 5.70 and 5.71 show barebody pressure coefficient  $C_p$  vs. circumferential location  $\phi$  distributions for different  $x/L$  locations at  $\alpha = 10^\circ$ . Each figure has 10  $x/L$  locations which gives a total number of 20 streamwise measurement stations at a specific angle of attack. The first station is located at  $x/L = 0.112$  and the last one at  $x/L = 0.845$ . Note that the pressure measurement stations are slightly downstream of the corresponding skin-friction measurement locations. However, the difference is approximately 0.2% of the overall model length and can be considered as negligible. All measurement stations given in  $C_p$  figures lie on the long sensor row of the model. Figures 5.72 and 5.73 show the same kind of distribution for  $\alpha = 20^\circ$ .

In figures 5.70 to 5.73,  $C_p$  values are presented for two wind tunnel wall configurations. Solid symbols represent the solid wall results and the open symbols stand for the slotted wall case. As can be seen from these figures,  $C_p$  values of the solid wall case are more negative compared to the ones obtained in the slotted wall case through all  $\phi$  locations. This is an expected result, since in the solid wall case the fluid over the measurement stations is accelerated more compared to the real flow conditions due to the blockage effect of the model at angle of attack. This extra pressure gradient term makes the



$C_p$  values more negative. On the other hand, in the slotted wall configuration with an open-air ratio of 38%, the blockage effect can be reduced significantly and more reliable pressure and skin-friction values can be obtained. The difference between the slotted and solid wall results is more significant for  $\alpha = 20^\circ$ .

At both angles of attack, a favorable pressure gradient can be observed on the windward side of the model for each sensor. The leeward side of model can be thought as a pressure recovery region. However due to the crossflow separation on the leeward side of the model, the general  $C_p$  trend does not follow a monotonic increase. Especially at  $\alpha = 20^\circ$ , a local minimum in  $C_p$  distribution can be detected on the leeward side of the model at each station between  $x/L = 0.288$  and  $x/L = 0.777$ . As also observed by Wetzel [2] in the prolate spheroid case, these minima are the result of the flow separation and may coincide beneath the coherent vortices that form in such an open separation. These vortices with relatively high circulation induce again higher local velocities which in turn lead to a local pressure decrease immediately beneath the vortical core. The  $C_p$  distributions of the last two stations  $x/L = 0.821$  and  $x/L = 0.865$  follow a different trend on the leeward side of the model at both angles of attack compared to the other stations. As in the skin-friction case, a relatively flat  $C_p$  profile can be observed on the circumferential locations corresponding to the low speed separated flow region of the stern.

Figures 5.74 and 5.75 show  $C_p$  vs.  $\phi$  distributions for different  $x/L$  locations at  $\alpha = 10^\circ$  for the sail-on-side case. The data are compared with the barebody case on the non-sail region of the model. Solid symbols represent the  $C_p$  values of the sail-on-side case while the open symbols are used for the barebody case. Both sail-on-side and barebody results are obtained with the slotted wall configuration. Figures 5.76 and 5.77 show the same kind of distribution for  $\alpha = 20^\circ$ . Note that the scales of the  $C_p$  axes are different for  $\alpha = 10^\circ$  and  $\alpha = 20^\circ$  cases. On the non-sail region of the model (between  $\phi = 0^\circ$  and  $\phi = 180^\circ$ ), the  $C_p$  distributions follow the same trend as the one obtained for the barebody case at both angles of attack and the values are approximately the same within the uncertainties. On the sail side, the mean pressure distributions are affected by the presence of the sail except the first four stations on the nose part of the model. These four stations show a symmetric pressure distribution with respect to  $\phi = 180^\circ$ . For the other stations, this symmetry can not be observed. The effect of the sail is significant at the stations located between  $x/L = 0.210$  and  $x/L = 0.308$ . The station at  $x/L = 0.210$  is just upstream of the sail and the pressure increase due the stagnation process can be

clearly seen between  $\phi = 260^\circ$  and  $\phi = 280^\circ$ . The  $C_p$  value takes its maximum value approximately at  $\phi = 280^\circ$  for both angles of attack. The pressure distributions in the vicinity of the leading edge of the sail are of particular interest, since they are responsible for the formation of the horseshoe vortices in this region as described by Simpson [31]. During the measurements two stations were under the sail: station  $x/L = 0.268$  between  $\phi = 262^\circ$  and  $\phi = 270^\circ$ , and station  $x/L = 0.288$  between  $\phi = 267^\circ$  and  $\phi = 269^\circ$ . For these two stations, the  $C_p$  values at the  $\phi$  locations under the sail are left blank in the figures.

Figures 5.78 through 5.81 show the  $C_p$  vs.  $x/L$  distributions obtained with slotted walls for different  $\phi$  locations at  $10^\circ$  and  $20^\circ$  angles of attack. Figures 5.78 and 5.79 give the results for the barebody case. For  $\alpha = 10^\circ$ , a smooth change of  $C_p$  with  $x/L$  at different  $\phi$  values can be observed. At  $\alpha = 20^\circ$ ,  $C_p$  values are more scattered and the magnitude difference between each  $\phi$  position is bigger. Sail-on-side results are given in figures 5.80 and 5.81. At both angles of attack, the effect of the sail on the pressure distribution can be seen on the leeward side of the model, especially at  $\phi = 210^\circ$  and  $\phi = 270^\circ$ .

In order to determine the circumferential behavior of the mean pressure in the separated flow regions,  $C_p$  distributions are compared with the  $C_f$  variations at the same  $x/L$  locations.  $C_f$  distributions of  $x/L = 0.501$  and  $x/L = 0.774$  at  $\alpha = 11.3^\circ$  and  $\alpha = 21.4^\circ$  are compared with the  $C_p$  variations of  $x/L = 0.503$  and  $x/L = 0.777$  at  $\alpha = 10^\circ$  and  $\alpha = 20^\circ$ . Figures 5.82 to 5.85 show the comparison of the barebody case at the conditions given above, while the figures 5.86 to 5.89 show the comparison of the sail-on-side case. A common characteristic of the pressure distributions in the vicinity of the separation locations can be observed from the barebody figures: the mean pressure values are approximately constant over the separated fluid regions. This zero pressure gradient region is obvious at  $x/L = 0.777$  for  $\alpha = 20^\circ$  given by the figure 5.85. The flat pressure profile on the leeward side of the model covers the region between  $\phi = 111^\circ$  and  $\phi = 153^\circ$  and includes both the primary and the secondary separation locations. The same  $C_p$  trend can be observed on the leeward side of the non-sail region in the sail-on-side case. As discussed before, at relatively low angles of attack, two separation locations can be observed on the sail region of model. In figure 5.86, these two separation locations can be seen on the leeward side of the sail region at  $x/L = 0.501$  for  $\alpha = 11.3^\circ$ . Over the first separation location ( $\phi = 216^\circ$ ), the pressure gradient is not zero whereas for the second separation location ( $\phi = 260^\circ$ ) a constant pressure region exists. At higher

angles of attack, only the second separation location remains and the first one vanishes. In figure 5.89, at  $x/L = 0.777$  for  $\alpha = 20^\circ$ , again a flat pressure profile over the separation location on the leeward side of the sail region can be detected. As discussed in Wetzel et al. [32], although the pressure data are used often to indicate the existence of massive separation, it is not a good indicator of the separation location. This is due to the fact that the crossflow separation is the result of a local flow phenomena, but pressure at a given point in space is strongly influenced by the entire flow field. The results of this study also support the aforementioned principle. One can think of using the flat pressure profile in regions of separation to locate the separation locations, however it is difficult to determine the exact point where this flat pressure distribution begins.

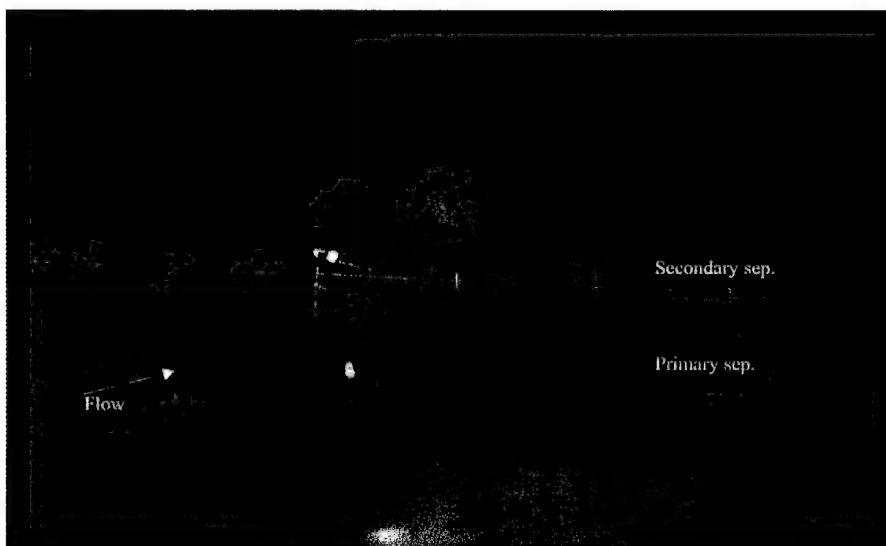


Figure 5.1: Oil flow visualization showing the cross flow separation topology on the constant diameter region of the model for the barebody case at  $\alpha = 20^\circ$ ,  $Re = 4.5 \times 10^6$ . Flow is from left to right.

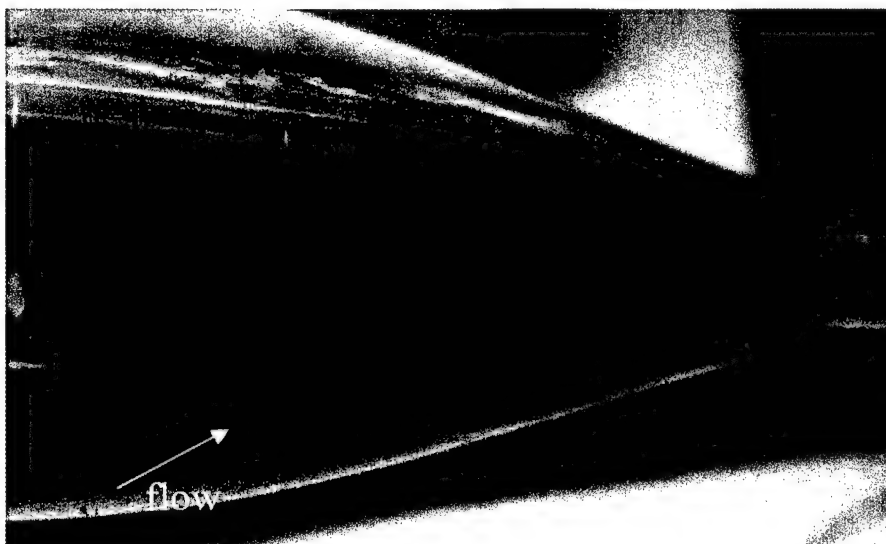


Figure 5.2: Oil flow visualization showing the low speed fluid region on the stern of the model for the barebody case at  $\alpha = 15^\circ$ ,  $Re = 4.5 \times 10^6$ . Flow is from left to right.

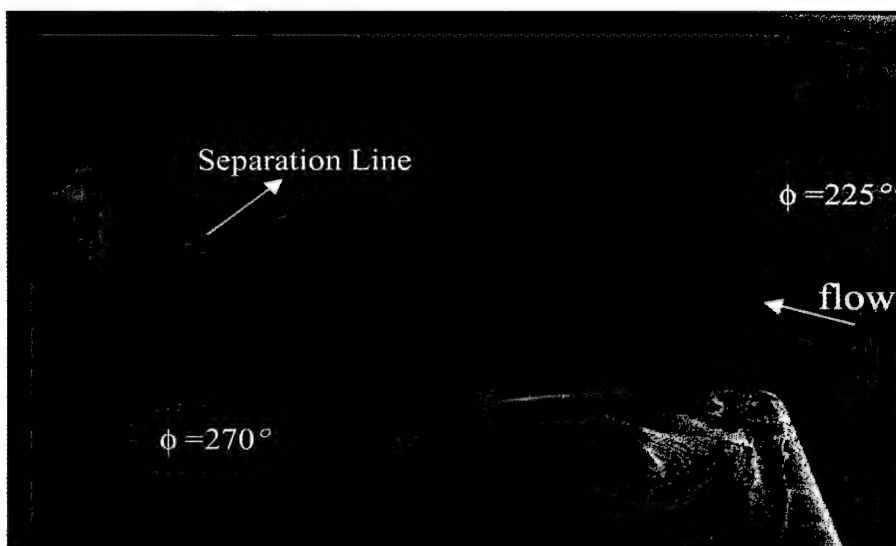


Figure 5.3: Oil flow pattern showing the separation in the vicinity of the sail at  $\alpha = 15^\circ$ ,  $Re = 4.5 \times 10^6$ . Flow is from right to left.

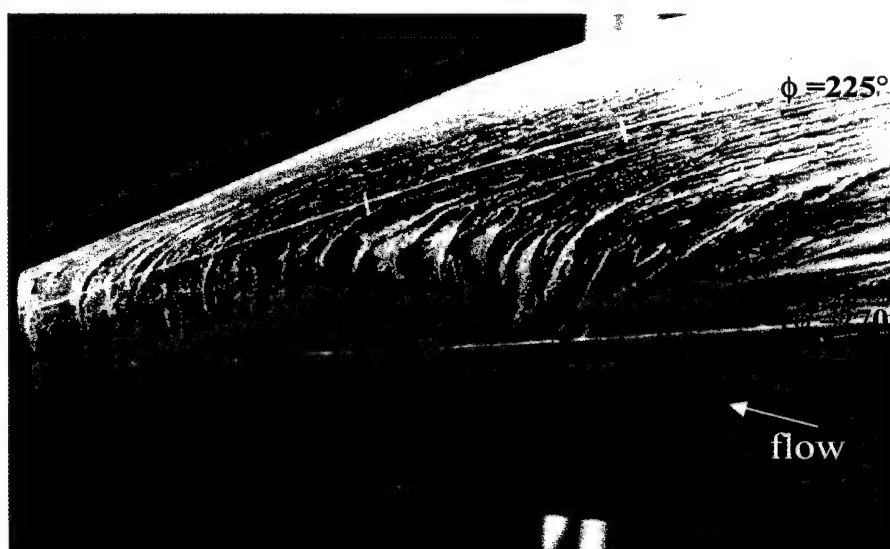


Figure 5.4: Oil flow visualization of the sail side showing the low speed fluid region on the stern of the model for the sail-on-side case at  $\alpha = 10^\circ$ ,  $Re = 4.5 \times 10^6$ . Flow is from right to left.

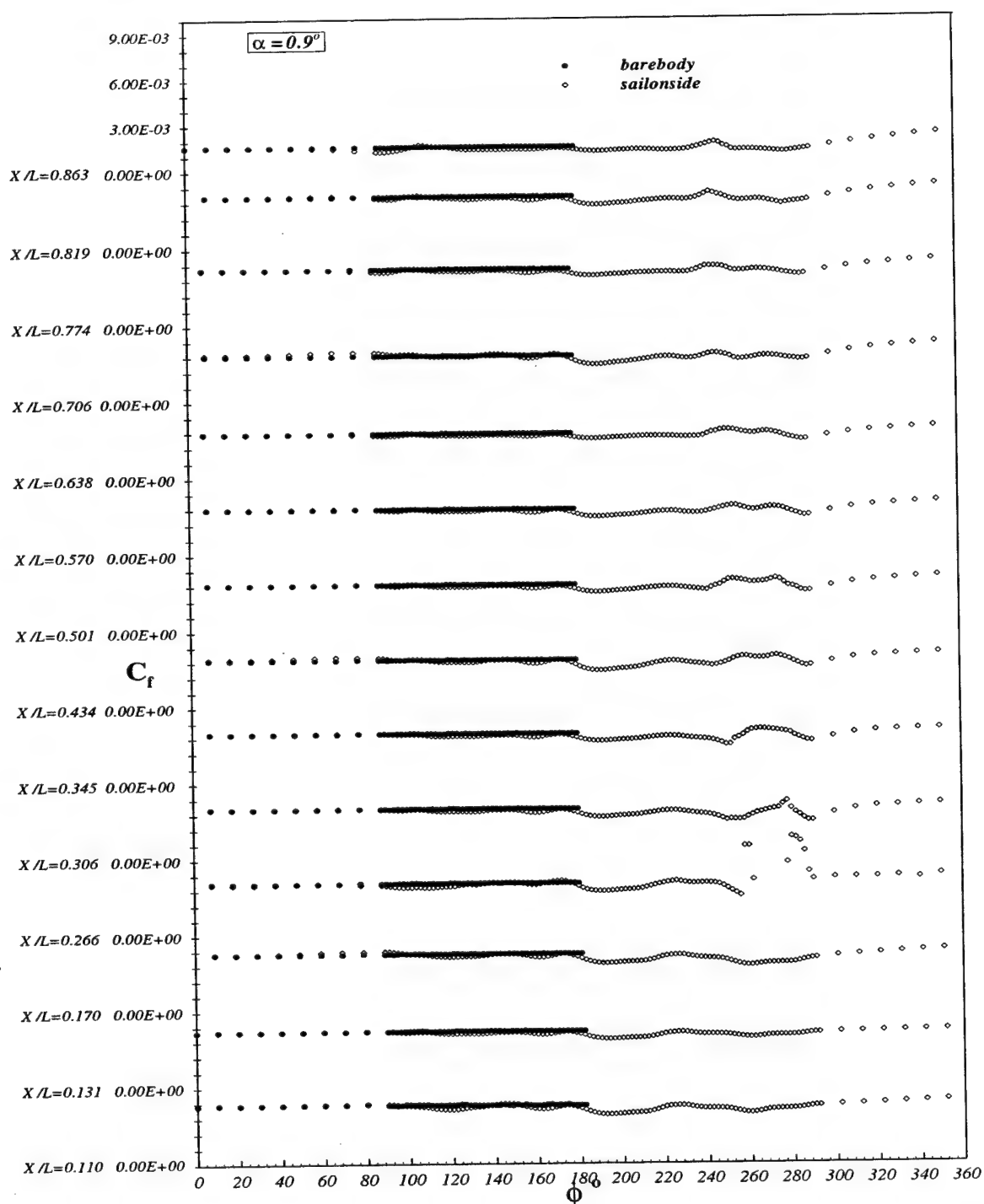


Figure 5.5:  $C_f$  vs.  $\phi$  for all  $x/L$  locations at  $\alpha = 0.9^\circ$  for steady barebody and sail-on-side cases. Sail side on the right of the figure starting from  $\phi = 180^\circ$ .

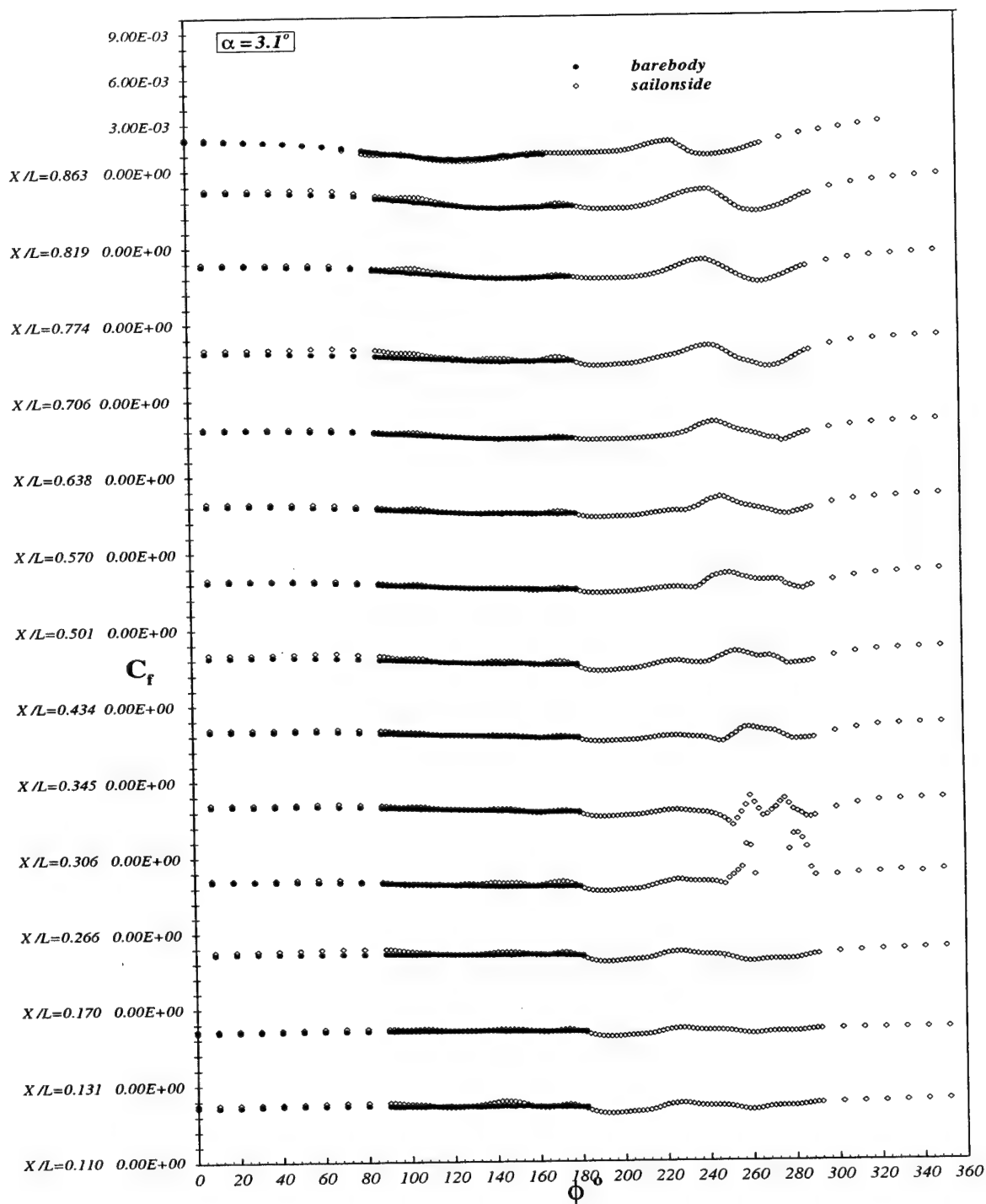


Figure 5.6:  $C_f$  vs.  $\phi$  for all  $x/L$  locations at  $\alpha = 3.1^\circ$  for steady barebody and sail-on-side cases. Sail side on the right of the figure starting from  $\phi = 180^\circ$ .

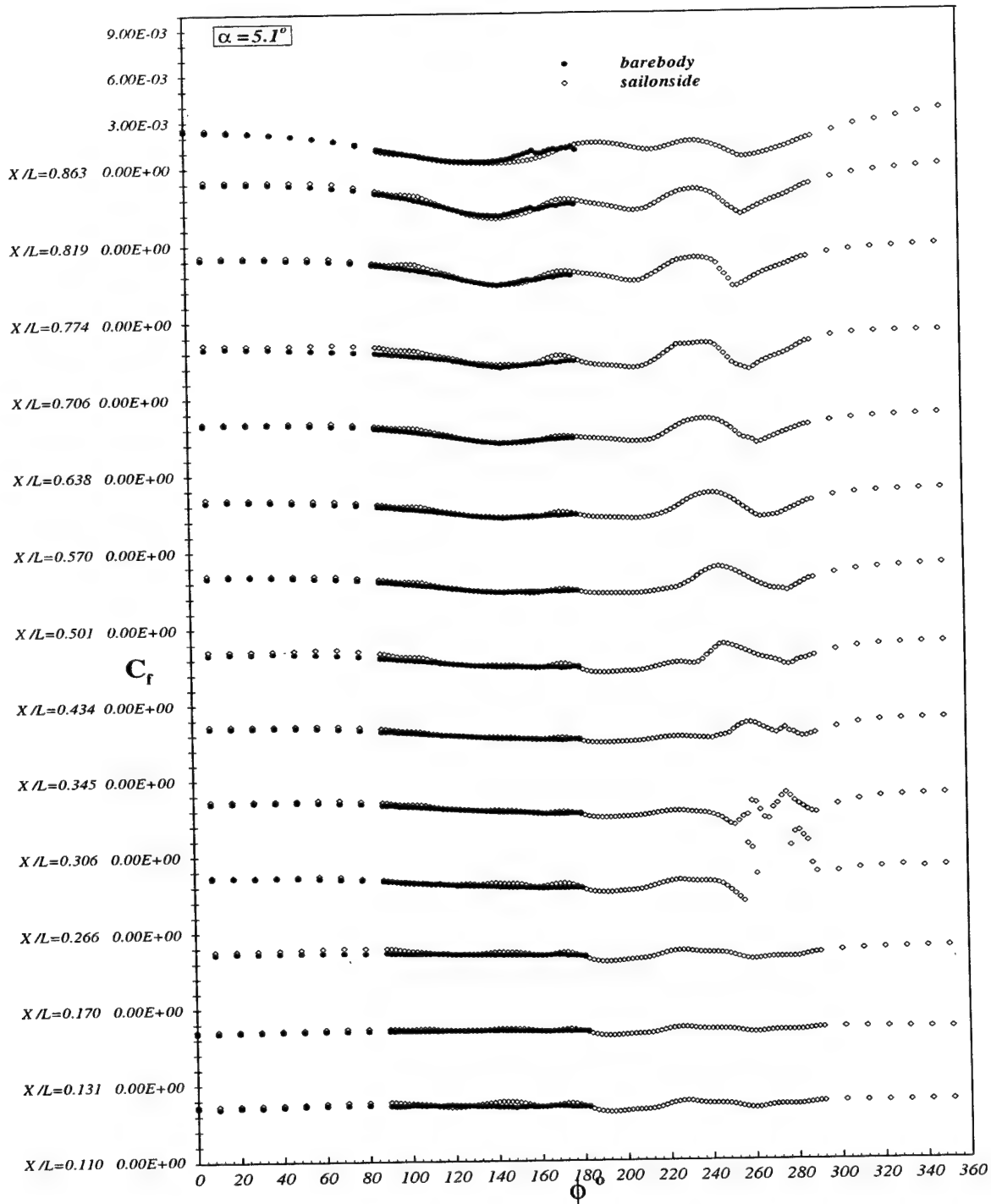


Figure 5.7:  $C_f$  vs.  $\phi$  for all  $x/L$  locations at  $\alpha = 5.1^\circ$  for steady barebody and sail-on-side cases. Sail side on the right of the figure starting from  $\phi = 180^\circ$ .



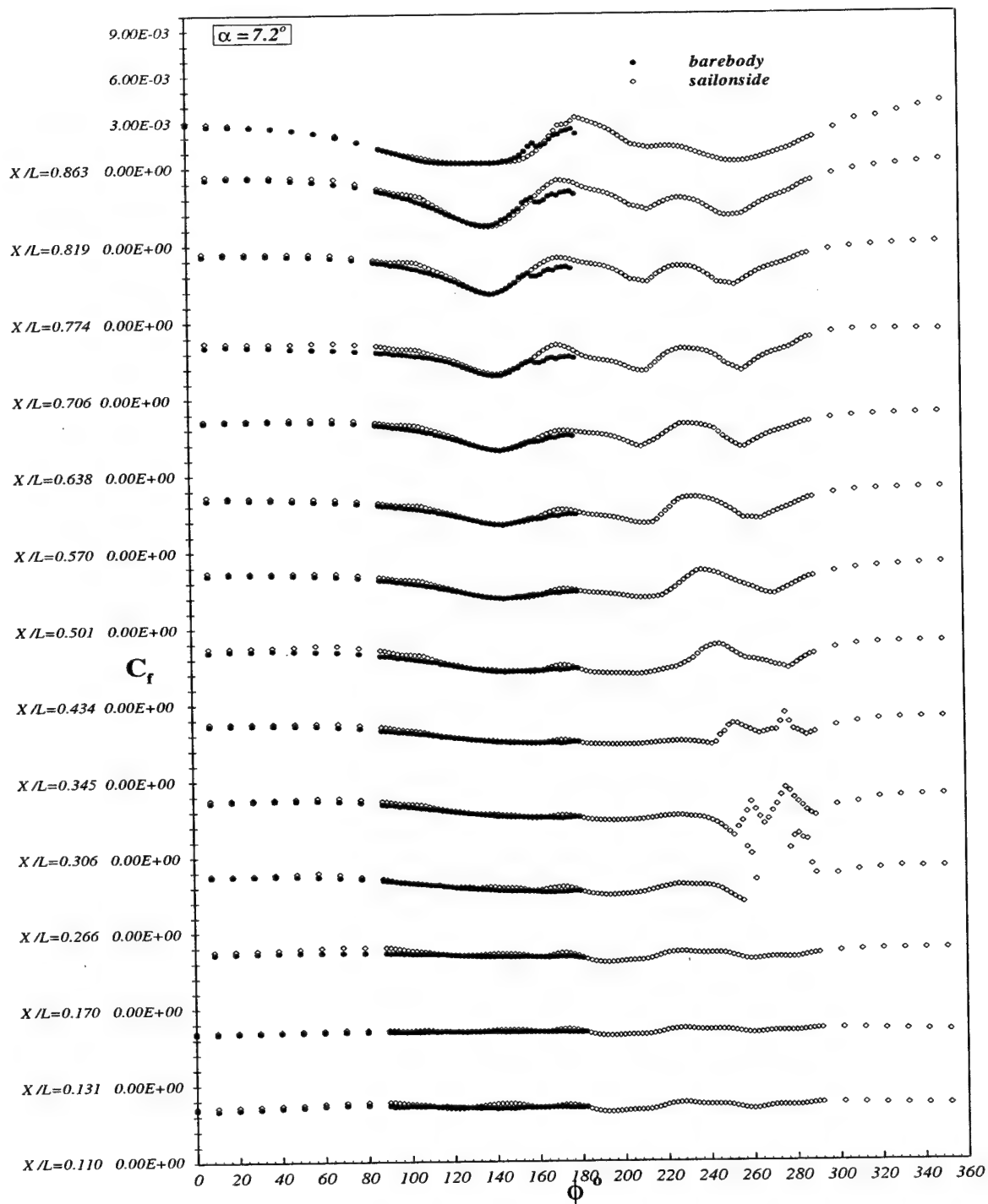


Figure 5.8:  $C_f$  vs.  $\phi$  for all  $x/L$  locations at  $\alpha = 7.2^\circ$  for steady barebody and sail-on-side cases. Sail side on the right of the figure starting from  $\phi = 180^\circ$ .

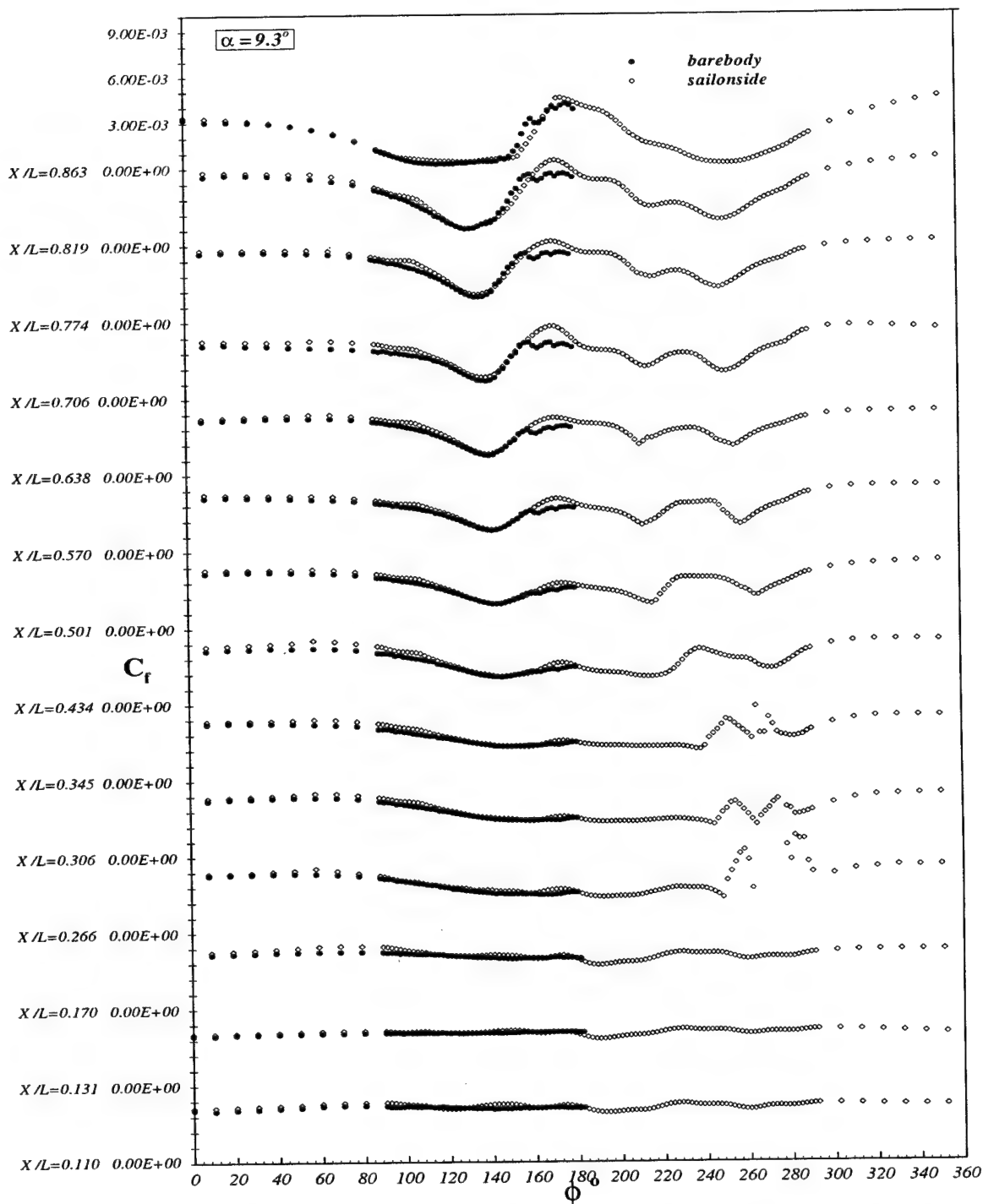


Figure 5.9:  $C_f$  vs.  $\phi$  for all  $x/L$  locations at  $\alpha = 9.3^\circ$  for steady barebody and sail-on-side cases. Sail side on the right of the figure starting from  $\phi = 180^\circ$ .

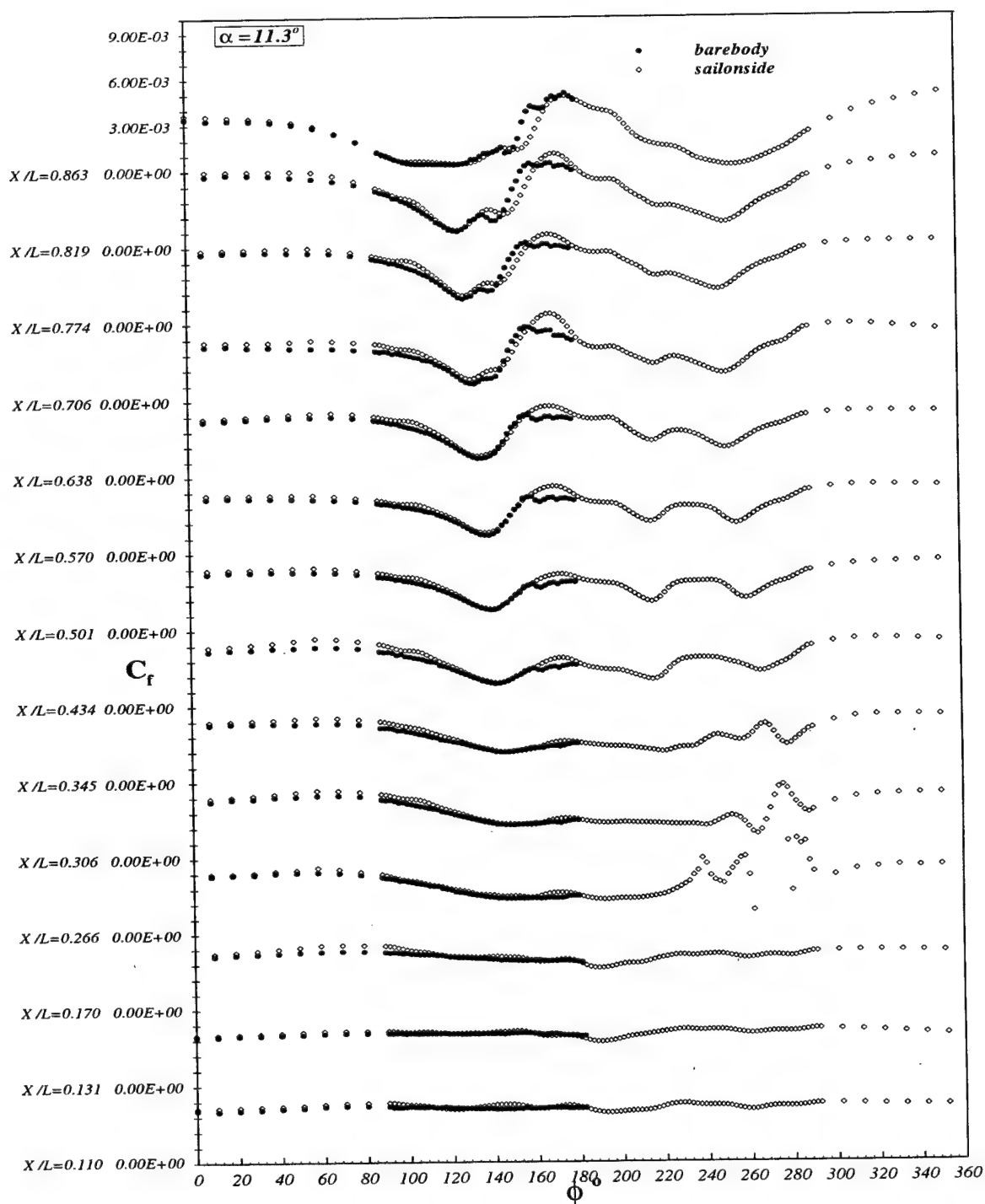


Figure 5.10:  $C_f$  vs.  $\phi$  for all  $x/L$  locations at  $\alpha = 11.3^\circ$  for steady barebody and sail-on-side cases. Sail side on the right of the figure starting from  $\phi = 180^\circ$ .

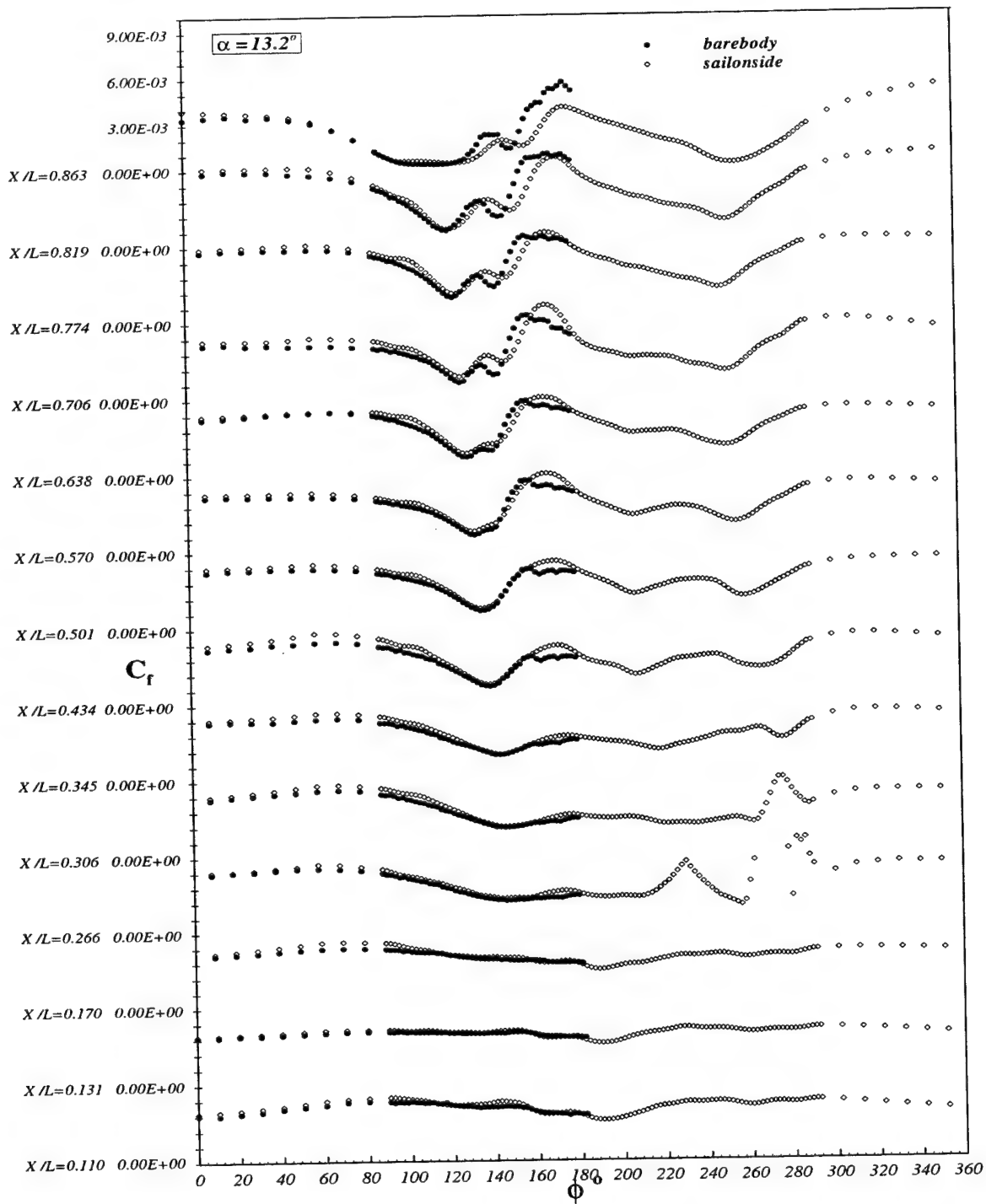


Figure 5.11:  $C_f$  vs.  $\phi$  for all  $x/L$  locations at  $\alpha = 13.2^\circ$  for steady barebody and sail-on-side cases. Sail side on the right of the figure starting from  $\phi = 180^\circ$ .

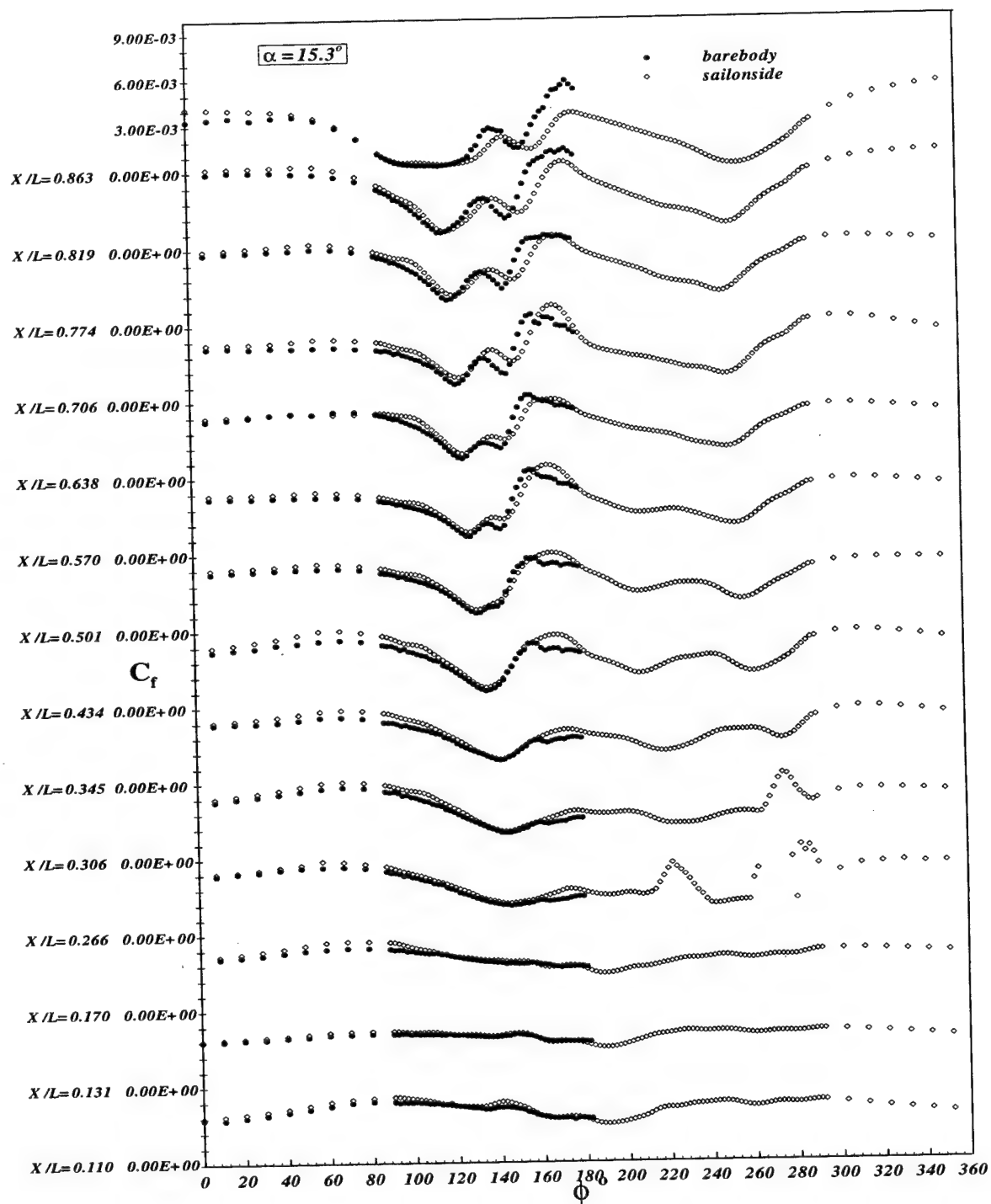


Figure 5.12:  $C_f$  vs.  $\phi$  for all  $x/L$  locations at  $\alpha = 15.3^\circ$  for steady barebody and sail-on-side cases. Sail side on the right of the figure starting from  $\phi = 180^\circ$ .

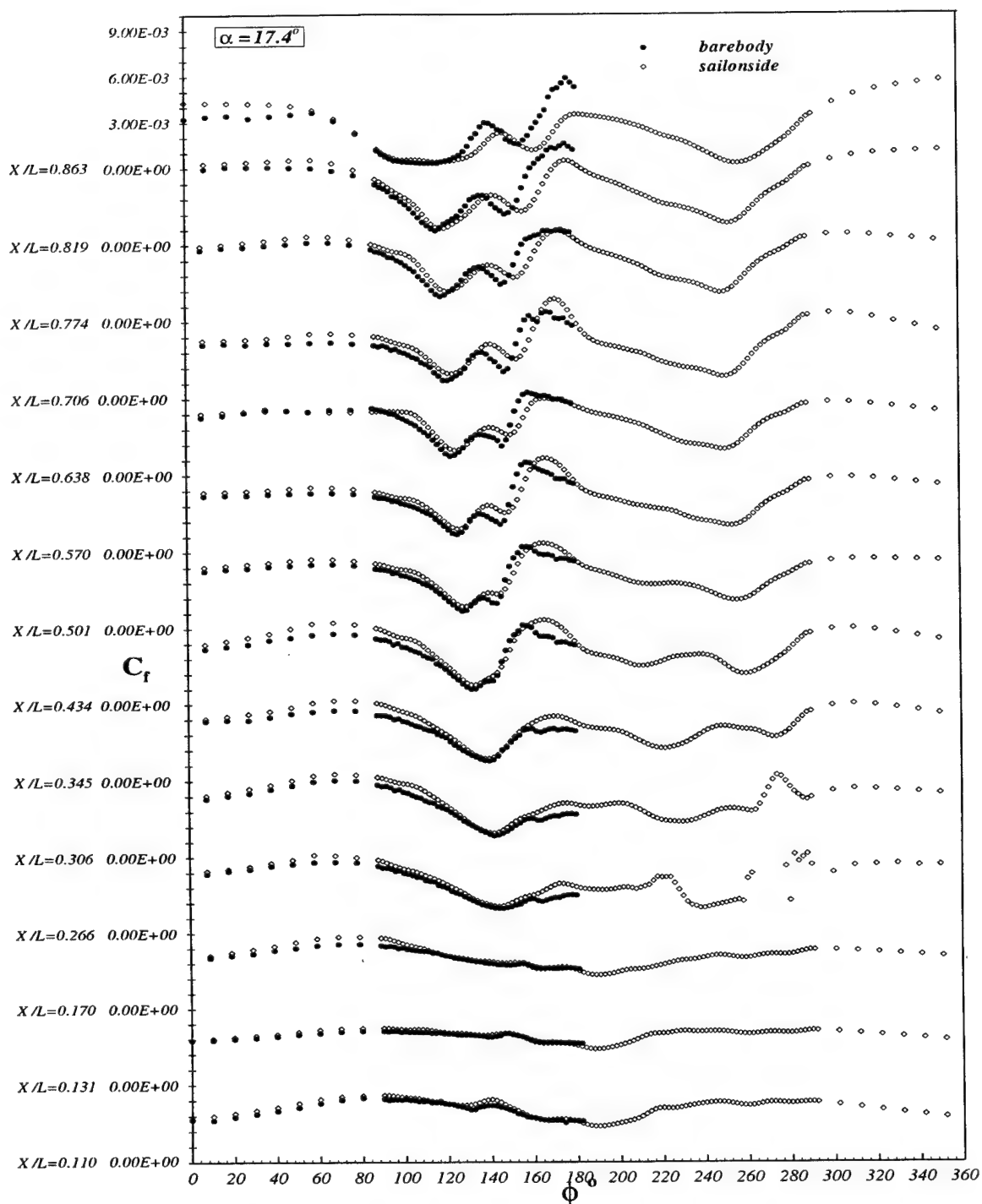


Figure 5.13:  $C_f$  vs.  $\phi$  for all  $x/L$  locations at  $\alpha = 17.4^\circ$  for steady barebody and sail-on-side cases. Sail side on the right of the figure starting from  $\phi = 180^\circ$ .

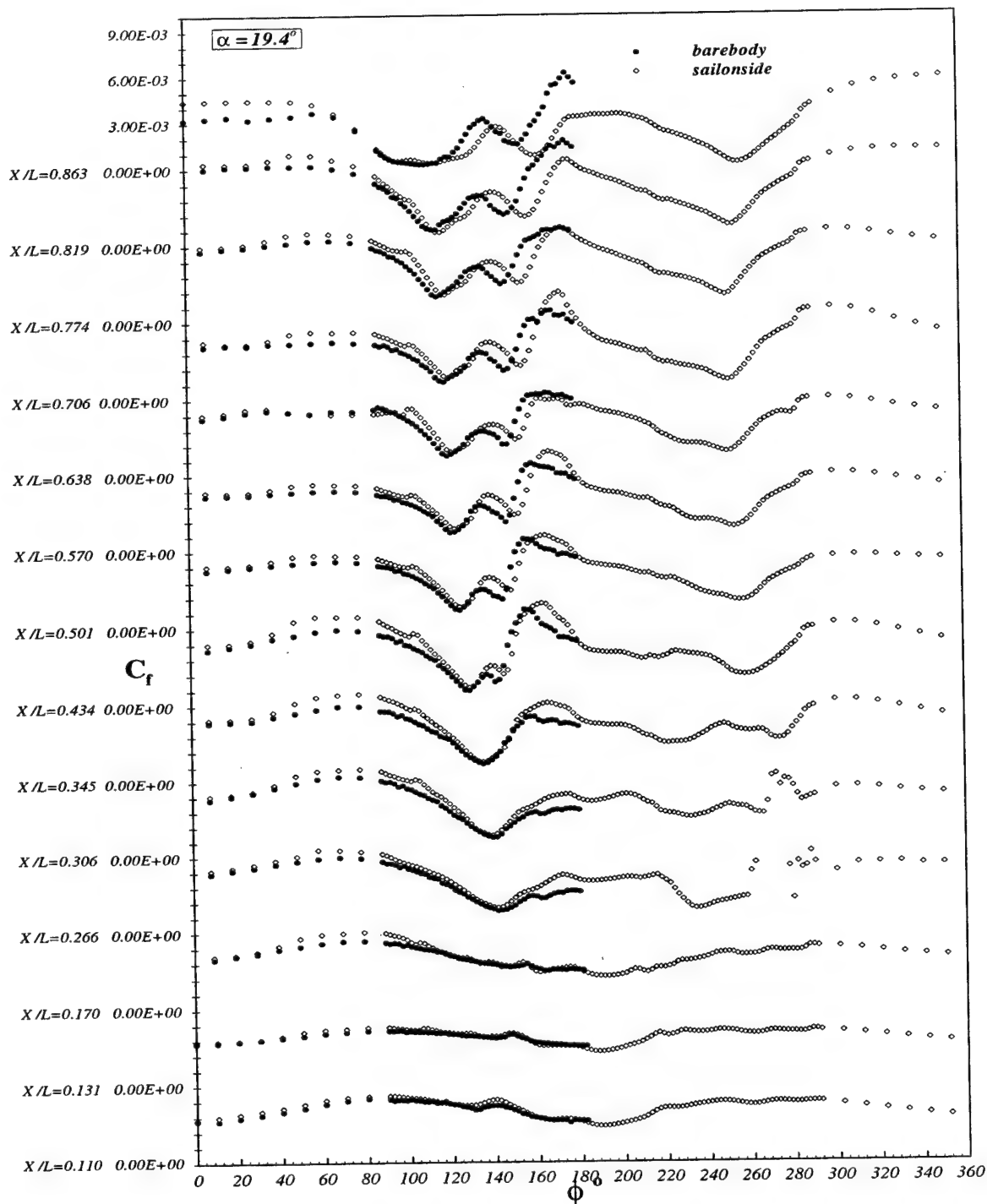


Figure 5.14:  $C_f$  vs.  $\phi$  for all  $x/L$  locations at  $\alpha = 19.4^\circ$  for steady barebody and sail-on-side cases. Sail side on the right of the figure starting from  $\phi = 180^\circ$ .

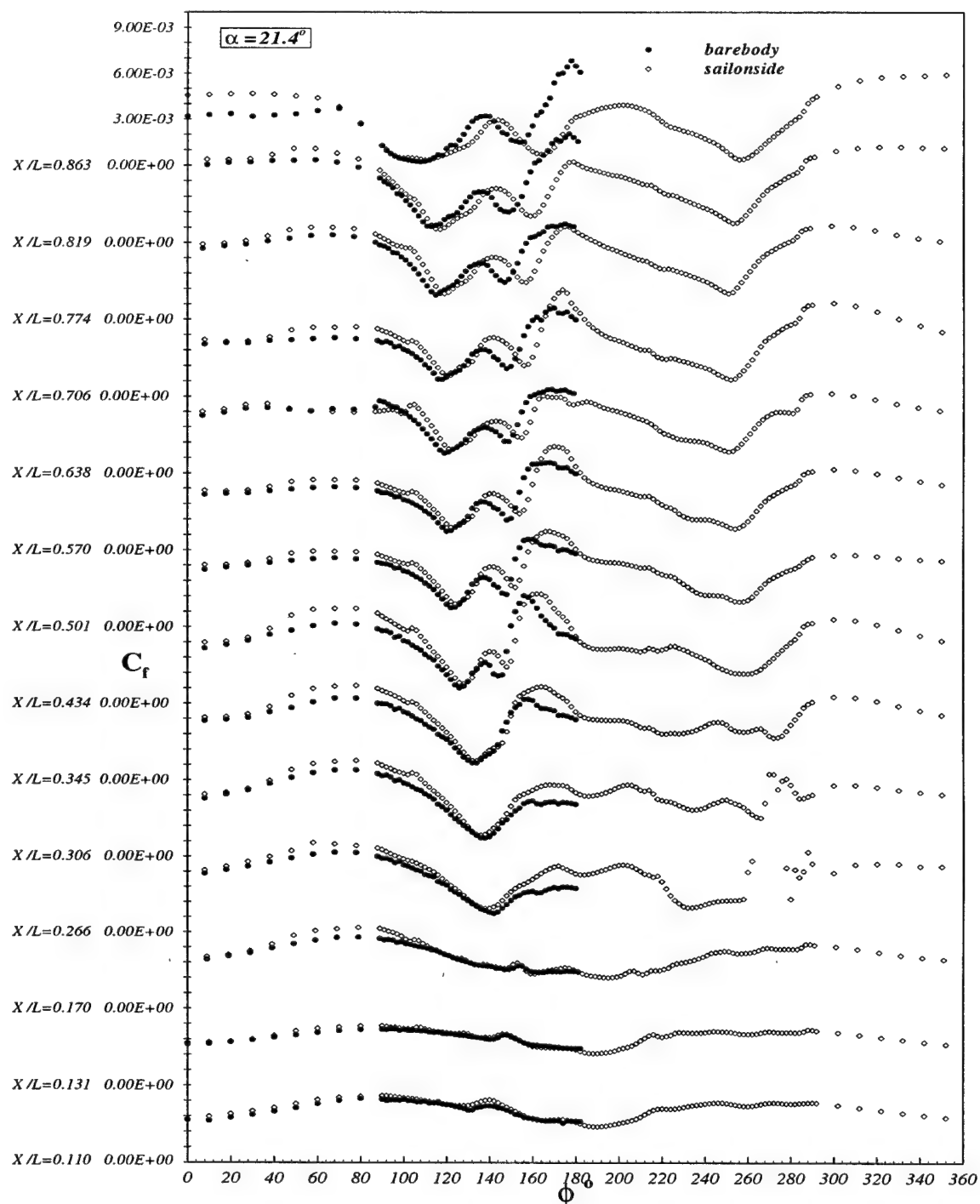


Figure 5.15:  $C_f$  vs.  $\phi$  for all  $x/L$  locations at  $\alpha = 21.4^\circ$  for steady barebody and sail-on-side cases. Sail side on the right of the figure starting from  $\phi = 180^\circ$ .



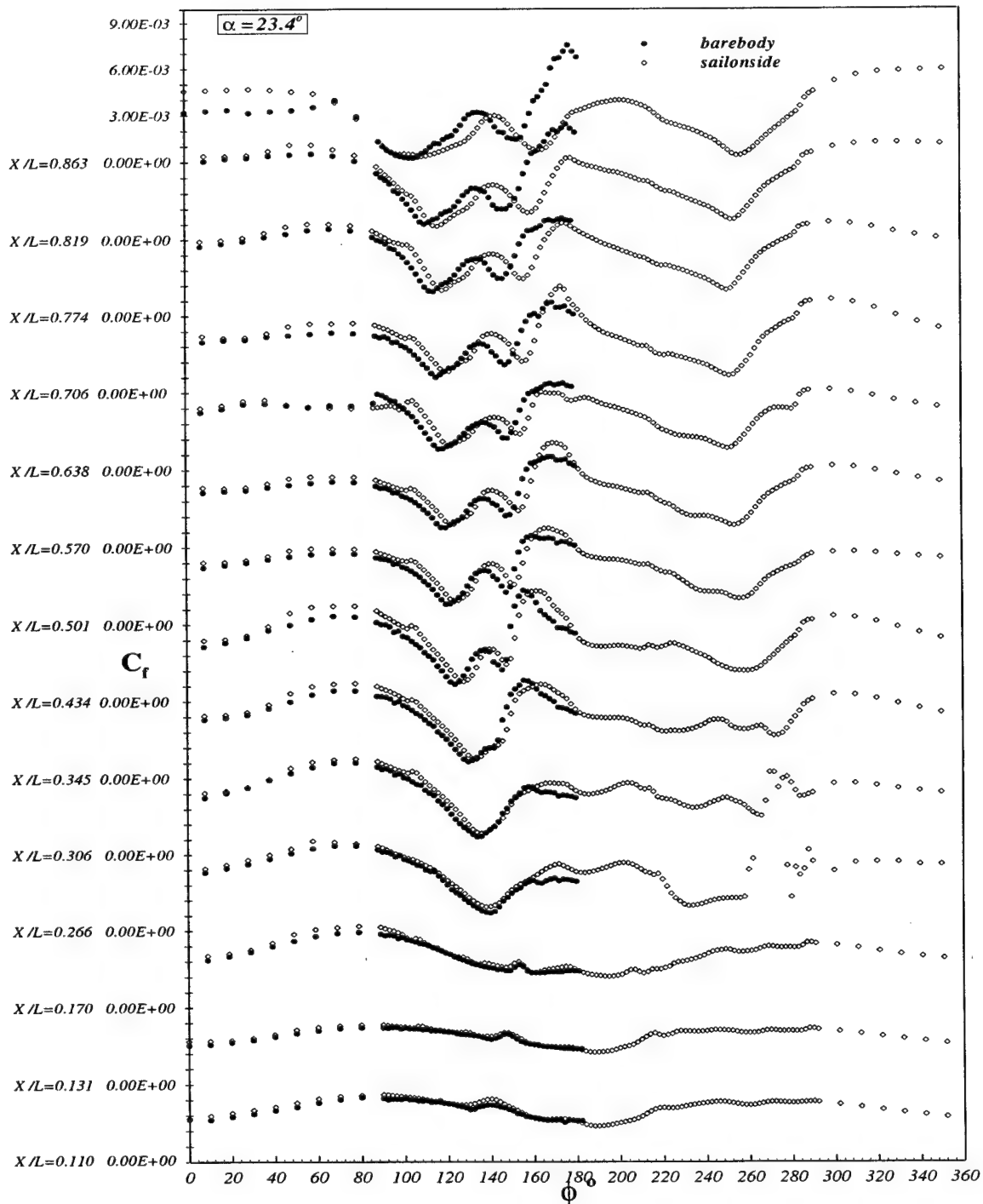


Figure 5.16:  $C_f$  vs.  $\phi$  for all  $x/L$  locations at  $\alpha = 23.4^\circ$  for steady barebody and sail-on-side cases. Sail side on the right of the figure starting from  $\phi = 180^\circ$ .

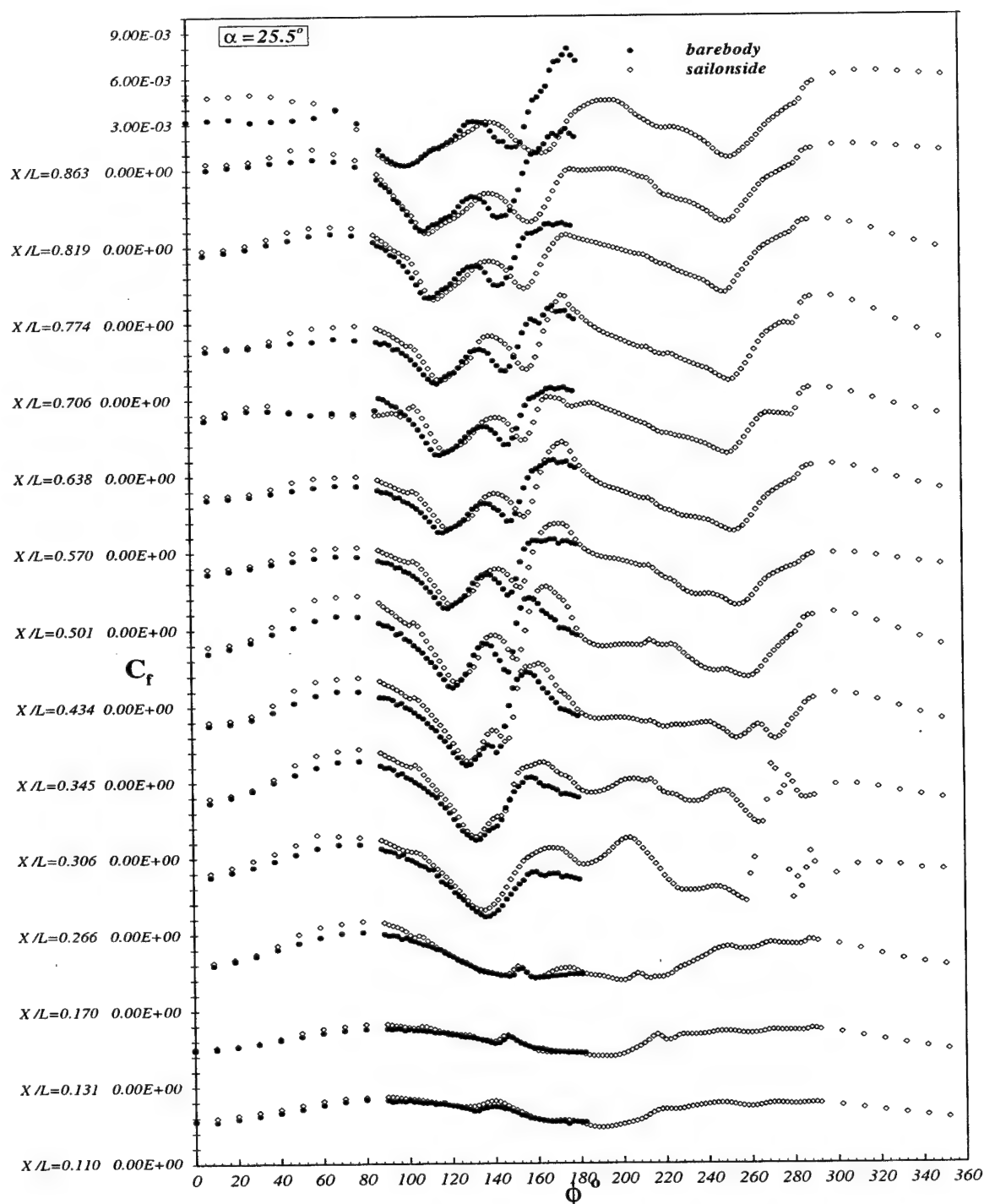


Figure 5.17:  $C_f$  vs.  $\phi$  for all  $x/L$  locations at  $\alpha = 25.5^\circ$  for steady barebody and sail-on-side cases. Sail side on the right of the figure starting from  $\phi = 180^\circ$ .

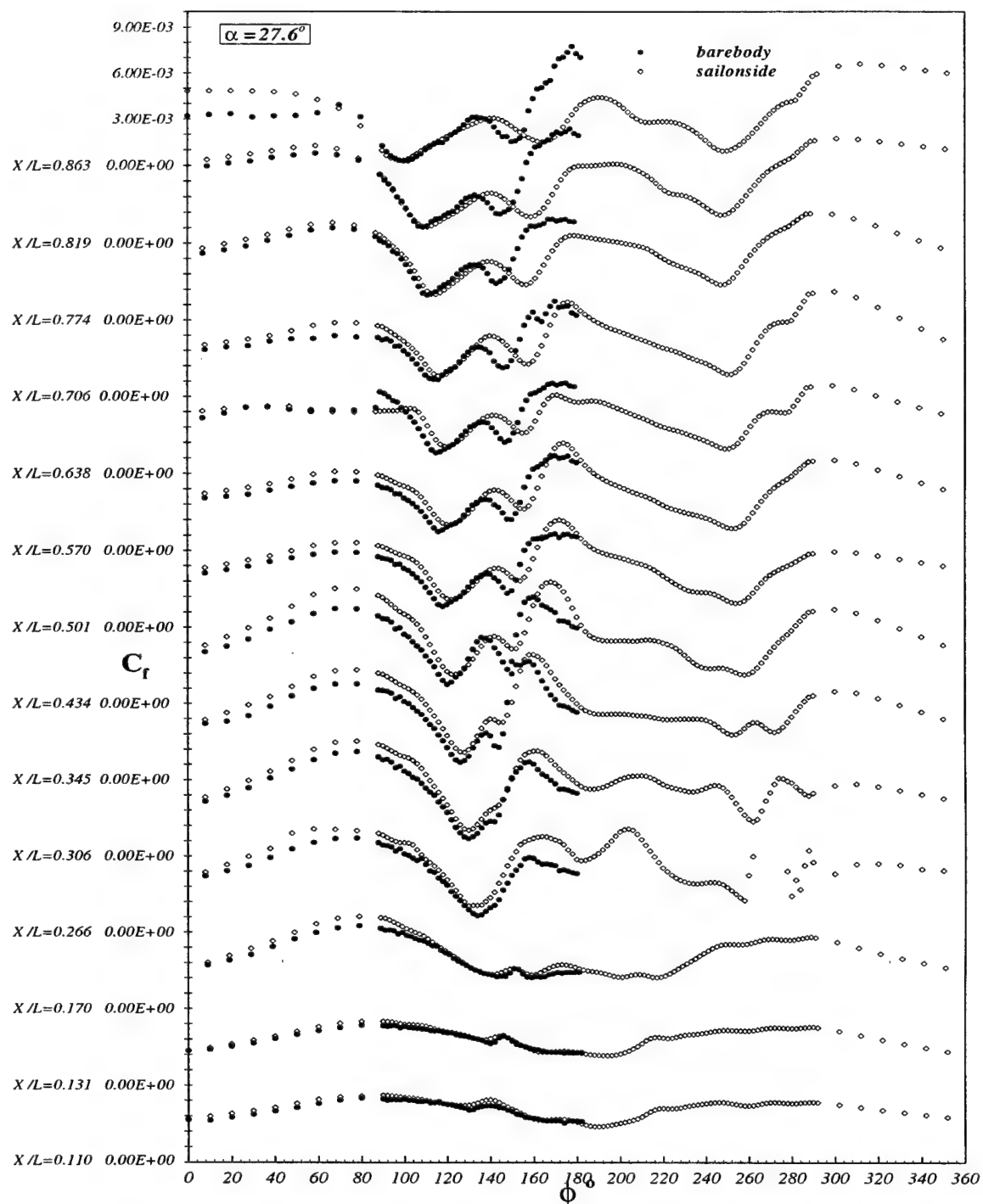


Figure 5.18:  $C_f$  vs.  $\phi$  for all  $x/L$  locations at  $\alpha = 27.6^\circ$  for steady barebody and sail-on-side cases. Sail side on the right of the figure starting from  $\phi = 180^\circ$ .

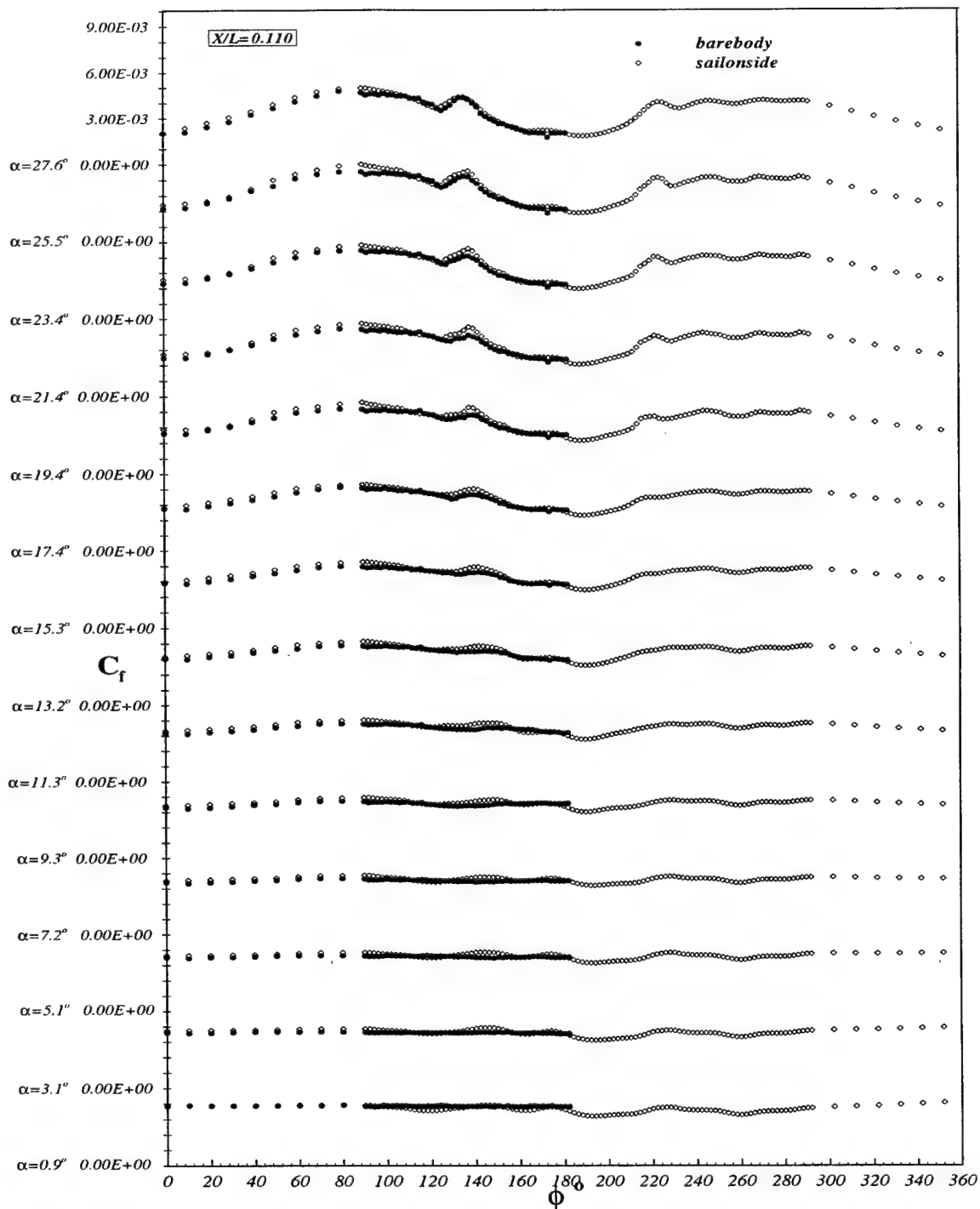


Figure 5.19:  $C_f$  vs.  $\phi$  for all  $\alpha$  at  $x/L = 0.110$  for steady barebody and sail-on-side cases. Sail side on the right of the figure starting from  $\phi = 180^\circ$ .

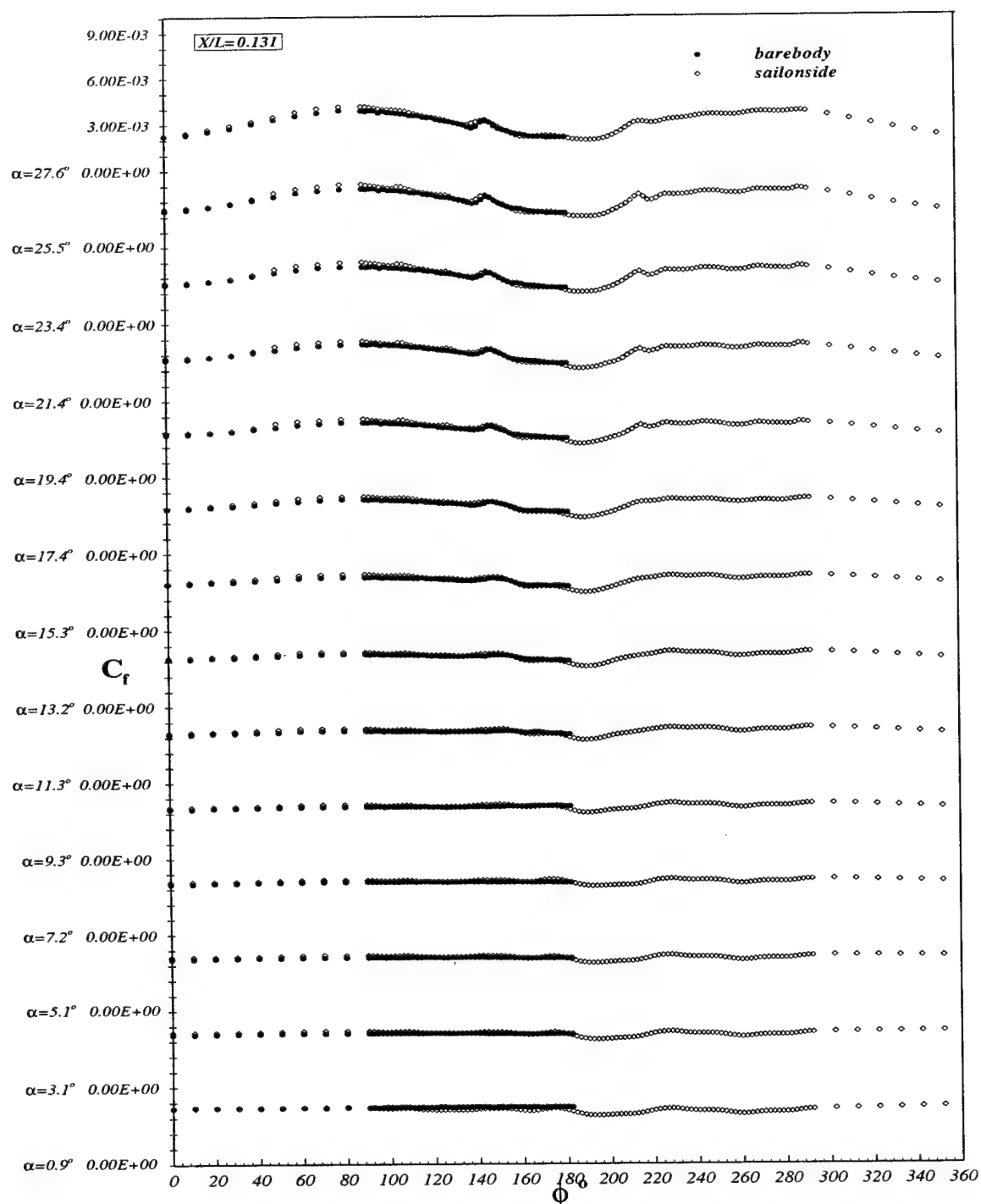


Figure 5.20:  $C_f$  vs.  $\phi$  for all  $\alpha$  at  $x/L = 0.131$  for steady barebody and sail-on-side cases. Sail side on the right of the figure starting from  $\phi = 180^\circ$ .

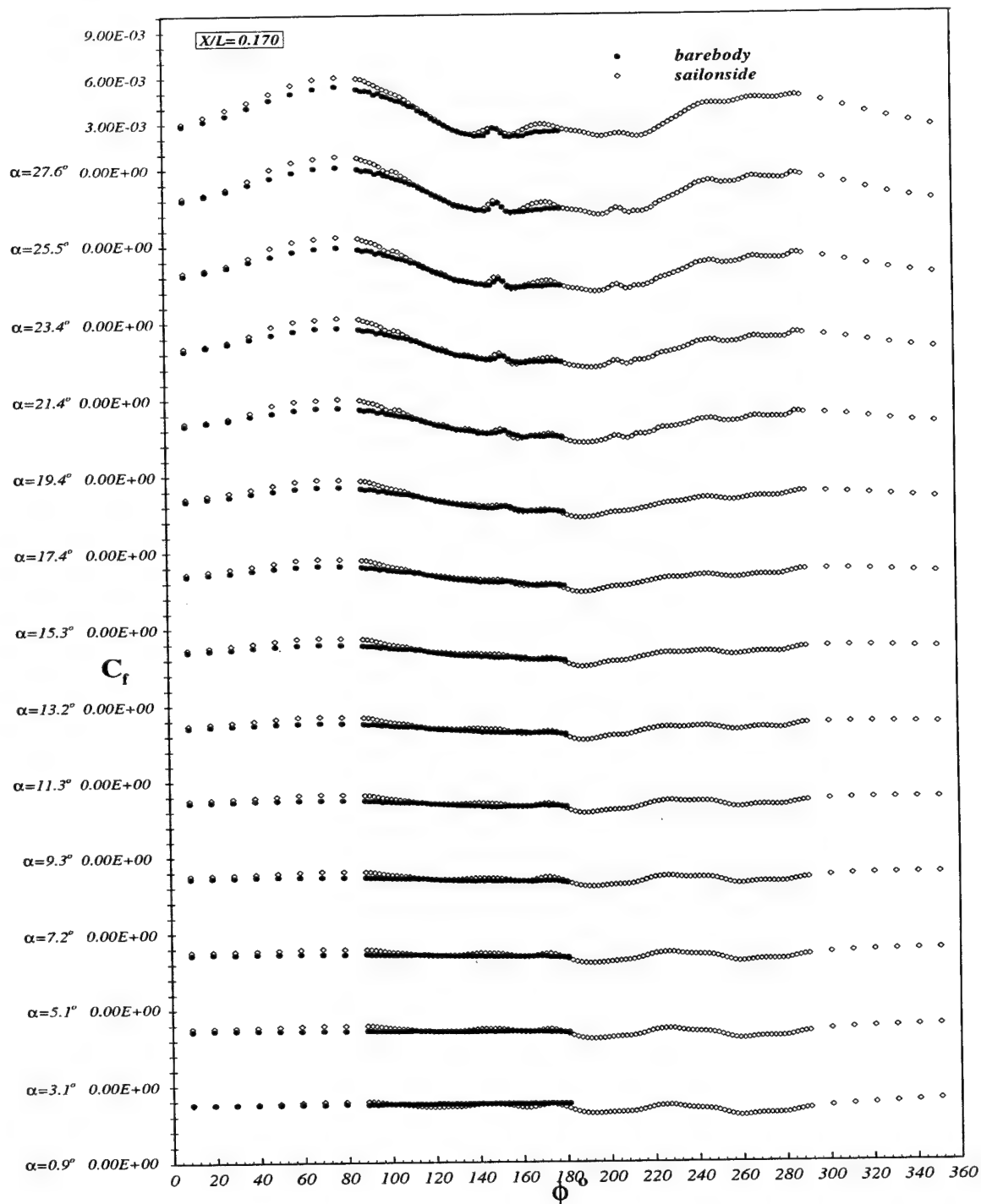


Figure 5.21:  $C_f$  vs.  $\phi$  for all  $\alpha$  at  $x/L = 0.170$  for steady barebody and sail-on-side cases. Sail side on the right of the figure starting from  $\phi = 180^\circ$ .

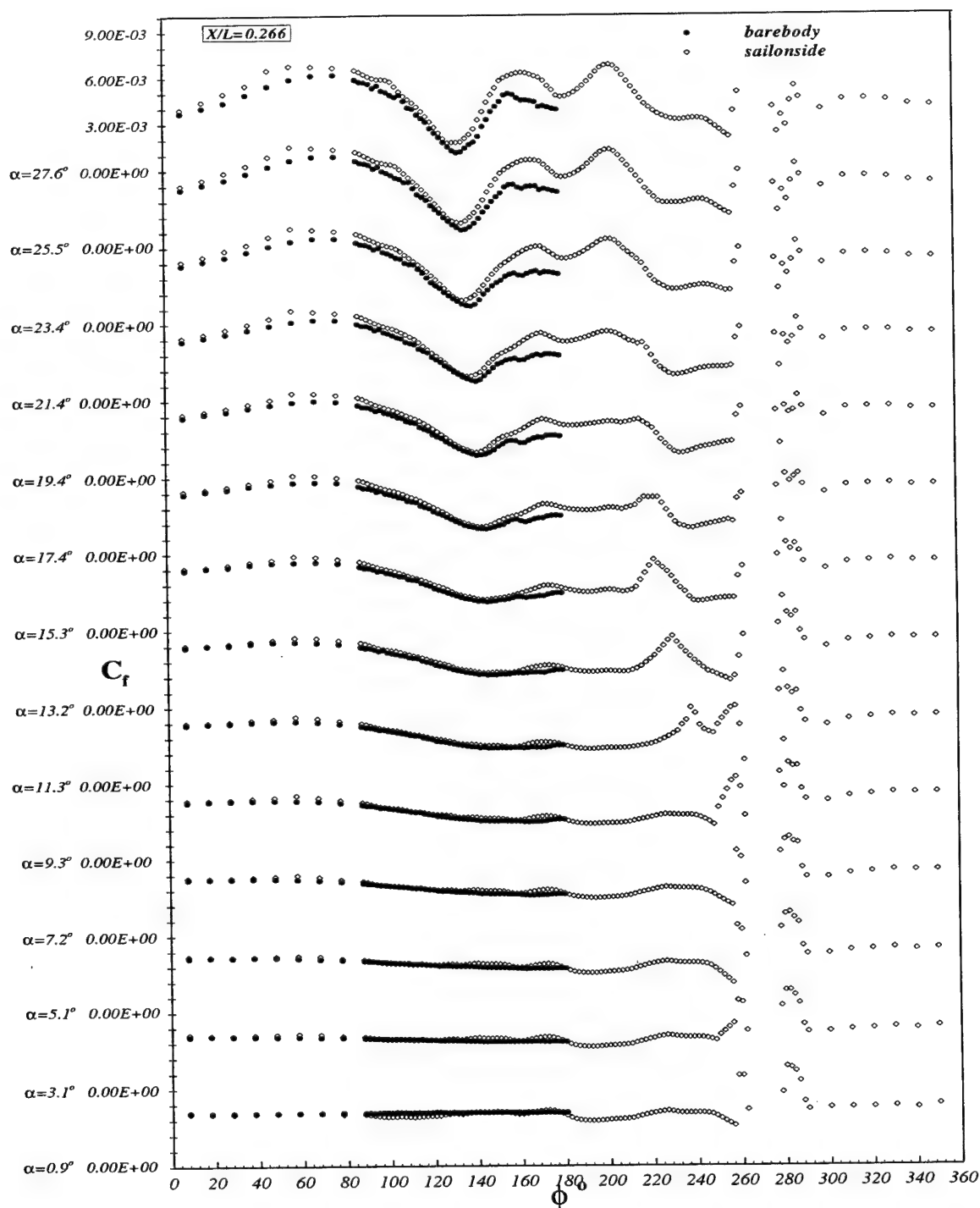


Figure 5.22:  $C_f$  vs.  $\phi$  for all  $\alpha$  at  $x/L = 0.266$  for steady barebody and sail-on-side cases. Sail side on the right of the figure starting from  $\phi = 180^\circ$ .

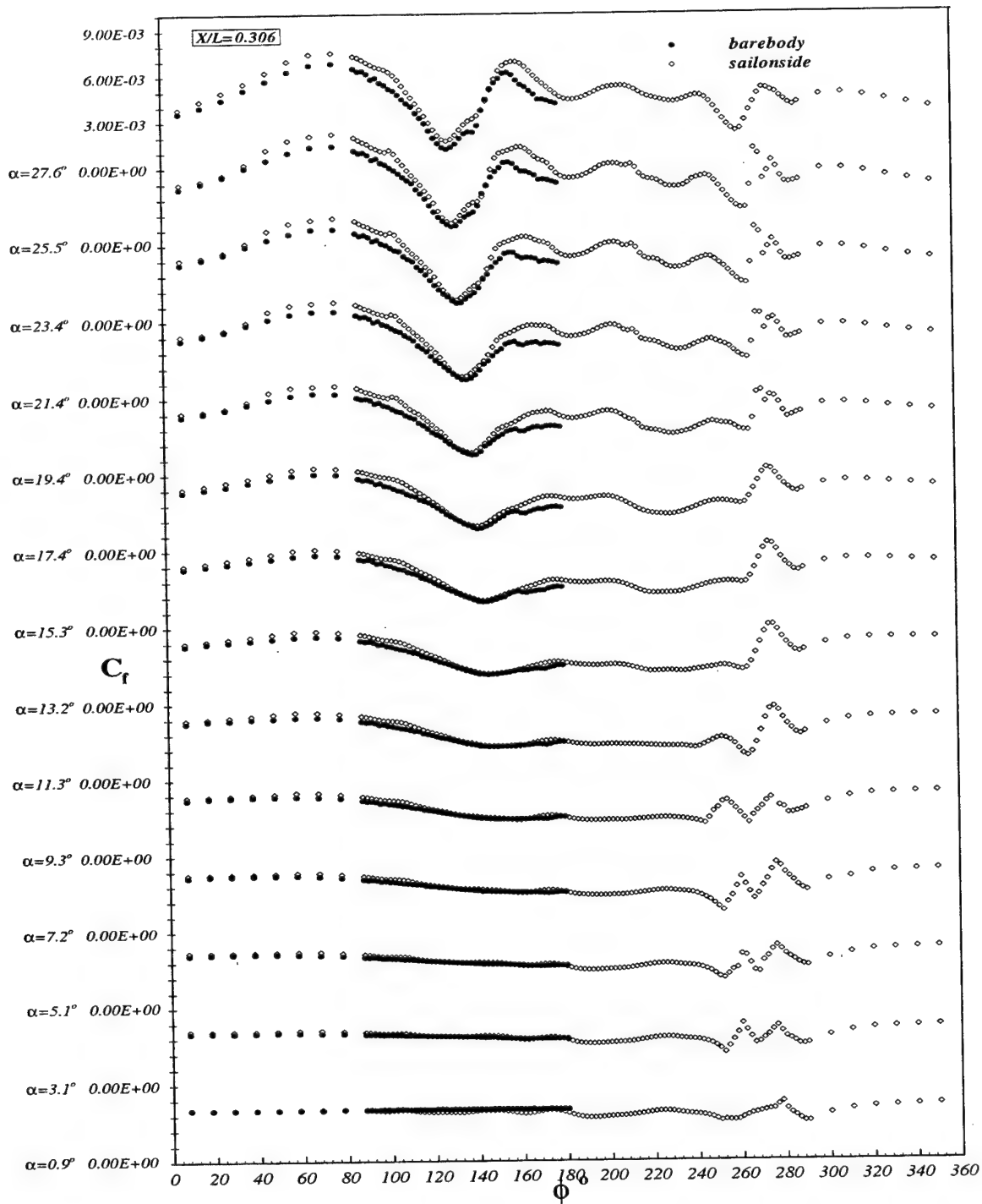


Figure 5.23:  $C_f$  vs.  $\phi$  for all  $\alpha$  at  $x/L = 0.306$  for steady barebody and sail-on-side cases. Sail side on the right of the figure starting from  $\phi = 180^\circ$ .



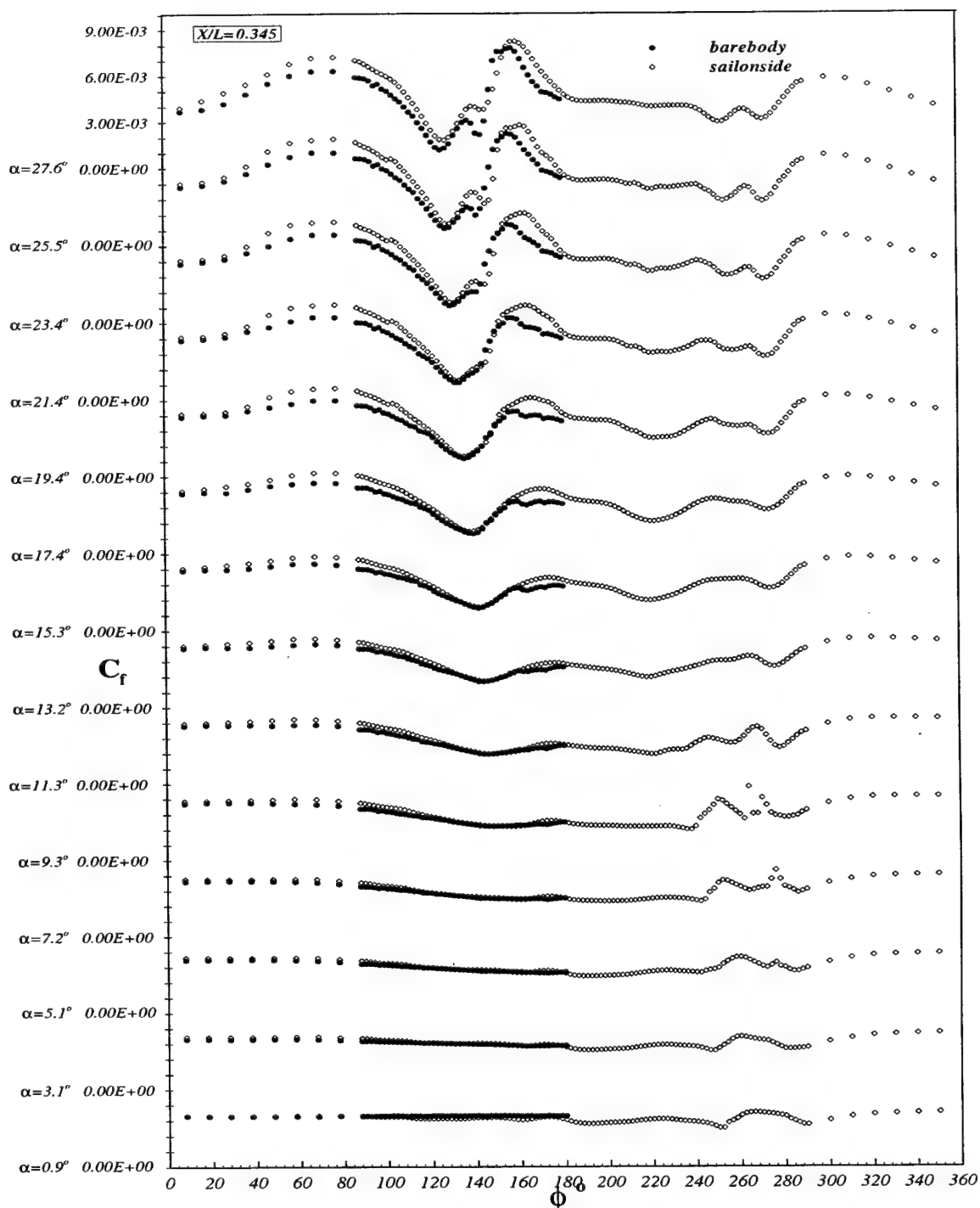


Figure 5.24:  $C_f$  vs.  $\phi$  for all  $\alpha$  at  $x/L = 0.345$  for steady barebody and sail-on-side cases. Sail side on the right of the figure starting from  $\phi = 180^\circ$ .

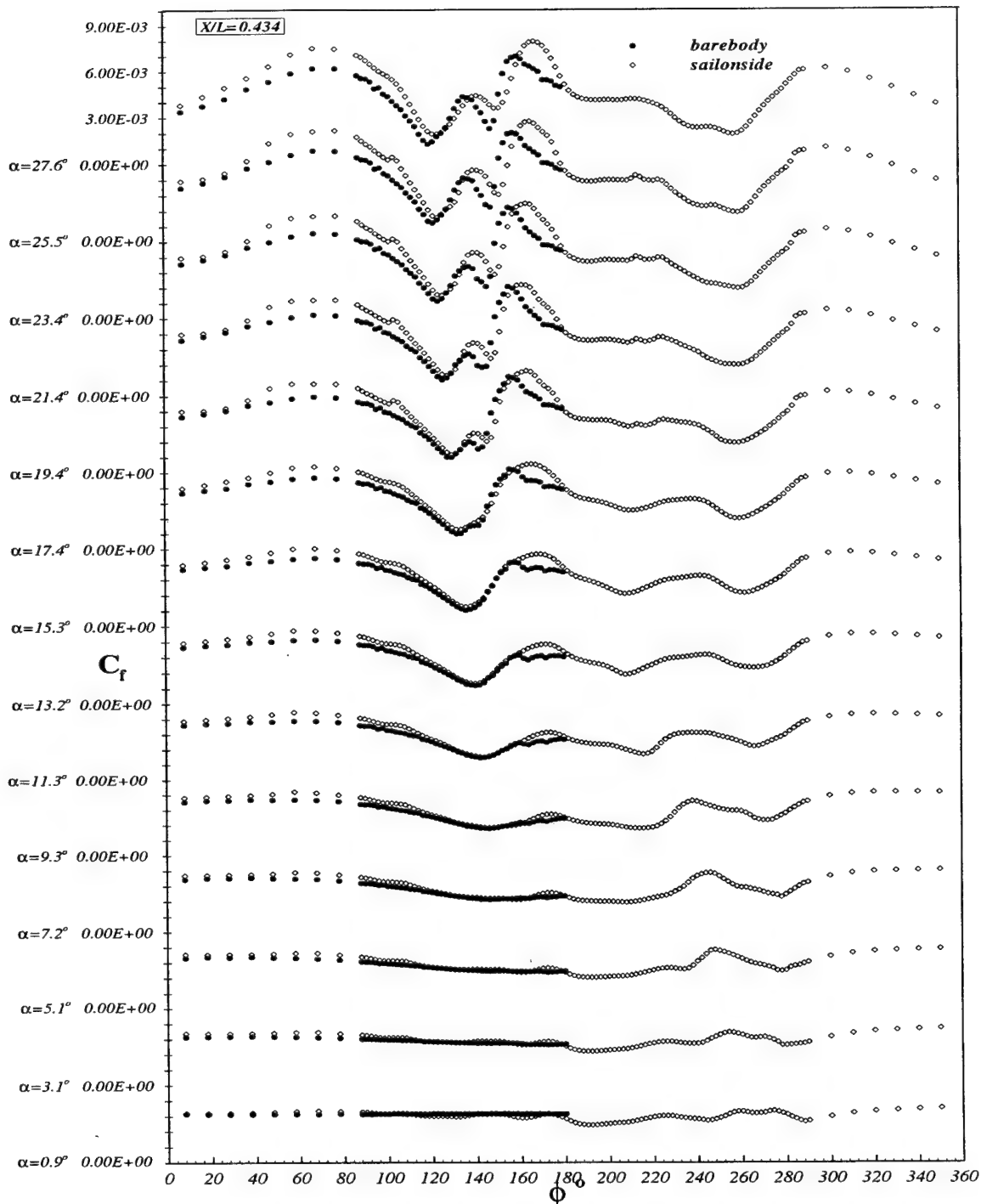


Figure 5.25:  $C_f$  vs.  $\phi$  for all  $\alpha$  at  $x/L = 0.434$  for steady barebody and sail-on-side cases. Sail side on the right of the figure starting from  $\phi = 180^\circ$ .

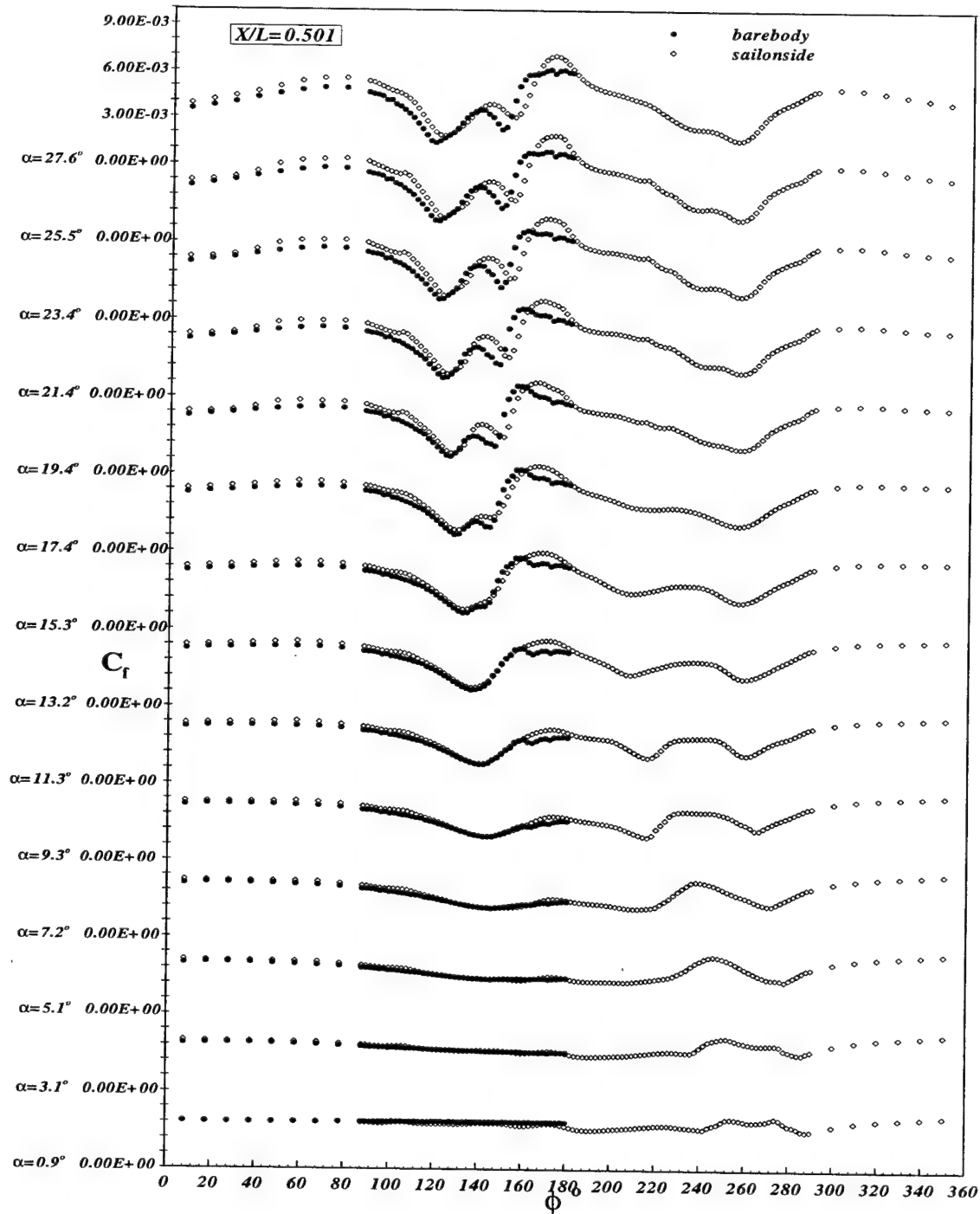


Figure 5.26:  $C_f$  vs.  $\phi$  for all  $\alpha$  at  $x/L = 0.501$  for steady barebody and sail-on-side cases. Sail side on the right of the figure starting from  $\phi = 180^\circ$ .

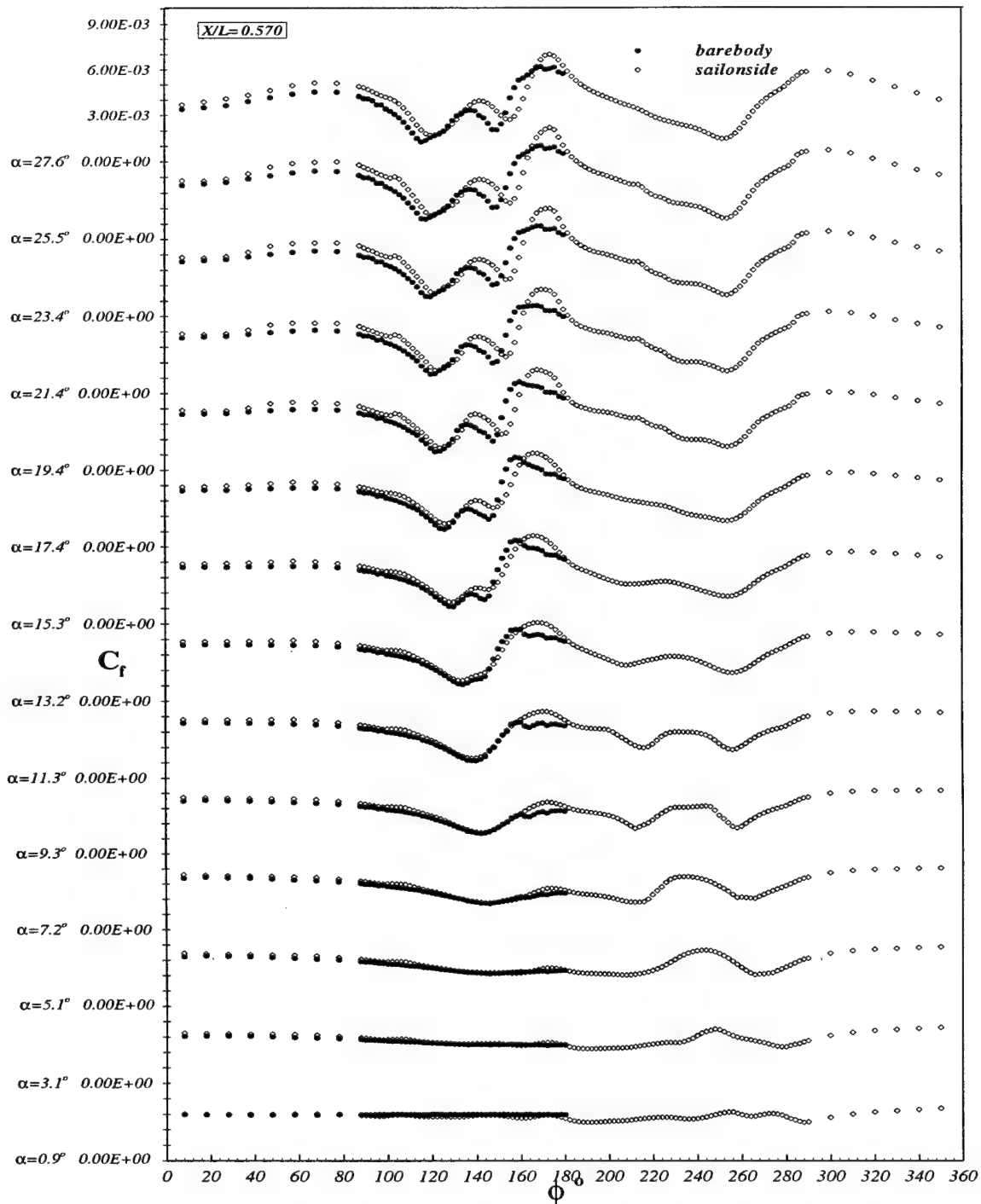


Figure 5.27:  $C_f$  vs.  $\phi$  for all  $\alpha$  at  $x/L = 0.570$  for steady barebody and sail-on-side cases. Sail side on the right of the figure starting from  $\phi = 180^\circ$ .

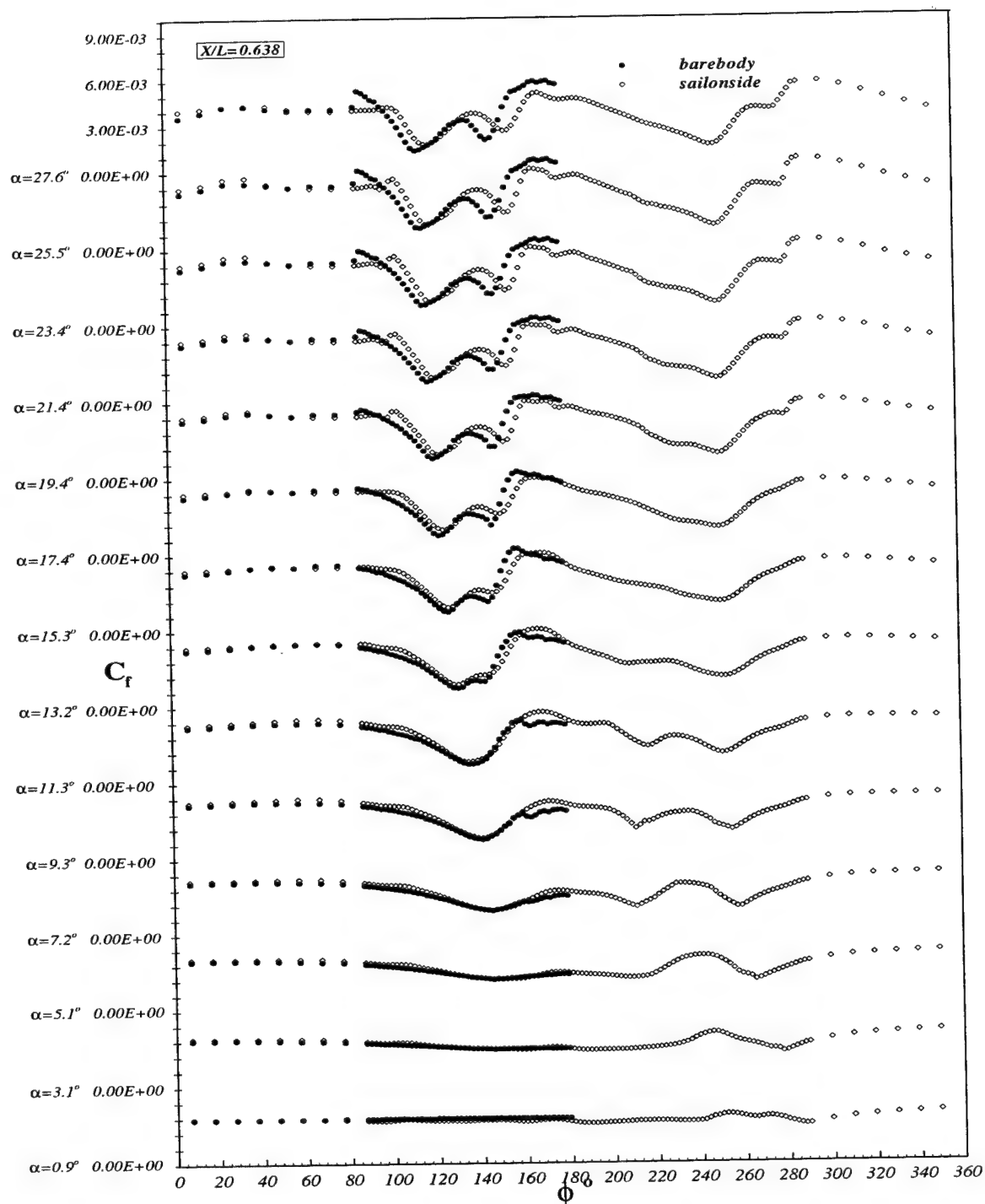


Figure 5.28:  $C_f$  vs.  $\phi$  for all  $\alpha$  at  $x/L = 0.638$  for steady barebody and sail-on-side cases. Sail side on the right of the figure starting from  $\phi = 180^\circ$ .

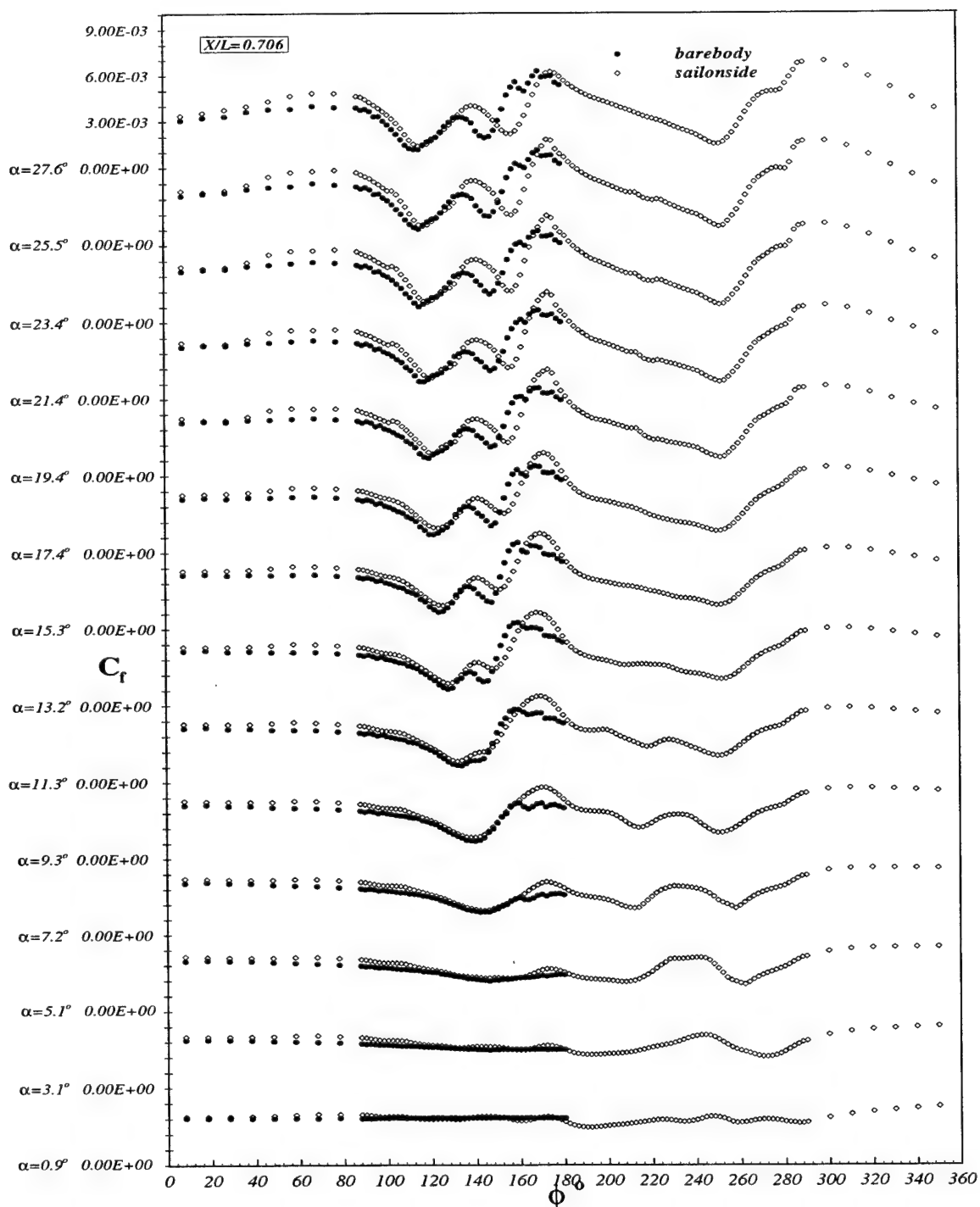


Figure 5.29:  $C_f$  vs.  $\phi$  for all  $\alpha$  at  $x/L = 0.706$  for steady barebody and sail-on-side cases. Sail side on the right of the figure starting from  $\phi = 180^\circ$ .

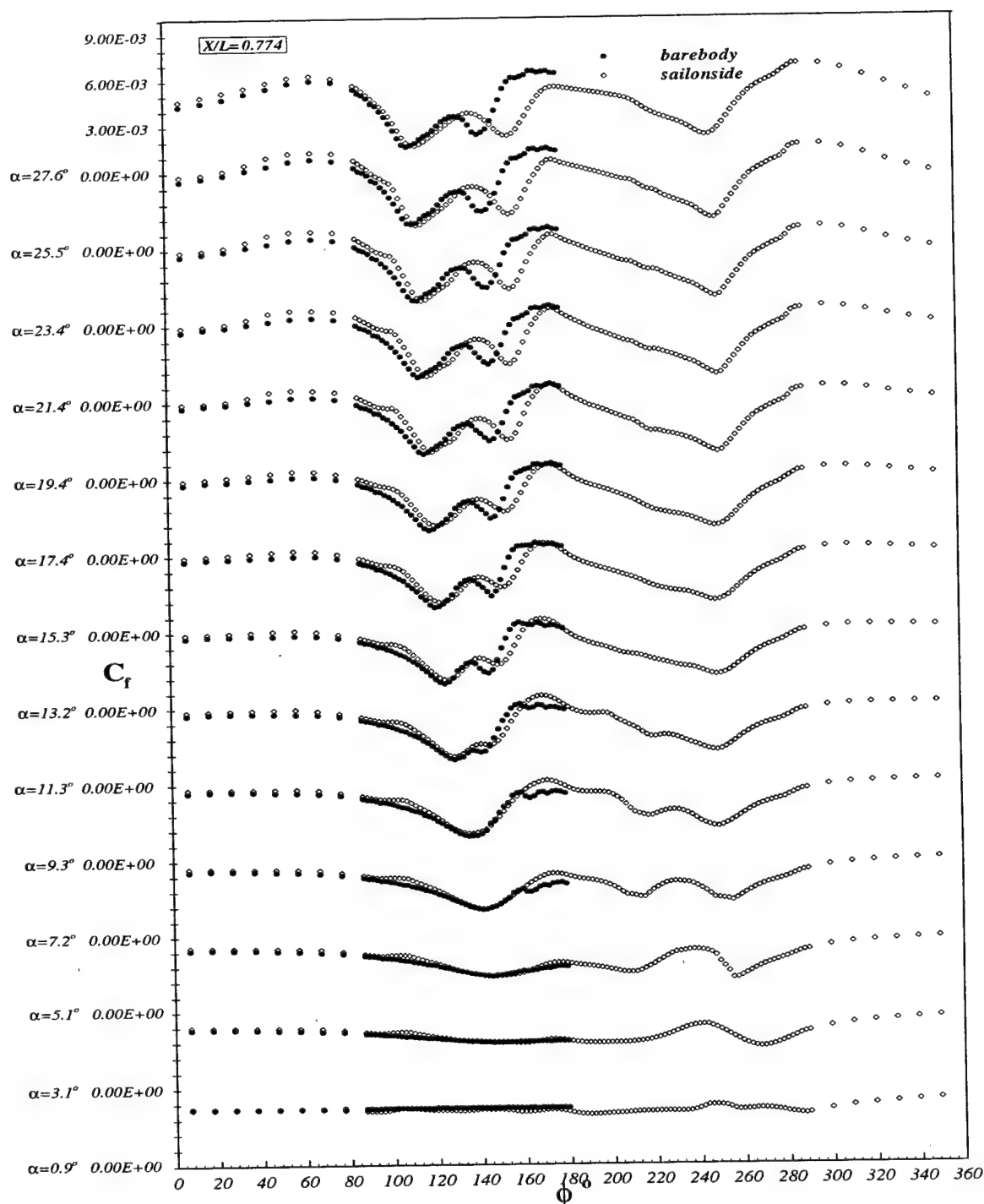


Figure 5.30:  $C_f$  vs.  $\phi$  for all  $\alpha$  at  $x/L = 0.774$  for steady barebody and sail-on-side cases. Sail side on the right of the figure starting from  $\phi = 180^\circ$ .

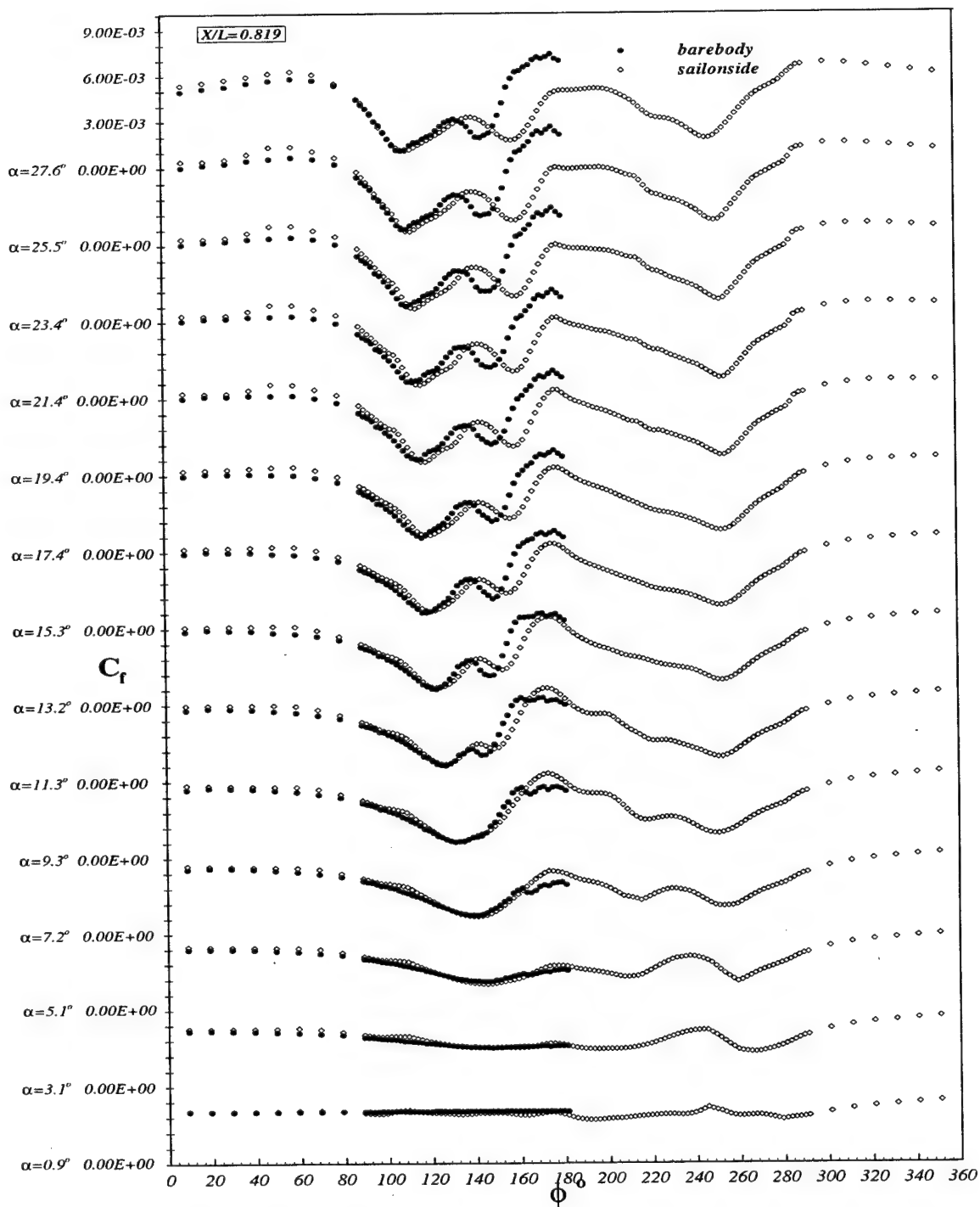


Figure 5.31:  $C_f$  vs.  $\phi$  for all  $\alpha$  at  $x/L = 0.819$  for steady barebody and sail-on-side cases. Sail side on the right of the figure starting from  $\phi = 180^\circ$ .



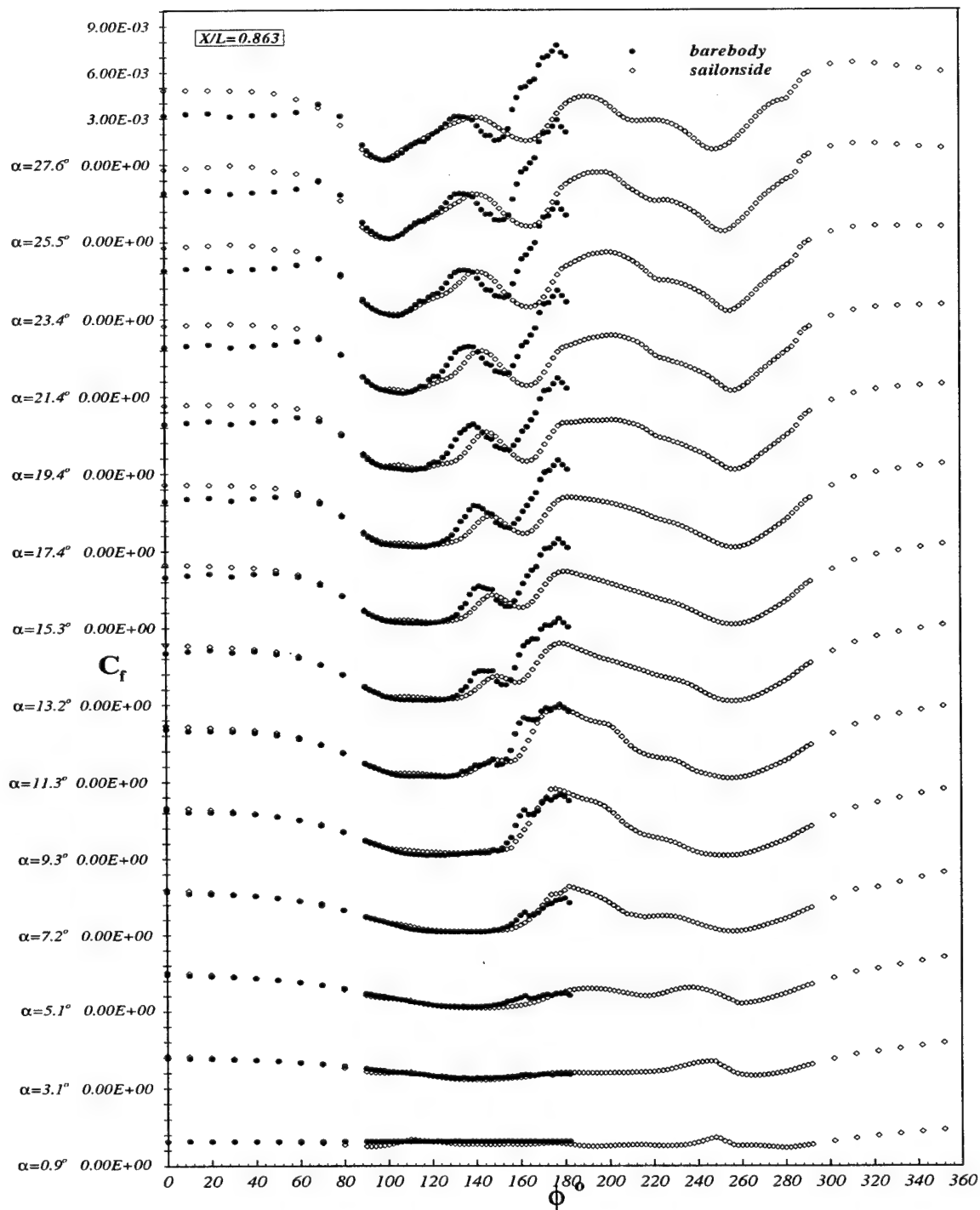
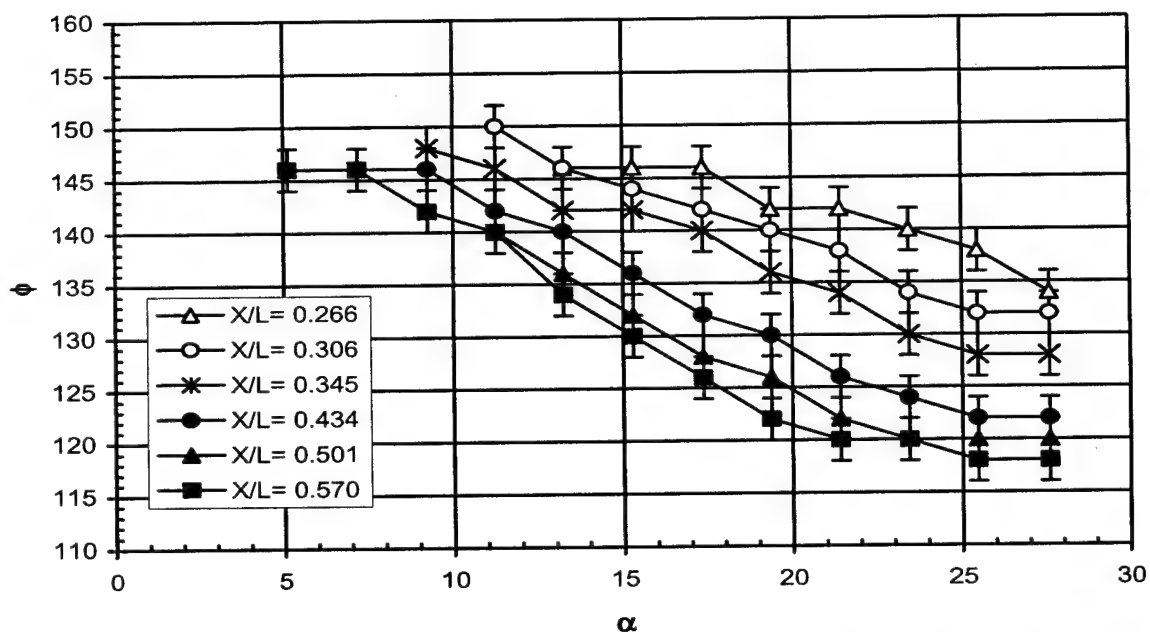
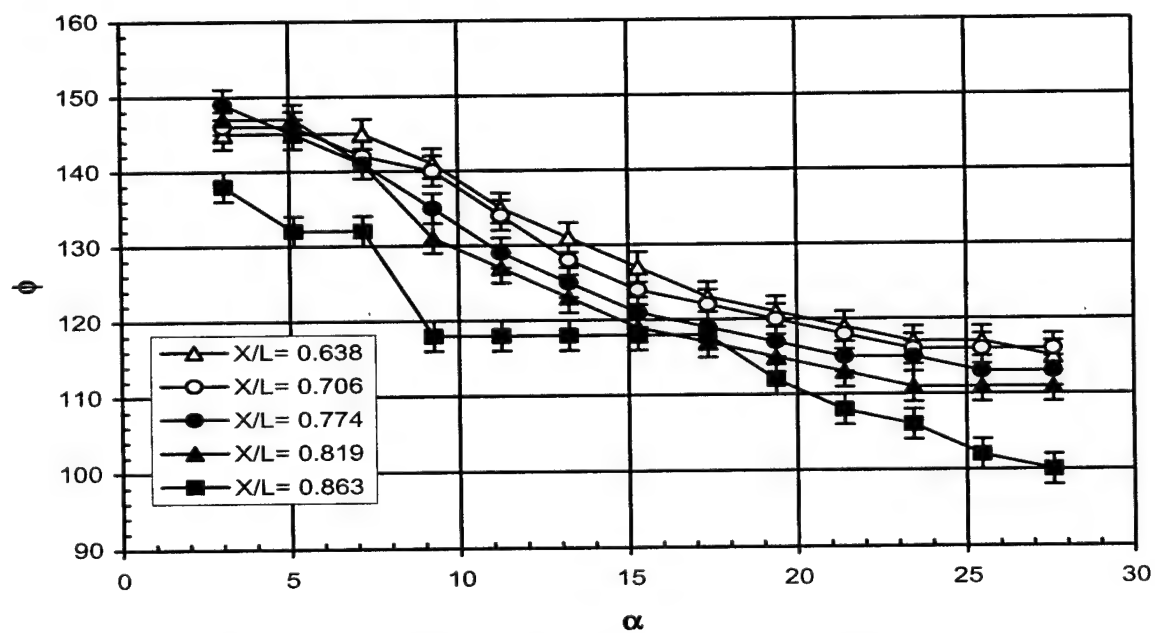
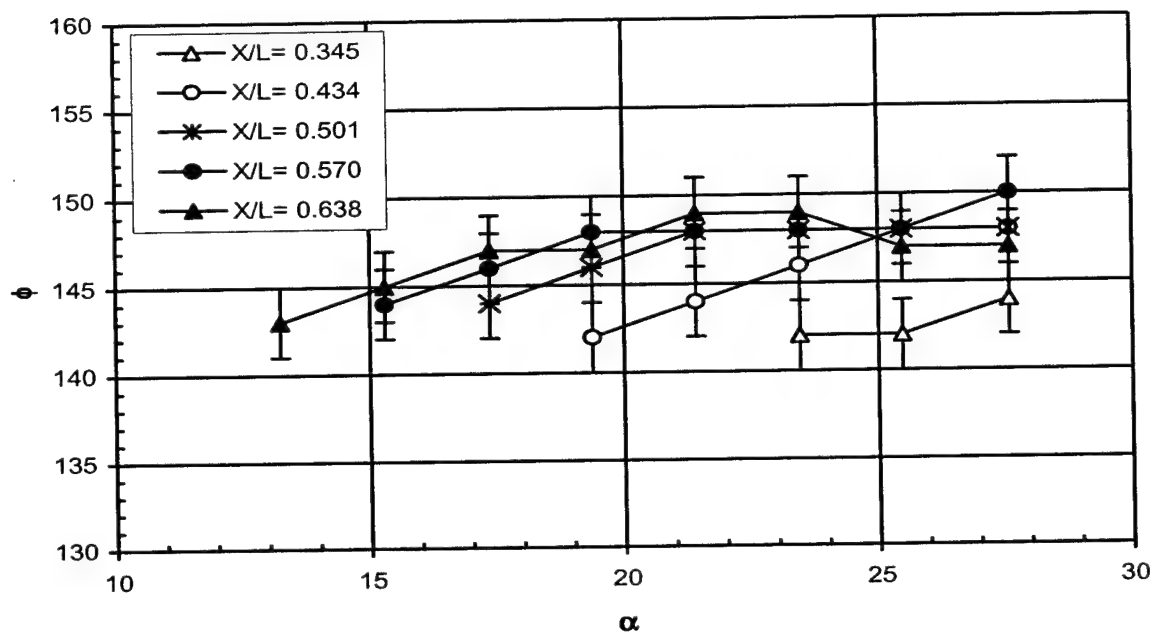
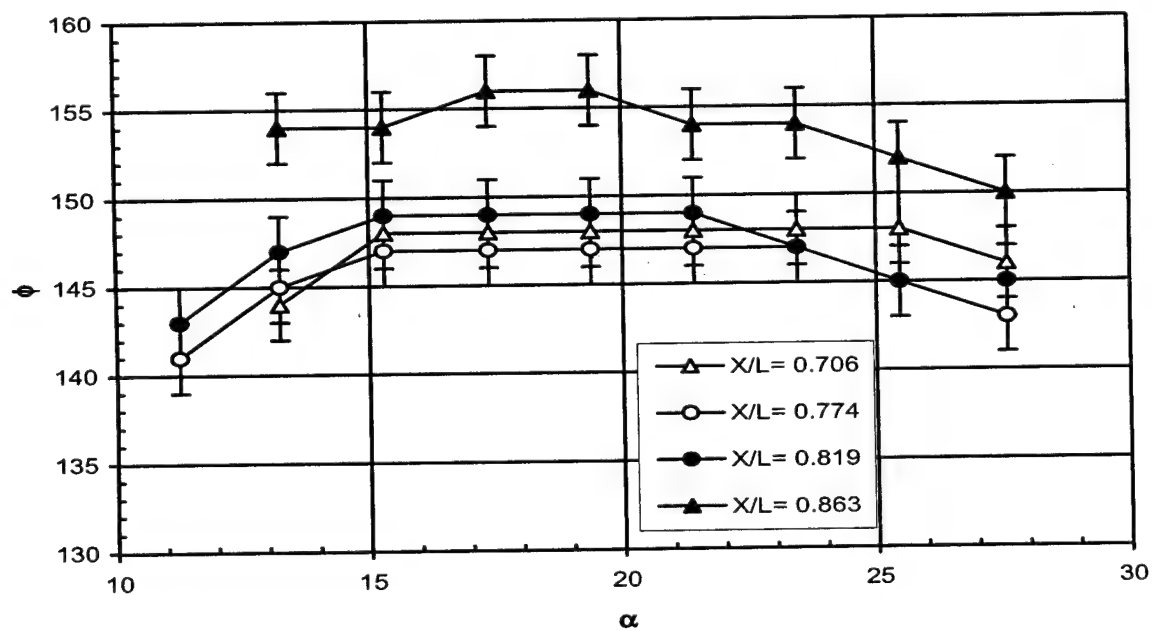


Figure 5.32:  $C_f$  vs.  $\phi$  for all  $\alpha$  at  $x/L = 0.863$  for steady barebody and sail-on-side cases. Sail side on the right of the figure starting from  $\phi = 180^\circ$ .

Figure 5.33: Steady primary separation locations vs.  $\alpha$  for the barebody case.Figure 5.34: Steady primary separation locations vs.  $\alpha$  for the barebody case (continued).

Figure 5.35: Steady secondary separation locations vs.  $\alpha$  for the barebody case.Figure 5.36: Steady secondary separation locations vs.  $\alpha$  for the barebody case (continued).

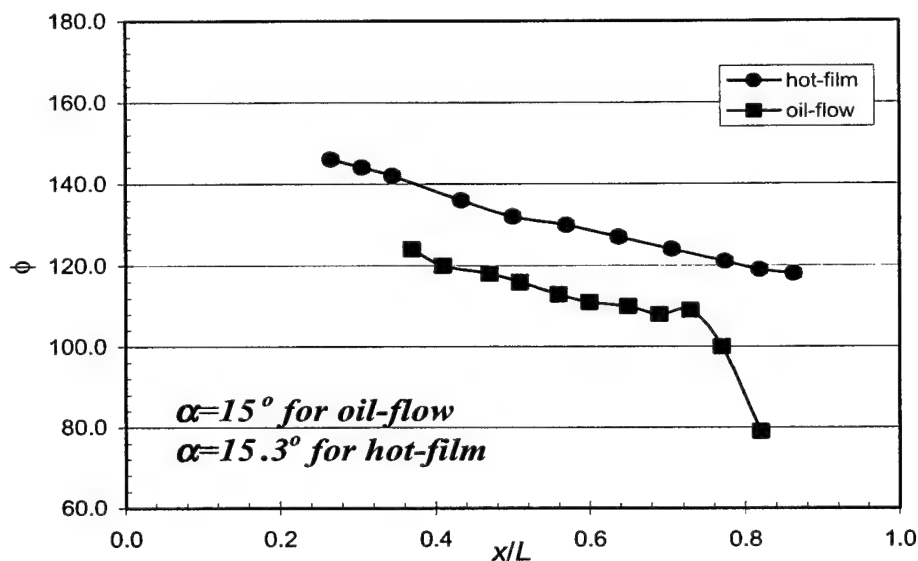


Figure 5.37: Comparison of the oil-flow primary separation locations with the hot-film primary separation locations for the barebody case. For the hot-film measurements  $\alpha = 15.3^\circ$  and for the oil-flow results  $\alpha = 15^\circ$ .

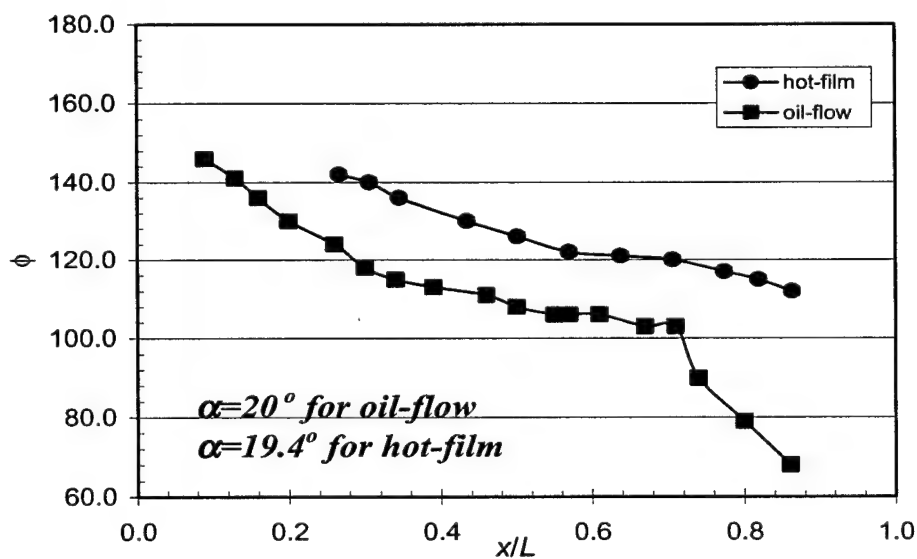


Figure 5.38: Comparison of the oil-flow primary separation locations with the hot-film primary separation locations for the barebody case. For the hot-film measurements  $\alpha = 19.4^\circ$  and for the oil-flow results  $\alpha = 20^\circ$ .

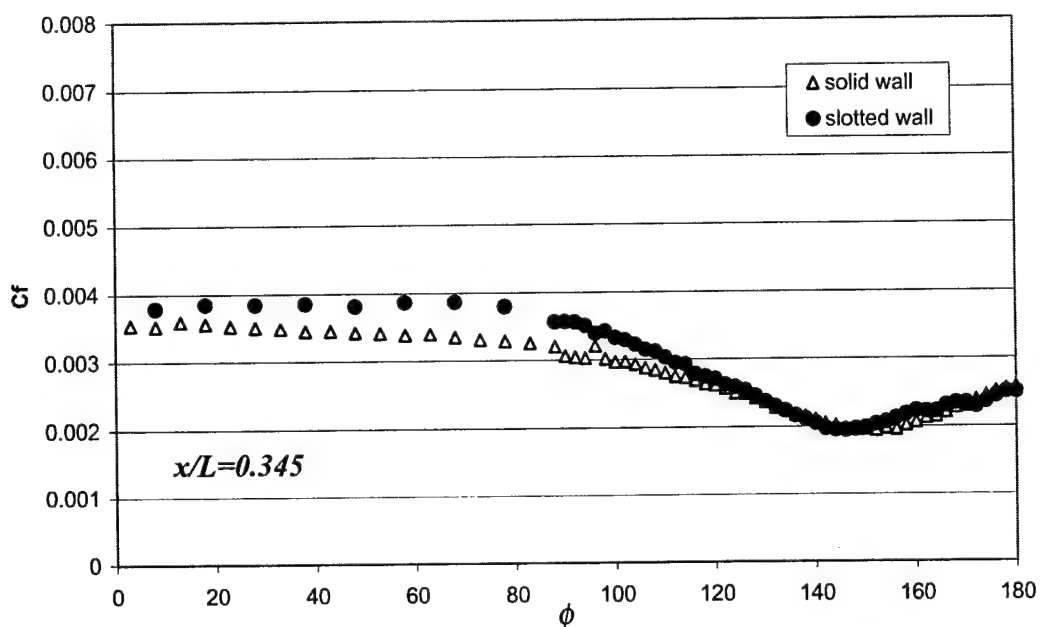


Figure 5.39: Solid vs. slotted wall comparison for the barebody  $C_f$  vs  $\phi$  distribution at  $x/L = 0.345$ .  $\alpha = 10^\circ$  for the solid wall case, and  $\alpha = 9.3^\circ$  for the slotted wall case.

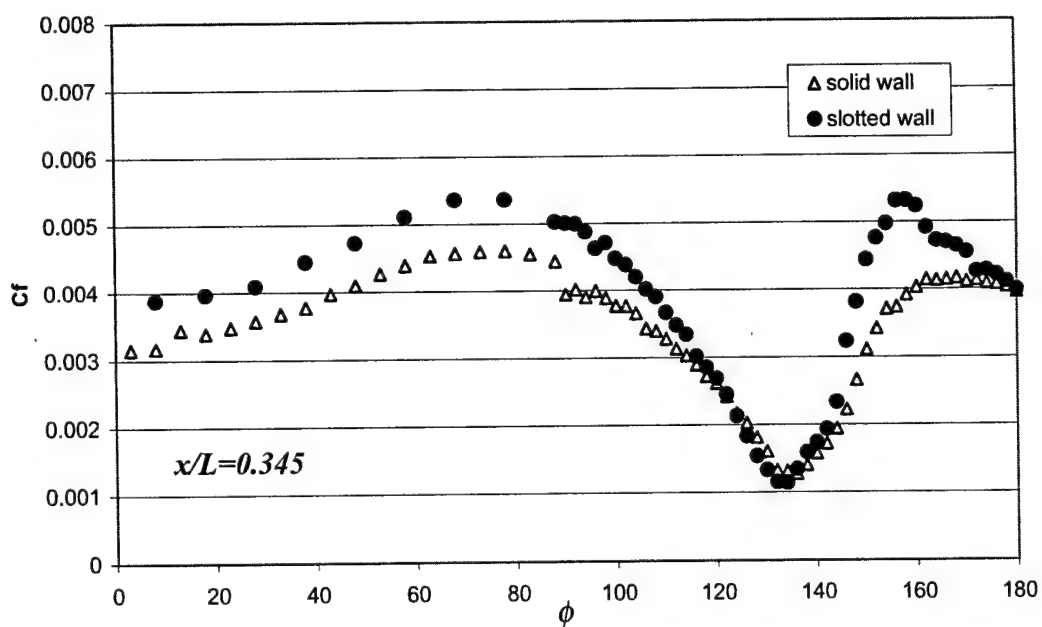


Figure 5.40: Solid vs. slotted wall comparison for the barebody  $C_f$  vs  $\phi$  distribution at  $x/L = 0.345$ .  $\alpha = 20^\circ$  for the solid wall case, and  $\alpha = 19.4^\circ$  for the slotted wall case.

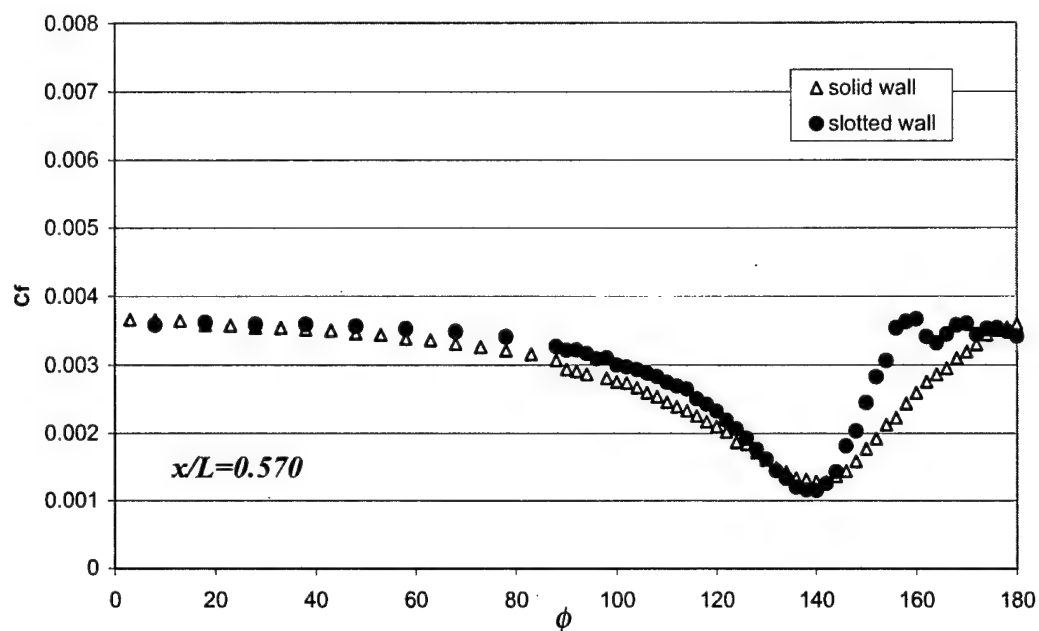


Figure 5.41: Solid vs. slotted wall comparison for the barebody  $C_f$  vs  $\phi$  distribution at  $x/L = 0.570$ .  $\alpha = 10^\circ$  for the solid wall case, and  $\alpha = 9.3^\circ$  for the slotted wall case.

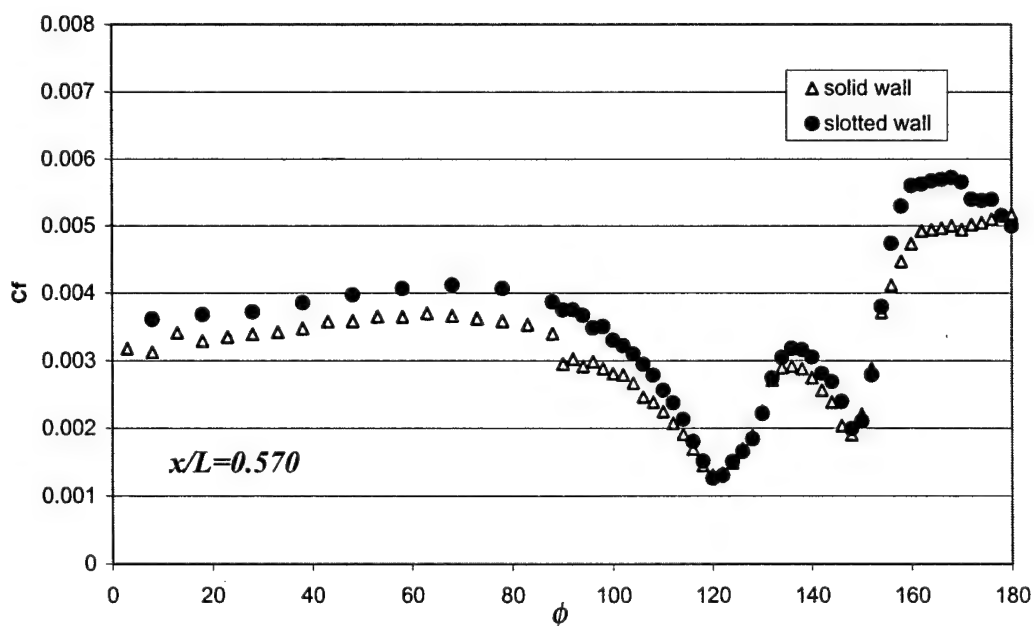


Figure 5.42: Solid vs. slotted wall comparison for the barebody  $C_f$  vs  $\phi$  distribution at  $x/L = 0.570$ .  $\alpha = 20^\circ$  for the solid wall case, and  $\alpha = 19.4^\circ$  for the slotted wall case.

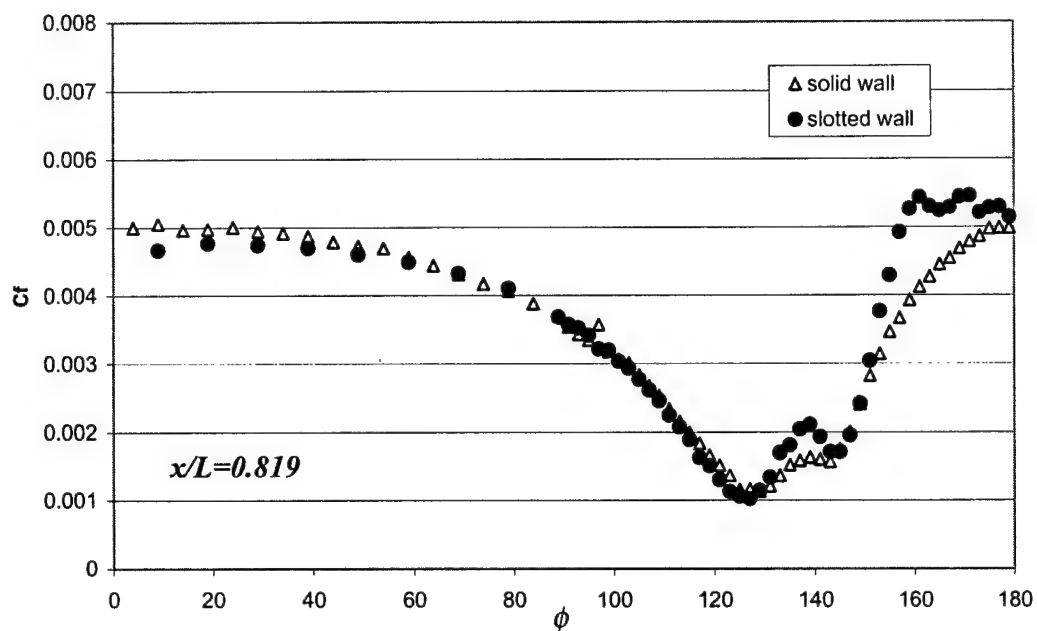


Figure 5.43: Solid vs. slotted wall comparison for the barebody  $C_f$  vs  $\phi$  distribution at  $x/L = 0.819$ .  $\alpha = 10^\circ$  for the solid wall case, and  $\alpha = 9.3^\circ$  for the slotted wall case.

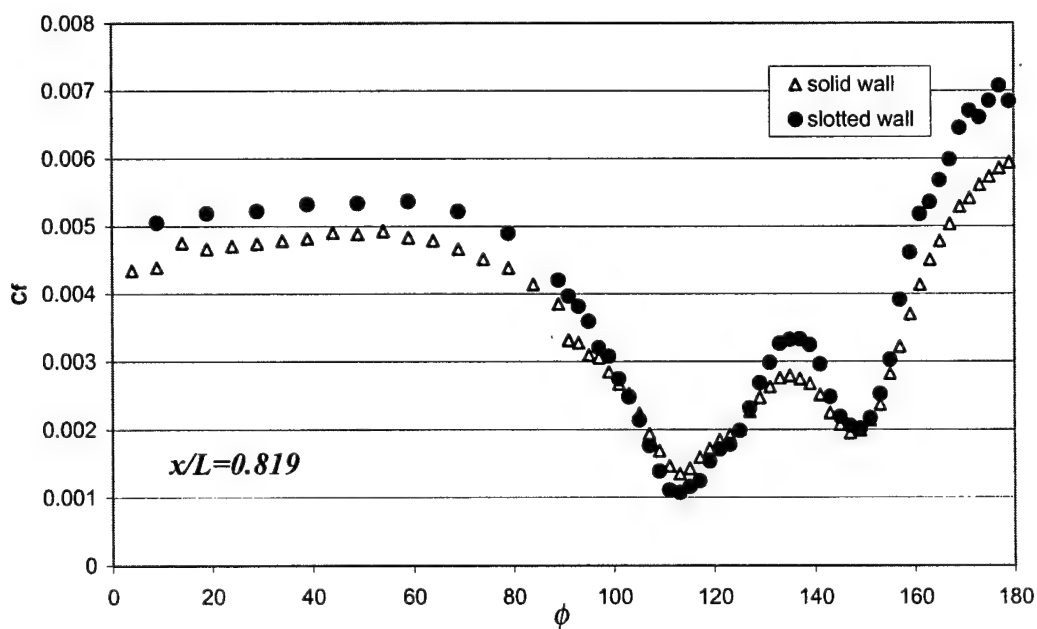


Figure 5.44: Solid vs. slotted wall comparison for the barebody  $C_f$  vs  $\phi$  distribution at  $x/L = 0.819$ .  $\alpha = 20^\circ$  for the solid wall case, and  $\alpha = 19.4^\circ$  for the slotted wall case.

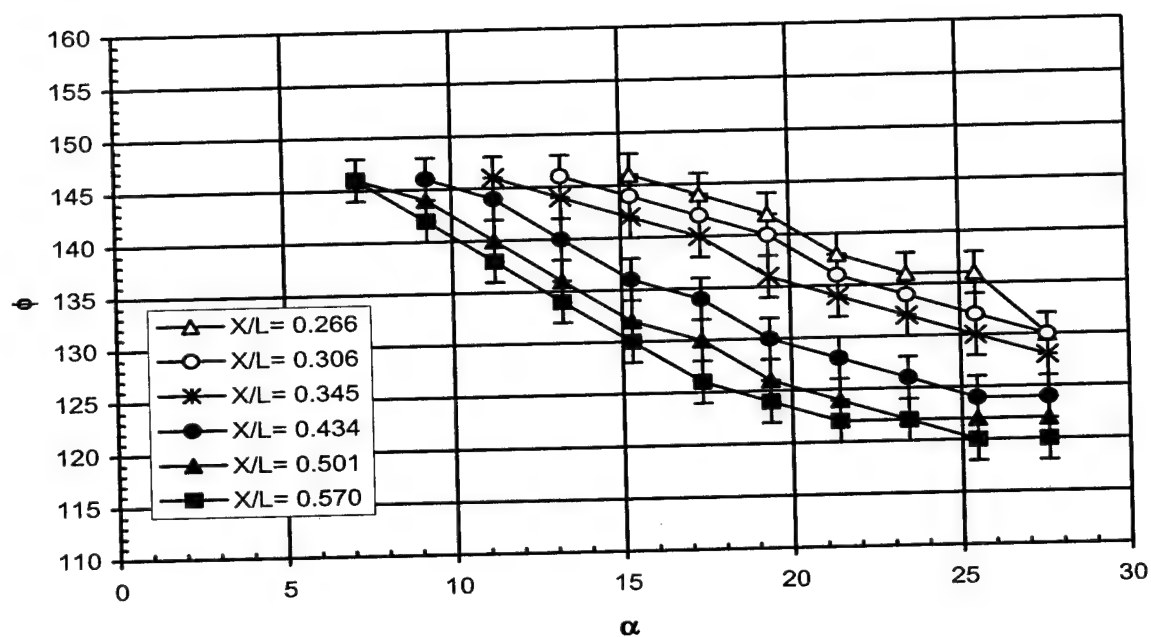


Figure 5.45: Steady primary separation locations vs.  $\alpha$  for the sail-on-side (region without sail) case.

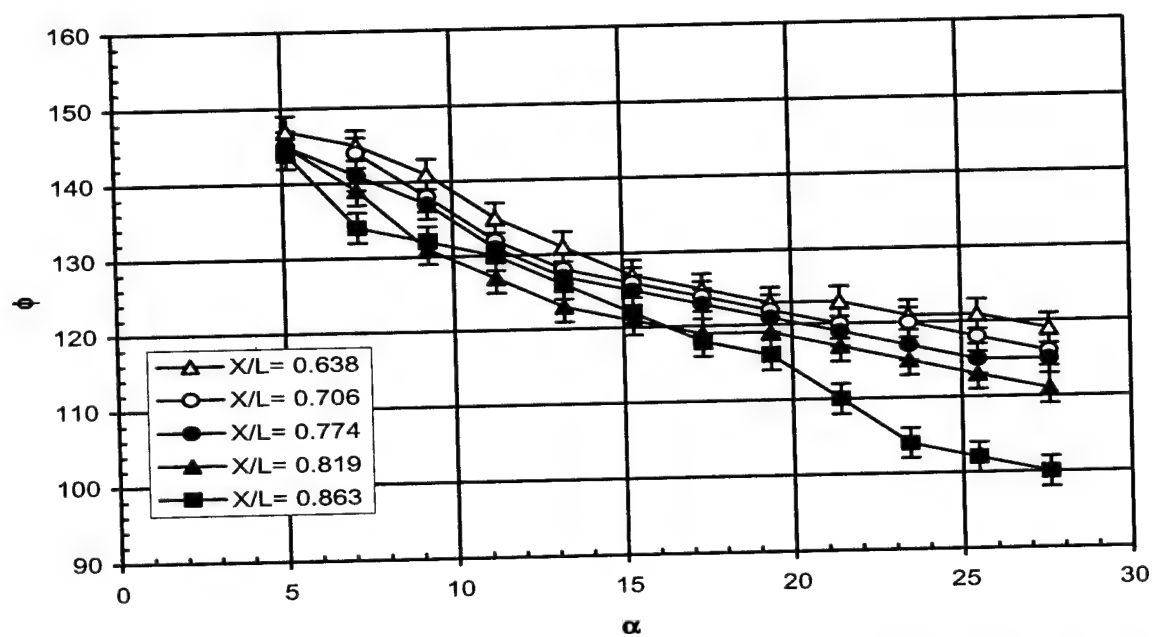


Figure 5.46: Steady primary separation locations vs.  $\alpha$  for the sail-on-side (region without sail) case (continued).



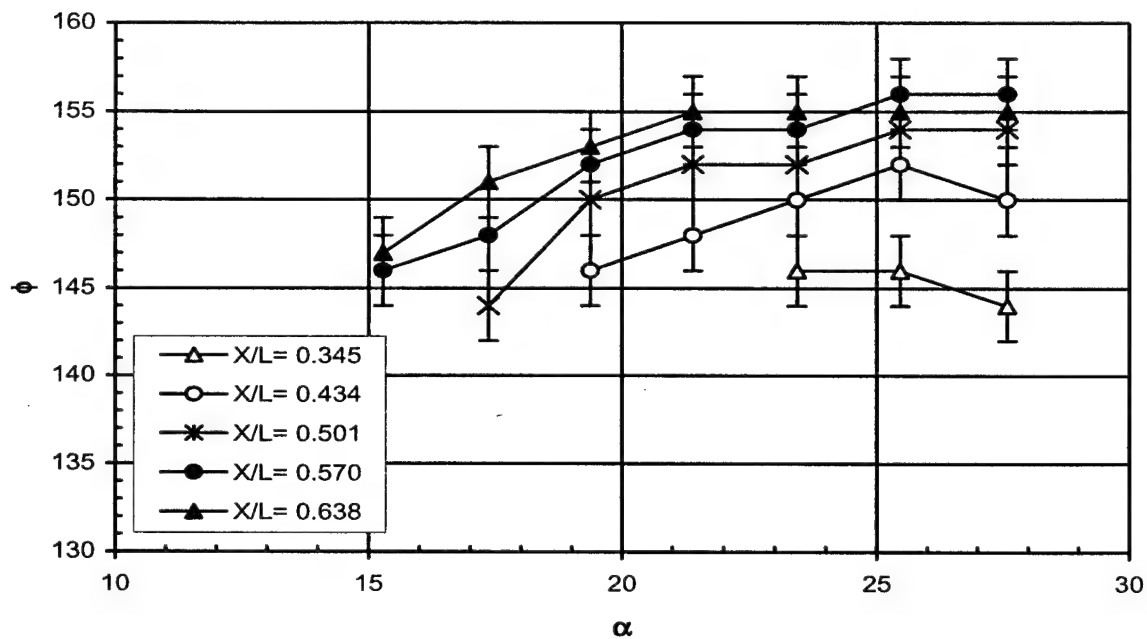


Figure 5.47: Steady secondary separation locations vs.  $\alpha$  for the sail-on-side (region without sail) case.

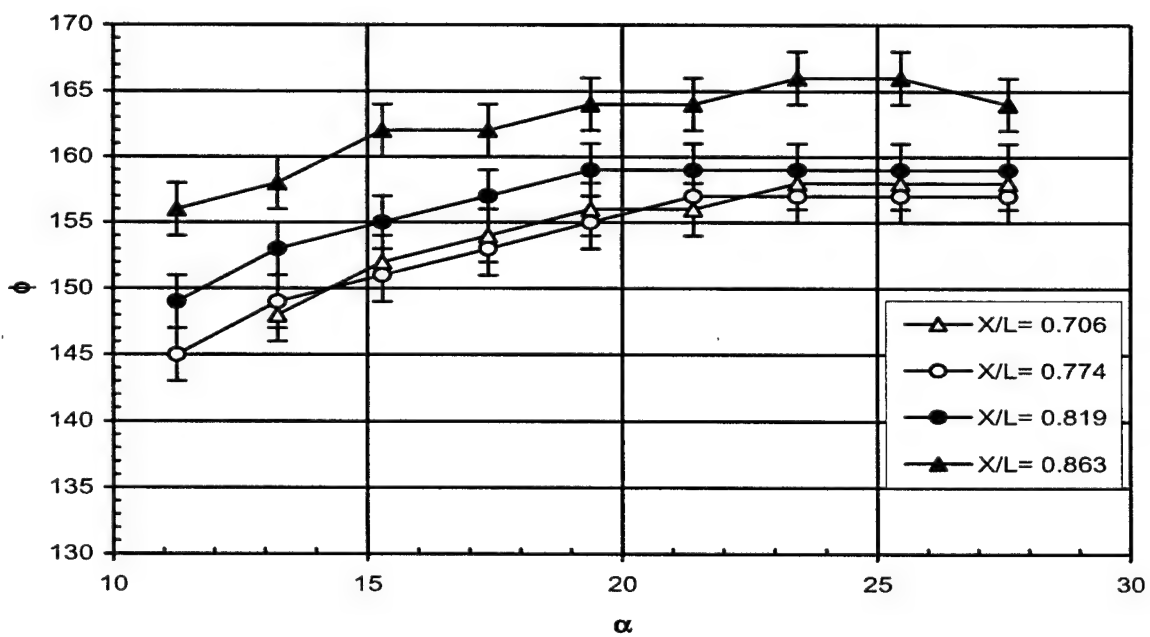


Figure 5.48: Steady secondary separation locations vs.  $\alpha$  for the sail-on-side (region without sail) case (continued).

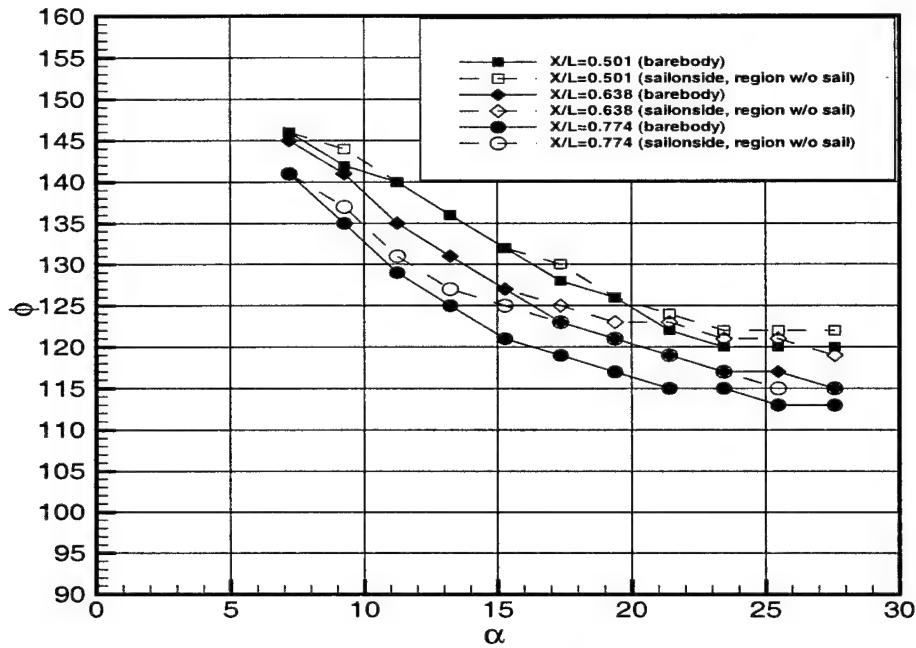


Figure 5.49: Comparison for steady primary separation locations vs.  $\alpha$  for barebody and the sail-on-side (region without sail) case at  $x/L = 0.501, 0.638$  and  $0.774$ .

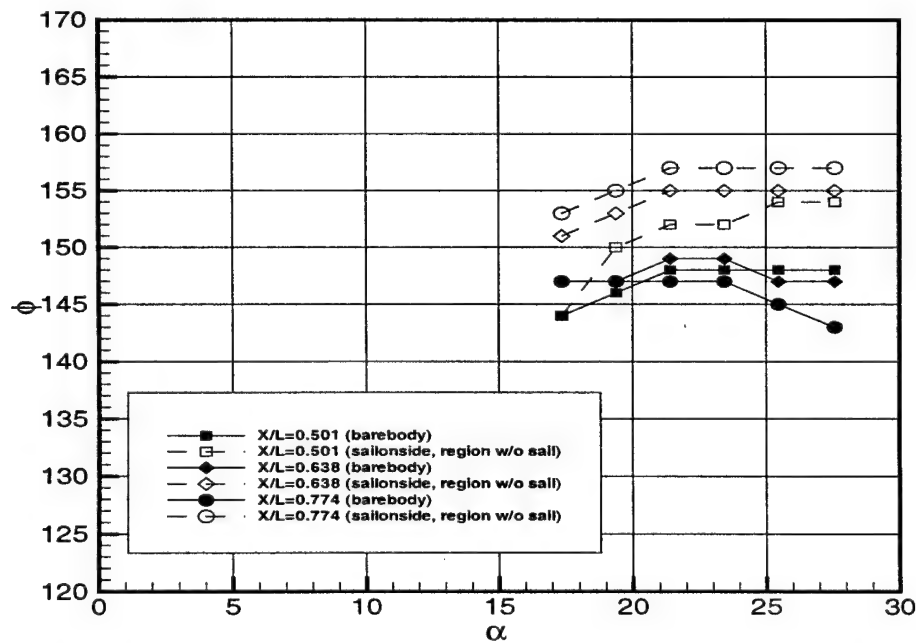


Figure 5.50: Comparison for steady secondary separation locations vs.  $\alpha$  for barebody and the sail-on-side (region without sail) case at  $x/L = 0.501, 0.638$  and  $0.774$ .

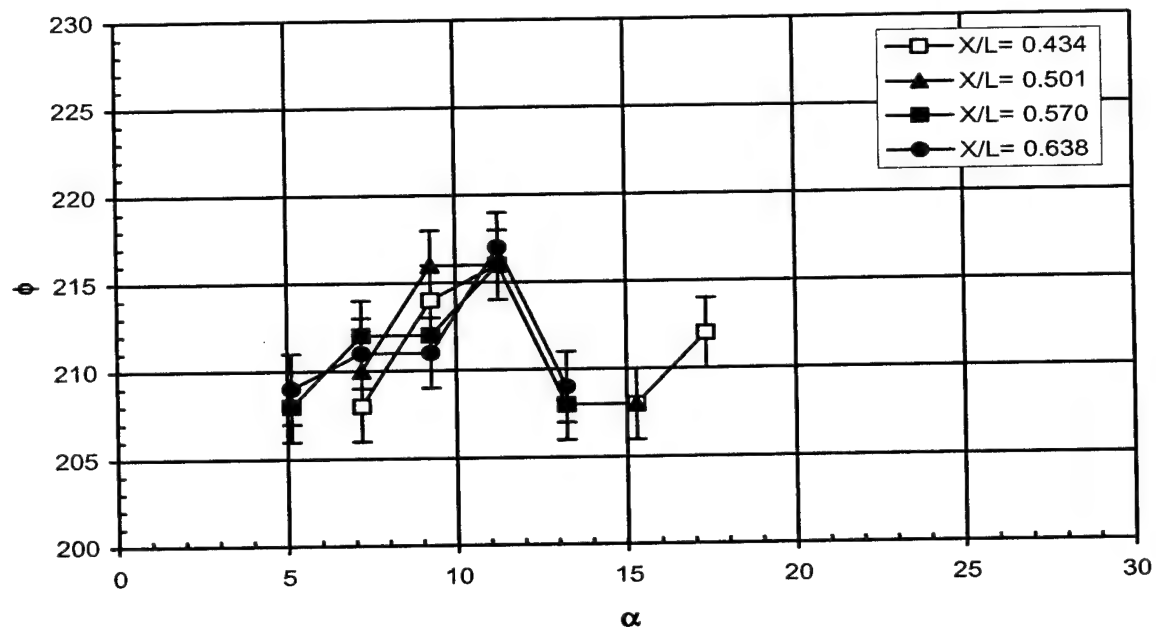


Figure 5.51: Steady 1<sup>st</sup> separation locations vs.  $\alpha$  for the sail-on-side (region with sail) case.

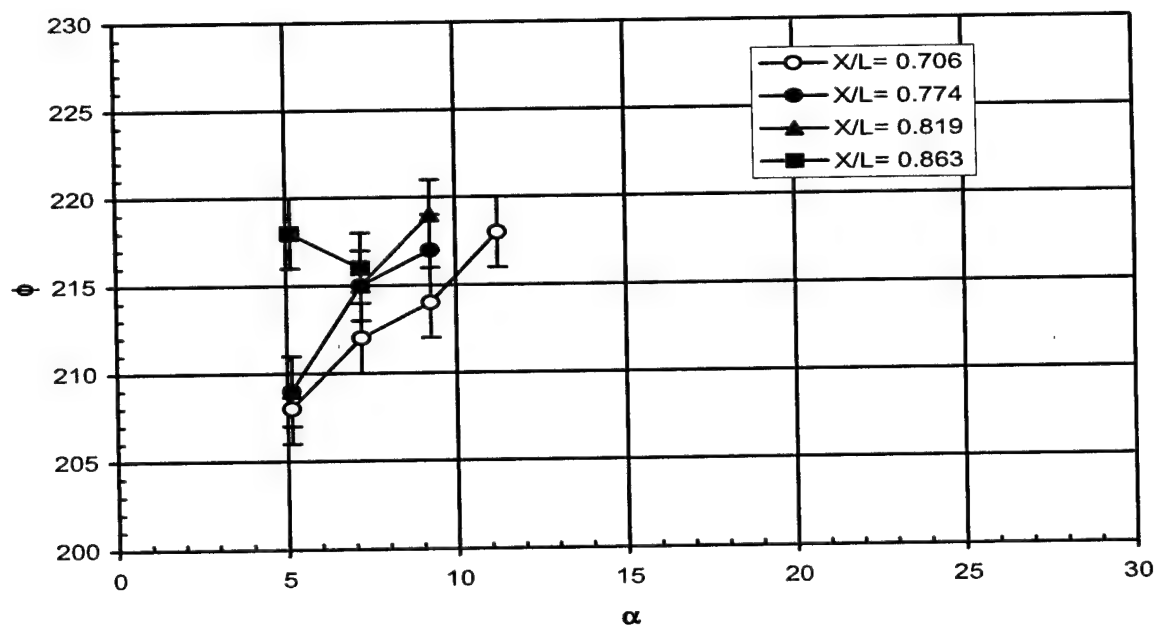


Figure 5.52: Steady 1<sup>st</sup> separation locations vs.  $\alpha$  for the sail-on-side (region with sail) case (continued).

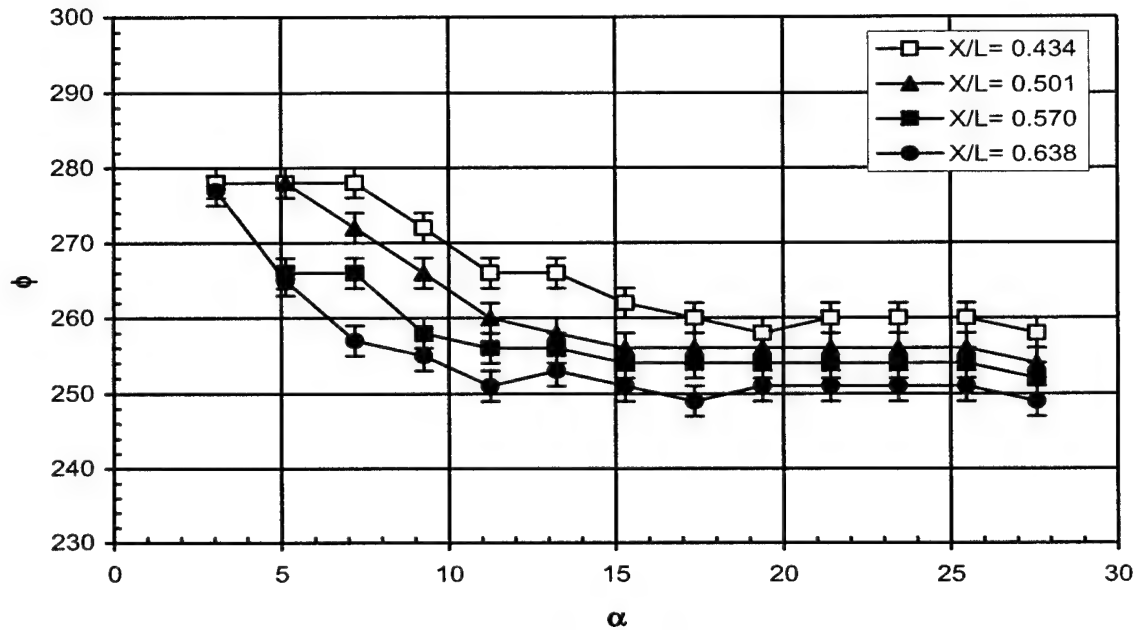


Figure 5.53: Steady 2<sup>nd</sup> separation locations vs.  $\alpha$  for the sail-on-side (region with sail) case.

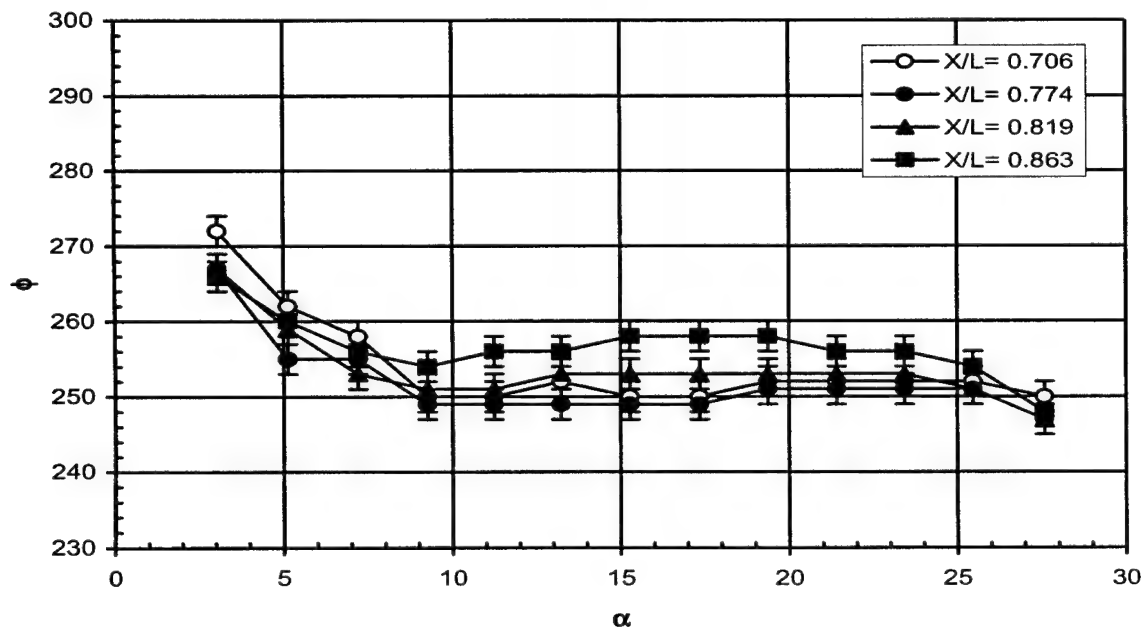
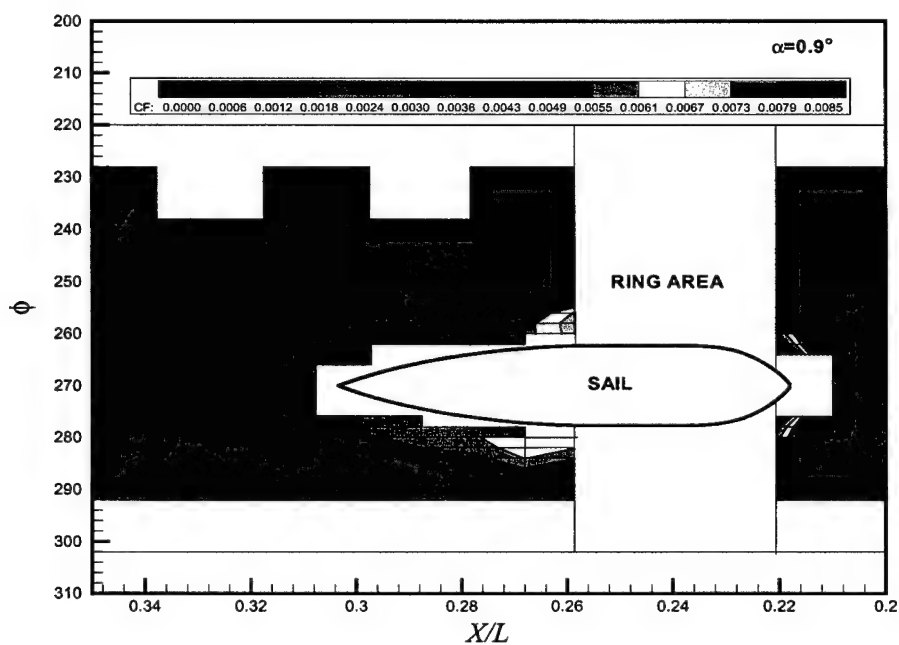
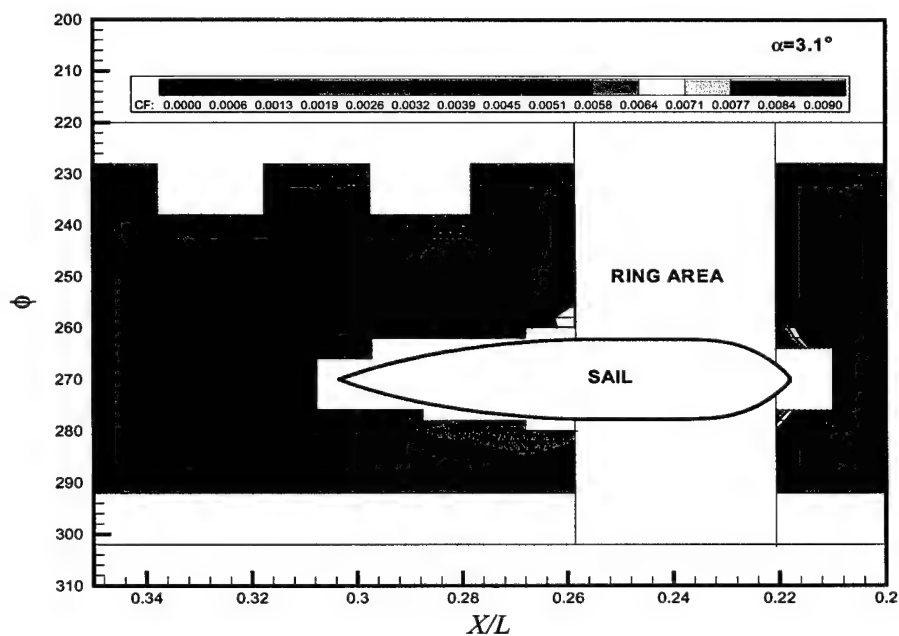
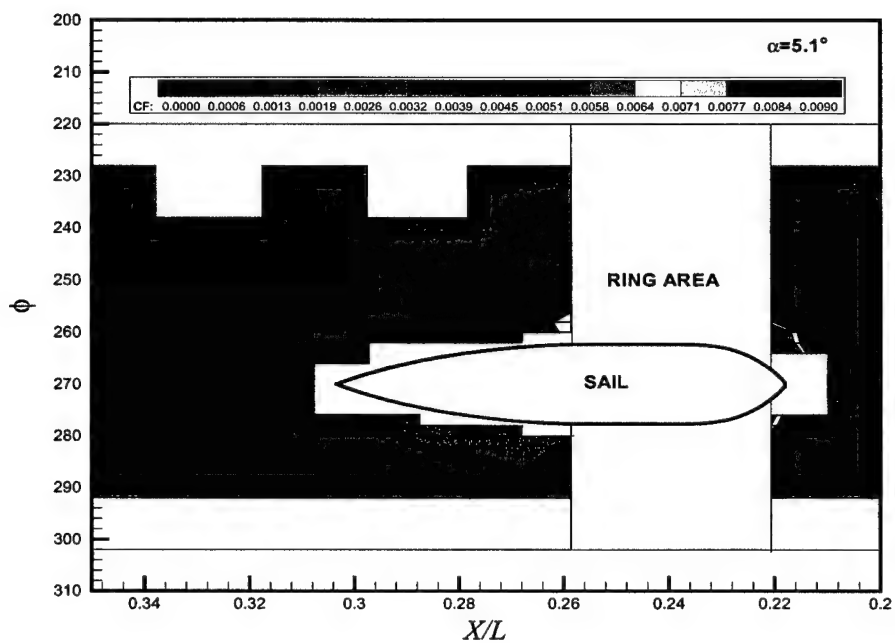
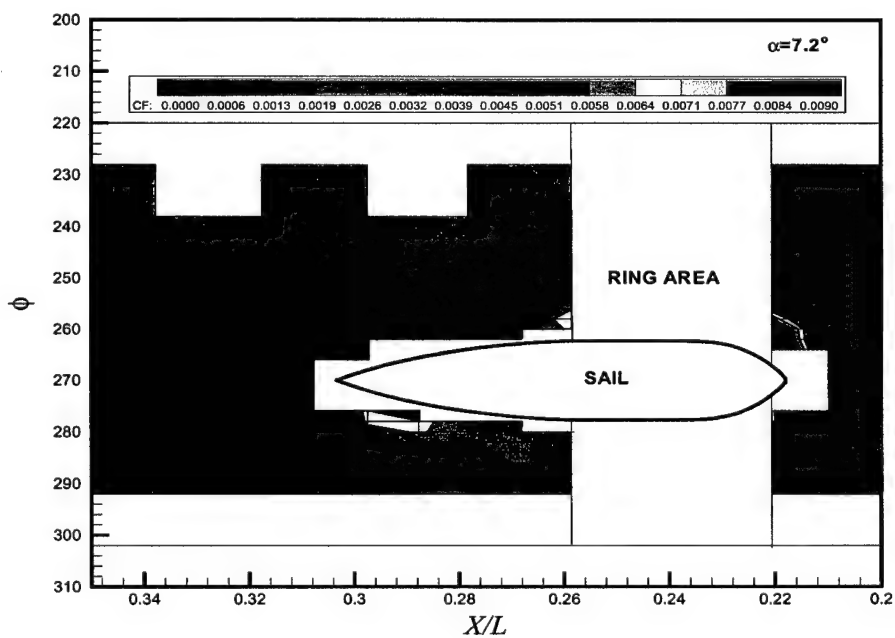
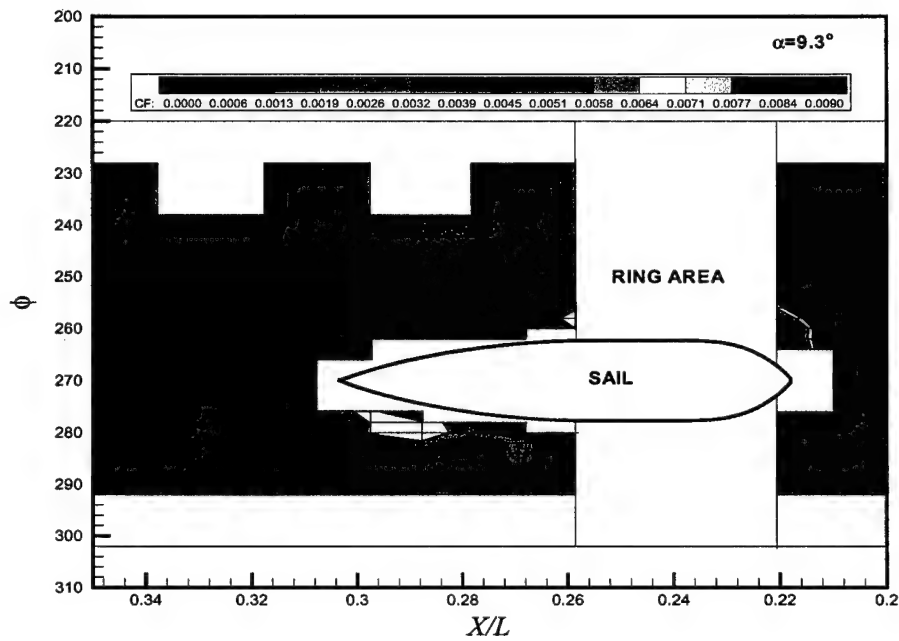
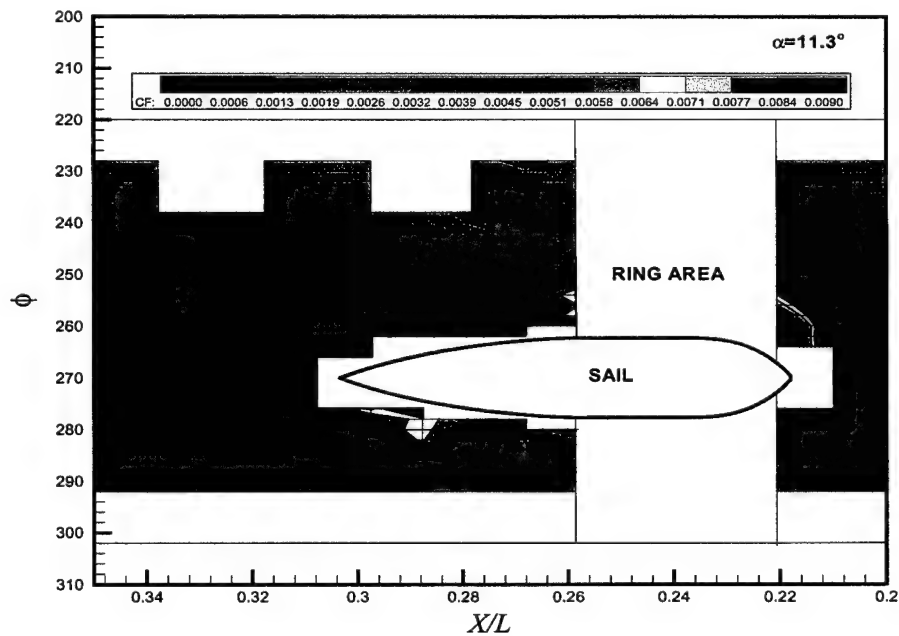
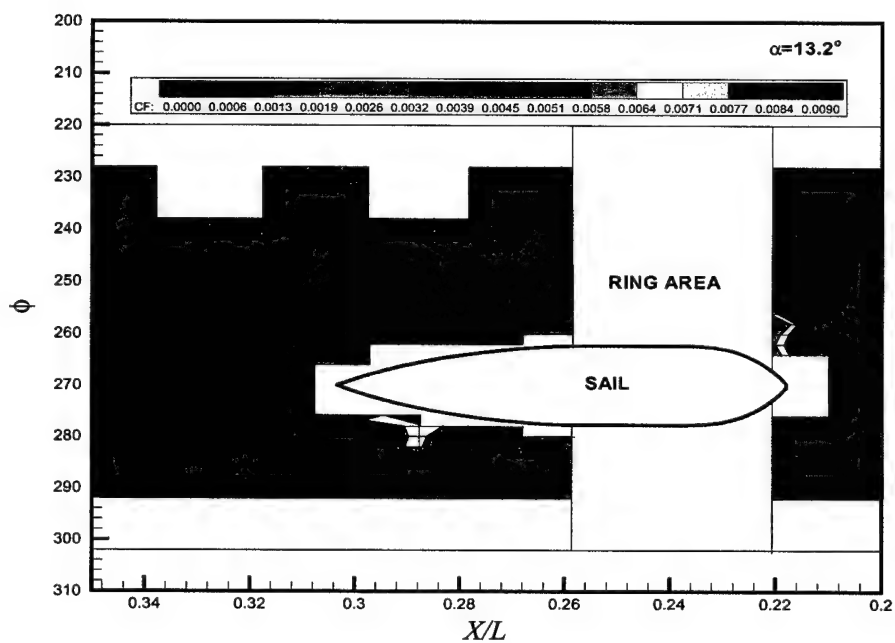
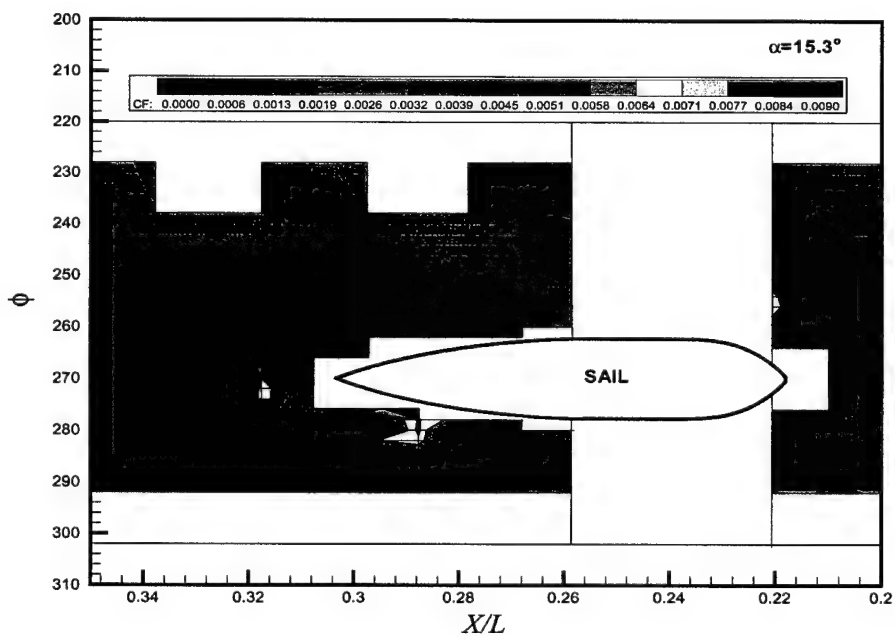


Figure 5.54: Steady 2<sup>nd</sup> separation locations vs.  $\alpha$  for the sail-on-side (region with sail) case (continued)

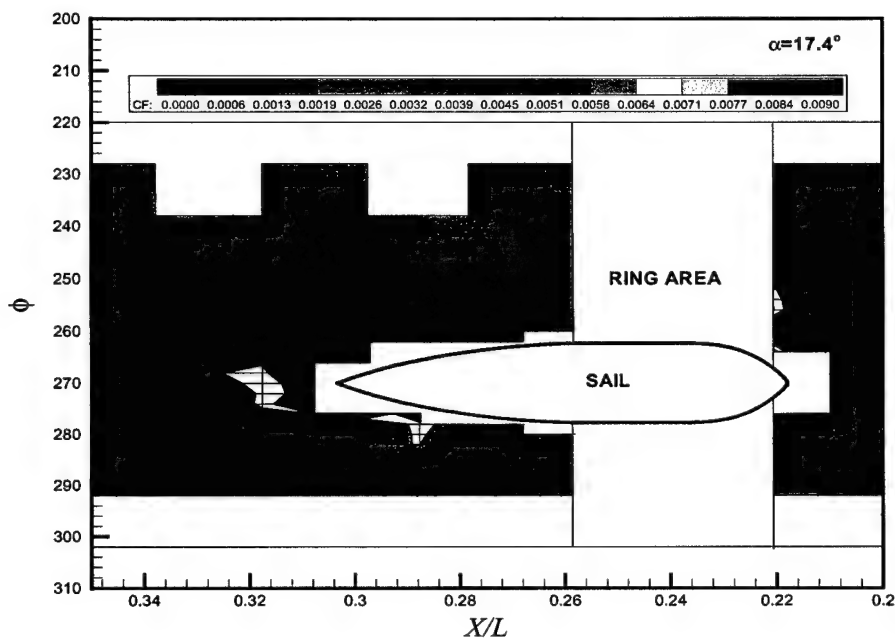
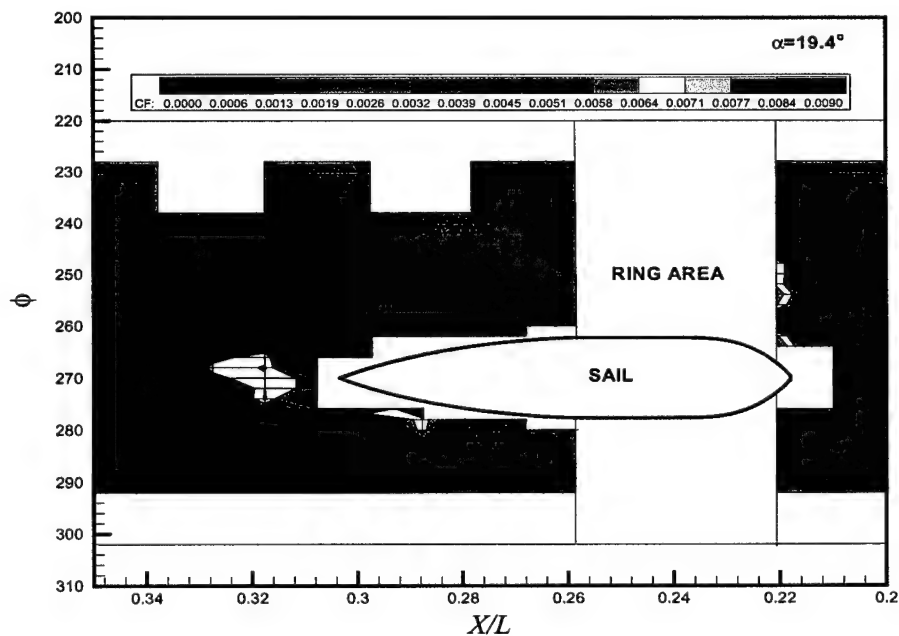
Figure 5.55: Steady  $C_f$  contours in the vicinity of sail at  $\alpha = 0.9^\circ$ .Figure 5.56: Steady  $C_f$  contours in the vicinity of sail at  $\alpha = 3.1^\circ$ .

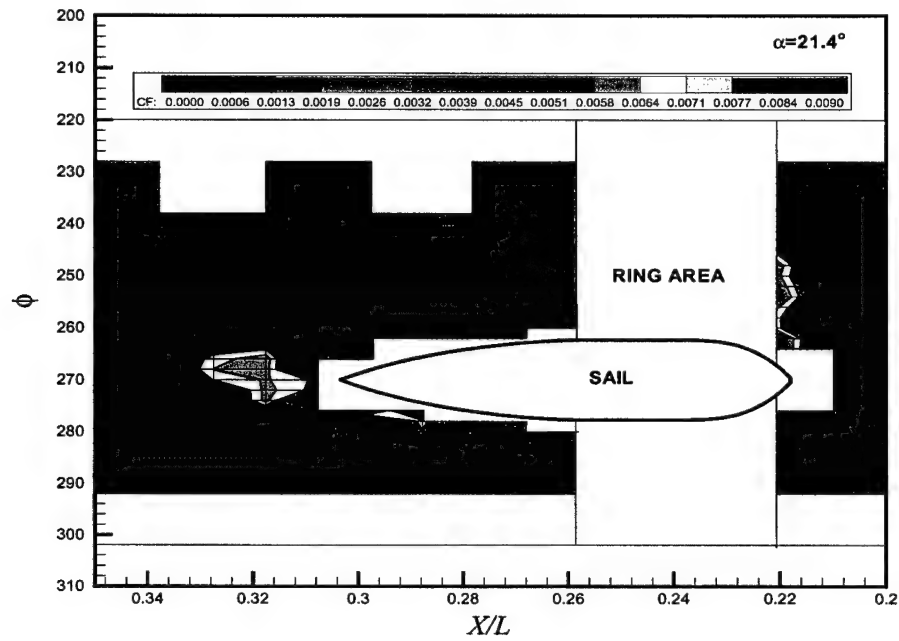
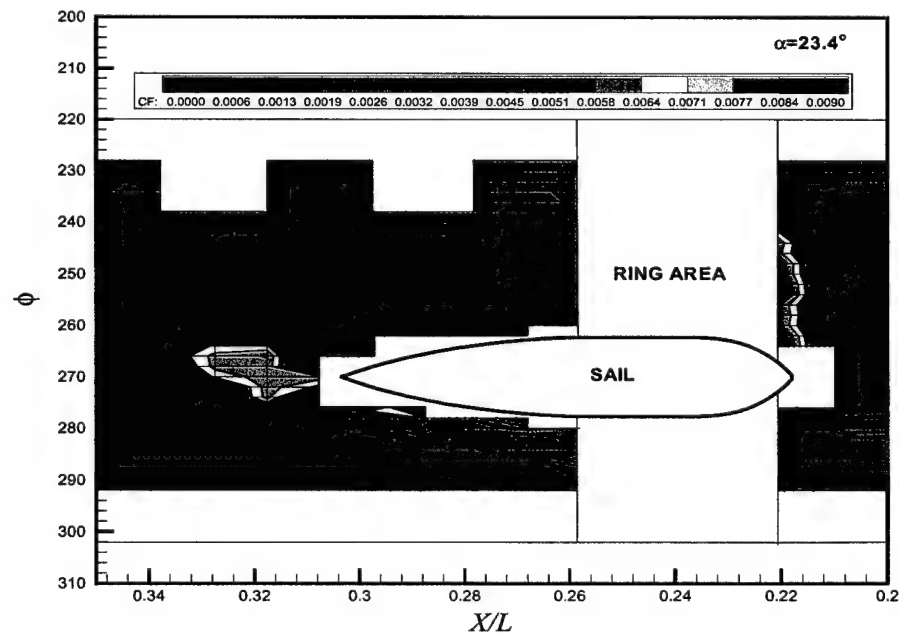
Figure 5.57: Steady  $C_f$  contours in the vicinity of sail at  $\alpha = 5.1^\circ$ .Figure 5.58: Steady  $C_f$  contours in the vicinity of sail at  $\alpha = 7.2^\circ$ .

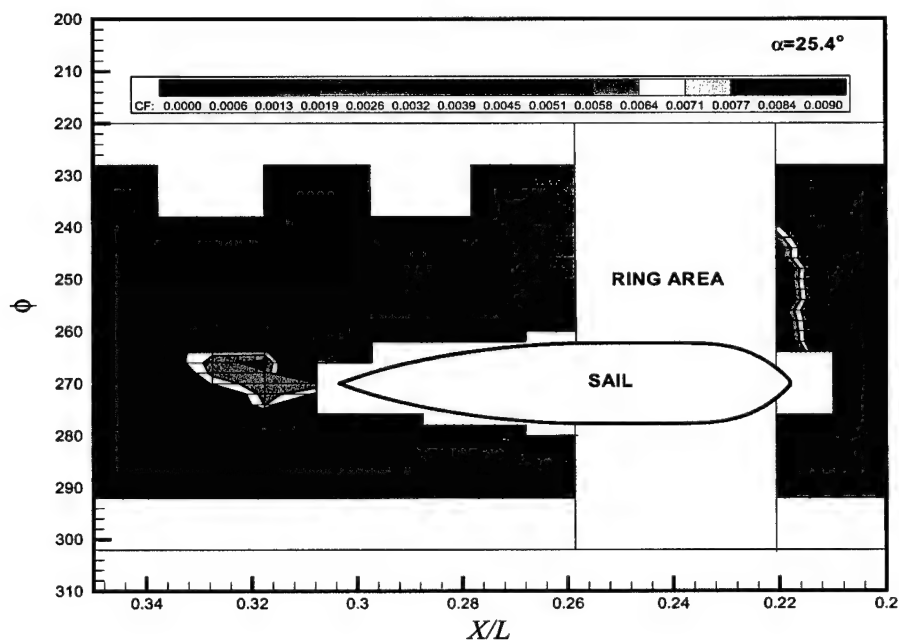
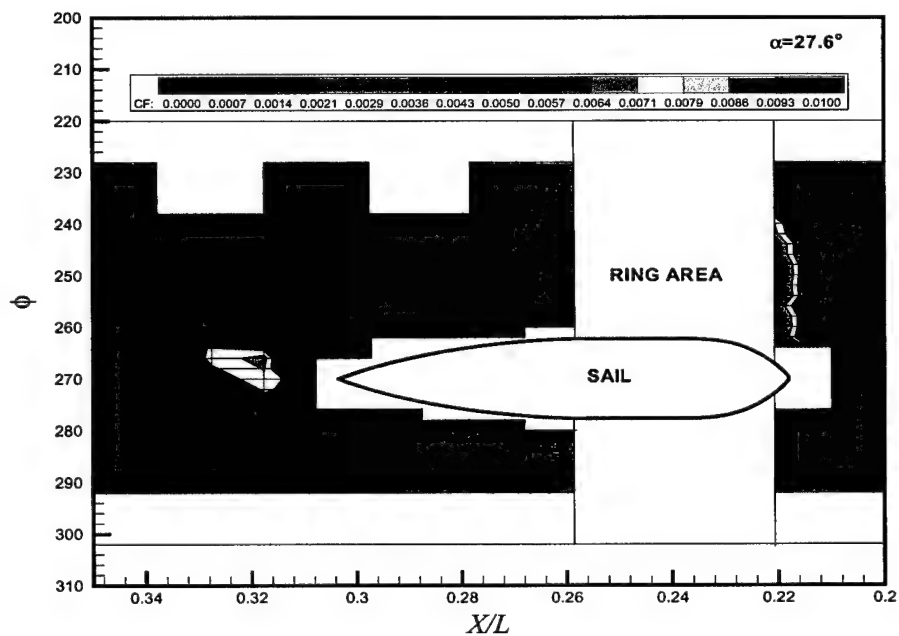
Figure 5.59: Steady  $C_f$  contours in the vicinity of sail at  $\alpha = 9.3^\circ$ .Figure 5.60: Steady  $C_f$  contours in the vicinity of sail at  $\alpha = 11.3^\circ$ .

Figure 5.61: Steady  $C_f$  contours in the vicinity of sail at  $\alpha = 13.2^\circ$ .Figure 5.62: Steady  $C_f$  contours in the vicinity of sail at  $\alpha = 15.3^\circ$ .



Figure 5.63: Steady  $C_f$  contours in the vicinity of sail at  $\alpha = 17.4^\circ$ .Figure 5.64: Steady  $C_f$  contours in the vicinity of sail at  $\alpha = 19.4^\circ$ .

Figure 5.65: Steady  $C_f$  contours in the vicinity of sail at  $\alpha = 21.4^\circ$ .Figure 5.66: Steady  $C_f$  contours in the vicinity of sail at  $\alpha = 23.4^\circ$ .

Figure 5.67: Steady  $C_f$  contours in the vicinity of sail at  $\alpha = 25.5^\circ$ .Figure 5.68: Steady  $C_f$  contours in the vicinity of sail at  $\alpha = 27.6^\circ$ .

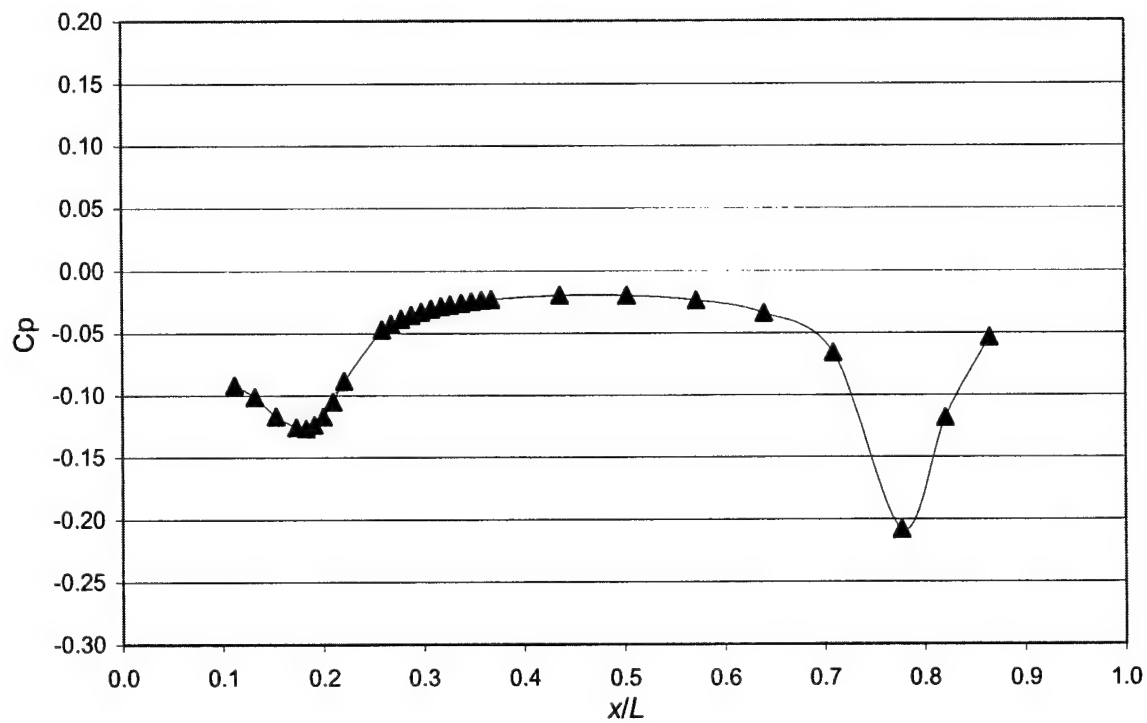


Figure 5.69:  $C_p$  vs.  $x/L$  distribution obtained from RANS code at  $0^\circ$  angle of attack.

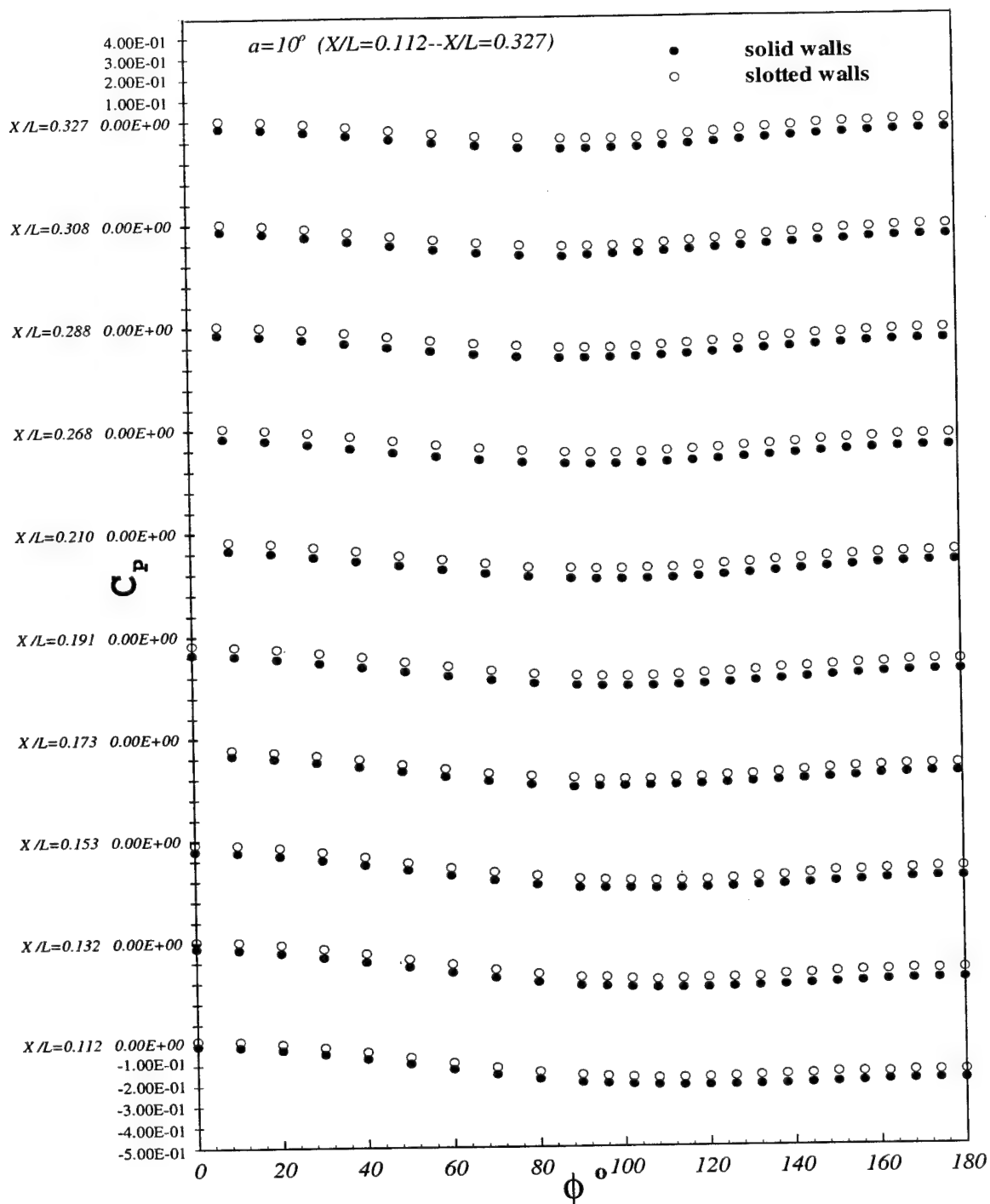


Figure 5.70:  $C_p$  vs.  $\phi$  for the stations between  $x/L = 0.112$  and  $x/L = 0.327$  at  $\alpha = 10.0^\circ$  for the barebody case. Solid and slotted wind tunnel wall configurations.

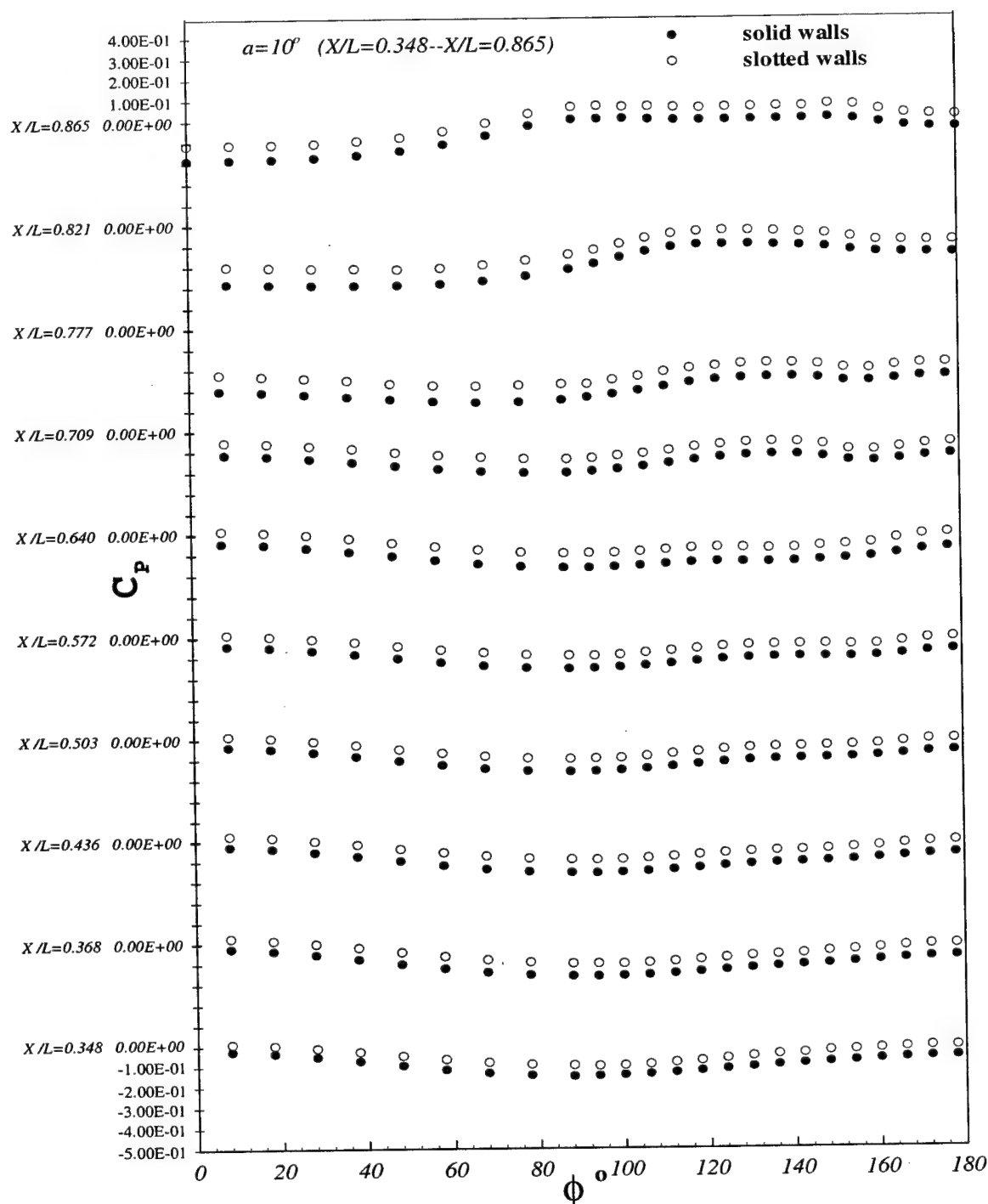


Figure 5.71:  $C_p$  vs.  $\phi$  for the stations between  $x/L = 0.348$  and  $x/L = 0.865$  at  $\alpha = 10.0^\circ$  for the barebody case. Solid and slotted wind tunnel wall configurations.

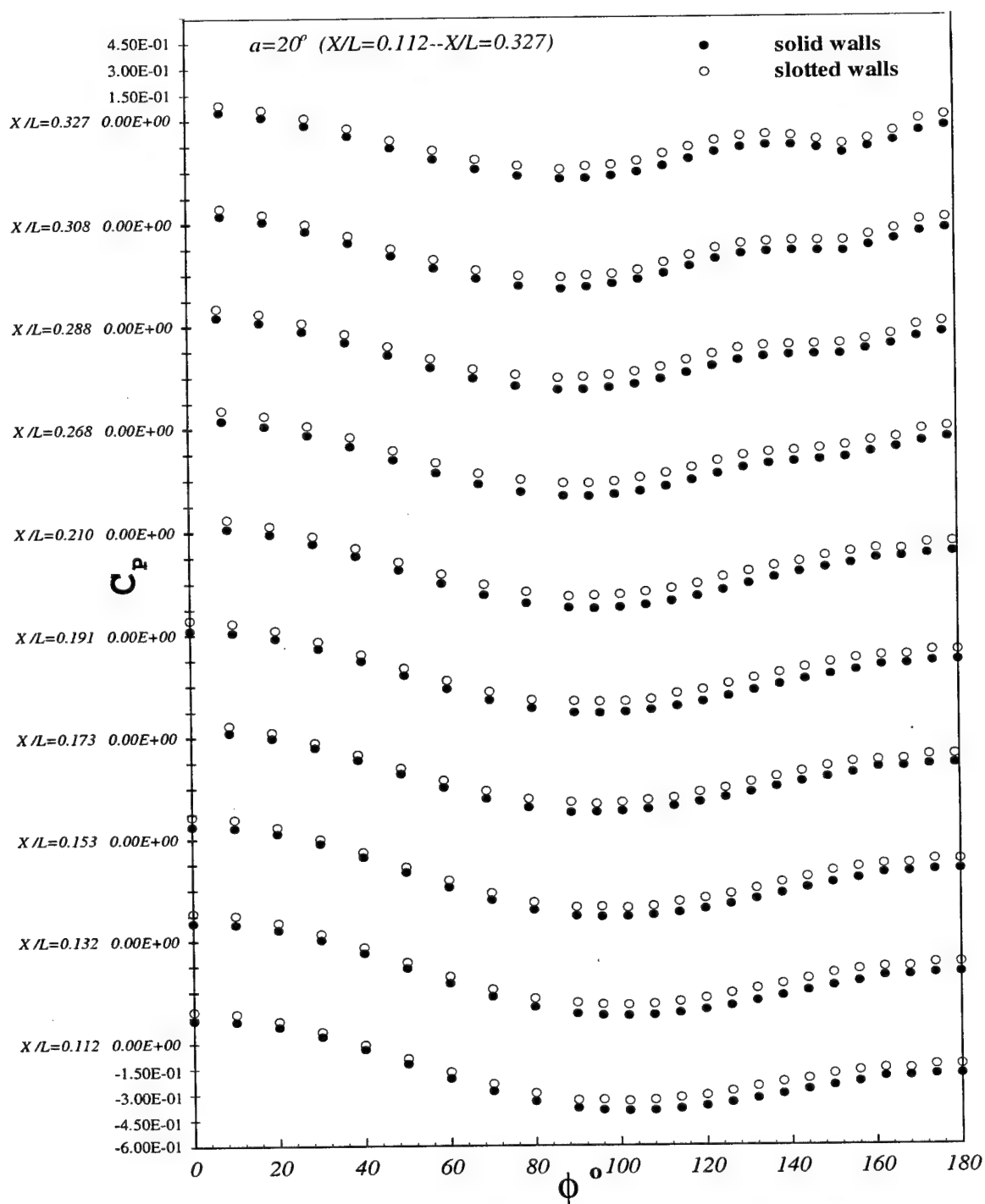


Figure 5.72:  $C_p$  vs.  $\phi$  for the stations between  $x/L = 0.112$  and  $x/L = 0.327$  at  $\alpha = 20.0^\circ$  for the barebody case. Solid and slotted wind tunnel wall configurations.

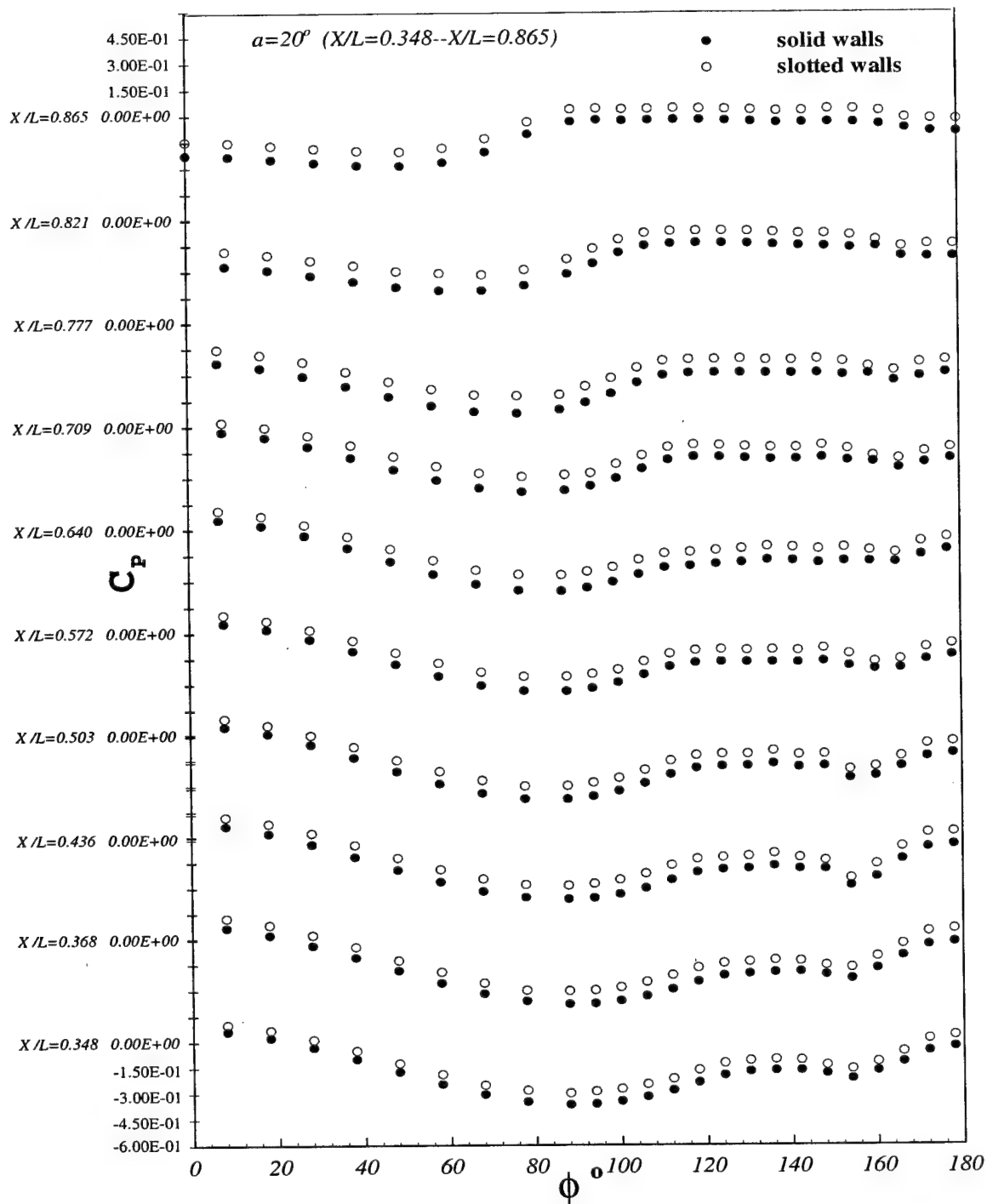


Figure 5.73:  $C_p$  vs.  $\phi$  for the stations between  $x/L = 0.348$  and  $x/L = 0.865$  at  $\alpha = 20.0^\circ$  for the barebody case. Solid and slotted wind tunnel wall configurations.



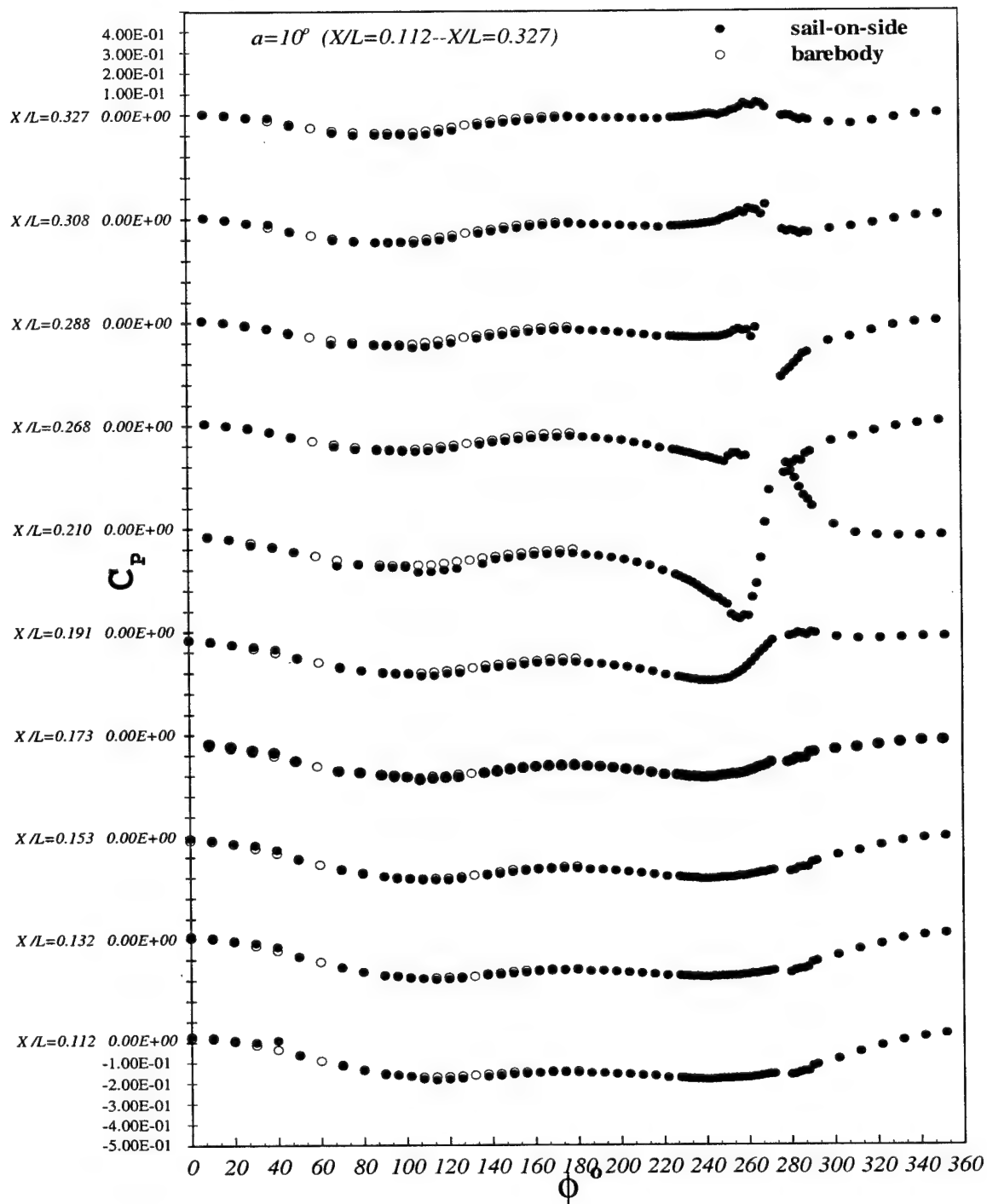


Figure 5.74:  $C_p$  vs.  $\phi$  for the stations between  $x/L = 0.112$  and  $x/L = 0.327$  at  $\alpha = 10.0^\circ$  for the barebody case and sail-on-side cases. Sail side on the right of the figure starting from  $\phi = 180^\circ$ . Slotted wind tunnel wall configuration.

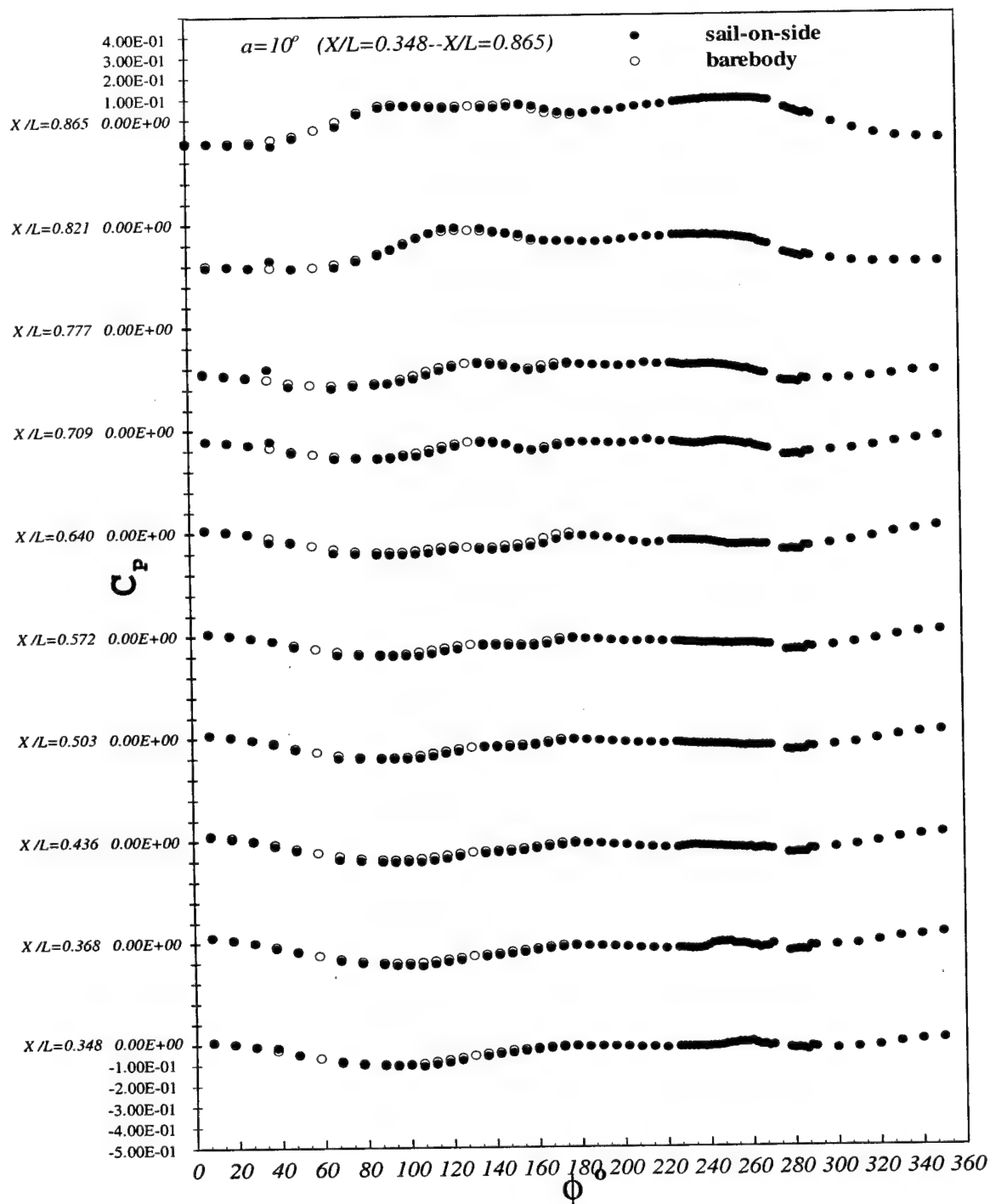


Figure 5.75:  $C_p$  vs.  $\phi$  for the stations between  $x/L = 0.348$  and  $x/L = 0.865$  at  $\alpha = 10.0^\circ$  for the barebody case and sail-on-side cases. Sail side on the right of the figure starting from  $\phi = 180^\circ$ . Slotted wind tunnel wall configuration.

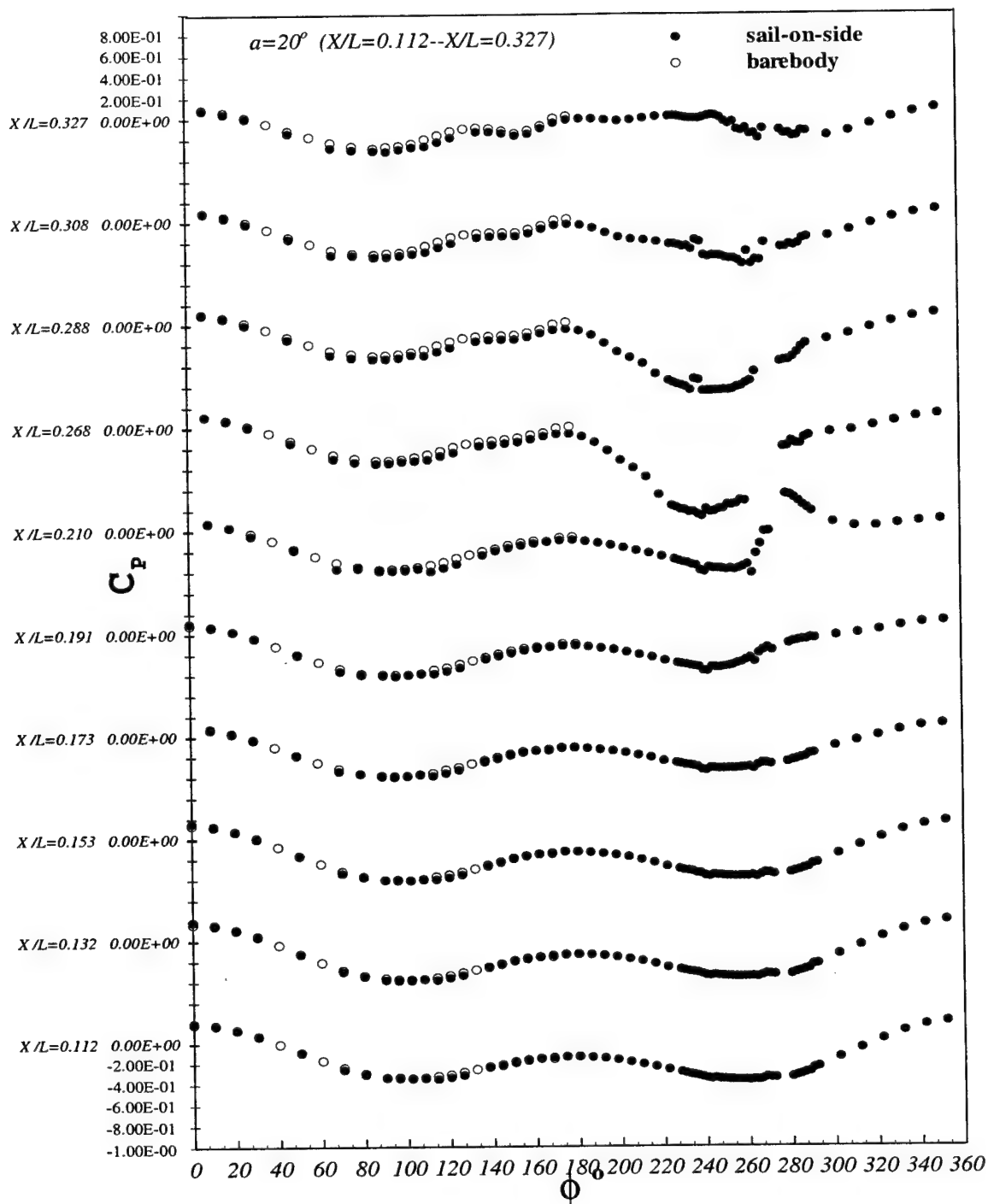


Figure 5.76:  $C_p$  vs.  $\phi$  for the stations between  $x/L = 0.112$  and  $x/L = 0.327$  at  $\alpha = 20.0^\circ$  for the barebody case and sail-on-side cases. Sail side on the right of the figure starting from  $\phi = 180^\circ$ . Slotted wind tunnel wall configuration.

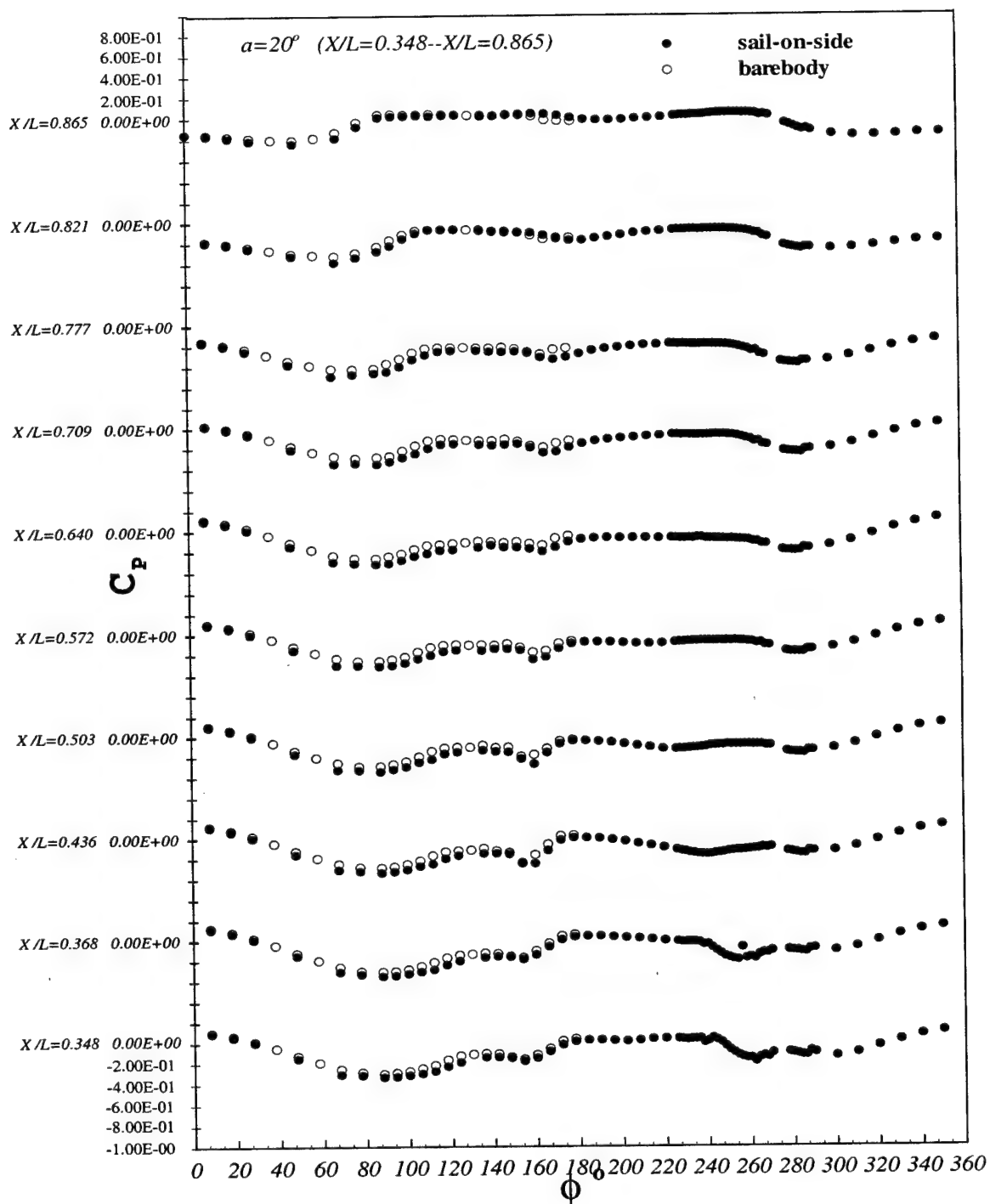


Figure 5.77:  $C_p$  vs.  $\phi$  for the stations between  $x/L = 0.348$  and  $x/L = 0.865$  at  $\alpha = 20.0^\circ$  for the barebody case and sail-on-side cases. Sail side on the right of the figure starting from  $\phi = 180^\circ$ . Slotted wind tunnel wall configuration.

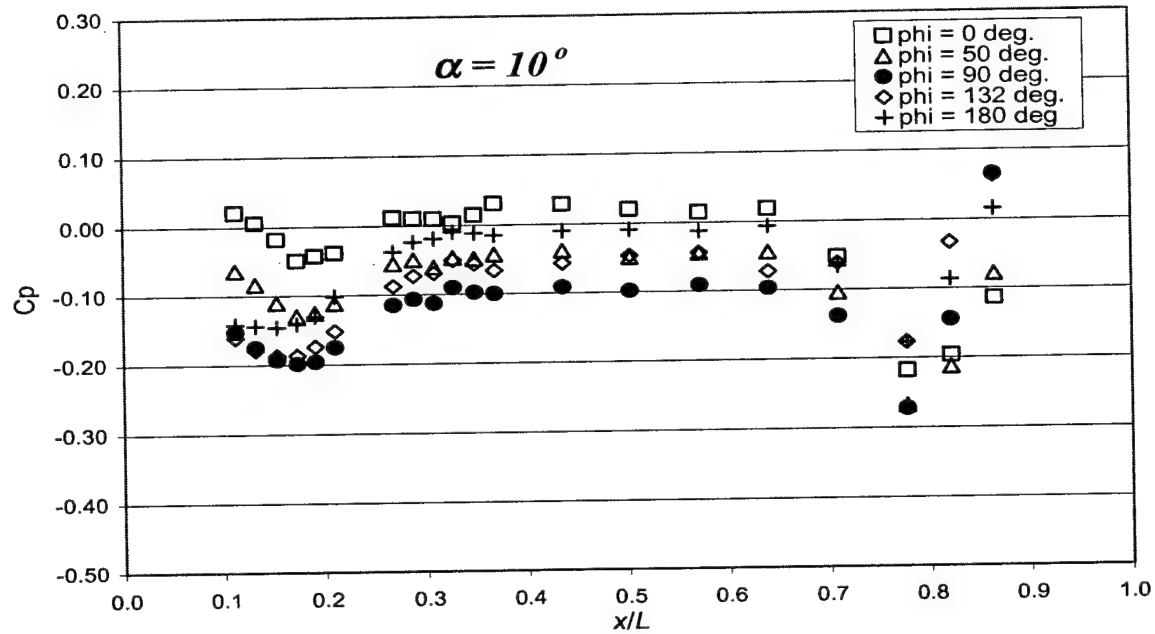


Figure 5.78: Barebody  $C_p$  vs.  $x/L$  distributions for different  $\phi$  locations at  $\alpha = 10^\circ$ .

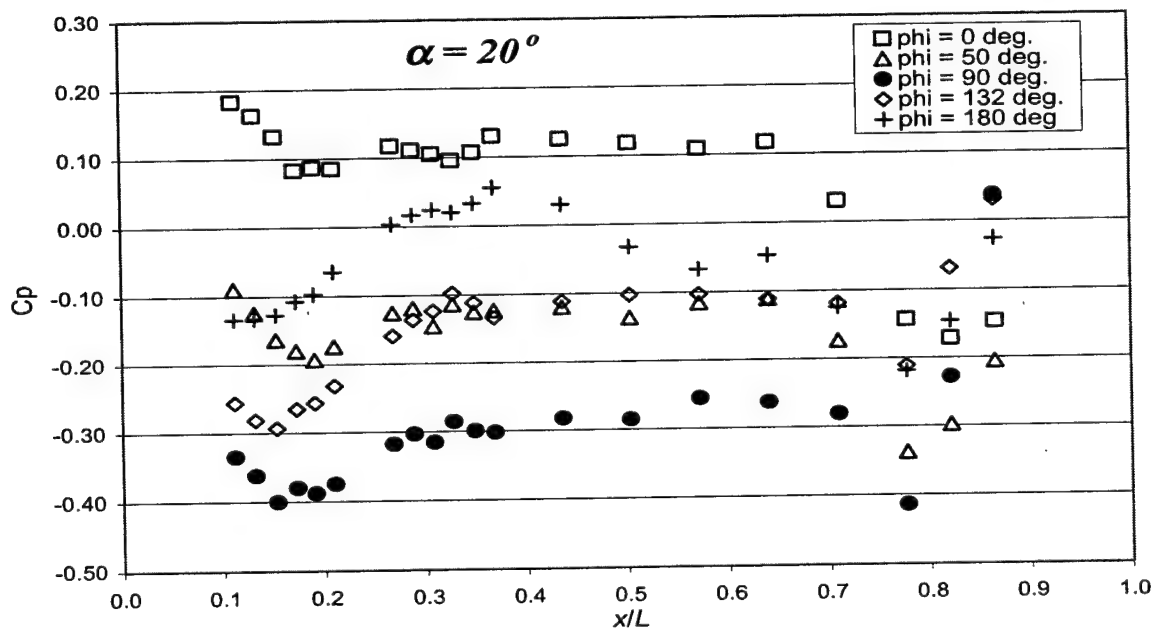


Figure 5.79: Barebody  $C_p$  vs.  $x/L$  distributions for different  $\phi$  locations at  $\alpha = 20^\circ$ .

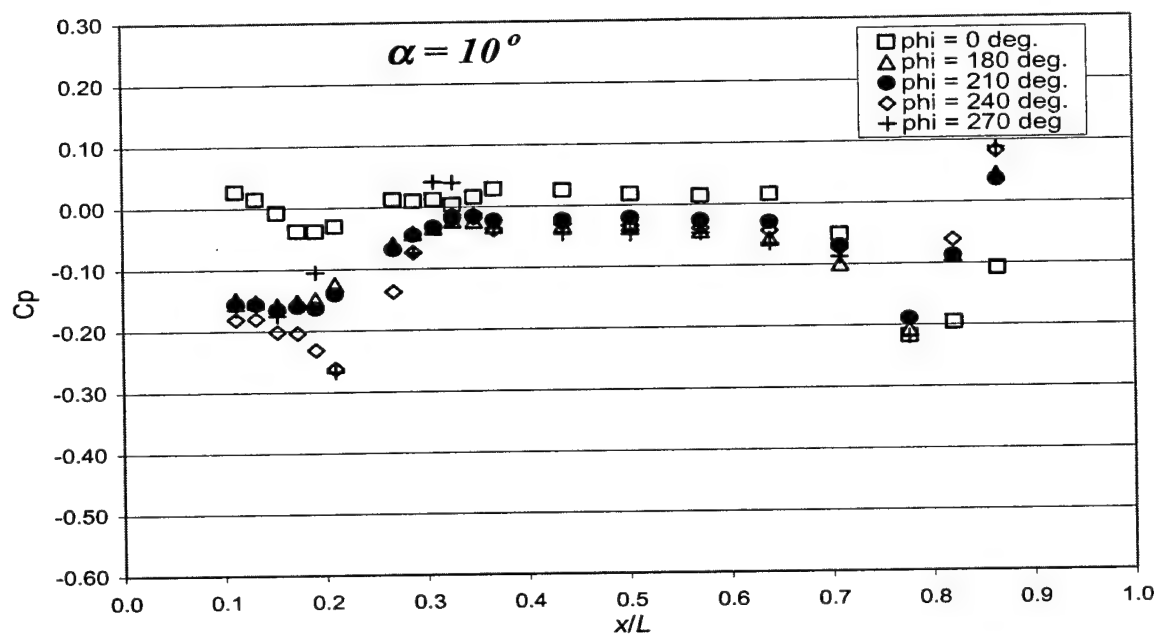


Figure 5.80: Sail-on-side  $C_p$  vs.  $x/L$  distributions for different  $\phi$  locations at  $\alpha = 10^\circ$ .

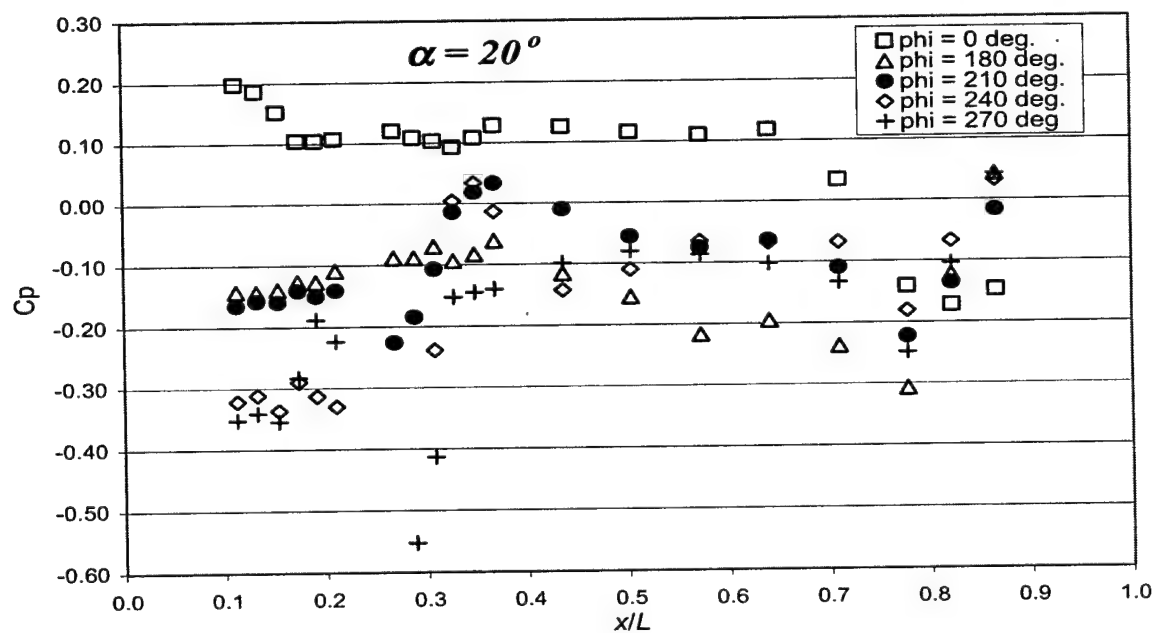


Figure 5.81: Sail-on-side  $C_p$  vs.  $x/L$  distributions for different  $\phi$  locations at  $\alpha = 20^\circ$ .

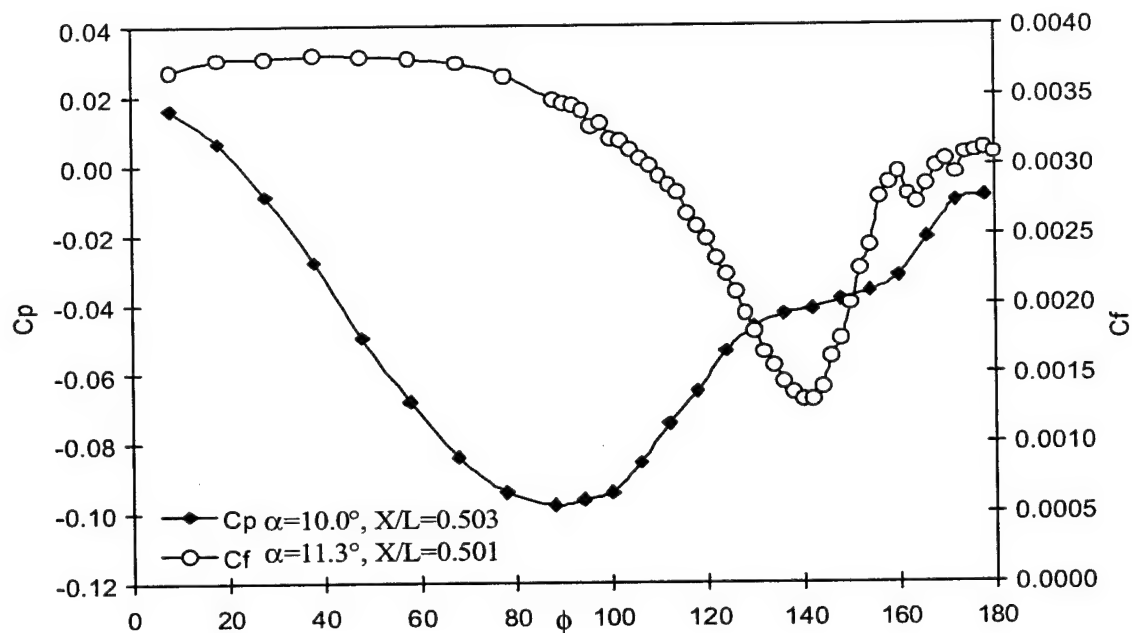


Figure 5.82: Steady  $C_p$  and  $C_f$  vs.  $\phi$  for the barebody case. For  $C_p$  measurements  $\alpha = 10.0^\circ$  and  $x/L = 0.503$ . For  $C_f$  measurements  $\alpha = 11.3^\circ$  and  $x/L = 0.501$ .

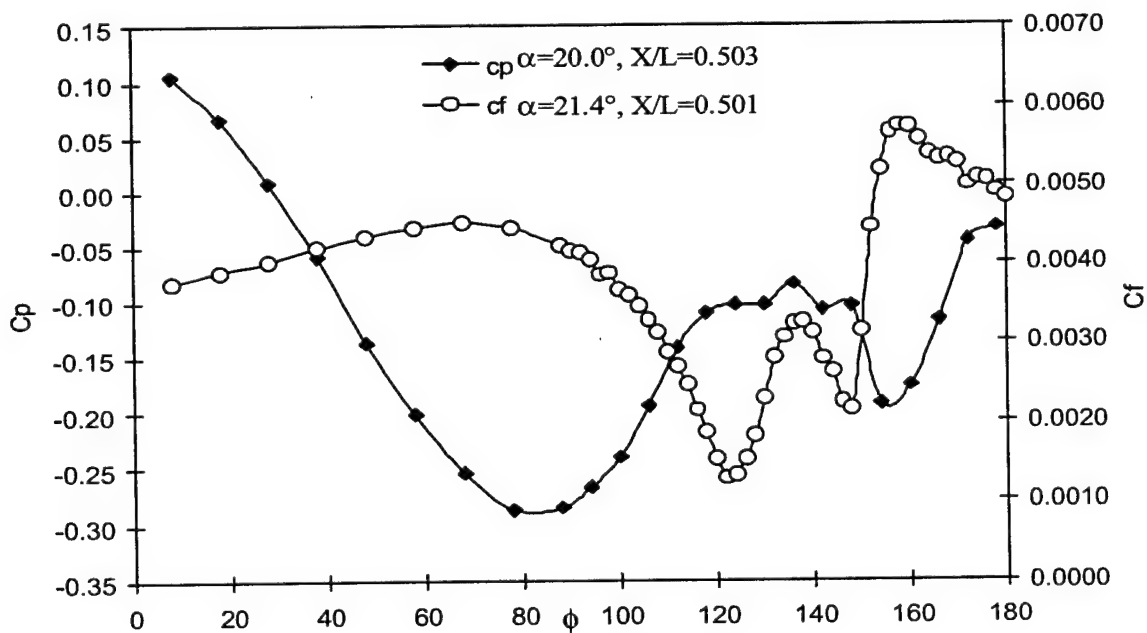


Figure 5.83: Steady  $C_p$  and  $C_f$  vs.  $\phi$  for the barebody case. For  $C_p$  measurements  $\alpha = 20.0^\circ$  and  $x/L = 0.503$ . For  $C_f$  measurements  $\alpha = 21.4^\circ$  and  $x/L = 0.501$ .

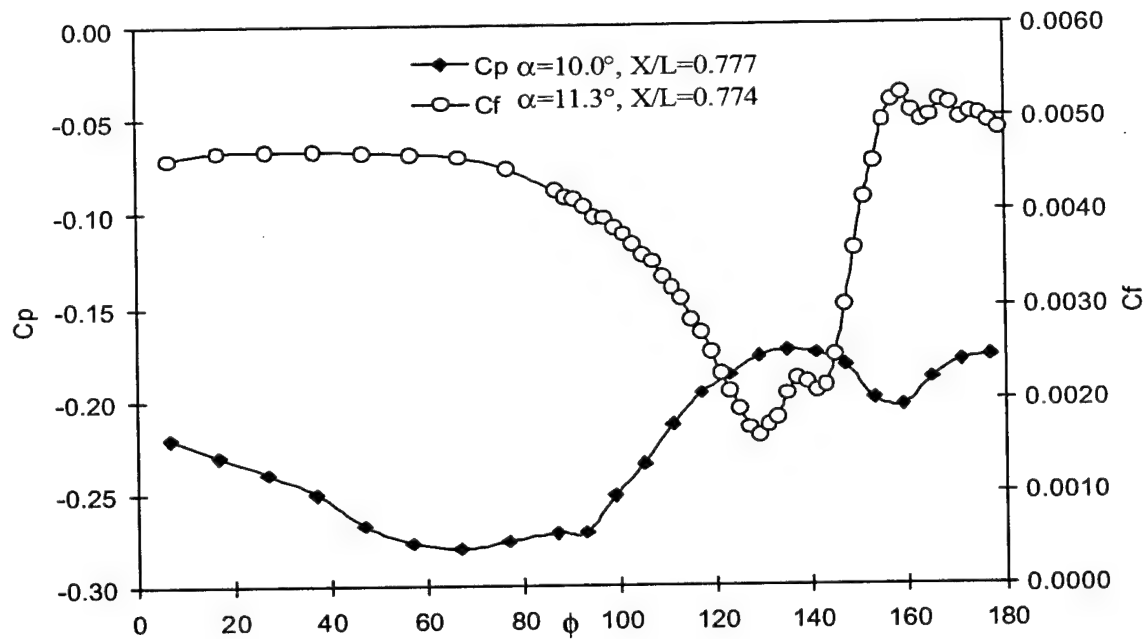


Figure 5.84: Steady  $C_p$  and  $C_f$  vs.  $\phi$  for the barebody case. For  $C_p$  measurements  $\alpha = 10.0^\circ$  and  $x/L = 0.777$ . For  $C_f$  measurements  $\alpha = 11.3^\circ$  and  $x/L = 0.774$ .

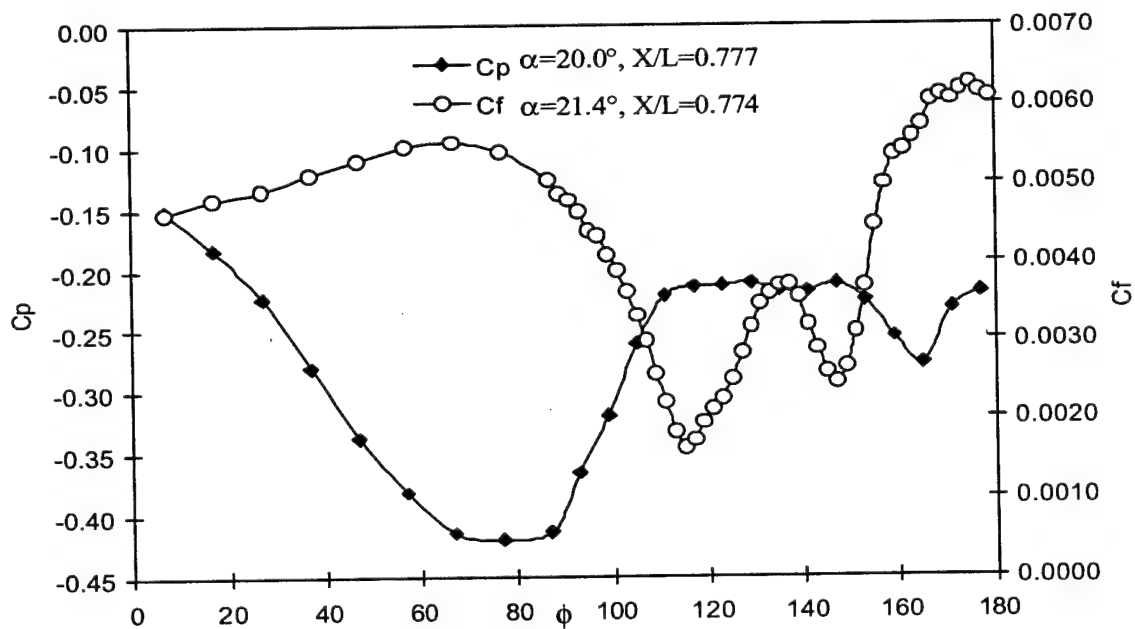


Figure 5.85: Steady  $C_p$  and  $C_f$  vs.  $\phi$  for the barebody case. For  $C_p$  measurements  $\alpha = 20.0^\circ$  and  $x/L = 0.777$ . For  $C_f$  measurements  $\alpha = 21.4^\circ$  and  $x/L = 0.774$ .



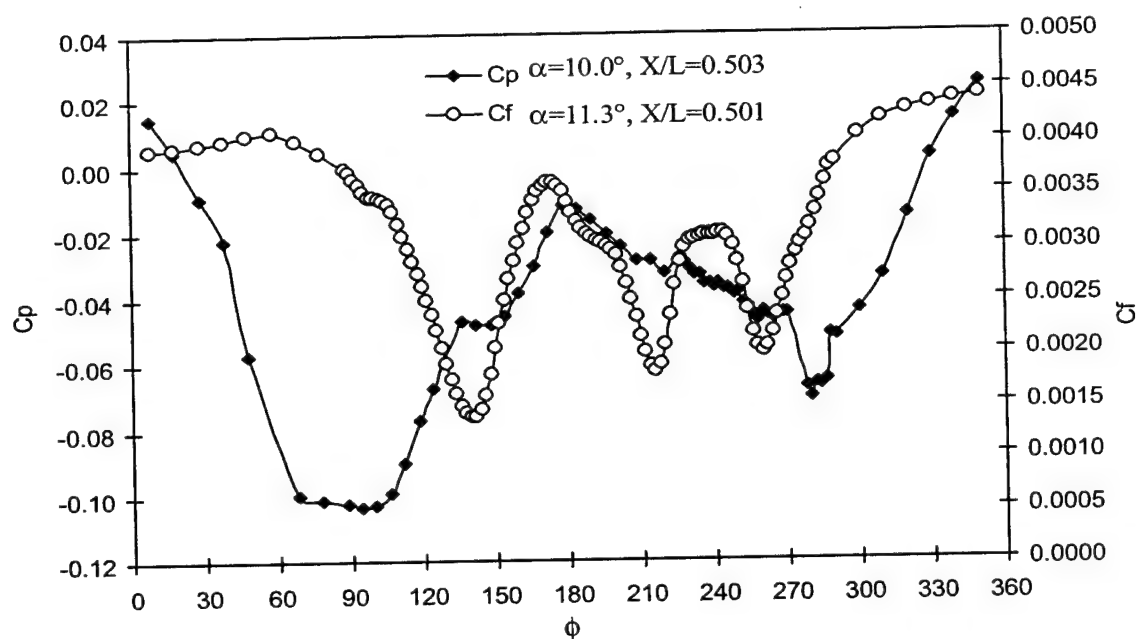


Figure 5.86: Steady  $C_p$  and  $C_f$  vs.  $\phi$  for the sail-on-side case. For  $C_p$  measurements  $\alpha = 10.0^\circ$  and  $x/L = 0.503$ . For  $C_f$  measurements  $\alpha = 11.3^\circ$  and  $x/L = 0.501$ .

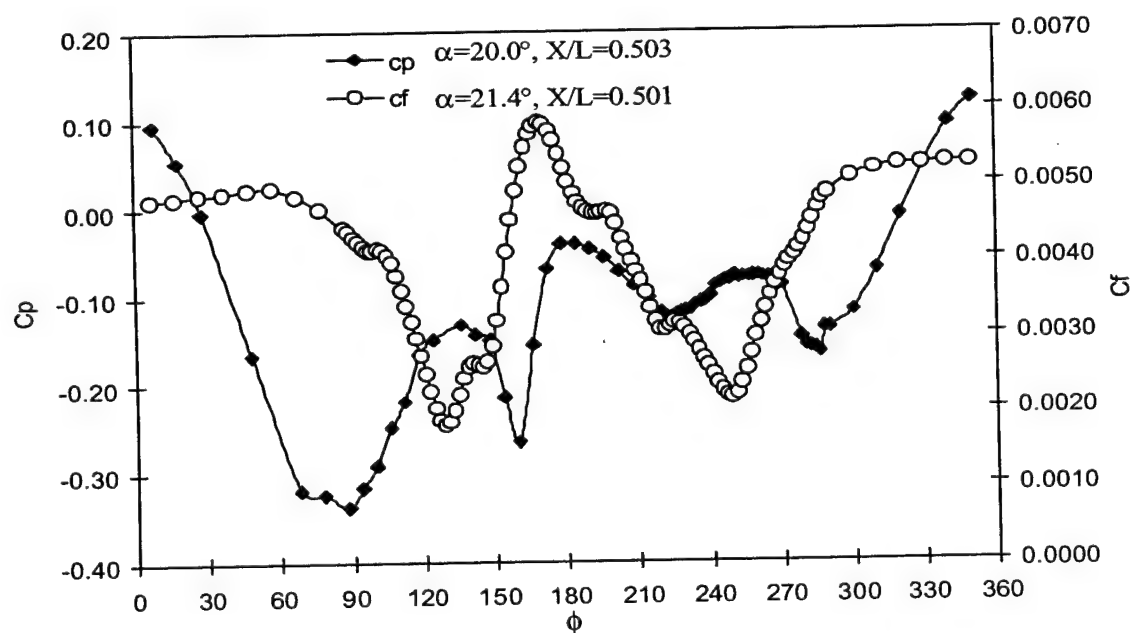


Figure 5.87: Steady  $C_p$  and  $C_f$  vs.  $\phi$  for the sail-on-side case. For  $C_p$  measurements  $\alpha = 20.0^\circ$  and  $x/L = 0.503$ . For  $C_f$  measurements  $\alpha = 21.4^\circ$  and  $x/L = 0.501$ .

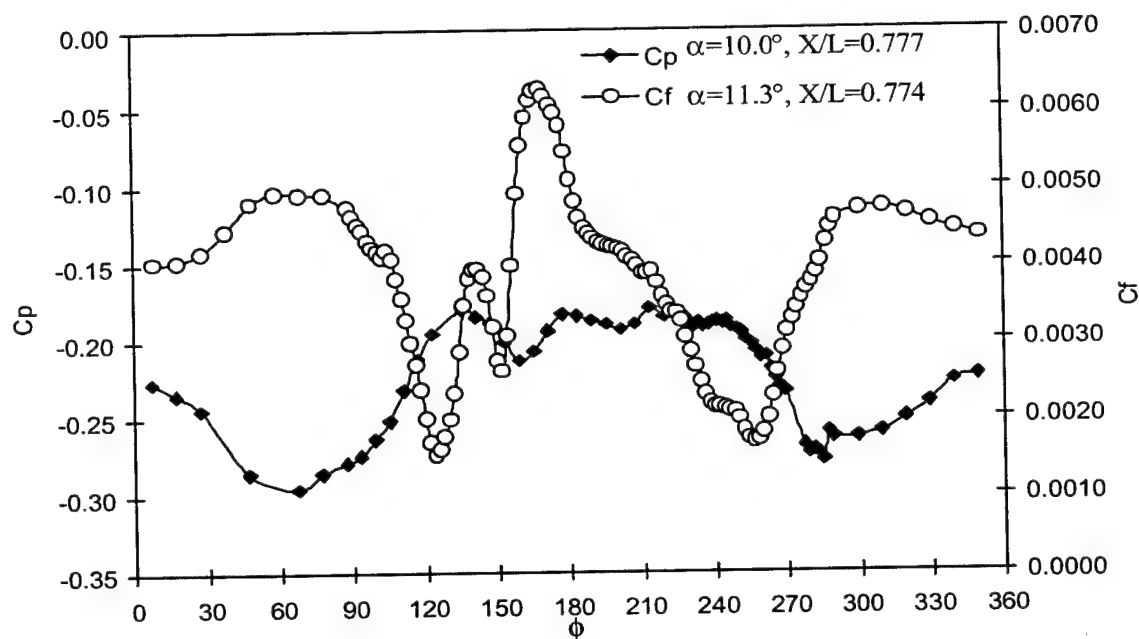


Figure 5.88: Steady  $C_p$  and  $C_f$  vs.  $\phi$  for the sail-on-side case. For  $C_p$  measurements  $\alpha = 10.0^\circ$  and  $x/L = 0.777$ . For  $C_f$  measurements  $\alpha = 11.3^\circ$  and  $x/L = 0.774$ .

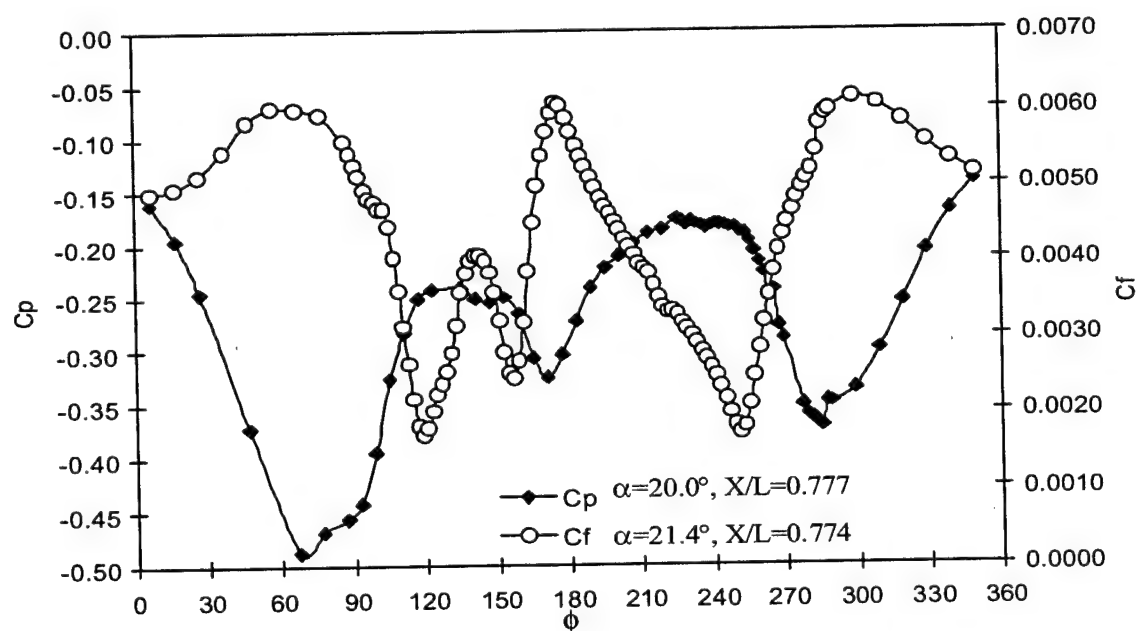


Figure 5.89: Steady  $C_p$  and  $C_f$  vs.  $\phi$  for the sail-on-side case. For  $C_p$  measurements  $\alpha = 20.0^\circ$  and  $x/L = 0.777$ . For  $C_f$  measurements  $\alpha = 21.4^\circ$  and  $x/L = 0.774$ .

## Chapter 6

# Results and Discussion for Unsteady Measurements

### 6.1 Data Acquisition and Reduction

The unsteady voltage values  $E(t')$  from the constant temperature anemometers, each connected to a hot-film sensor, were acquired by using a custom written Labview software program. This program also provided the control and the adjustment of the tunnel data acquisition hardware for the unsteady hot-film measurements. The number of samples taken in time for each unsteady maneuver was 1500. The unsteady voltage signals were acquired with a sample rate of 1000 Hz. Note that sampling frequency is well above the frequency response of the constant temperature anemometers (200 Hz). Total sampling time was 1.5 seconds. The actual maneuver covered approximately 0.33 seconds of this time period. The rest of the sampling time was spent for taking the pre-maneuver and the post-maneuver data. The pitch-up maneuver was executed 10 times at each roll angle position in order to reduce the uncertainty of unsteady data.

As used in the steady data reduction part, the measured unsteady values are represented as arrays of indexed variables in order to simplify the description of the data reduction procedure. In the unsteady data reduction process, the unsteady voltage value acquired from each anemometer can be written as

$$E(t') = E(t_j, s_k, r_l, \phi_m) \quad (6.1)$$

$$j = 1, \dots, 1500 \quad k = 1, \dots, 15 \quad l = 1, \dots, 10 \quad \text{and} \quad m = 1, \dots, nroll \quad (6.2)$$

where  $t_j$  corresponds to a point in time;  $s_k$  to the sensor number or the location;  $r_l$  to the repetition number of the pitch-up maneuver; and  $\phi_m$  to the DyPPiR roll angle of the model. Total number of the roll angles covered during the experiments,  $nroll$ , changes with respect to the model configuration. For the barebody case, 56 roll angle positions were covered. For the sail-on-side case, total number of roll angles was 117. However, data of the non-sail region and the data from sail region were reduced separately. For the non-sail region, total number of 71 roll angles were reduced, while for the sail side data reduction was made with 76 roll angles. The last 30 angles of the non-sail region and the first 30 angles of the sail side were the same. This was done in order to keep the continuity of the skin-friction distributions between the two regions during the smoothing process, which will be described later in this section.

The steps of the unsteady skin-friction data reduction can be outlined as follows:

1. At each roll angle position, the free-stream temperature  $T(t_j, r_l, \phi_m)$ , the dynamic pressure  $q(t_j, r_l, \phi_m)$ , and the atmospheric pressure  $p(t_j, r_l, \phi_m)$  are calculated from the corresponding voltage values by the use of the calibration.
2. At each roll angle position, the plunge position  $z(t_j, r_l, \phi_m)$  and the instantaneous angle of attack  $\alpha(t_j, r_l, \phi_m)$  of the model are determined through the use of the DyPPiR plunge and pitch calibrations.
3. Each time point is non-dimensionalized by the reference time,  $t_{ref} = L/U_\infty$  where  $L$  is the model length and  $U_\infty$  is the free-stream velocity.
4. Instantaneous skin friction values  $C_f(t_j, s_k, r_l, \phi_m)$  for each roll angle, sensor and the repetition are calculated by

$$C_f(t_j, s_k, r_l, \phi_m) = \frac{\tau_w(t_j, s_k, r_l, \phi_m)}{q(t_j, r_l, \phi_m)} \quad (6.3)$$

where  $\tau_w$  is the unsteady wall shear stress value obtained by the use of King's law given by the equation 4.10

$$\tau_w(t_j, s_k, r_l, \phi_m) = \left[ \frac{E^2(t_j, s_k, r_l, \phi_m) - A(s_k, \phi_m)}{B(s_k, \phi_m)} \right]^3 \quad (6.4)$$

In equation 6.4,  $A(s_k, \phi_m)$  and  $B(s_k, \phi_m)$  are the calibration coefficients obtained for each sensor by the procedure described in chapter IV. Note that at a particular roll angle position of the model, the calibration coefficients used in the unsteady measurements are the same as the ones used for the steady measurements, since the maneuvers are performed just after the last steady angle of attack and the change in the free-stream temperature between the steady and the unsteady measurements at a specific roll angle is negligible.

5. To reduce the noise in the unsteady measurements, the skin-friction values of each sensor, the plunge position and instantaneous angle of attack from 10 repetitions of the pitch-up maneuver performed at a specific roll angle position of the model are ensemble averaged:

$$C_{f_{avg}}(t_j, s_k, \phi_m) = \frac{\sum_{l=1}^{10} C_f(t_j, s_k, r_l, \phi_m)}{10} \quad (6.5)$$

$$z_{avg}(t_j, \phi_m) = \frac{\sum_{l=1}^{10} z(t_j, r_l, \phi_m)}{10} \quad (6.6)$$

$$\alpha_{avg}(t_j, \phi_m) = \frac{\sum_{l=1}^{10} \alpha(t_j, r_l, \phi_m)}{10} \quad (6.7)$$

6. Standard deviations  $\sigma(t_j, s_k, \phi_m)$  of the ensemble averaged skin-friction values are calculated. The results from the unsteady experiments showed that the standard deviations of the ensemble averaged voltage values were two orders of magnitude smaller than the average values in most cases, therefore the unsteady data was highly repeatable and 10 repetitions for the pitchup maneuver at each roll angle position were sufficient to reduce the noise.
7. In order to determine the bad skin-friction values and exclude them from ensemble averaging, a statistical outlier detection method is used. In order to determine the outliers, a *student's t - distribution* is assumed for the 10 repetitions of the skin-friction values  $C_f(t_j, s_k, r_l, \phi_m)$  at each roll angle position. Then the difference  $d(t_j, s_k, \phi_m)$  from the mean value  $C_{f_{avg}}(t_j, s_k, \phi_m)$  is calculated for each  $C_f(t_j, s_k, r_l, \phi_m)$ :

$$d(t_j, s_k, \phi_m) = \sqrt{[C_f(t_j, s_k, r_l, \phi_m) - C_{f_{avg}}(t_j, s_k, \phi_m)]^2} \quad (6.8)$$

and the condition

$$d \geq t \times \sigma(t_j, s_k, \phi_m) \quad (6.9)$$

is checked. Here  $t$  value is chosen for 9 degrees of freedom with 90% confidence interval and equal to 1.833 (Holman [33]). The  $C_f(t_j, s_k, r_l, \phi_m)$  values that satisfy the above condition are marked as outliers and their values are set to zero. The new  $C_{f_{avg}}(t_j, s_k, \phi_m)$  are calculated by:

$$C_{f_{avg}}(t_j, s_k, \phi_m) = \frac{\sum_{l=1}^{10} C_f(t_j, s_k, r_l, \phi_m)}{10 - n_{outlier}} \quad (6.10)$$

where  $n_{outlier}$  is the total number of outliers detected.

8. In order to reject the high frequency noise in  $C_{f_{avg}}(t_j, s_k, \phi_m)$ , a third-order digital Butterworth filter is used. As for the cutoff frequency, 20 Hz. is used. Wetzel [2] used the same value in the unsteady data reduction of the prolate spheroid work. In this study, different cutoff frequency values were tried. It has been seen that this value is high enough to preserve the frequency content and the magnitude of the unsteady data while filtering the high frequency noise.
9. Unsteady separation locations are obtained and the data are arranged for different output formats.

### 6.1.1 Determination of the unsteady separation locations

For the determination of the unsteady primary separation locations,  $C_f = C_{f_{avg}}(t_j, s_k, \phi_m)$  vs.  $\phi = \phi_m$  ( $m = 1, \dots, n_{roll}$ ) distributions for each sensor have to be analyzed. Since the actual maneuver starts at  $t' = 3.0$  and ends at approximately  $t' = 10.3$ , there is no need to consider all the time steps in the maneuver. Between these two time values, a total number of 40 equally spaced time points are used. This corresponds to a time increment of  $\Delta t = 0.01$  seconds between the start of the pitch-up and the end of the maneuver. The total number of time points to be used in the separation location determination is obtained as a result of many trials and it has been seen that further increase of the total number of points does not change the unsteady separation pattern obtained with 40 points.

An automated scheme is needed to find the unsteady separation locations at each time step and the sensor location, since it is impossible to determine the separation locations graphically (as done in the steady case) due to the large number of data sets to be examined. For this purpose, three methods were tried: in the first method, the minimum in

$C_f$  from each unsteady circumferential distribution is determined and the corresponding  $\phi$  is taken to be the unsteady separation location. However, this method is not robust and accurate enough in the presence of outliers or wiggles in the separation region and gives misleading results. In the second method, after the minimum in  $C_f$  is determined, a quadratic curve is fit to the concave separation region by the least squares method. In the fit process 11  $(C_f, \phi)$  points are used with the center value being the minimum of  $C_f$  obtained from the first method. This helps smoothing the data near the separation region and improves the separation location determination. However, as observed in most of the actual cases, the  $C_f$  distribution in the separation region is not symmetric with respect to the minimum  $C_f$  value, therefore using a quadratic fit shifts the minimum from the true value. This offset is not constant for each distribution, so a bias correction to the data cannot be applied. The third method removed the problems encountered in the previous methods. In this approach, the *loess* method is used as described in the steady data reduction of the sail-on-side case. This method is considered in order to smooth the  $C_f$  vs.  $\phi$  distributions at each time step without changing the circumferential skin-friction pattern and to exclude the deviant points that distort the smoothed data. By using this technique, the asymmetry in the vicinity of the separation location is preserved, while the noise from the data is removed. The magnitude changes in the skin-friction values due to smoothing is found to be within the uncertainties. As a result, this last method is used to find the unsteady separation locations and to obtain the  $C_f$  vs.  $\phi$  distributions at each time step.

## 6.2 Unsteady Flow Topology

One of the methods to investigate the difference between the steady and the unsteady flow over the model is to compare the steady  $C_f$  vs.  $\phi$  distribution obtained at a certain pitch angle  $\alpha$  with the unsteady one acquired at the corresponding instantaneous pitch angle  $\alpha(t')$  for a specific  $x/L$  location. Figures 6.1 through 6.39 show this comparison for all the  $x/L$  locations of the sensor set B. Figures from 6.1 to 6.13 give the barebody results. Figures 6.14 to 6.26 show the data of the non-sail region of the sail-on-side case, and the figures between 6.27 and 6.39 give the comparison of the region with the sail. Note that, for each figure, the steady angle of attack and the instantaneous angle of attack are the same. The non-dimensional time  $t'$  corresponding to the instantaneous

angle of attack is also shown in each figure. All the unsteady experiments were done with the slotted walls.

Unsteady  $C_f$  distribution of the barebody case and the non-sail region of the sail-on-side case show similar trends compared to the steady distributions of each. As seen from figures 6.1 and 6.14, at  $\alpha = 3.1^\circ$ , the skin-friction magnitudes of the steady and the unsteady cases are approximately the same and the distributions of both are flat profiles. As the steady angle of attack is increased, the steady data start to deviate from this flat profile, and minima in  $C_f$  distributions indicating primary separation can be observed. However, the unsteady skin-friction pattern remains approximately flat until  $\alpha(t') = 13.2^\circ$ . At this instantaneous angle of attack, the unsteady primary separation starts to develop at the downstream stations starting from  $x/L = 0.706$ . Figures 6.6 and 6.19 show the  $C_f$  distributions at this angle of attack for the barebody and the sail-on-side case respectively. At higher angles of attack, the difference between the steady and the unsteady flow separation pattern is more obvious. At  $\alpha = 21.4^\circ$ , in figures 6.10 and 6.23, steady primary separation starts from  $x/L = 0.266$  and shifts towards the windward side at the downstream stations. The unsteady separation can be first located at  $x/L = 0.345$  and also moves towards the windward side as  $x/L$  increases. Compared to the steady primary separation locations at the same  $x/L$  stations, the unsteady separation locations are found to be more leeward. In particular, at  $x/L = 0.501$ , the primary separation location for the steady data is  $\phi = 122^\circ$ , while the unsteady primary separation occurs at  $\phi = 136^\circ$  for the barebody case. From the same figures, another important observation can be made about the secondary flow separation. In the steady case, secondary separation starts to develop at  $x/L = 0.434$ , and can be seen as the second minima of the  $C_f$  for the rest of the stations downstream. On the other hand, no secondary separation formation can be detected at any of the  $x/L$  stations for the unsteady case. A weak unsteady secondary separation can be seen at the last instantaneous angle of attack  $\alpha(t') = 27.6^\circ$ , at the last four  $x/L$  stations. As previously described in the steady results, at the first three stations on the nose region, a weak separation/reattachment pattern can be seen on the leeward side of the model at high steady angles of attack. However, this flow behavior cannot be observed for the unsteady case at the corresponding instantaneous angles of attack. In general, the magnitudes of the unsteady  $C_f$  are lower than that of the steady ones at the same angle of attack and the  $x/L$  location. This difference can be observed starting from  $\alpha = 5.1^\circ$  and become



more obvious at higher angles of attack, especially on the leeward side of the model.

For the sail region, the unsteady data start to deviate from the steady  $C_f$  values even at the first instantaneous angle of attack  $\alpha(t') = 3.1^\circ$ . In figure 6.27, the disturbances created by the sail can be seen on the  $C_f$  distribution at the stations just downstream of the sail for the steady case, while the unsteady data do not show the same trend but follow a more flat pattern. (Note that the unsteady  $C_f$  values at  $x/L = 0.266$  are not shown for the  $\phi$  values after  $256^\circ$  in figures 6.27 through 6.39, since the data at these locations were too scattered and could not be distinguished from the noise.) No clear unsteady separation pattern like the first or the second minima seen in the steady case can be observed up to  $\alpha(t') = 13.2^\circ$ . After this angle of attack, minima in the  $C_f$  indicating the unsteady separation can be located. As also seen in the steady case, the unsteady separation structure of the sail side is different from the unsteady crossflow separation topology observed on the barebody and the non-sail region of the sail-on-side case. Again, no clear categorization of the separation locations could be made. From figure 6.38, for  $\alpha(t') = 25.5^\circ$ , the second minima in the unsteady  $C_f$  distributions at the sensor stations downstream of  $x/L = 0.638$  can be seen to appear more leeward compared to the second minima of the steady case.

The results above show that in unsteady flows the separation topology is different from the one in an equivalent steady configuration. For the barebody and the non-sail region of the sail-on-side case, this difference originates from the fact that the unsteady separation location lags the steady separation. This can be clearly seen from the figures 6.40 through 6.59 where the quasi-steady and the unsteady primary separation locations are plotted against the non-dimensional time  $t'$  for different  $x/L$  stations. The quasi-steady data distribution are formed by first taking the steady separation locations and the corresponding steady angles of attack at a certain  $x/L$  location. By using the DyPPiR pitch feedback data, the instantaneous angles of attack that match with the steady angles are selected. Then the non-dimensional time  $t'$  for each steady separation location can be obtained and quasi-steady data as a function of  $t'$  can be generated. Open symbols stand for the quasi-steady data and the filled symbols represent the unsteady data. For a better understanding of the mathematical difference between the steady, quasi-steady, and the unsteady separation locations, the functional relations that are defined in chapter 1 should be referred.

Figures 6.40 to 6.49 show the separation locations for the barebody case, and the figures

from 6.50 to 6.59 give the primary separation locations for the non-sail region of the sail-on-side case. In these figures, the horizontal distance between the unsteady and the steady separation location is an indication of the presence of a time lag. Since the maneuvers were performed with a constant pitch rate, the instantaneous pitch angle is a linear function of  $t'$ . By considering this fact in examining figures 6.1 to 6.26, it can also be thought that at an instantaneous pitch angle, for a specific  $x/L$  location, the primary unsteady separation starts more leeward compared with the steady case. Therefore the total separated region occupies a smaller area, both on the model surface and in the flow field.

To understand why a lag exists, as described by Wetzel and Simpson [3], one should examine the path of a fluid particle during the maneuver. During the pitch-up maneuver, a fluid particle originally starts its trajectory on the windward side of the model at a lower angle of attack. Therefore, the particle experiences a less severe adverse pressure gradient along its path, and can travel farther around the leeside before separating when compared with a similar particle in a steady flow field. This history effect, the true total path the particle has traversed, differentiates the unsteady flow field from the steady one.

Figures 6.60 through 6.66 show the quasi-steady and the unsteady separation locations as a function of  $t'$  at seven  $x/L$  stations for the sail region of the sail-on-side case. The separation locations correspond to the second minima (at high  $\alpha(t')$  these become the only minima as in the steady case) of the  $C_f$  distributions measured from  $\phi = 180^\circ$ . Figures 6.60 and 6.61 show that the unsteady separation locations are approximately the same as the steady ones within the uncertainties at  $x/L = 0.434$  and  $x/L = 0.501$ . At these stations, the unsteady separation locations are detected for the time points starting from  $t' \simeq 8.0$  and the  $\phi$  values of the separation locations are constant. At the other stations,  $x/L = 0.570, 0.638, 0.706, 0.774$ , and  $0.819$ , the unsteady separation locations are more leeward compared to the quasi-steady ones at a given  $t'$  during the maneuver and they approach the steady values at the end of the maneuver. The difference between the unsteady and the quasi-steady data gets bigger as  $x/L$  increases.

Maybe the most important observation that can be made from these figures is about the unsteady separation pattern in the sail region as a function of  $t'$ . Except for  $x/L = 0.434$  and  $0.501$ , the unsteady separation data do not reach any of the steady separation locations at any instant of time during the maneuver. In other words, unsteady separation pattern do not follow the quasi-steady data with a time lag. In fact, a lag definition as

described for the unsteady crossflow separation may not be appropriate for the sail side separation topology based on the results obtained in this study. The results also indicate the complex nature of the unsteady flow separation on the sail side.

## 6.3 Time-Lag Models

The main interest is to be able to model or approximate the time lags associated with the unsteady flow fields. If one can determine the real physics behind the time-lag formation and approximate the lags with reasonable accuracy, then by using the quasi-steady data that are constructed through the use of the steady flow field information, the unsteady flow features such as unsteady skin-friction, force and moment coefficients can be estimated. In the next two sections, algebraic time-lag modelling and a first order differential time-lag model will be described with their application to the current study.

### 6.3.1 Algebraic Time-lag Models

Algebraic time lag modeling was a commonly used approach in the previous studies. Most of the algebraic time lag models are based on finding an effective angle of attack  $\alpha_{eff}$  by using the descriptions of the flow kinematics. If a model rotates about some point  $x_{cg}$  at a constant pitch rate  $\dot{\alpha}$ , a relative velocity normal to the model axis  $\dot{\alpha}(x - x_{cg})$  will exist at other  $x/L$  locations in addition to the velocity of the wind relative to the point of rotation. By using this fact, Montividas et al. [9] approximated an effective angle of attack as:

$$\alpha_{eff} = \alpha - \Delta\alpha_{eff} \quad (6.11)$$

where

$$\Delta\alpha_{eff} = \dot{\alpha} \frac{x_{cg} - x}{U_{\infty}} \quad (6.12)$$

However, this approximation did not describe the unsteady effects in their flow field associated with the onset of asymmetric vortex shedding at high angles of attack on ogive cylinders.

Ericsson [34] also studied the same problem and extended the effective angle of attack idea by including the convective lag effects in the flow field. He used the fact that a

vortex at a downstream station of the apex of the model (ogive cylinder) will react to the changed flow conditions at the apex at a time  $\Delta t$  later. He also approximated that the disturbances originating at the apex of the model would propagate downstream with the free-stream velocity  $U_\infty$  which would give  $\Delta t = x/U_\infty$ . Using equations 6.11 and 6.12, the effective angle of attack at the apex of the model ( $x = 0.0$ ) can be obtained as:

$$\alpha_{effA} = \alpha - \dot{\alpha} \frac{x_{cg}}{U_\infty} \quad (6.13)$$

According to Ericsson's theory, the effective angle of attack  $\alpha_{eff}(x, t')$  determining the vortex characteristics at station  $x$  downstream of the apex, is

$$\alpha_{eff}(x, t') = \alpha_{effA}(0, t - \Delta t) \quad (6.14)$$

where  $\Delta t = x/U_\infty$ . By using the Taylor series expansion at  $t$  for the effective angle of attack at the apex and assuming small non-dimensional rotation rates,  $(\dot{\alpha}L/U_\infty) \ll 1$ , one can write

$$\alpha_{eff}(x, t') = \alpha_{effA}(t) - \Delta t \frac{\partial \alpha_{effA}}{\partial t} \quad (6.15)$$

which gives

$$\alpha_{eff} = \alpha - \dot{\alpha} \frac{x_{cg} + x}{U_\infty} \quad (6.16)$$

Using the definition given by the equation 6.11, we can obtain  $\Delta\alpha_{eff}$  from equation 6.16 as:

$$\Delta\alpha_{eff} = \dot{\alpha} \frac{x_{cg} + x}{U_\infty} \quad (6.17)$$

Equation 6.17 did approximate the lags in asymmetric vortex shedding on the pitching ogive cylinder successfully.

In this study,  $\Delta\alpha_{eff}$  has been calculated both from the barebody experimental results and equation 6.17 for four different  $x/L$  locations. Since the pitch rate has a constant value of  $78^\circ/s$ , the lag equation 6.17 gave constant  $\Delta\alpha_{eff}$  values for each  $x/L$  locations. For calculating  $\Delta\alpha_{eff}$  from the experimental results, certain number of unsteady separation locations  $\phi_{sep}$  and corresponding instantaneous pitch angles  $\alpha(t')$  have been selected from the data. Then the same  $\phi_{sep}$  values for the steady data and the corresponding steady pitch angles have been picked. For a specific  $\phi_{sep}$ , the difference between the instantaneous pitch angle and the steady pitch angle has been calculated as the effective angle of attack increment. The  $\Delta\alpha_{eff}$  results obtained from equation 6.17 and the experimental

data have been compared in figure 6.67. As can be seen from this figure, there is a significant difference between experimental  $\Delta\alpha_{eff}$  and the one calculated from equation 6.17. Especially for the stations  $x/L \geq 0.501$ , the magnitudes of the experimental  $\Delta\alpha_{eff}$  are twice as much higher than that of obtained by using the model equation 6.17. Also, although the pitch rate is constant, experimental  $\Delta\alpha_{eff}$  does change with the instantaneous pitch angle thus with the time. This comparison shows the difference between the lags in the unsteady crossflow separation over the model used in the present experiment and the flowfield associated with the asymmetric vortex shedding on the ogive cylinder. A more sophisticated time-lag modeling technique should be used in order resolve the complex nature of the time history effects on the unsteady cross flow separation locations.

### 6.3.2 First-Order Differential Time-Lag Model

Goman and Khrabrov [35] have developed a first order time lag model in order to approximate the time history of a dominant flow feature such as the separation location in general unsteady flows. They applied this model to pitching two-dimensional airfoils, delta wings and the unsteady aerodynamics of a complex fighter aircraft configuration as well. They used the separation location as an internal state variable, and defined the forces and moments as functions of this state variable. For a given maneuver, by obtaining the time history of this state variable, they were able to calculate the unsteady force and moments. This model mainly introduces a first-order delay differential equation for an internal state variable  $x$  which accounts for unsteady effects associated with separated and vortex flow. The variable  $x$  may represent the location of trailing edge flow separation on a pitching airfoil or that of vortex breakdown on a delta wing. The original form of the differential equation governing  $x$  is given by:

$$\tau_1 \frac{dx}{dt} + x = x_0 \left( \alpha - \tau_2 \frac{d\alpha}{dt} \right) \quad (6.18)$$

where  $\tau_1$  and  $\tau_2$  are time constants and  $x_0$  describes the steady dependency of  $x$  on  $\alpha$ . Goman and Khrabrov [35] defined  $\tau_2$  as a quasi-steady time delay associated with changes in circulation, boundary layer convection lags, and/or boundary layer improvement effects, while  $\tau_1$  as a relaxation time constant associated with global transient aerodynamic effects, or dynamic properties of the separated flow adjustment.

Wetzel and Simpson [3] implemented an extended version of this model for approximating

the time varying nature of the unsteady separation locations over the maneuvering prolate spheroid. The approximation successfully fit the experimental unsteady separation locations and non-dimensional time lag values for different  $x/L$  stations of the prolate spheroid. The same extended version of the first-order differential lag model has been used in this study in order to approximate the unsteady primary separation locations of the barebody and the non-sail region of the sail-on-side case:

$$\tau' \left( \frac{x}{L} \right) \frac{d\phi_{uns}}{dt'} + \phi_{uns} \left( \frac{x}{L}, t' \right) = \phi_0 \left( \frac{x}{L}, \alpha(t') \right) \quad (6.19)$$

In equation 6.19,  $\phi_{uns}$  represents the approximation to the unsteady separation location and  $\tau'$  stands for the first-order non-dimensional time lag. The  $\phi_0$  is the quasi-steady separation location distribution which can be obtained from the steady separation data at each  $\alpha = \alpha(t')$ . Note that both the quasi-steady separation location  $\phi_0$  and the approximation to the unsteady separation location  $\phi_{uns}$  do also vary with  $x/L$ . This is one of the differences between the extended version and the original time lag model of Goman & Khrabrov [35]. In the original version, a single point of separation was considered. However, for the present study and the prolate spheroid case, since the crossflow separation occurs along a line rather than a point,  $\phi_{uns}$  and  $\phi_0$  were also functions of  $x/L$ . It should also be noted that the time lag  $\tau'$  taken as an unknown in equation 6.19 is let to vary in  $x/L$  and identified by fitting the model equation with the experimental data.

The first-order differential equation 6.19 mainly correlates the unsteady separation locations to the quasi-steady data by the time lag  $\tau'$ . Note that if we solve equation 6.19 at a constant  $x/L$  location, the only dependent variable would be the non-dimensional time  $t'$ . Then the solution to this initial value problem can be obtained by first taking the Laplace transform of each side:

$$\tau' [s\phi_{uns}(s) - \phi_{uns}(0)] + \phi_{uns}(s) = \phi_0(s) \quad (6.20)$$

After rearranging the above equation, we obtain:

$$\phi_{uns}(s) = \frac{\phi_{uns}(0)}{s + \frac{1}{\tau'}} + \frac{1}{\tau'} \left( \frac{\phi_0(s)}{s + \frac{1}{\tau'}} \right) \quad (6.21)$$

Now if we take the inverse Laplace transform of each side of equation 6.21, we can get the final expression for  $\phi_{uns}(t')$  as:

$$\phi_{uns}(t') = e^{-t'/\tau'} \left[ \phi_{uns}(0) + \frac{1}{\tau'} \int_0^{t'} \phi_0(\beta) e^{\beta/\tau'} d\beta \right] \quad (6.22)$$

In the solution procedure, the quasi-steady separation distribution  $\phi_0$  was obtained by fitting a cubic spline to the steady data. The independent variable was  $t'$  in the fitting procedure. As the initial value for  $\phi_{uns}$ , the first steady separation location in the steady data was used. Since equation 6.22 represents the solution to an initial value problem, the determination of the initial value for  $\phi_{uns}$  and thus the first steady separation location is important. However, in terms of getting the right time lag value, the choice of the initial value does not have a crucial role. As long as the pitch rate  $\dot{\alpha}$  is constant, the same time lag will be obtained even if the initial value is slightly different than the true value and the uncertainty in the initial value will only effect the initial transient part. The integral on the right hand side of the equation 6.22 was evaluated numerically for each  $t'$  value by using the trapezoidal approximation. For each  $x/L$  station, the model equation 6.22 was solved with different values of the  $\tau'$  in an iterative manner. The root mean square error between the approximated and experimental unsteady data was calculated at each iteration and the  $\tau'$  that gave the smallest error had been chosen for that specific  $x/L$  location.

The solid lines in figures 6.40 through 6.59 show the results of the time lag model approximation to the unsteady data at ten  $x/L$  locations for the barebody and the non-sail region of the sail-on-side case. Note that all the stations were not used in calculating the time lags. At the stations  $x/L \leq 0.266$ , no unsteady separation location at any instant of time was observed. At the last station  $x/L = 0.863$ , the determination of the unsteady separation location was not accurate enough because of the flat nature of the  $C_f$  profile near the minimum. For the rest of the stations, the first-order lag model approximation fits the measured unsteady separation locations reasonably well. In these graphs, for some of the  $x/L$  locations, the last value of the unsteady and the steady separation locations are slightly different although they should be the same ideally. However, the differences are within the uncertainty of separation locations that is  $\pm 2^\circ$ . The model fit results show that the first-order differential lag model of Goman and Khrabrov does capture the time-varying nature of the unsteady crossflow separation locations reasonably and may be used as part of the unsteady aerodynamic models used to describe the physics of such flows.

Since the unsteady separation locations do not follow the quasi-steady separation data with a time lag, a first-order lag model approximation to the unsteady data of the sail side cannot be obtained. The physical model given by the differential equation 6.19 does

not describe the unsteady separation phenomena of the sail side. In order to approximate the sail side unsteady separation pattern, a more complicated physical model should be developed.

### Time lags

The time lag values  $\tau'$  obtained from the first-order differential lag model equation fits for different  $x/L$  locations are shown in figure 6.68. In this figure, circles represent the time lags of the barebody case, and the triangles stand for the results of the non-sail region of the sail-on-side case. For the barebody case, near the model rotation point  $x_{cg}/L = 0.24$ , the time lag value is close to zero indicating that the quasi-steady data follows the unsteady data closely. Then an increase until  $x/L = 0.434$  can be seen. Since there are not enough points in this region, the nature of this increase (linear or non-linear) cannot be determined accurately. After this point, the time lag stays approximately constant between  $x/L = 0.434$  and  $x/L = 0.774$ , taking an average value of 1.40. At  $x/L = 0.819$ , this value drops to 1.24. The non-dimensional time lag  $\tau'$  vs.  $x/L$  distribution of the non-sail region shows a similar trend as the one obtained for the barebody case. However, at the first two stations, the time lag values are considerable higher than the barebody values. For the other stations, time lags are approximately constant with an average value of 1.50.

Both the barebody and the non-sail region  $\tau'$  vs  $x/L$  distributions are different from the one obtained for the prolate spheroid by Wetzel and Simpson [3]. In that case,  $\tau'$  changed approximately in a linear manner increasing in downstream direction over the prolate spheroid model. By making a linear fit to the time lag data and using the Ericsson's  $\Delta\alpha_{eff}$  approach (see equation 6.17) with an unknown convection velocity  $U_c$  for the propagation speed of the disturbances, Wetzel and Simpson [3] were able to determine that the disturbances propagate with a convection velocity of  $U_c \simeq 0.3 \times U_\infty$ . It should be noted that, for the prolate spheroid pitch-up maneuvers, the model center of rotation point was at  $x/L = 0.5$ , whereas in this study the rotation point is at  $x/L = 0.24$ . Also the Suboff model has a different geometry than the prolate spheroid, having a large proportion of a constant diameter region. Therefore, one may expect an influence of the rotation point and the model geometry on the time lags. However further study has to be done in order investigate the true complex nature of the time lags associated with the



unsteady flow field over this undersea vehicle geometry.

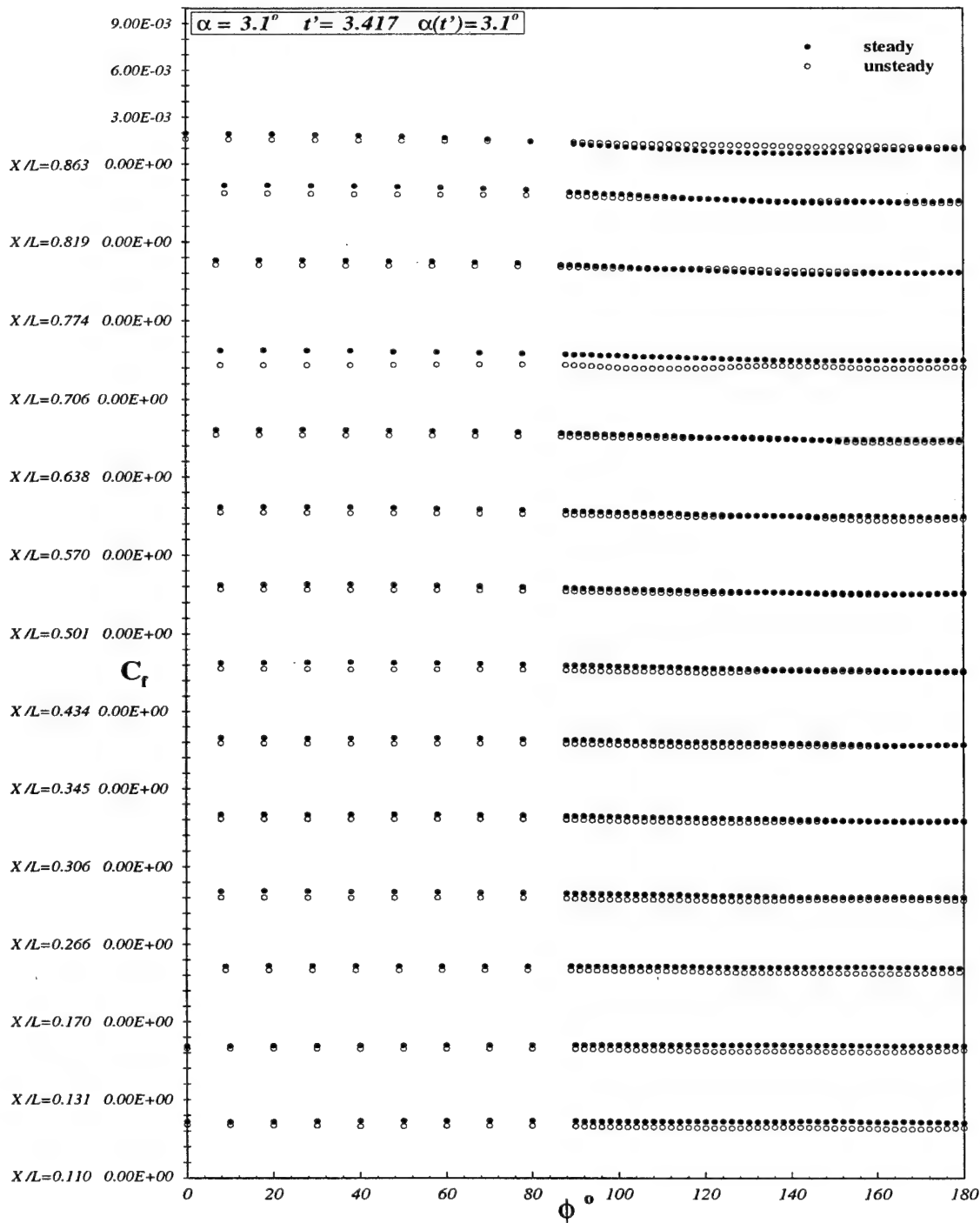


Figure 6.1: Comparison of barebody  $C_f$  vs.  $\phi$  distribution for steady and unsteady data at all  $x/L$  locations.  $\alpha = 3.1^\circ$ ,  $t' = 3.417$ ,  $\alpha(t') = 3.1^\circ$ .

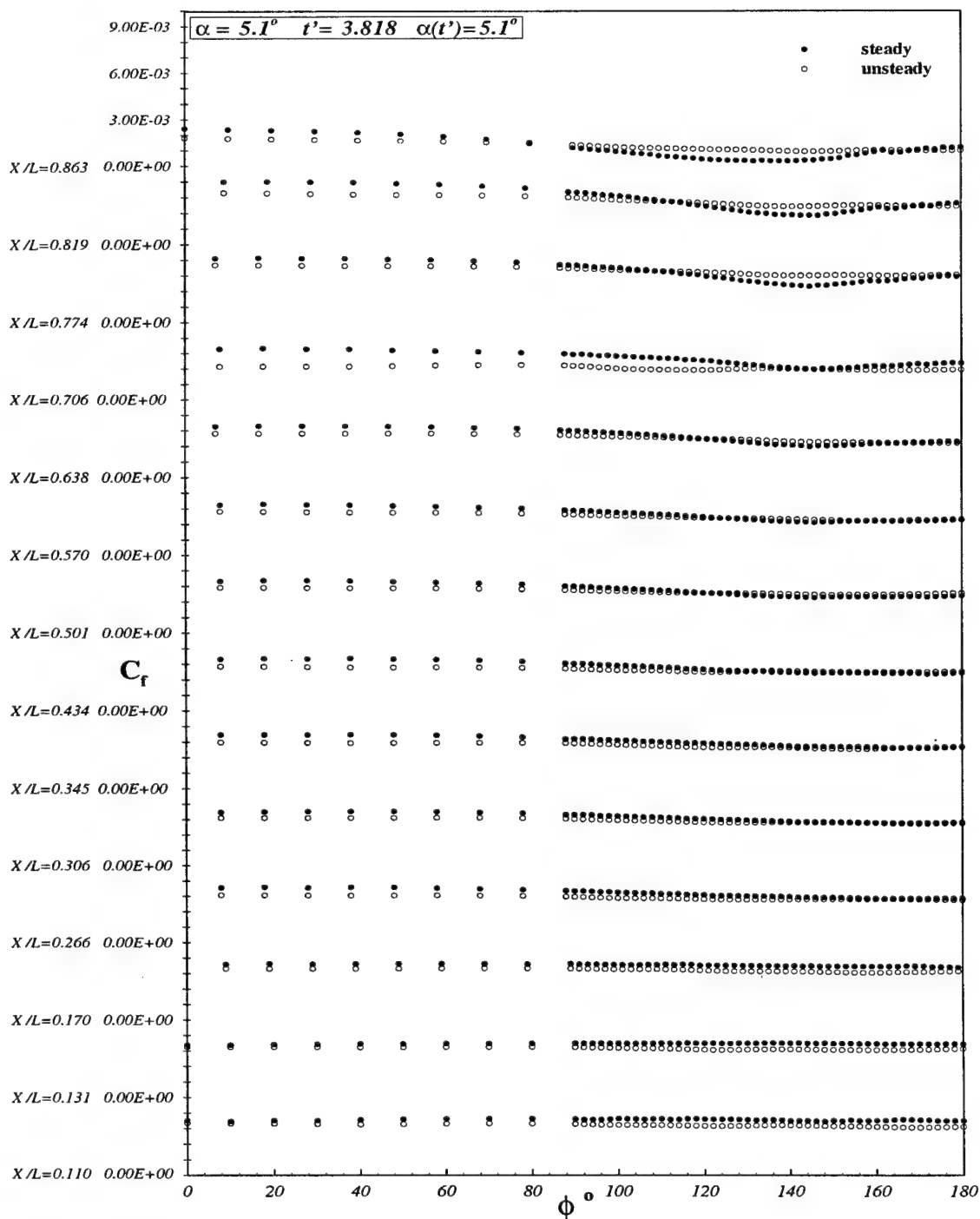


Figure 6.2: Comparison of barebody  $C_f$  vs.  $\phi$  distribution for steady and unsteady data at all  $x/L$  locations.  $\alpha = 5.1^\circ$ ,  $t' = 3.818$ ,  $\alpha(t') = 5.1^\circ$ .

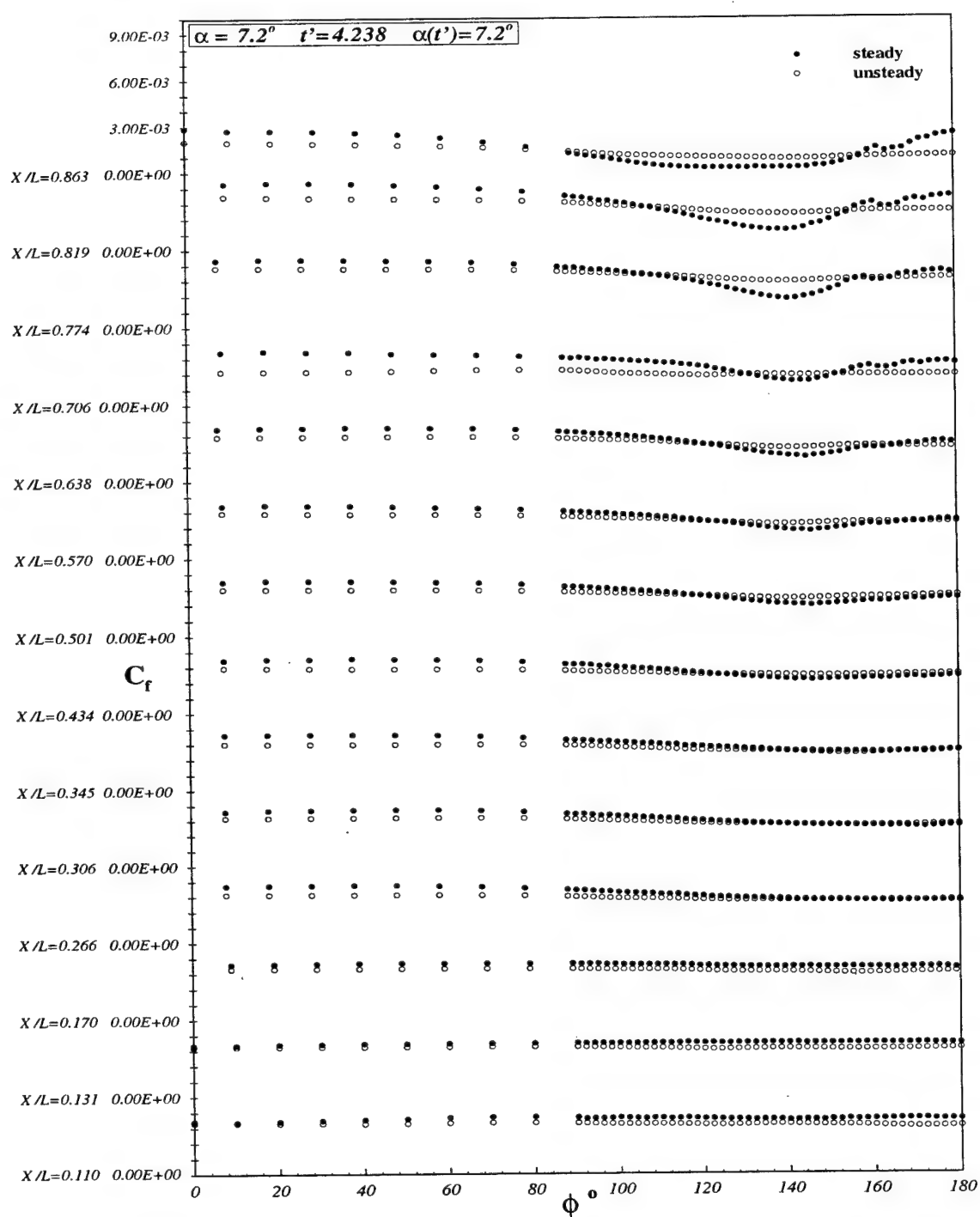


Figure 6.3: Comparison of barebody  $C_f$  vs.  $\phi$  distribution for steady and unsteady data at all  $x/L$  locations.  $\alpha = 7.2^\circ$ ,  $t' = 4.238$ ,  $\alpha(t') = 7.2^\circ$ .

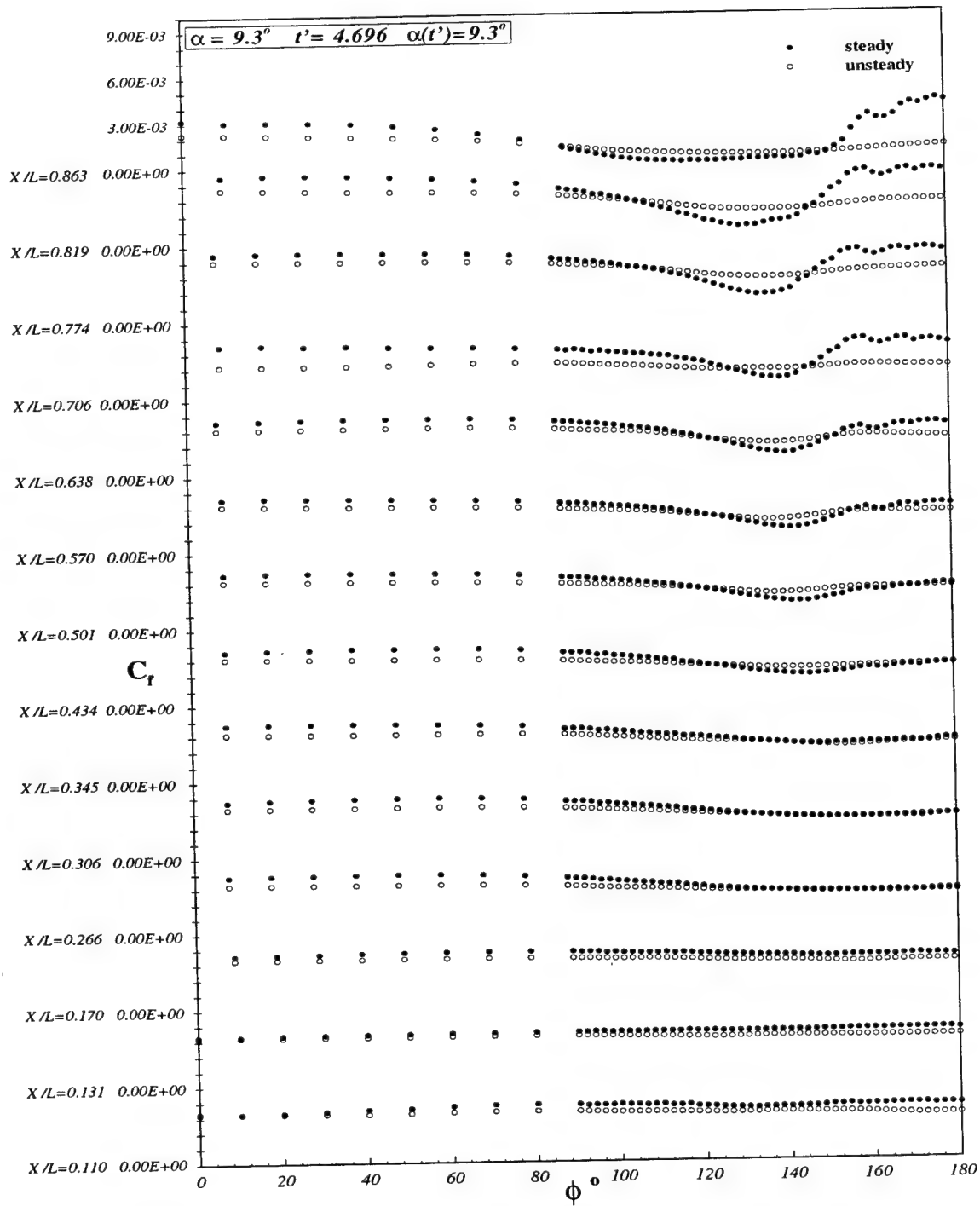


Figure 6.4: Comparison of barebody  $C_f$  vs.  $\phi$  distribution for steady and unsteady data at all  $x/L$  locations.  $\alpha = 9.3^\circ$ ,  $t' = 4.696$ ,  $\alpha(t') = 9.3^\circ$ .

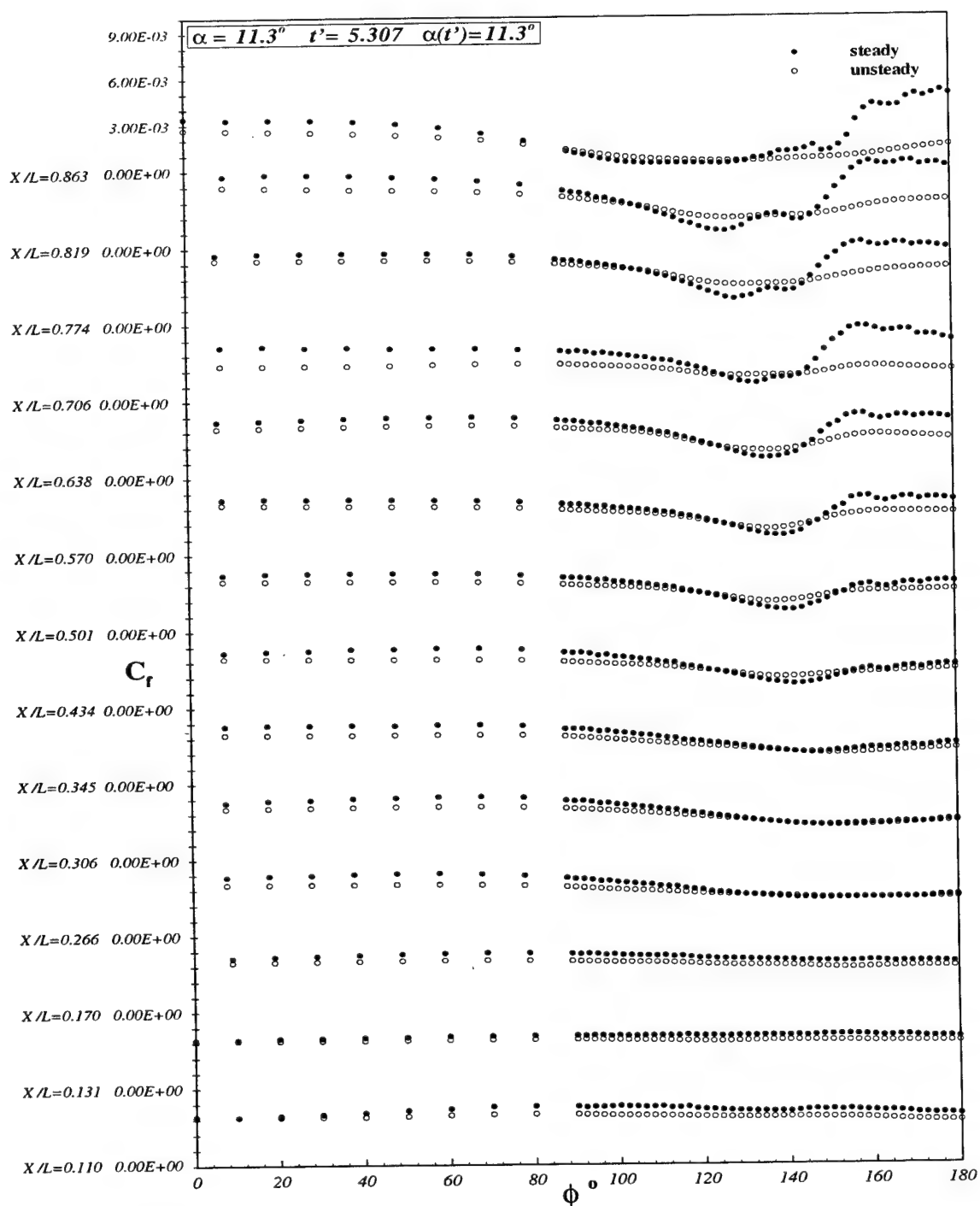


Figure 6.5: Comparison of barebody  $C_f$  vs.  $\phi$  distribution for steady and unsteady data at all  $x/L$  locations.  $\alpha = 11.3^\circ$ ,  $t' = 5.307$ ,  $\alpha(t') = 11.3^\circ$ .

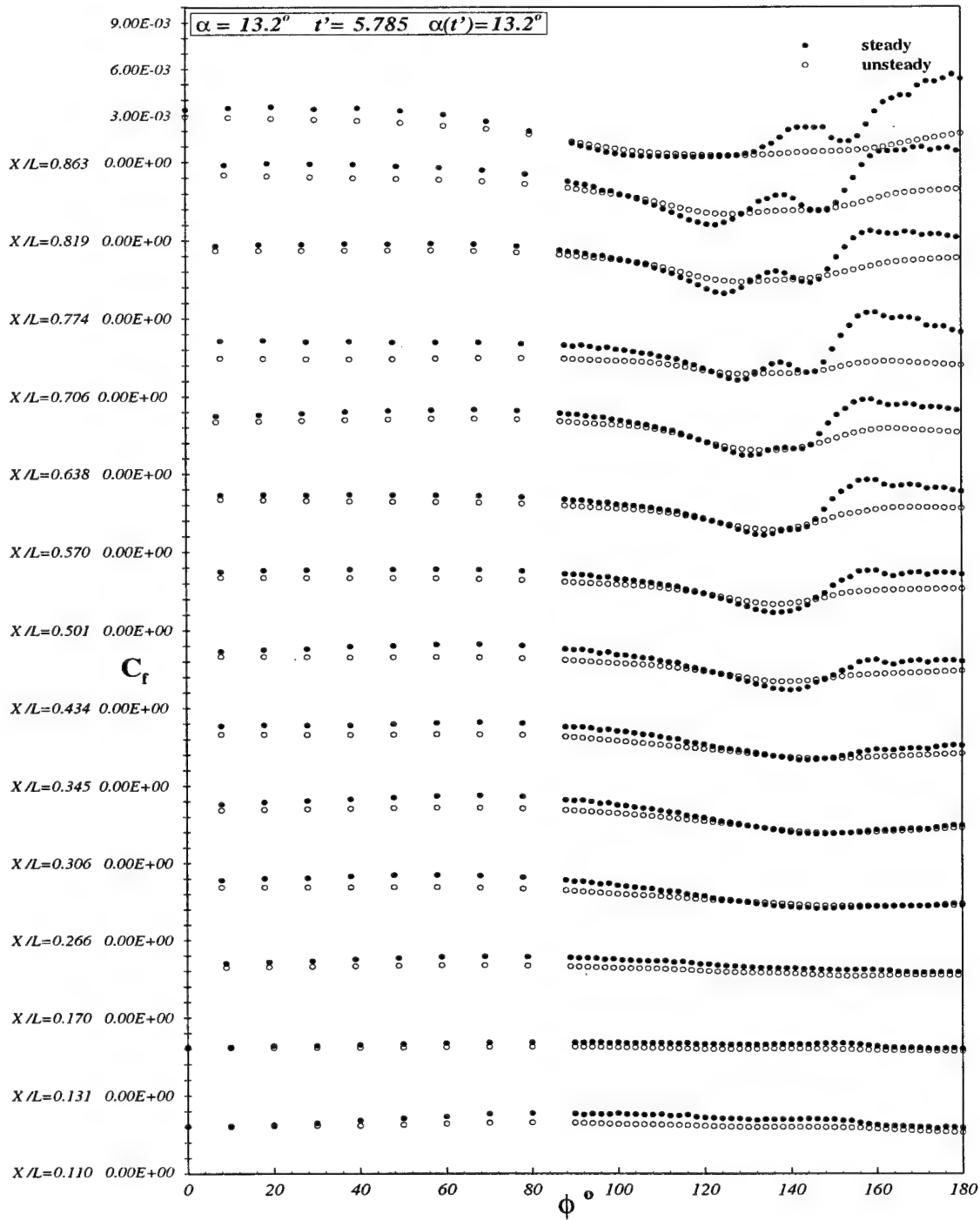


Figure 6.6: Comparison of barebody  $C_f$  vs.  $\phi$  distribution for steady and unsteady data at all  $x/L$  locations.  $\alpha = 13.2^\circ$ ,  $t' = 5.785$ ,  $\alpha(t') = 13.2^\circ$ .

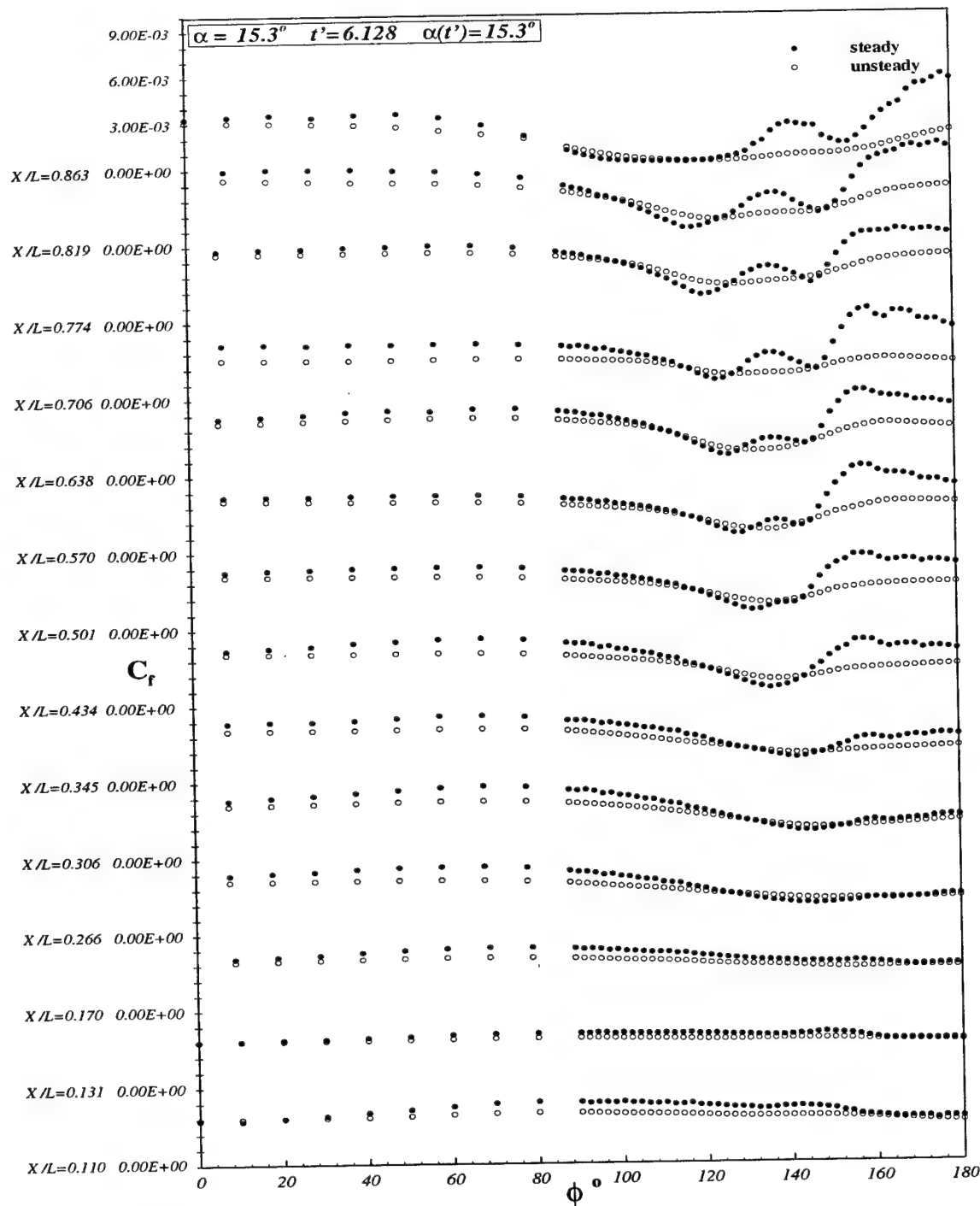


Figure 6.7: Comparison of barebody  $C_f$  vs.  $\phi$  distribution for steady and unsteady data at all  $x/L$  locations.  $\alpha = 15.3^\circ$ ,  $t' = 6.128$ ,  $\alpha(t') = 15.3^\circ$ .



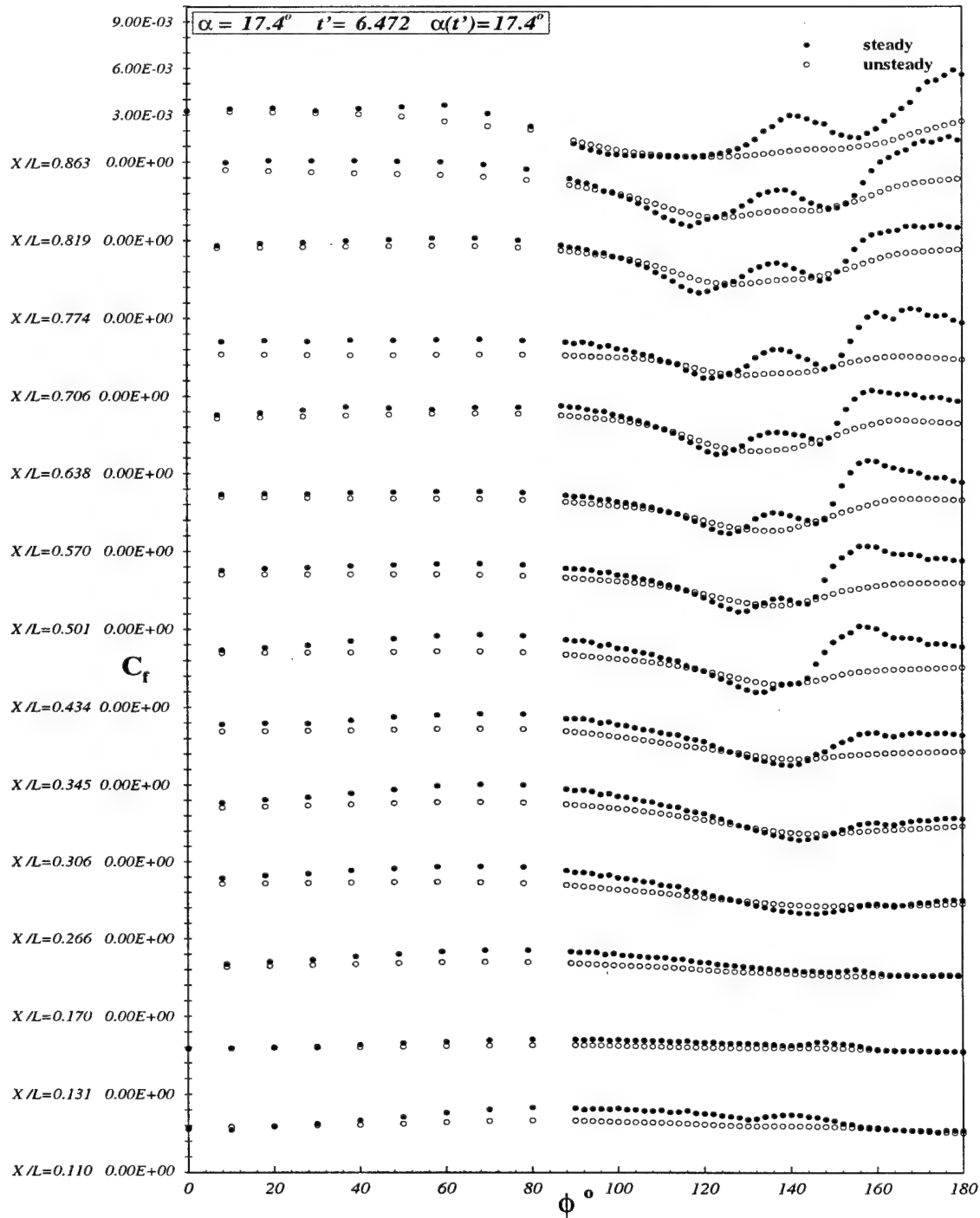


Figure 6.8: Comparison of barebody  $C_f$  vs.  $\phi$  distribution for steady and unsteady data at all  $x/L$  locations.  $\alpha = 17.4^\circ$ ,  $t' = 6.472$ ,  $\alpha(t') = 17.4^\circ$ .

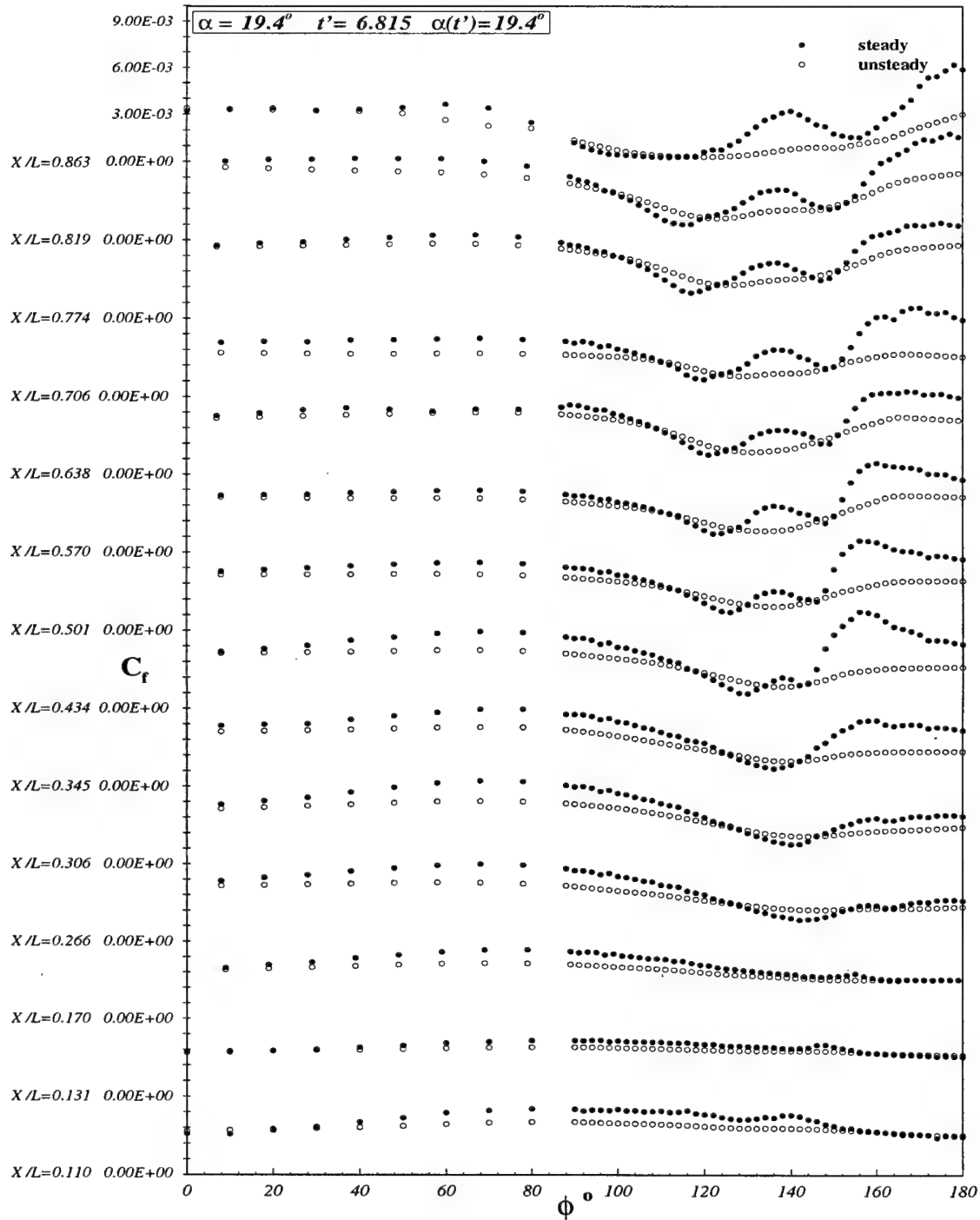


Figure 6.9: Comparison of barebody  $C_f$  vs.  $\phi$  distribution for steady and unsteady data at all  $x/L$  locations.  $\alpha = 19.4^\circ$ ,  $t' = 6.815$ ,  $\alpha(t') = 19.4^\circ$ .

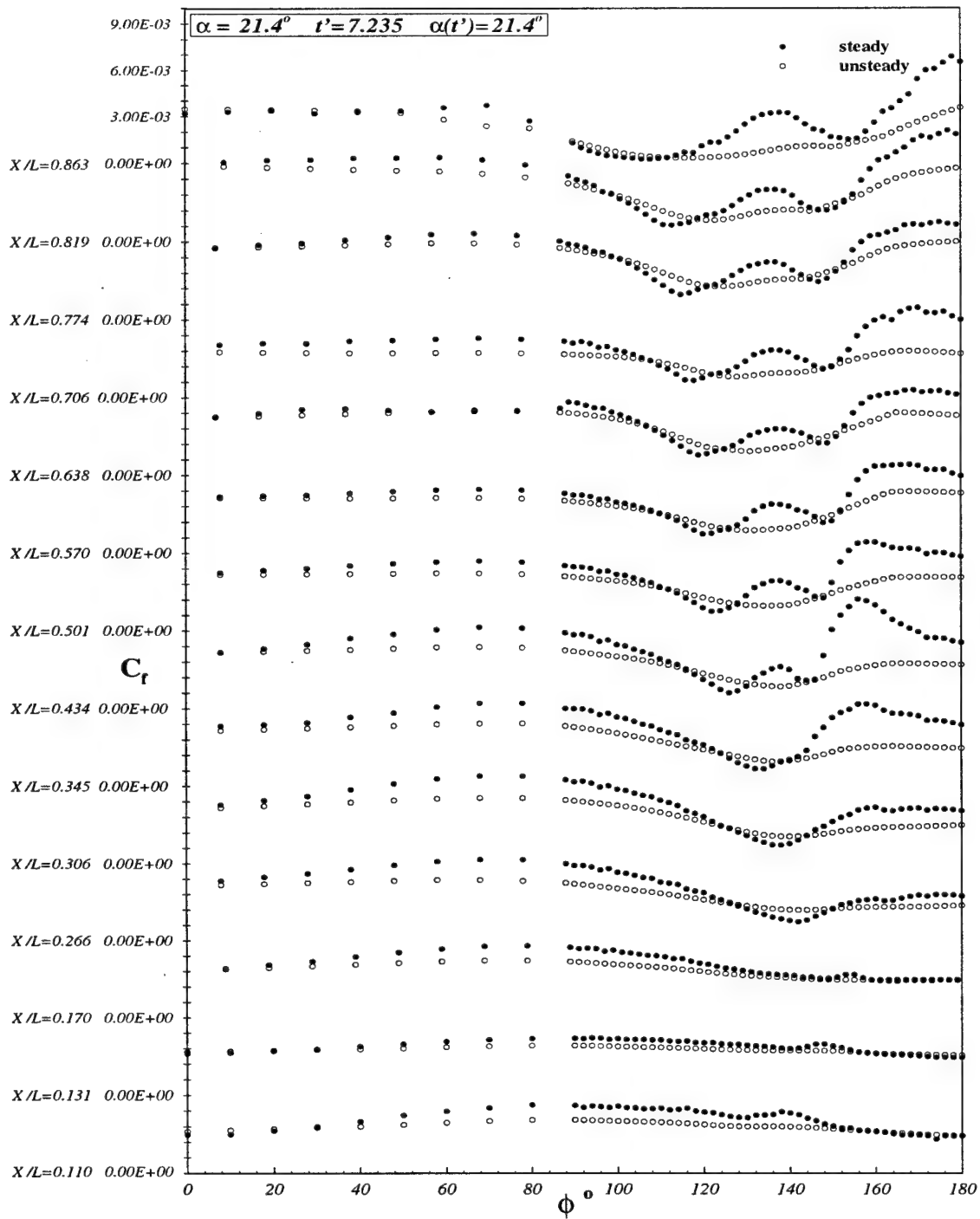


Figure 6.10: Comparison of barebody  $C_f$  vs.  $\phi$  distribution for steady and unsteady data at all  $x/L$  locations.  $\alpha = 21.4^\circ$ ,  $t' = 7.235$ ,  $\alpha(t') = 21.4^\circ$ .

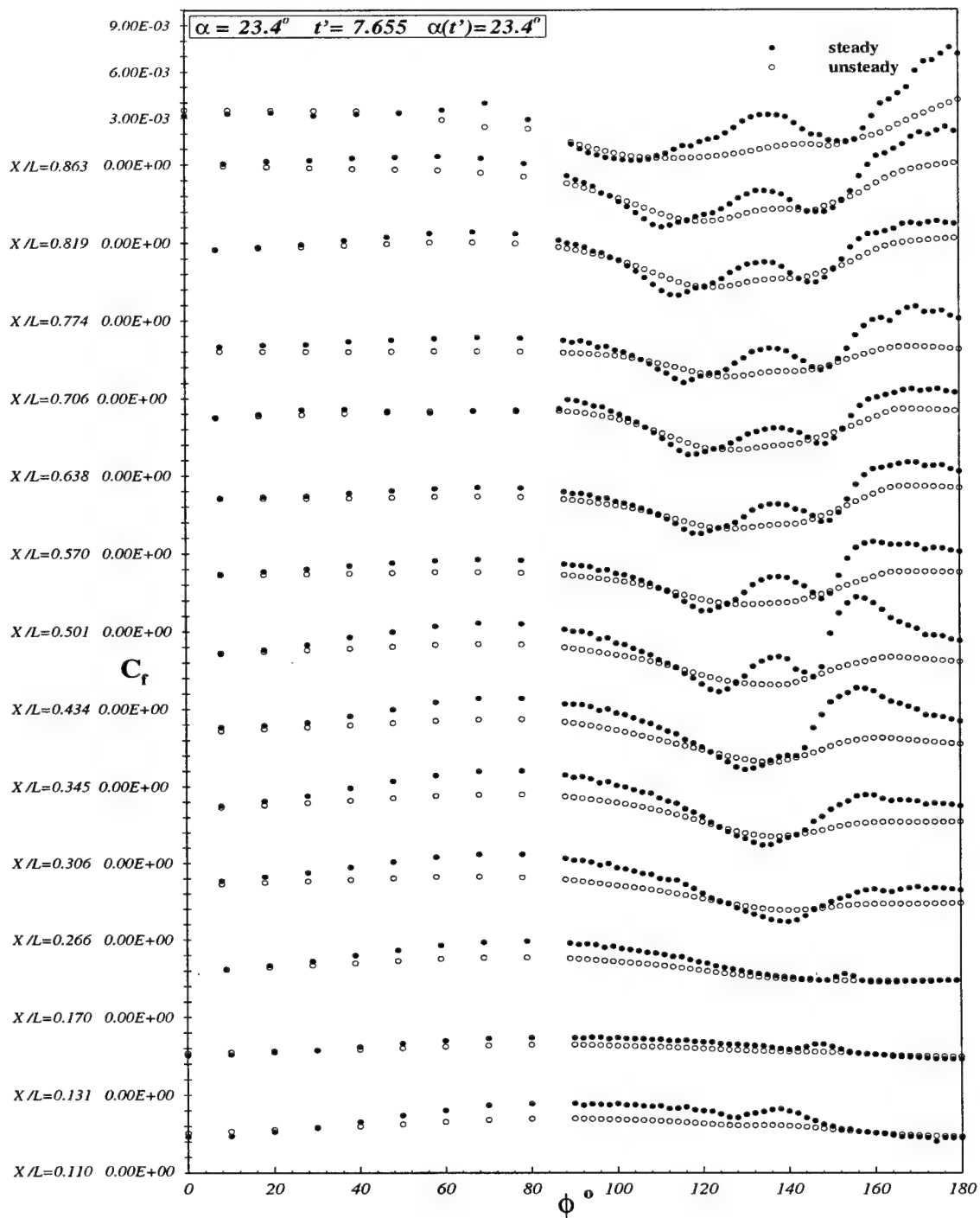


Figure 6.11: Comparison of barebody  $C_f$  vs.  $\phi$  distribution for steady and unsteady data at all  $x/L$  locations.  $\alpha = 23.4^\circ$ ,  $t' = 7.655$ ,  $\alpha(t') = 23.4^\circ$ .

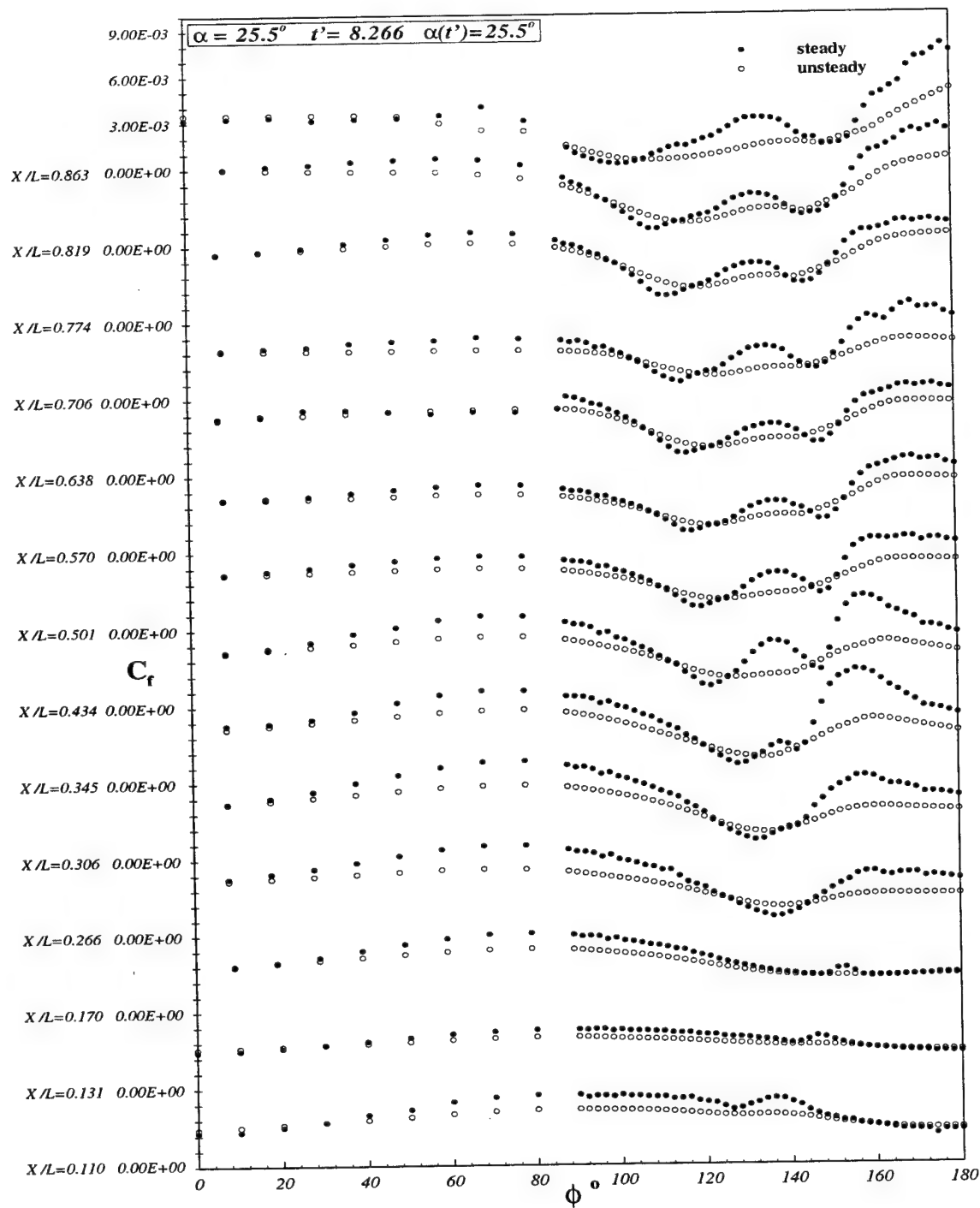


Figure 6.12: Comparison of barebody  $C_f$  vs.  $\phi$  distribution for steady and unsteady data at all  $x/L$  locations.  $\alpha = 25.5^\circ$ ,  $t' = 8.175$ ,  $\alpha(t') = 25.5^\circ$ .

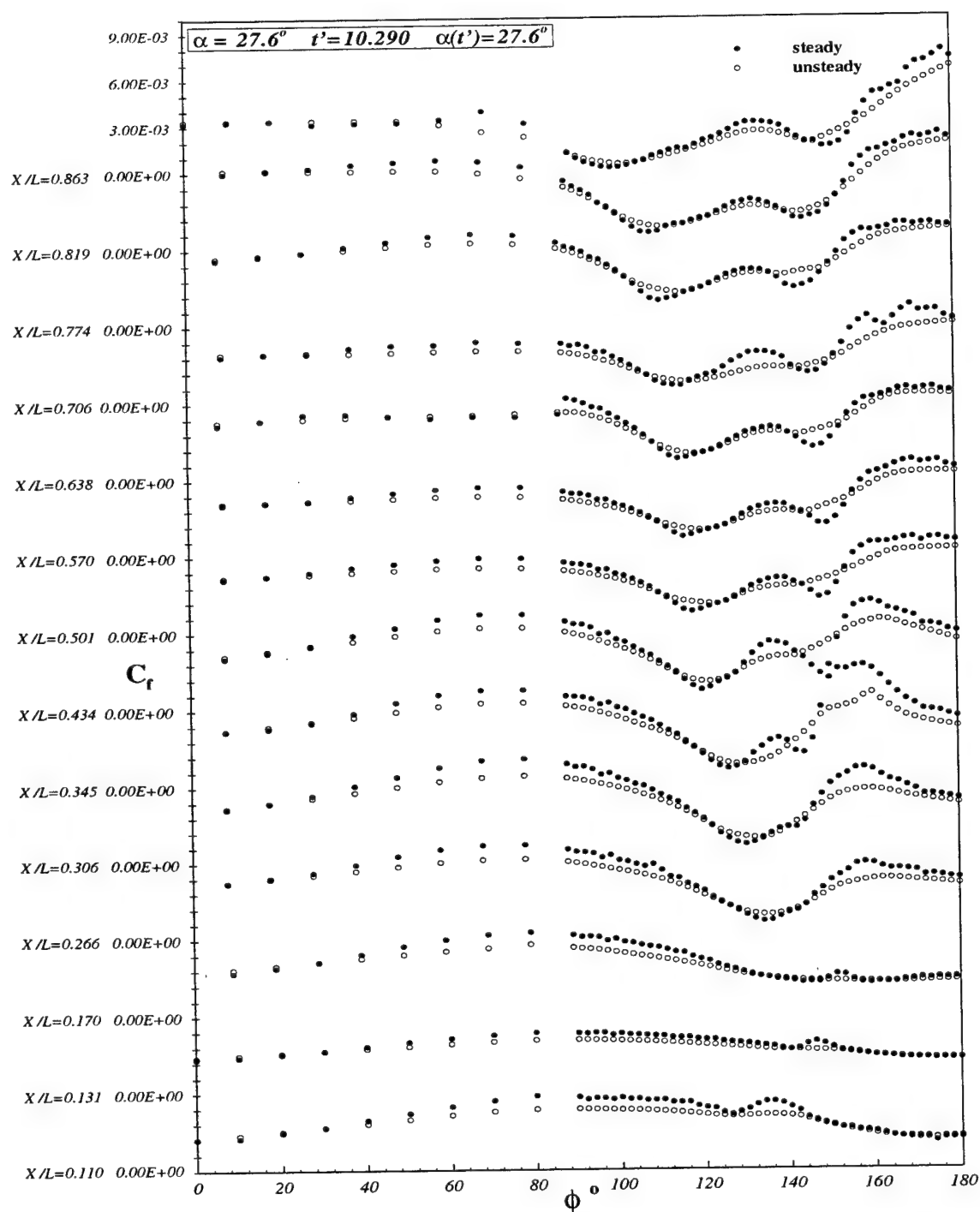


Figure 6.13: Comparison of barebody  $C_f$  vs.  $\phi$  distribution for steady and unsteady data at all  $x/L$  locations.  $\alpha = 27.6^\circ$ ,  $t' = 10.290$ ,  $\alpha(t') = 27.6^\circ$ .

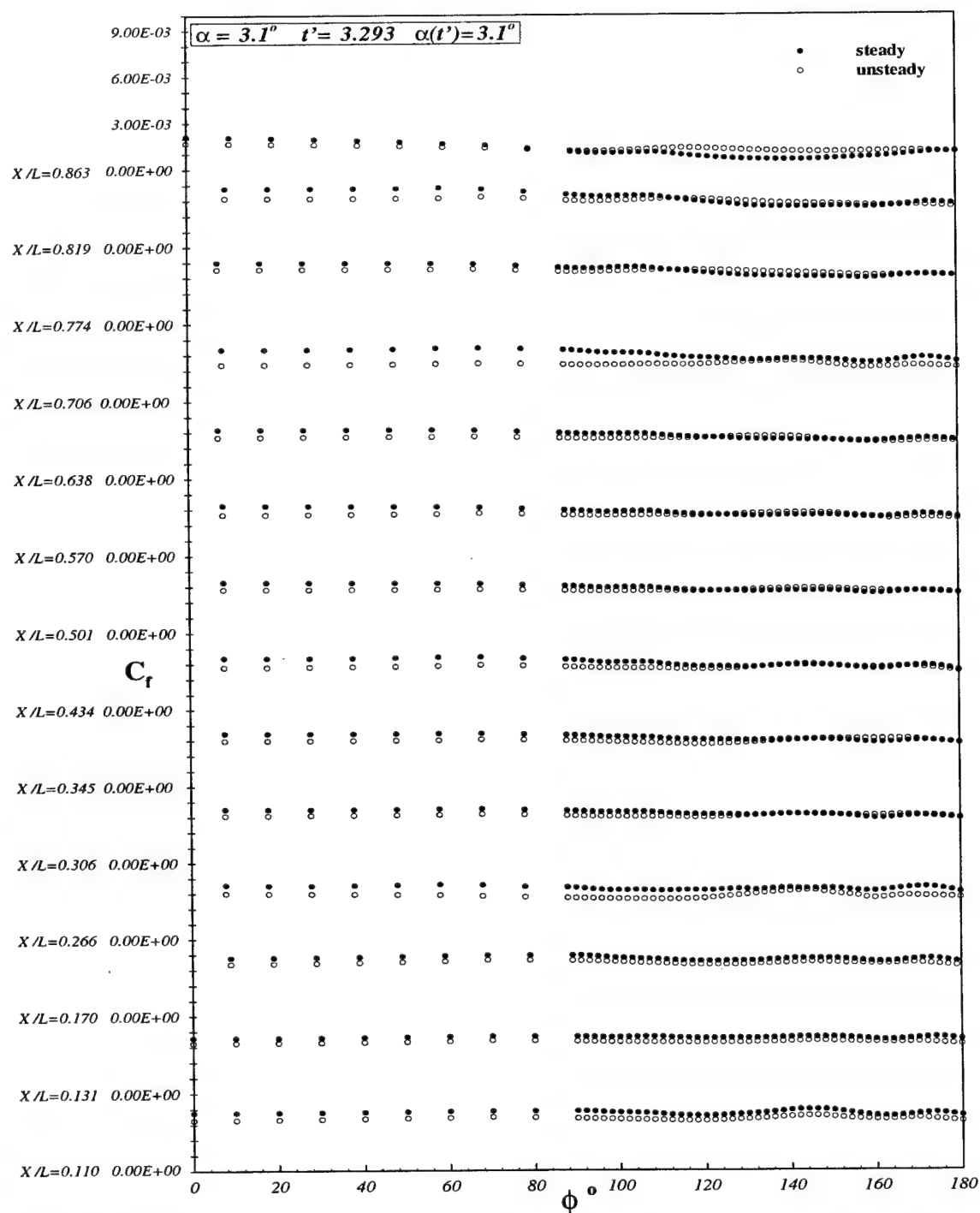


Figure 6.14: Comparison of sail-on-side (region without the sail)  $C_f$  vs.  $\phi$  distribution for steady and unsteady data at all  $x/L$  locations.  $\alpha = 3.1^\circ$ ,  $t' = 3.293$ ,  $\alpha(t') = 3.1^\circ$ .

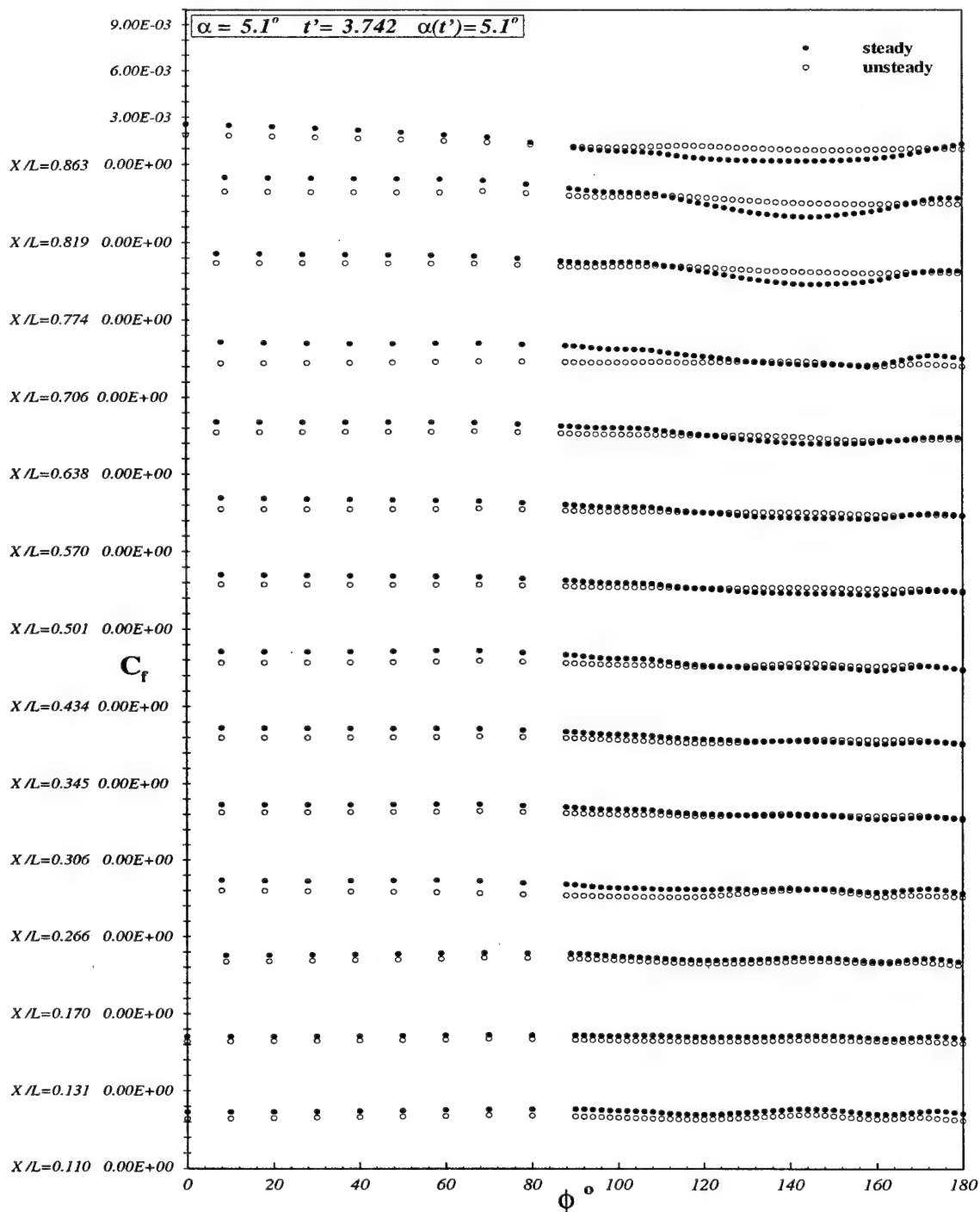


Figure 6.15: Comparison of sail-on-side (region without the sail)  $C_f$  vs.  $\phi$  distribution for steady and unsteady data at all  $x/L$  locations.  $\alpha = 5.1^\circ$ ,  $t' = 3.742$ ,  $\alpha(t') = 5.1^\circ$ .



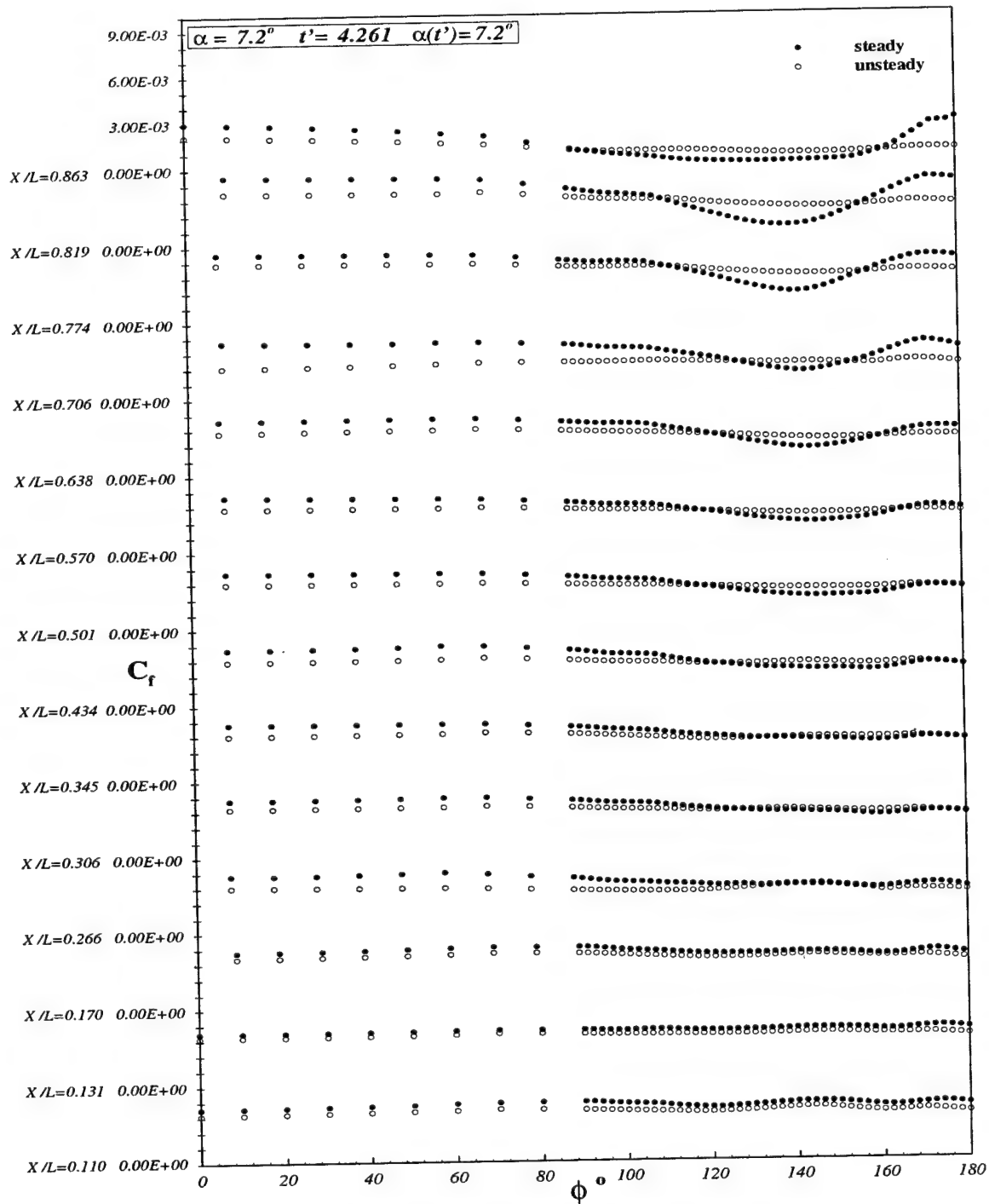


Figure 6.16: Comparison of sail-on-side (region without the sail)  $C_f$  vs.  $\phi$  distribution for steady and unsteady data at all  $x/L$  locations.  $\alpha = 7.2^\circ$ ,  $t' = 4.261$ ,  $\alpha(t') = 7.2^\circ$ .

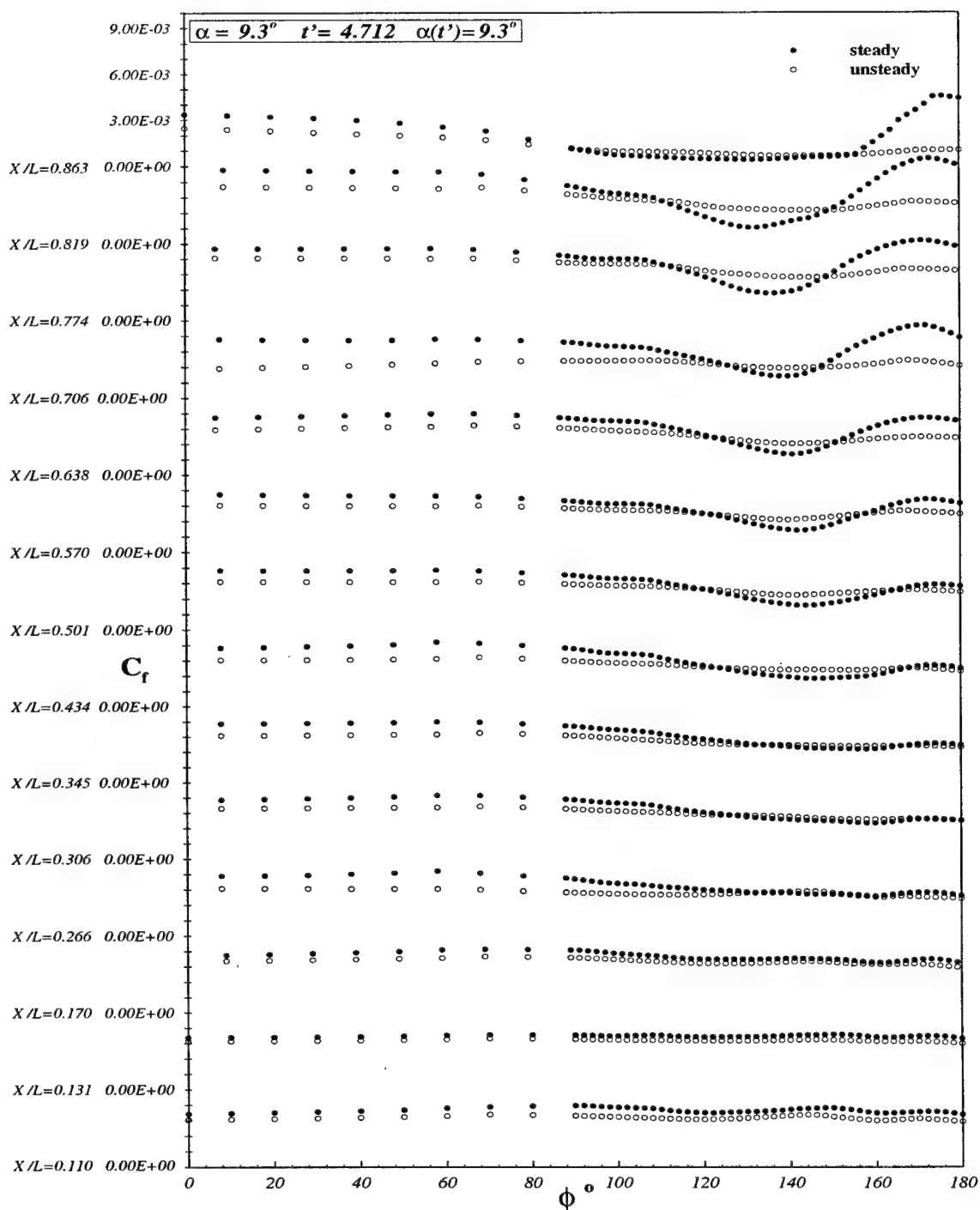


Figure 6.17: Comparison of sail-on-side (region without the sail)  $C_f$  vs.  $\phi$  distribution for steady and unsteady data at all  $x/L$  locations.  $\alpha = 9.3^\circ$ ,  $t' = 4.7123$ ,  $\alpha(t') = 9.3^\circ$ .

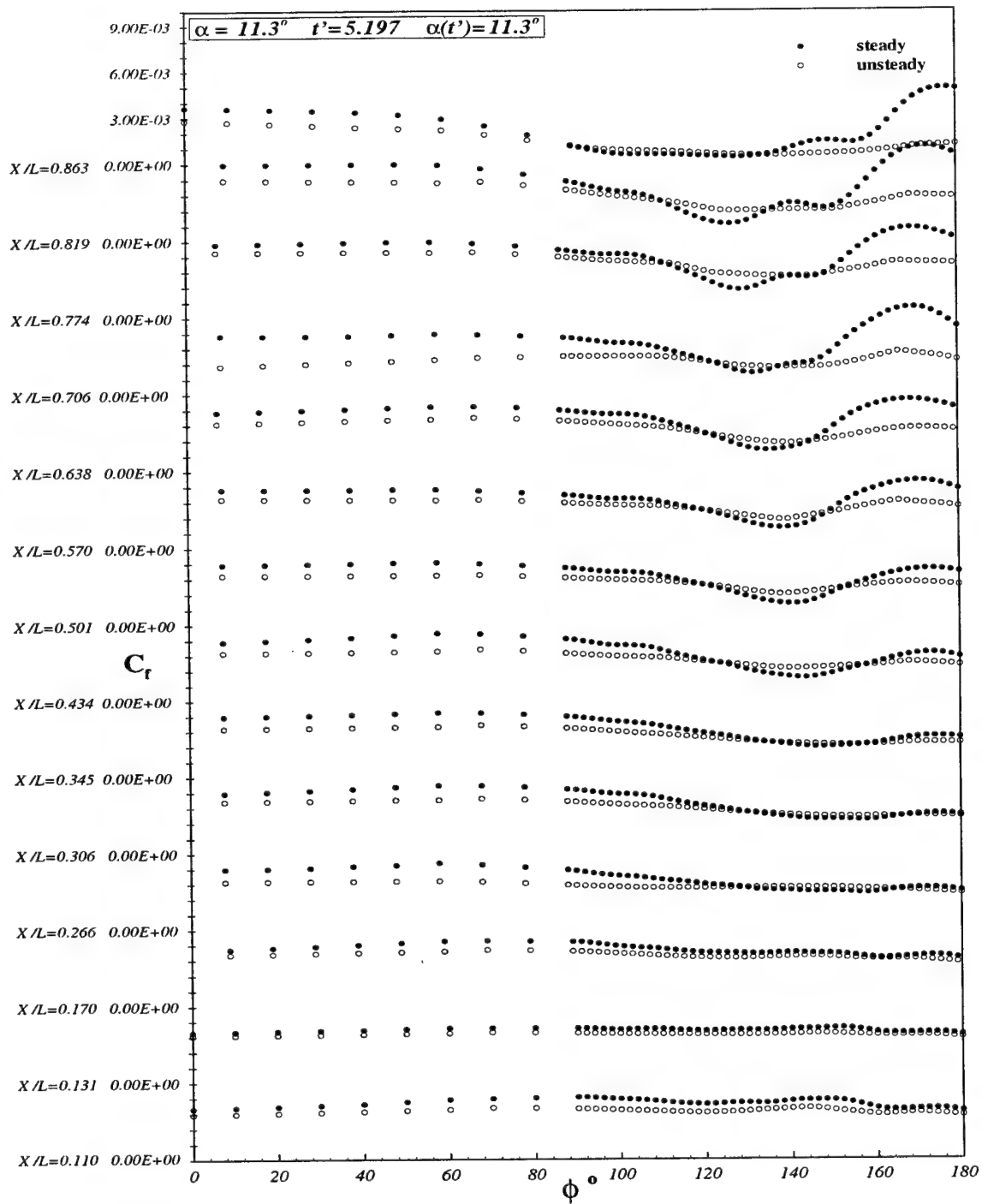


Figure 6.18: Comparison of sail-on-side (region without the sail)  $C_f$  vs.  $\phi$  distribution for steady and unsteady data at all  $x/L$  locations.  $\alpha = 11.3^\circ$ ,  $t' = 5.197$ ,  $\alpha(t') = 11.3^\circ$ .

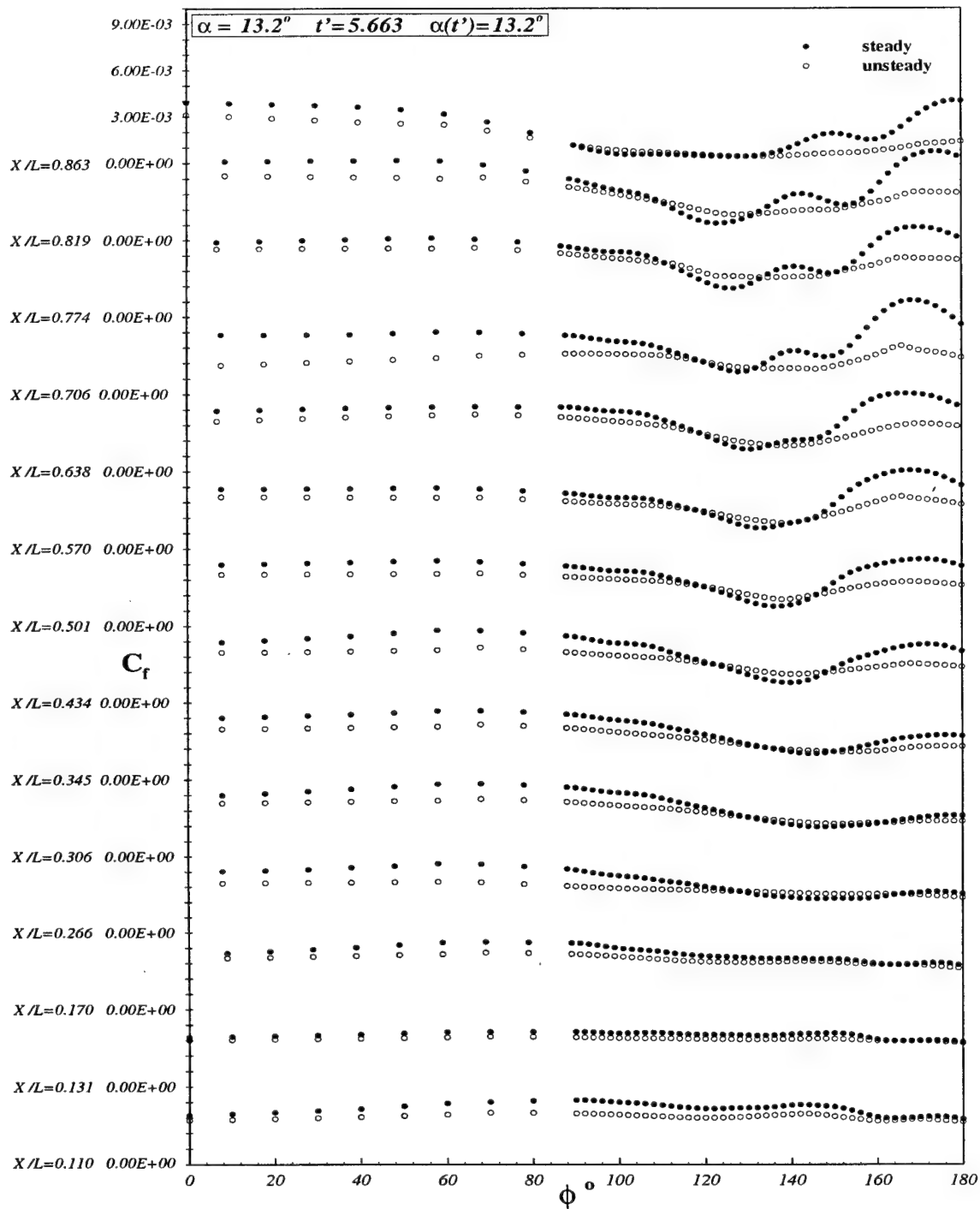


Figure 6.19: Comparison of sail-on-side (region without the sail)  $C_f$  vs.  $\phi$  distribution for steady and unsteady data at all  $x/L$  locations.  $\alpha = 13.2^\circ$ ,  $t' = 5.663$ ,  $\alpha(t') = 13.2^\circ$ .

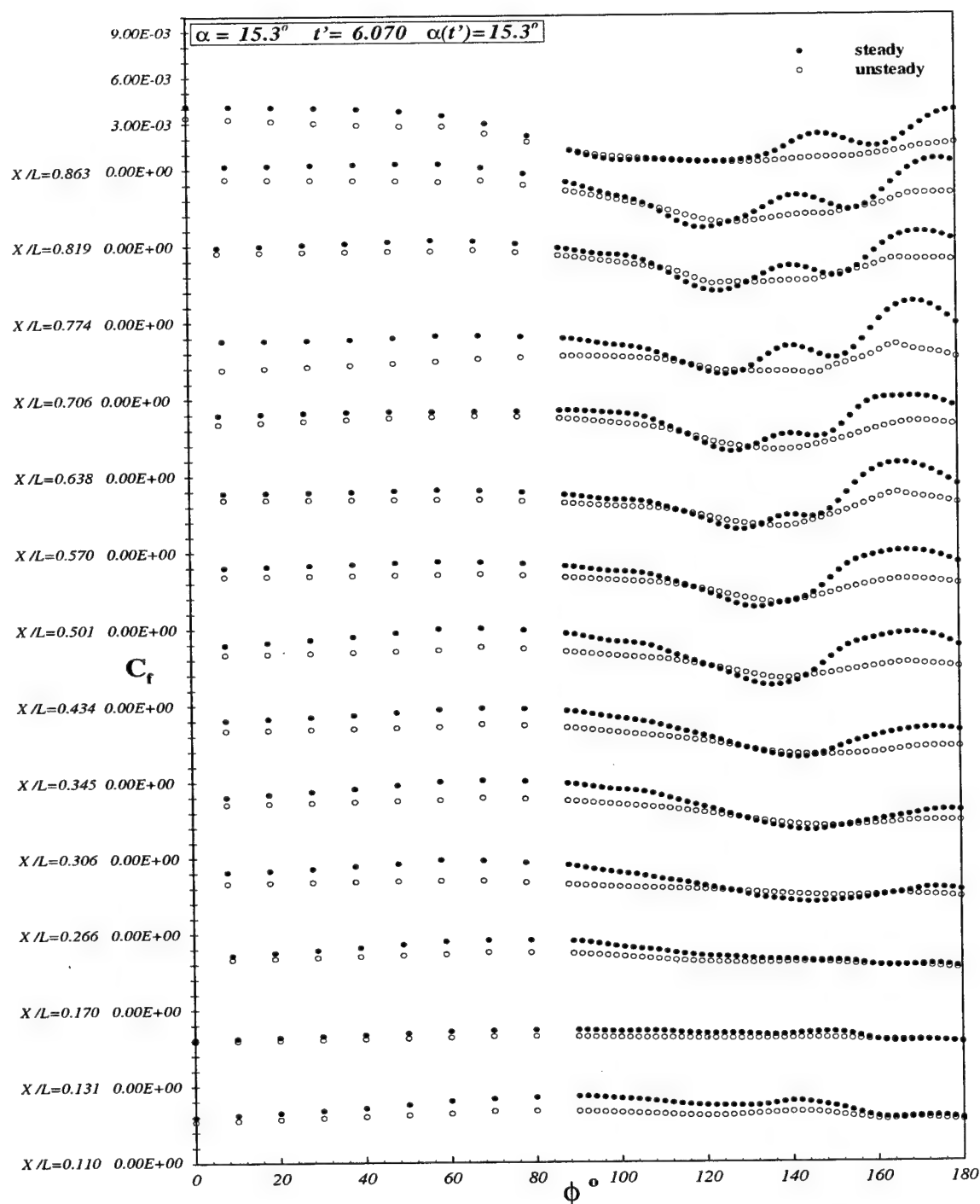


Figure 6.20: Comparison of sail-on-side (region without the sail)  $C_f$  vs.  $\phi$  distribution for steady and unsteady data at all  $x/L$  locations.  $\alpha = 15.3^\circ$ ,  $t' = 6.070$ ,  $\alpha(t') = 15.3^\circ$ .

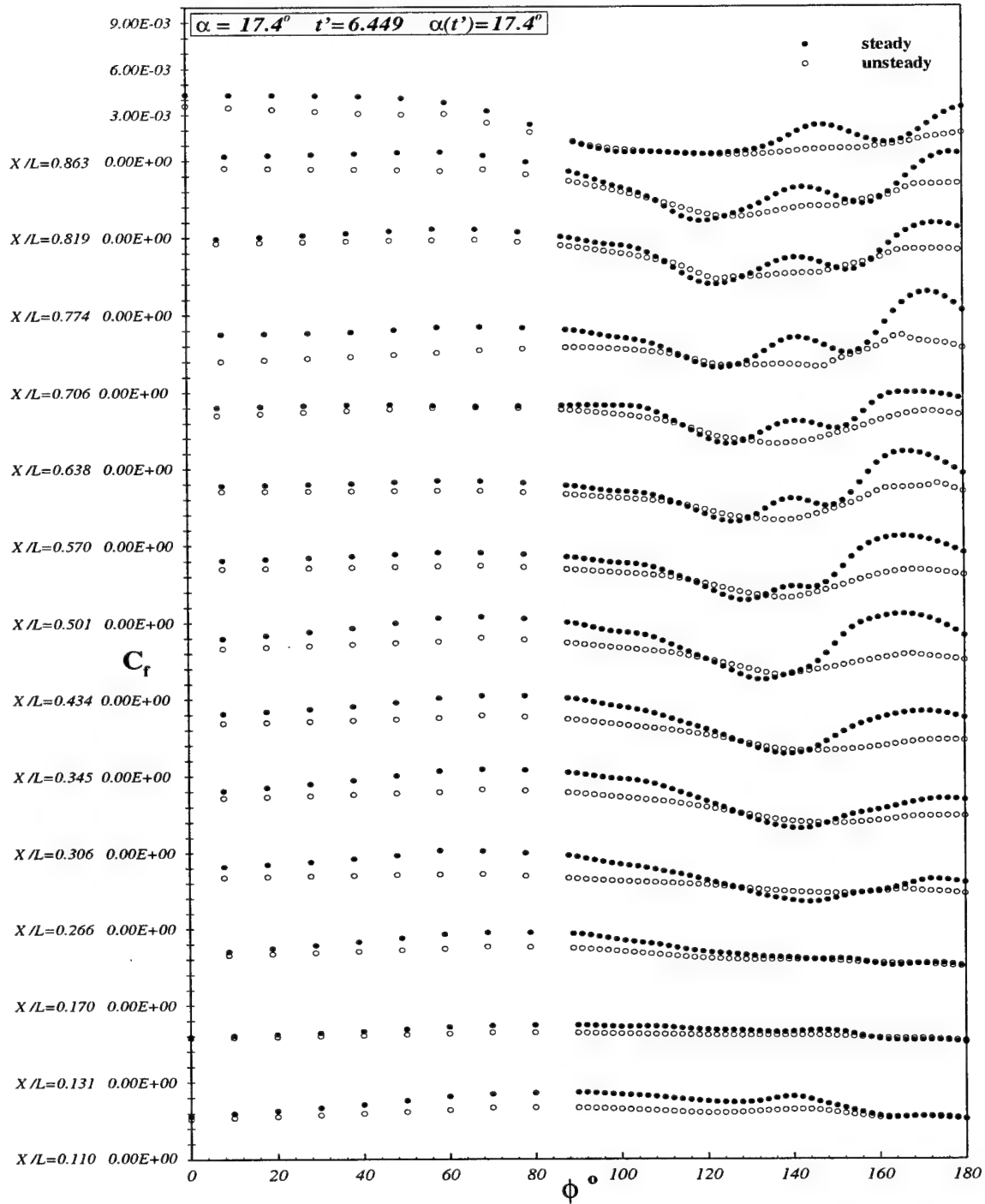


Figure 6.21: Comparison of sail-on-side (region without the sail)  $C_f$  vs.  $\phi$  distribution for steady and unsteady data at all  $x/L$  locations.  $\alpha = 17.4^\circ$ ,  $t' = 6.449$ ,  $\alpha(t') = 17.4^\circ$ .

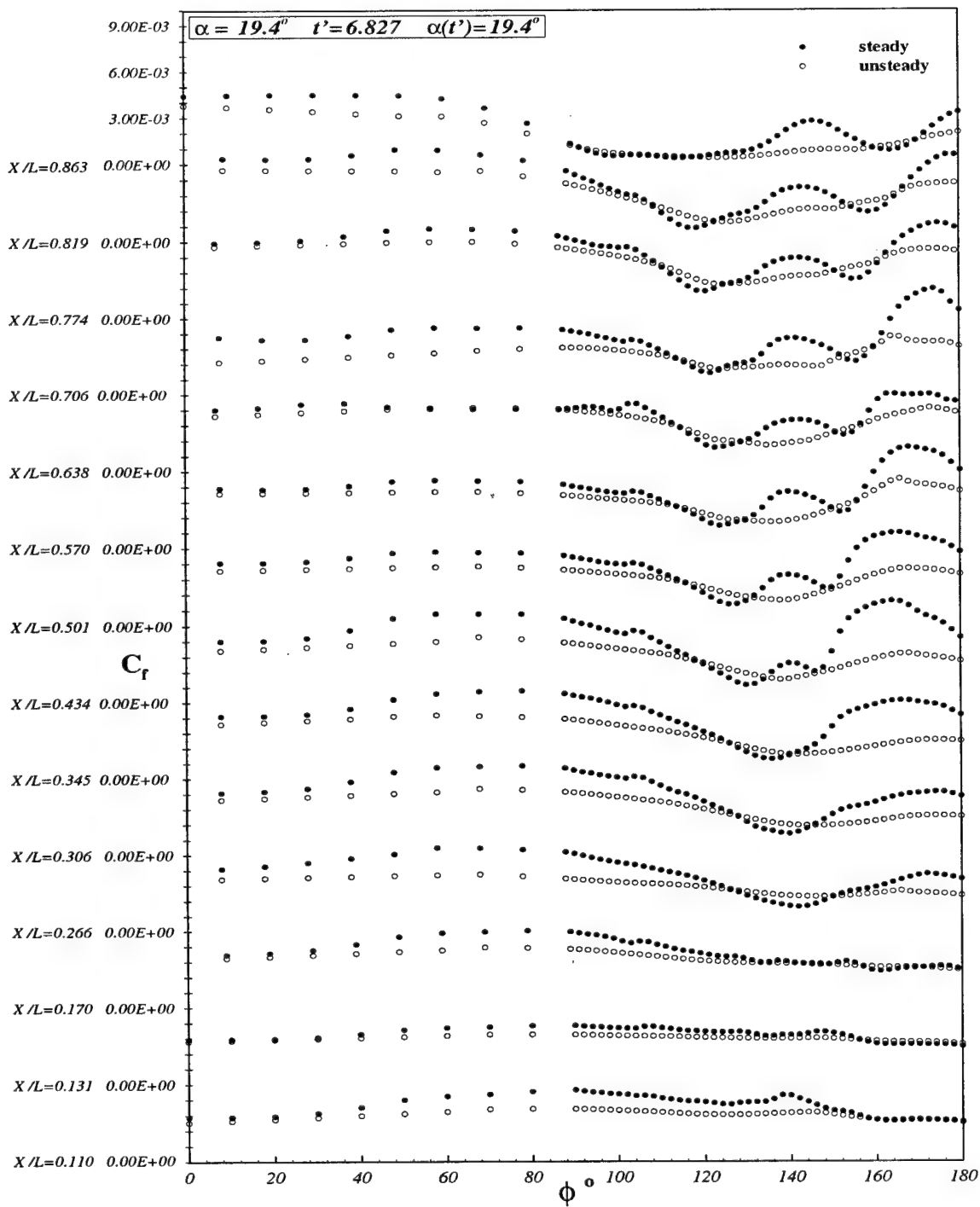


Figure 6.22: Comparison of sail-on-side (region without the sail)  $C_f$  vs.  $\phi$  distribution for steady and unsteady data at all  $x/L$  locations.  $\alpha = 19.4^\circ$ ,  $t' = 6.827$ ,  $\alpha(t') = 19.4^\circ$ .

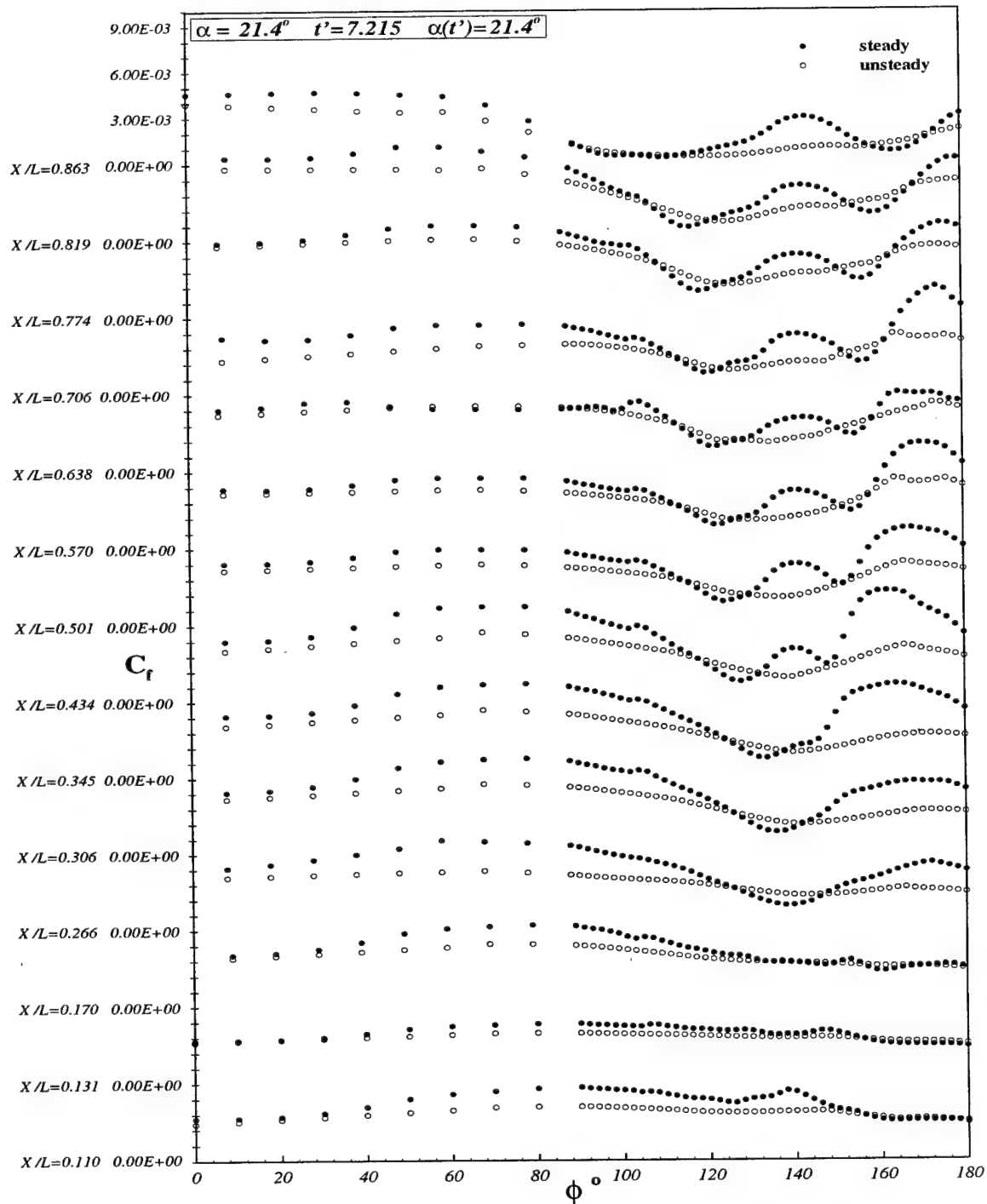


Figure 6.23: Comparison of sail-on-side (region without the sail)  $C_f$  vs.  $\phi$  distribution for steady and unsteady data at all  $x/L$  locations.  $\alpha = 21.4^\circ$ ,  $t' = 7.215$ ,  $\alpha(t') = 21.4^\circ$ .



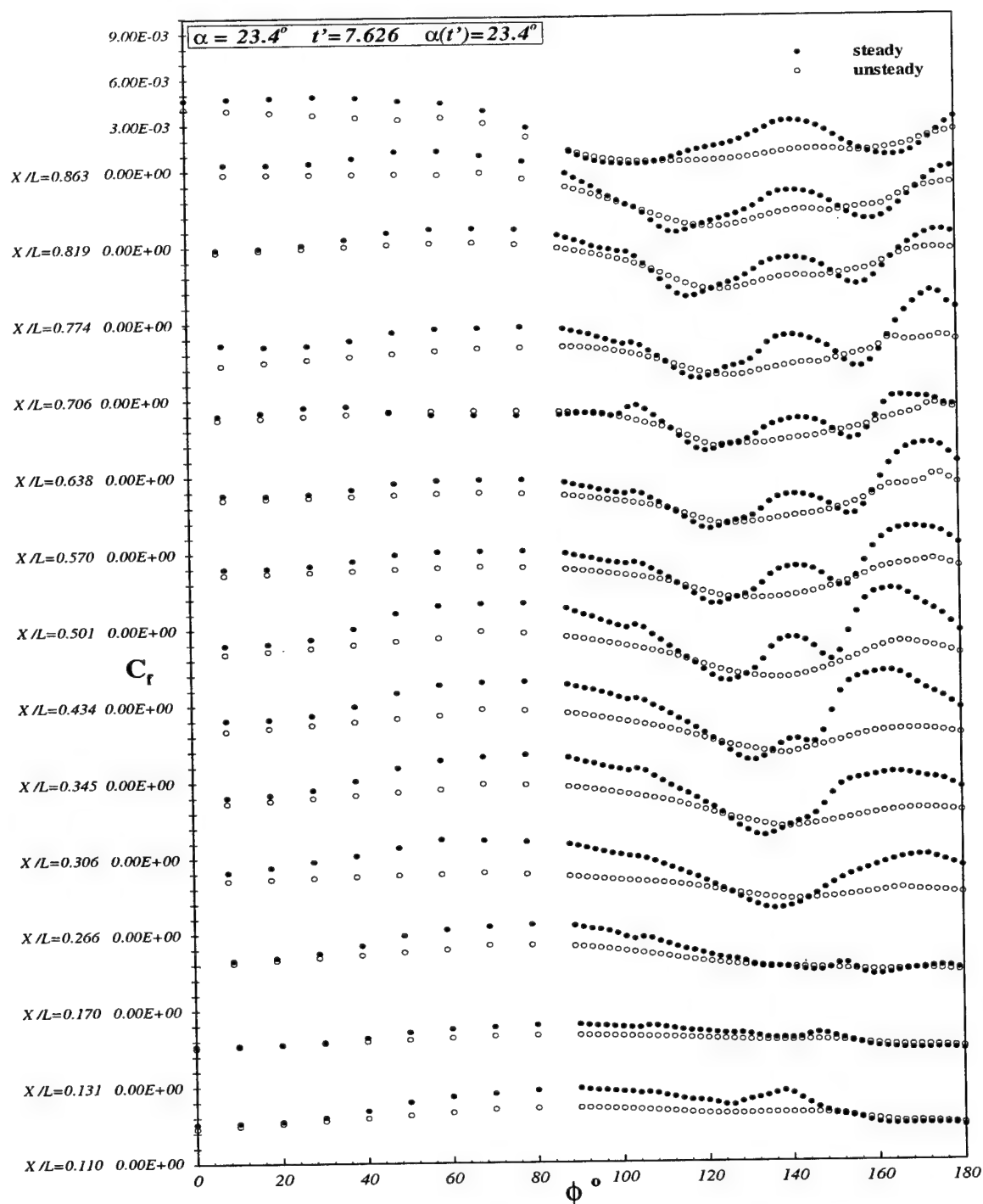


Figure 6.24: Comparison of sail-on-side (region without the sail)  $C_f$  vs.  $\phi$  distribution for steady and unsteady data at all  $x/L$  locations.  $\alpha = 23.4^\circ$ ,  $t' = 7.626$ ,  $\alpha(t') = 23.4^\circ$ .

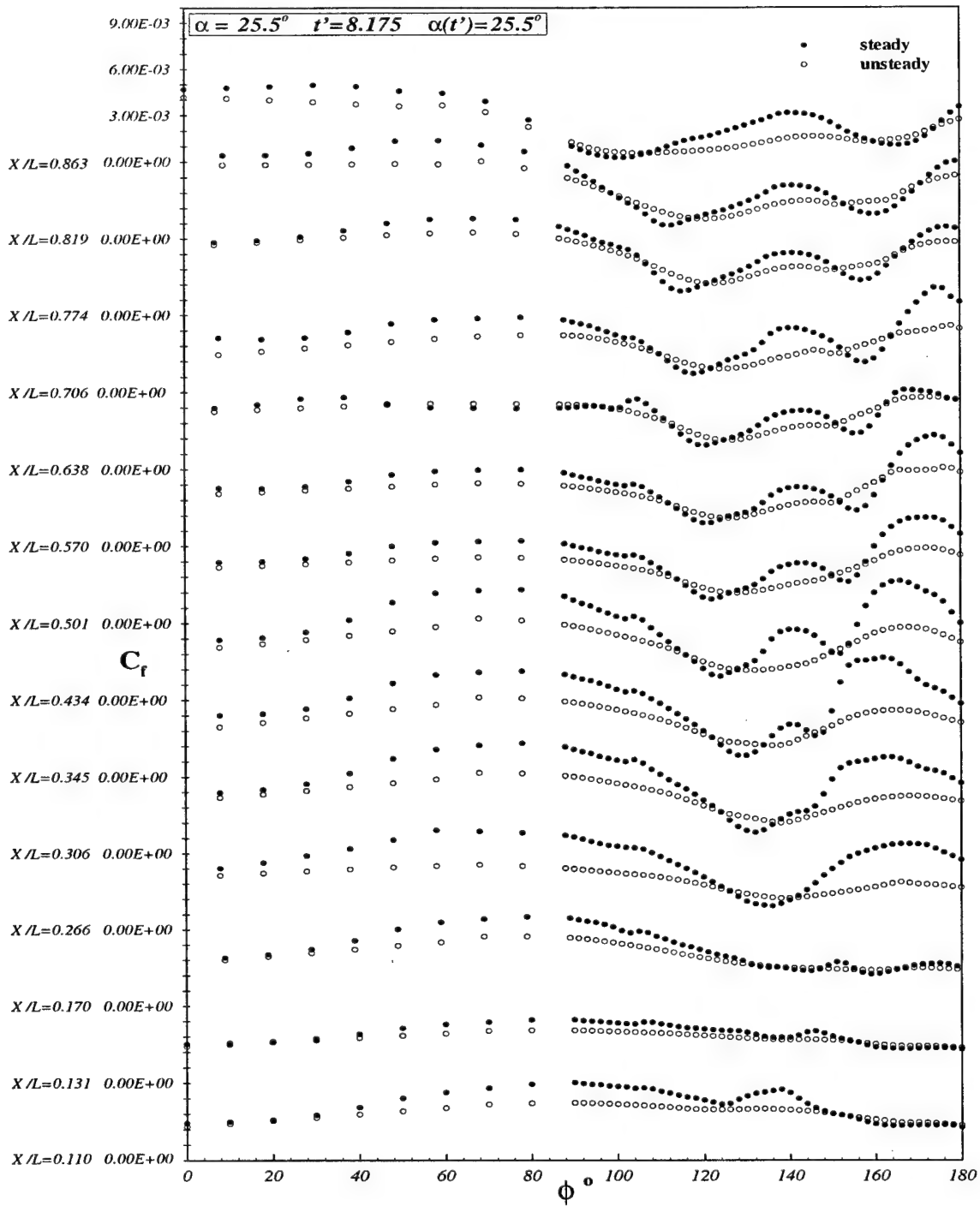


Figure 6.25: Comparison of sail-on-side (region without the sail)  $C_f$  vs.  $\phi$  distribution for steady and unsteady data at all  $x/L$  locations.  $\alpha = 25.5^\circ$ ,  $t' = 8.266$ ,  $\alpha(t') = 25.5^\circ$ .

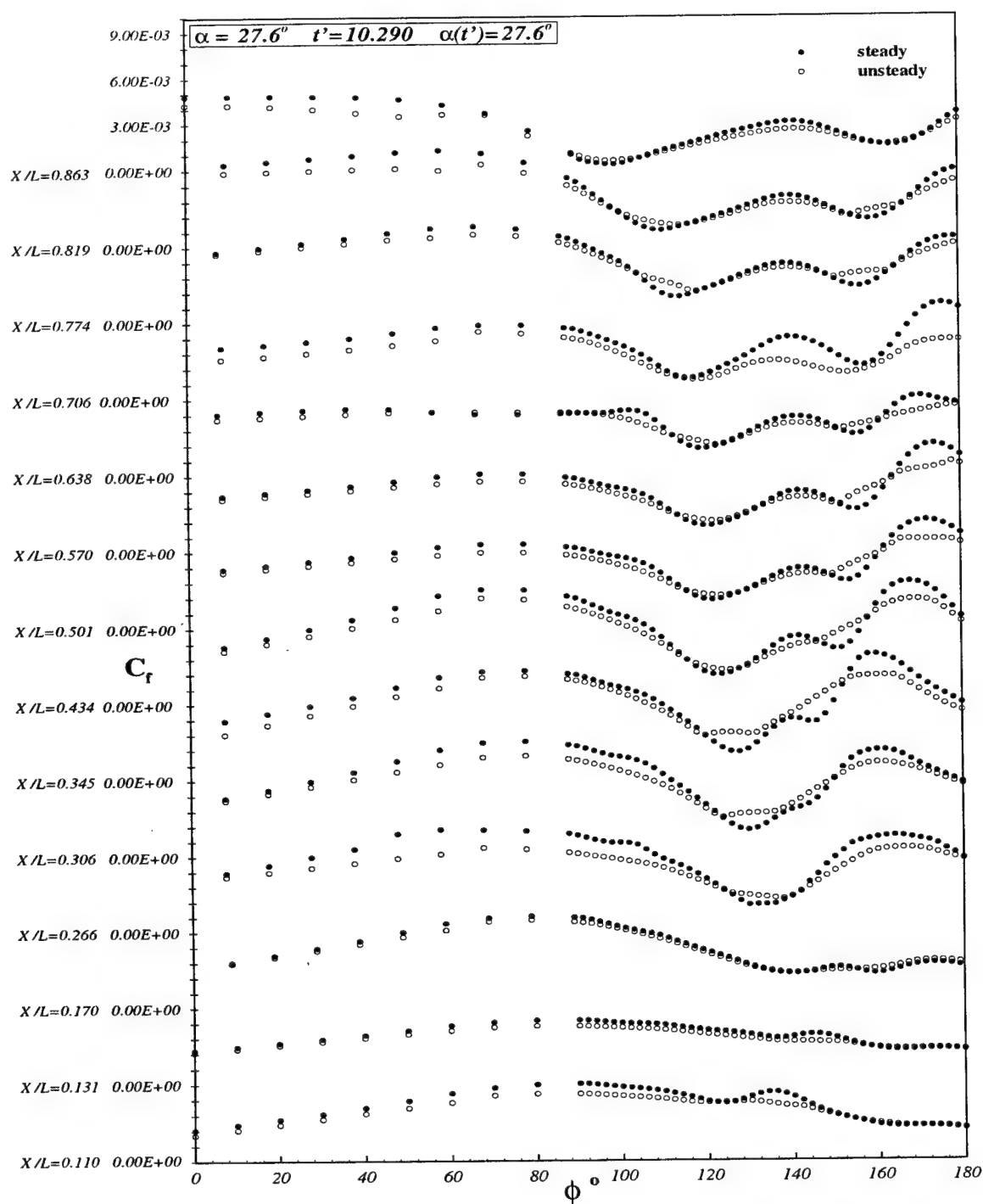


Figure 6.26: Comparison of sail-on-side (region without the sail)  $C_f$  vs.  $\phi$  distribution for steady and unsteady data at all  $x/L$  locations.  $\alpha = 27.6^\circ$ ,  $t' = 10.290$ ,  $\alpha(t') = 27.6^\circ$ .

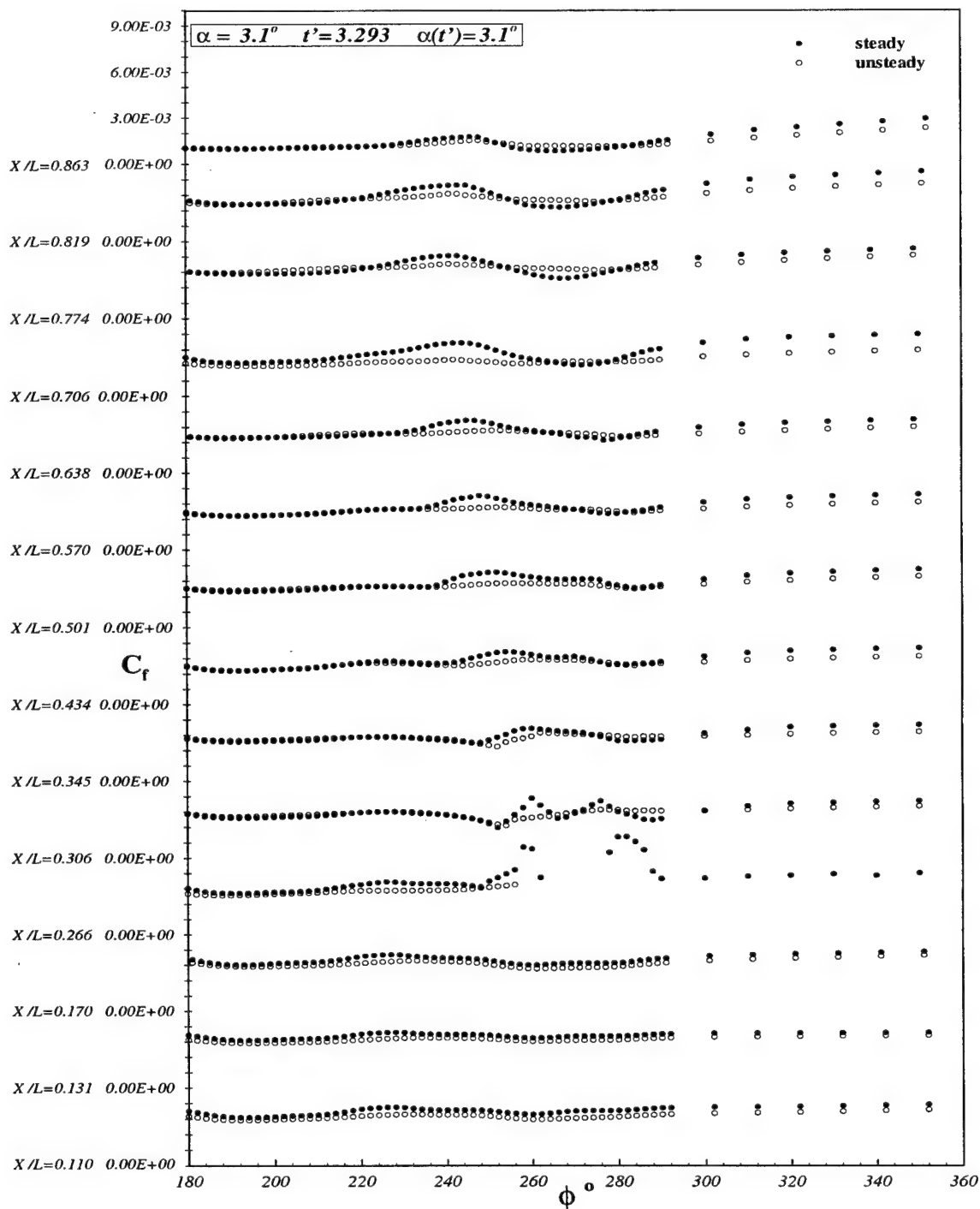


Figure 6.27: Comparison of sail-on-side (region with the sail)  $C_f$  vs.  $\phi$  distribution for steady and unsteady data at all  $x/L$  locations.  $\alpha = 3.1^\circ$ ,  $t' = 3.293$ ,  $\alpha(t') = 3.1^\circ$ .

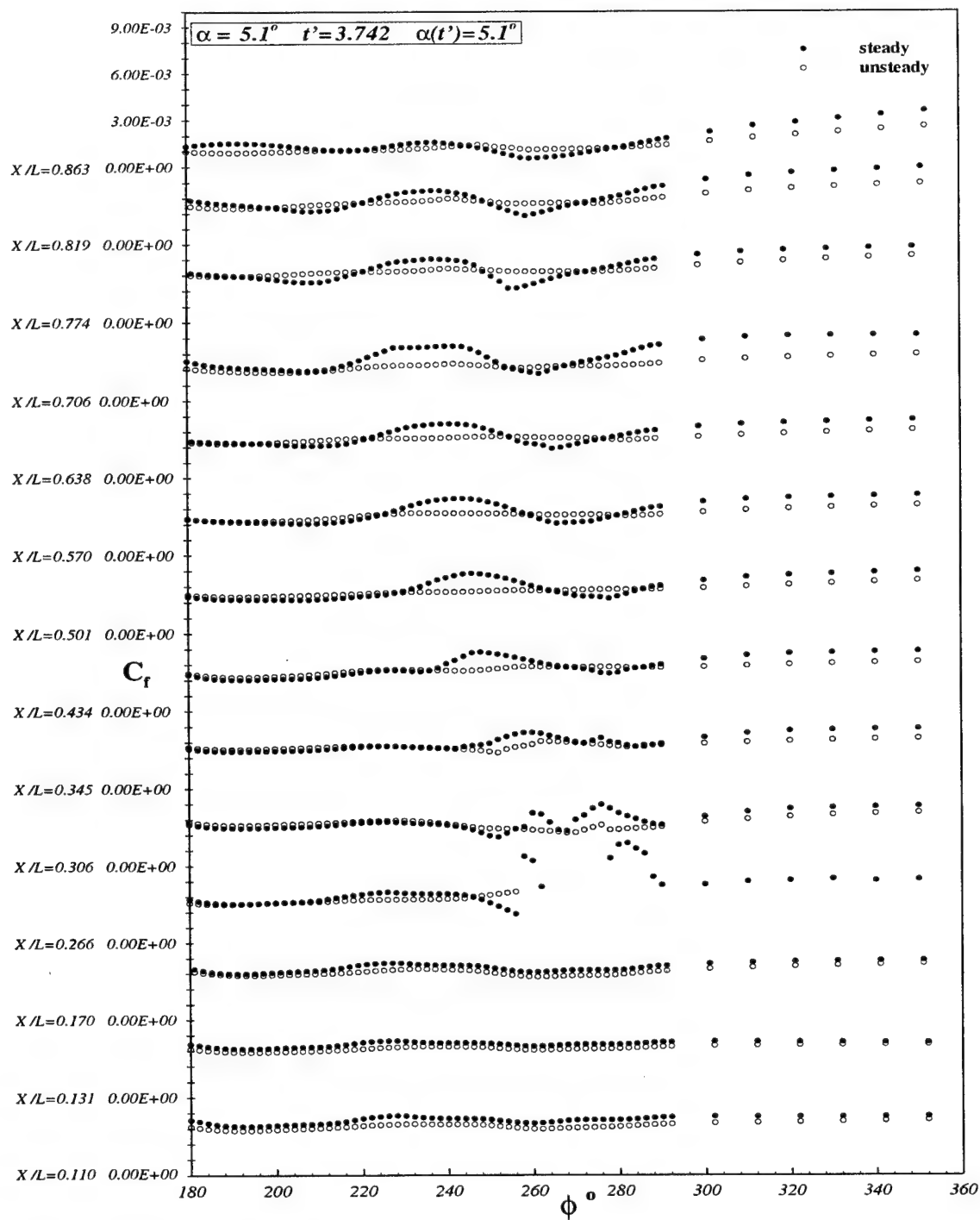


Figure 6.28: Comparison of sail-on-side (region with the sail)  $C_f$  vs.  $\phi$  distribution for steady and unsteady data at all  $x/L$  locations.  $\alpha = 5.1^\circ$ ,  $t' = 3.742$ ,  $\alpha(t') = 5.1^\circ$ .

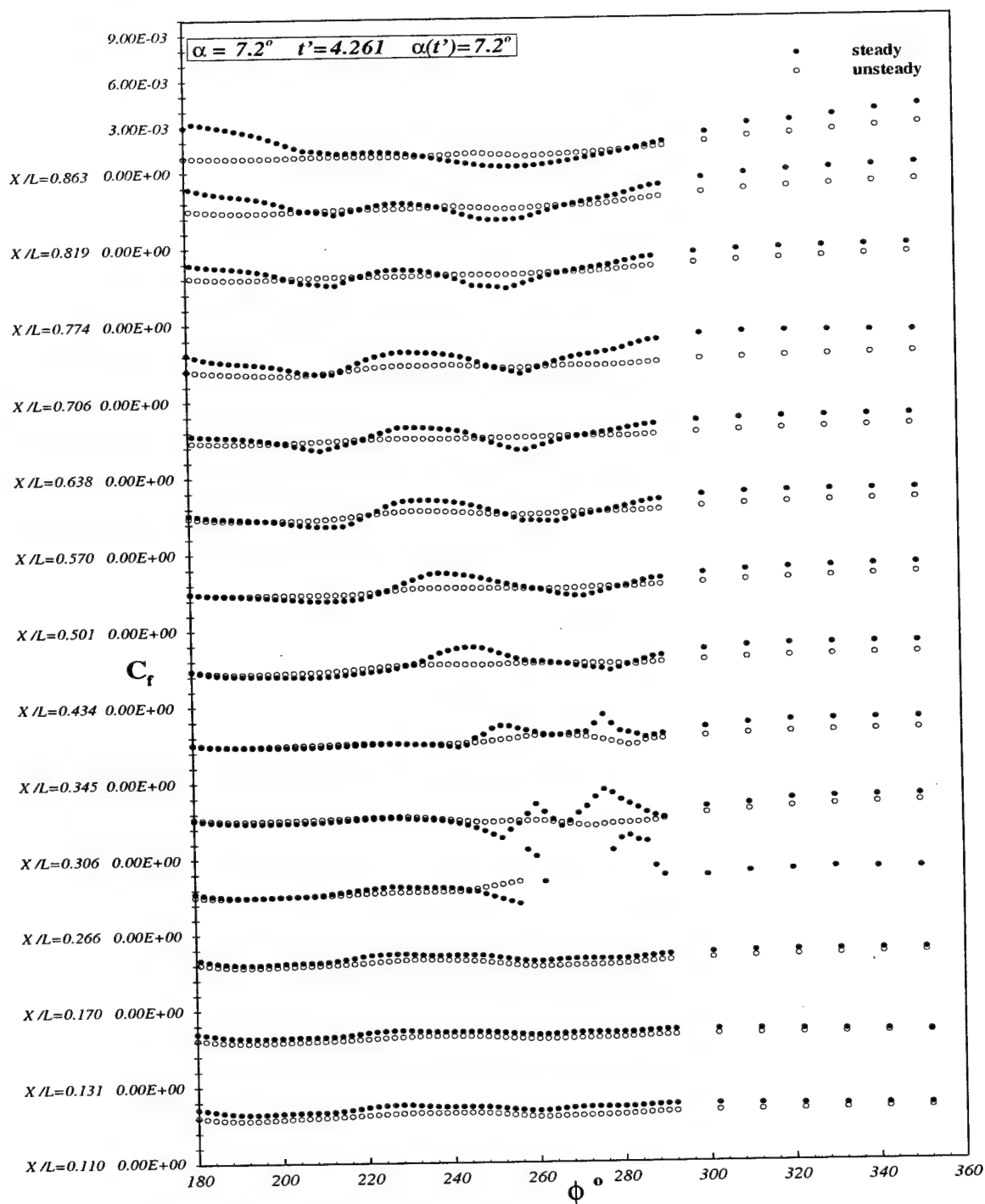


Figure 6.29: Comparison of sail-on-side (region with the sail)  $C_f$  vs.  $\phi$  distribution for steady and unsteady data at all  $x/L$  locations.  $\alpha = 7.2^\circ$ ,  $t' = 4.261$ ,  $\alpha(t') = 7.2^\circ$ .

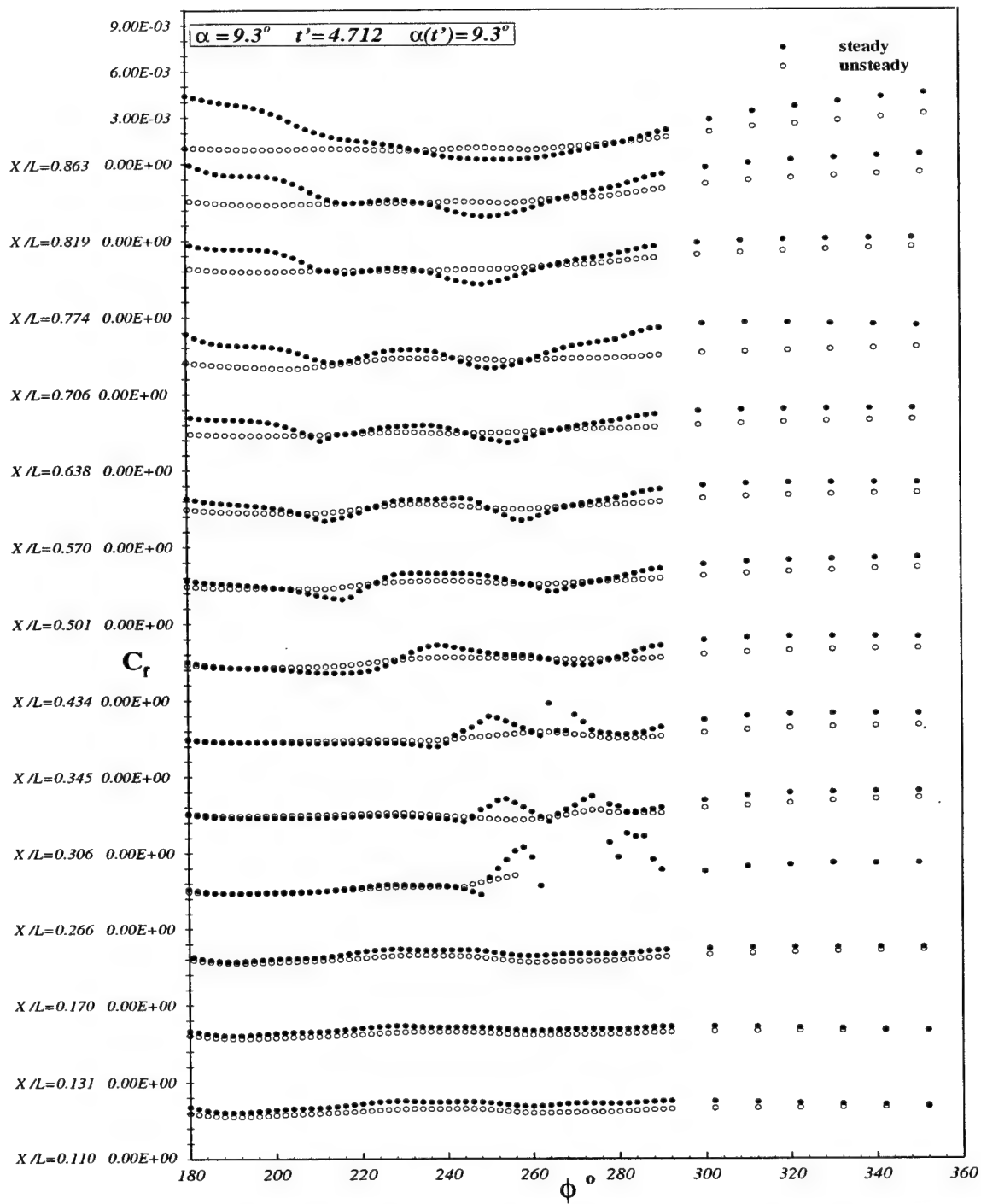


Figure 6.30: Comparison of sail-on-side (region with the sail)  $C_f$  vs.  $\phi$  distribution for steady and unsteady data at all  $x/L$  locations.  $\alpha = 9.3^\circ$ ,  $t' = 4.7123$ ,  $\alpha(t') = 9.3^\circ$ .

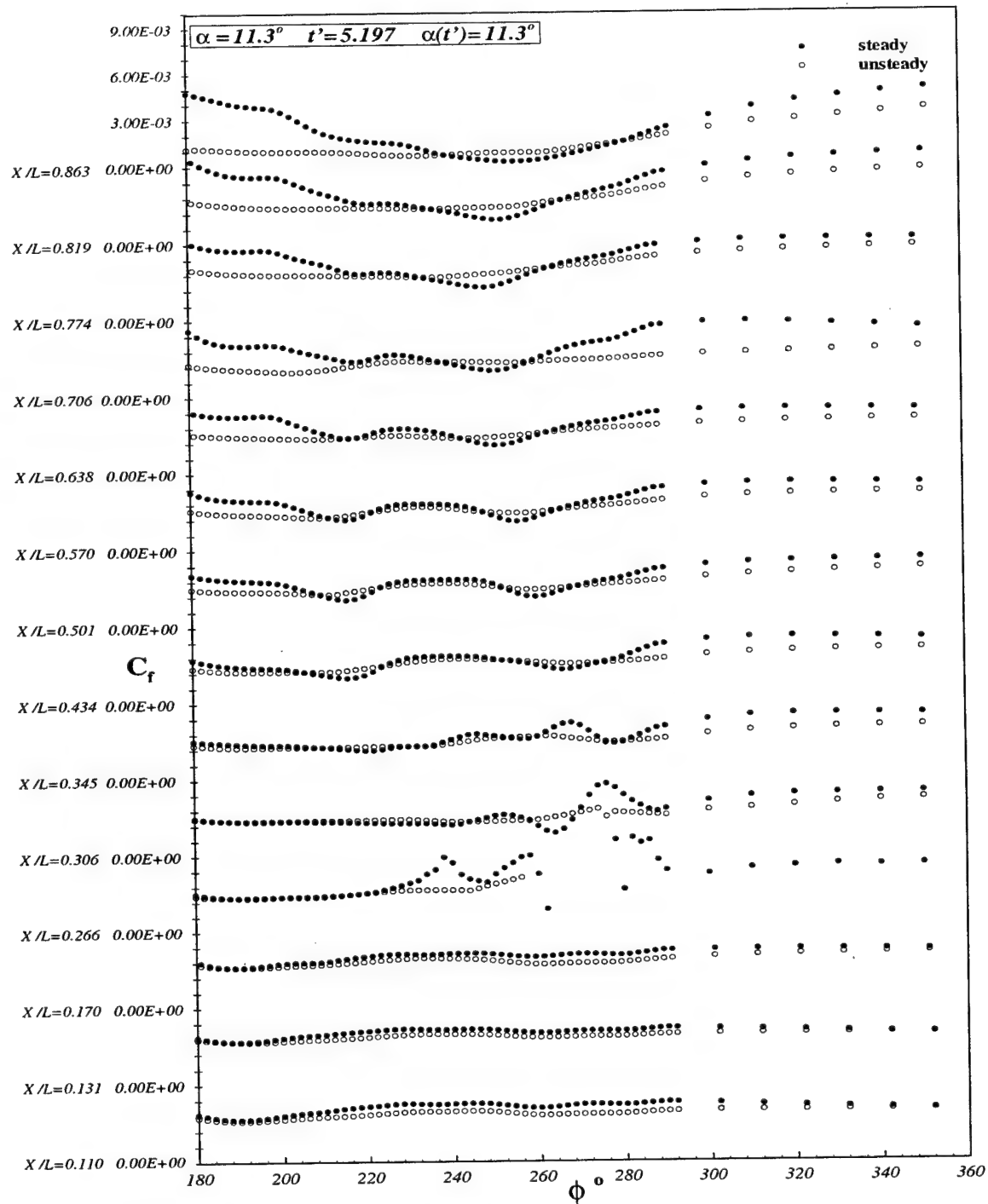


Figure 6.31: Comparison of sail-on-side (region with the sail)  $C_f$  vs.  $\phi$  distribution for steady and unsteady data at all  $x/L$  locations.  $\alpha = 11.3^\circ$ ,  $t' = 5.197$ ,  $\alpha(t') = 11.3^\circ$ .



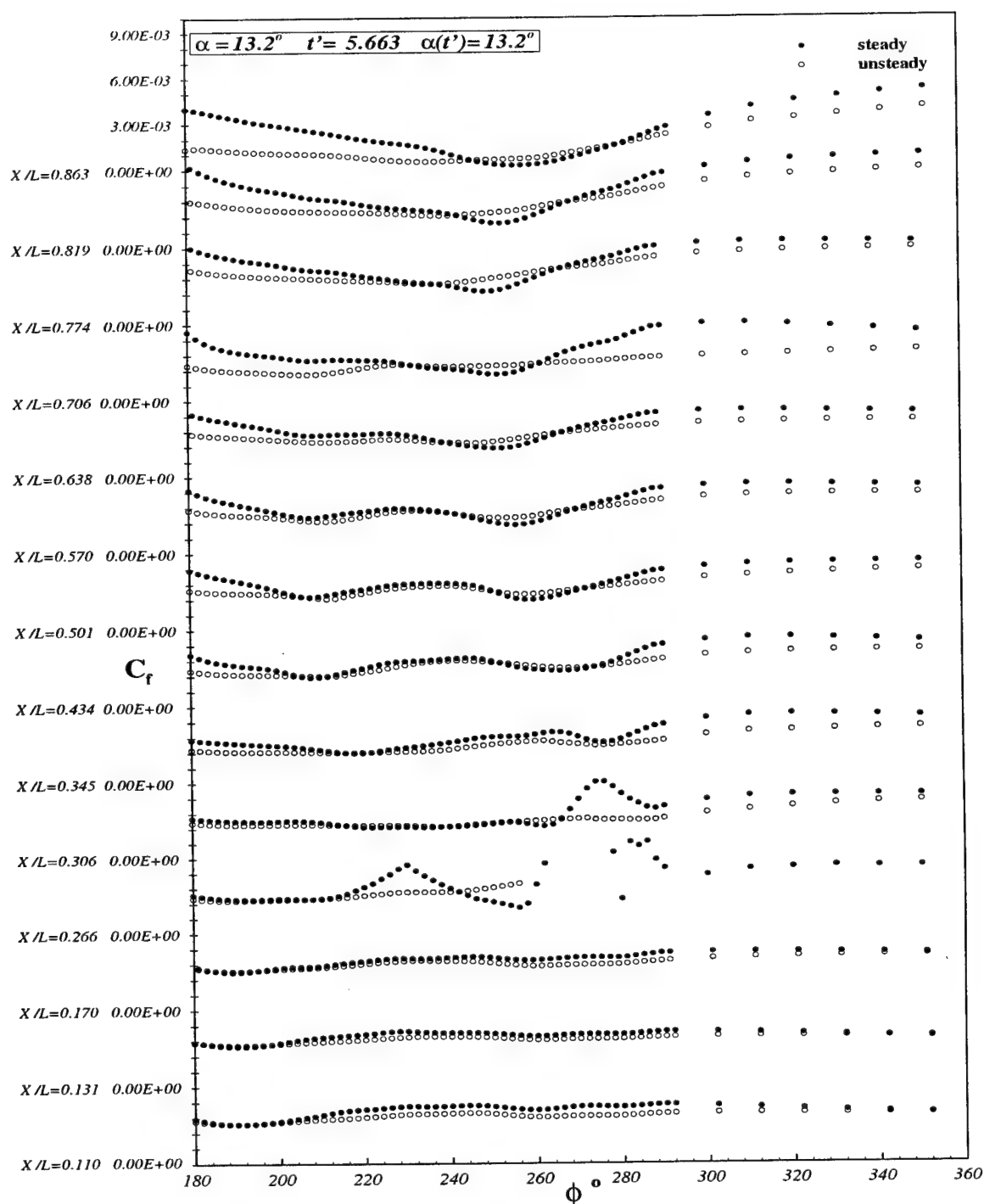


Figure 6.32: Comparison of sail-on-side (region with the sail)  $C_f$  vs.  $\phi$  distribution for steady and unsteady data at all  $x/L$  locations.  $\alpha = 13.2^\circ$ ,  $t' = 5.663$ ,  $\alpha(t') = 13.2^\circ$ .

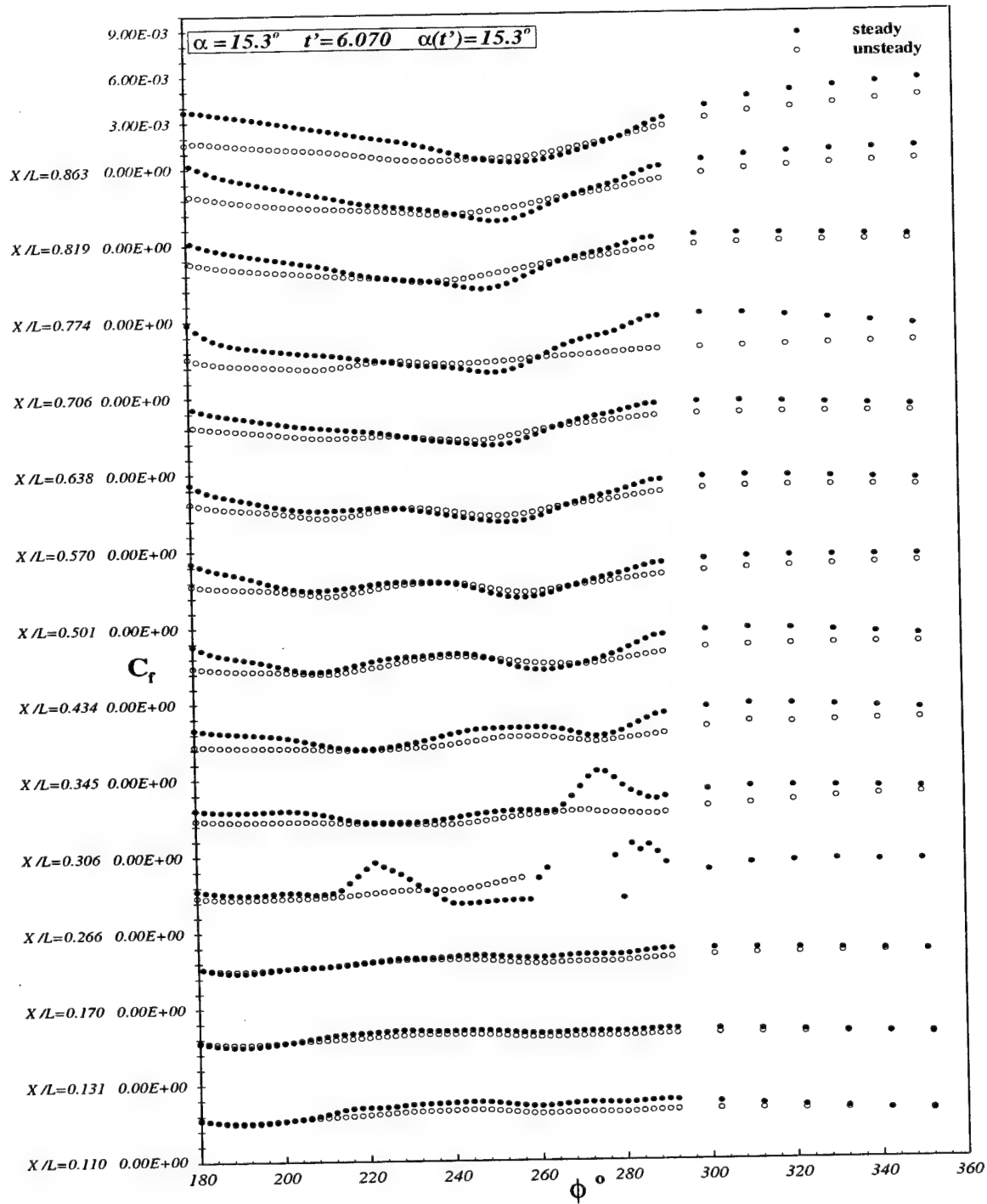


Figure 6.33: Comparison of sail-on-side (region with the sail)  $C_f$  vs.  $\phi$  distribution for steady and unsteady data at all  $x/L$  locations.  $\alpha = 15.3^\circ$ ,  $t' = 6.070$ ,  $\alpha(t') = 15.3^\circ$ .

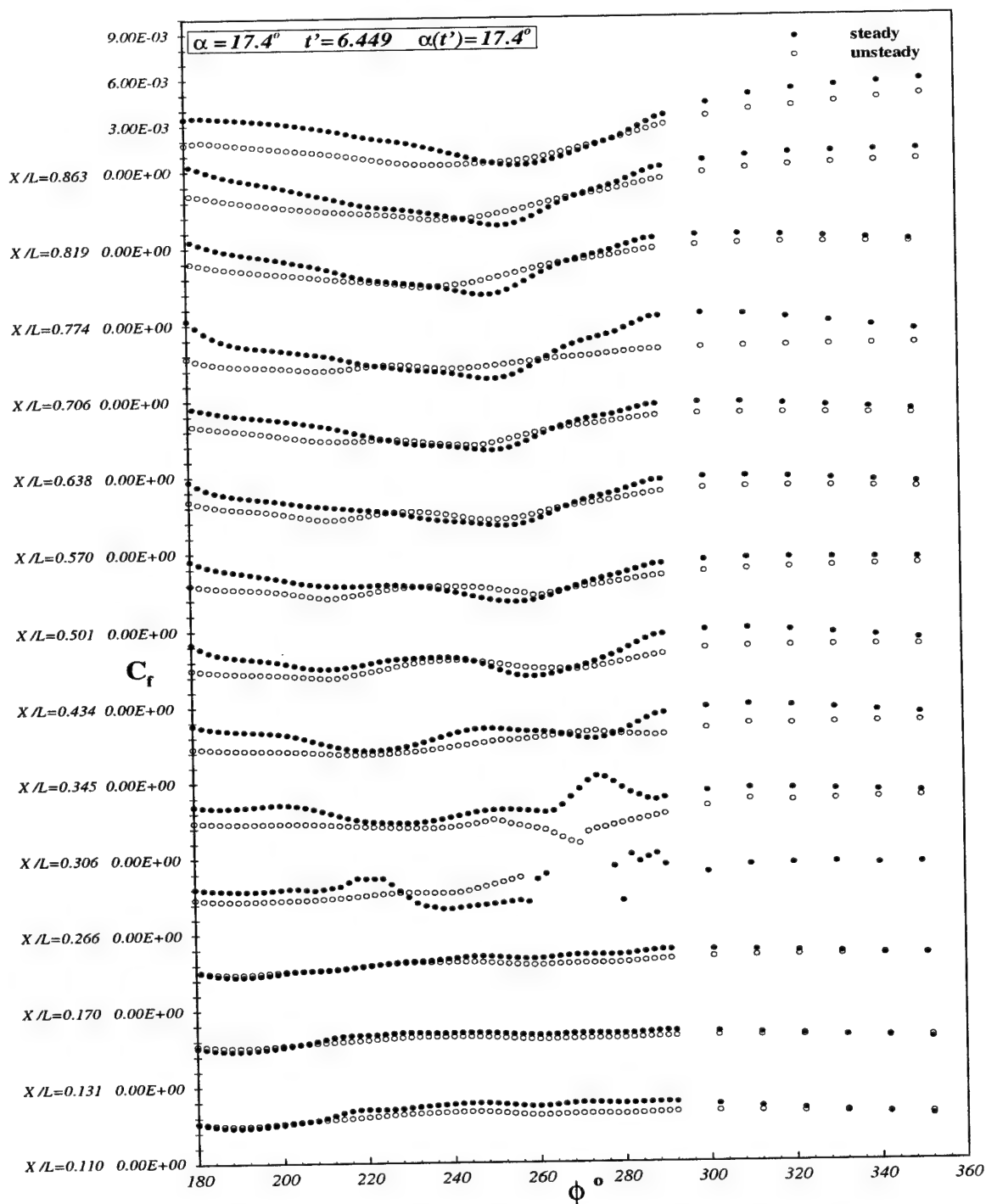


Figure 6.34: Comparison of sail-on-side (region with the sail)  $C_f$  vs.  $\phi$  distribution for steady and unsteady data at all  $x/L$  locations.  $\alpha = 17.4^\circ$ ,  $t' = 6.449$ ,  $\alpha(t') = 17.4^\circ$ .

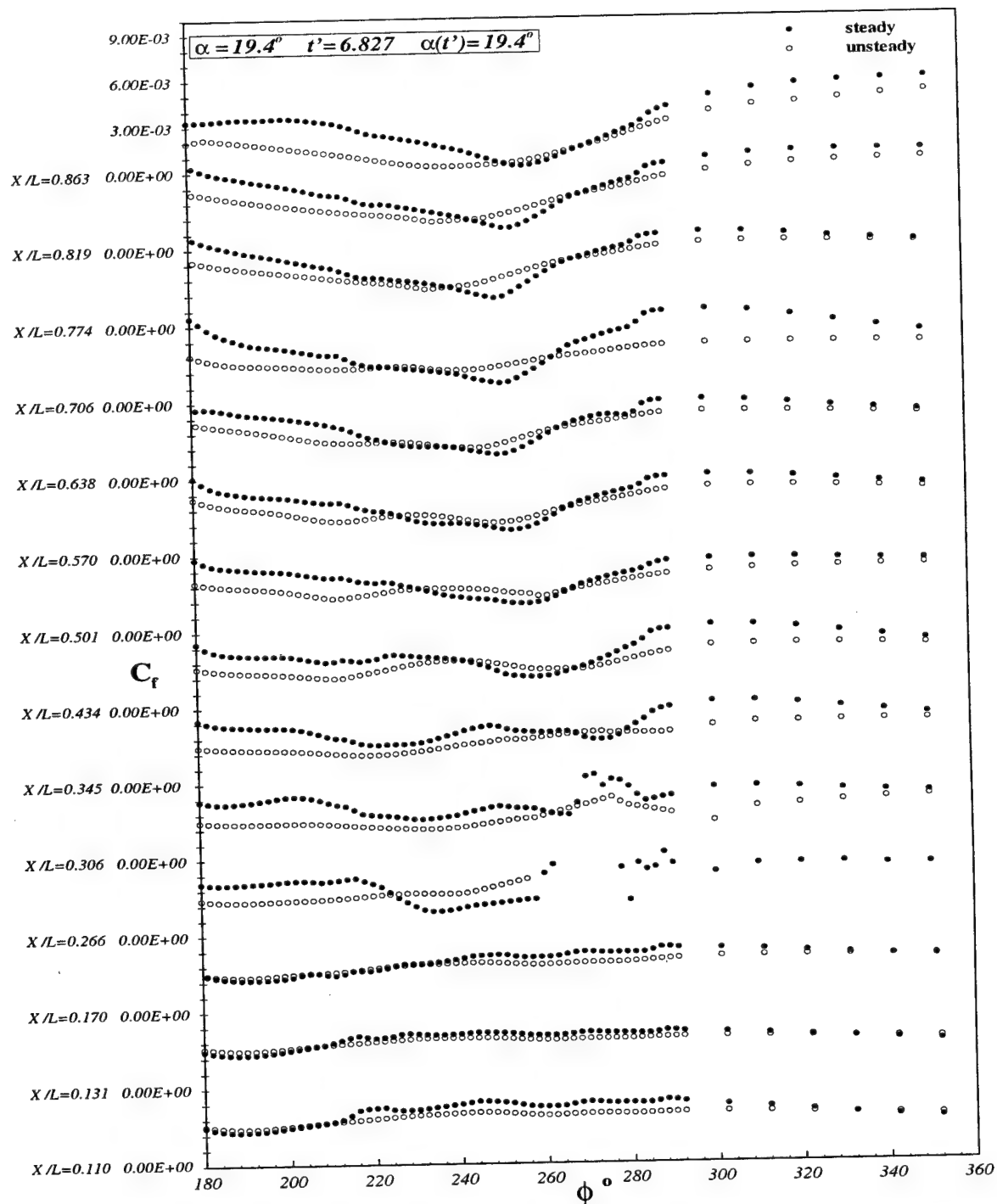


Figure 6.35: Comparison of sail-on-side (region with the sail)  $C_f$  vs.  $\phi$  distribution for steady and unsteady data at all  $x/L$  locations.  $\alpha = 19.4^\circ$ ,  $t' = 6.827$ ,  $\alpha(t') = 19.4^\circ$ .

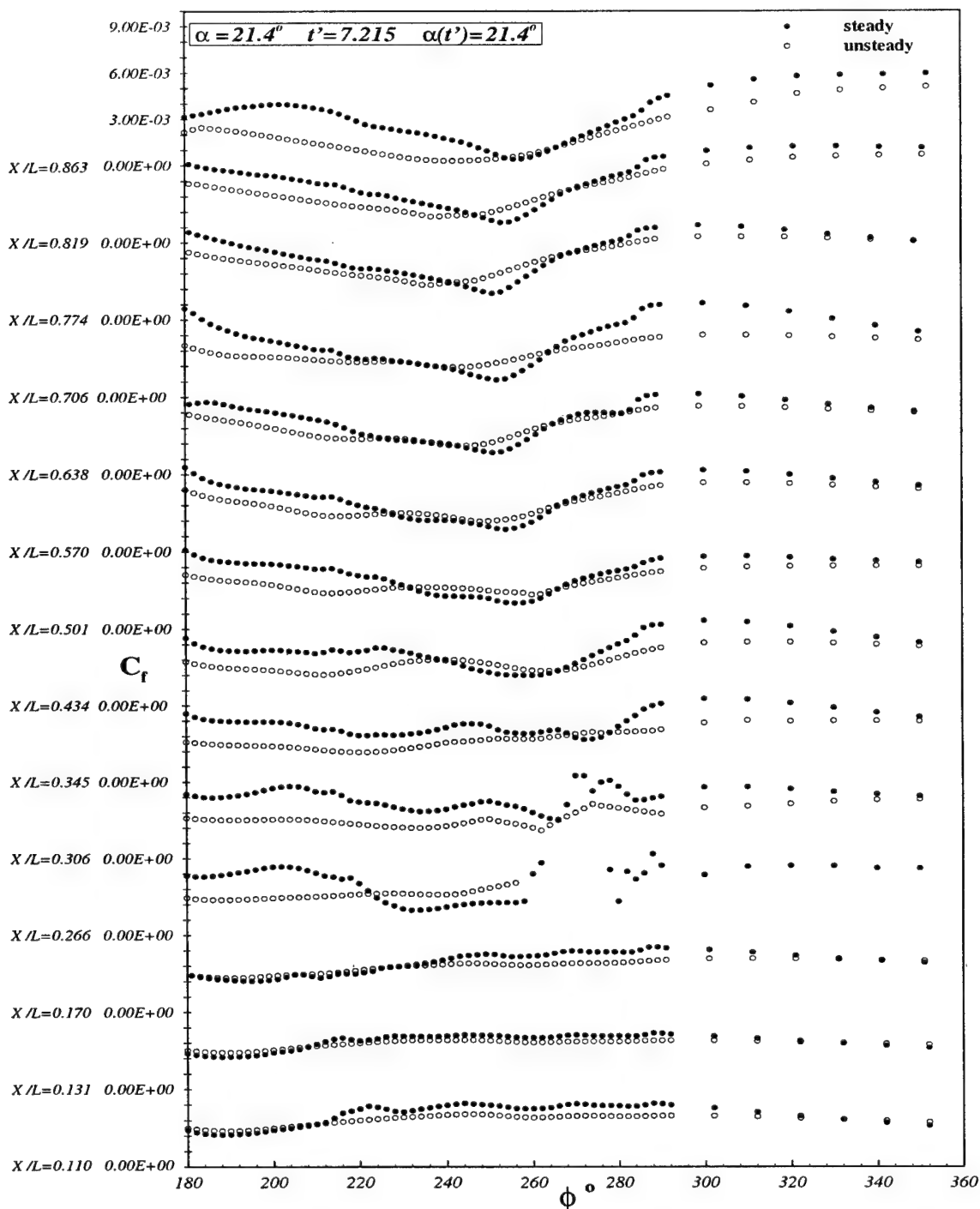


Figure 6.36: Comparison of sail-on-side (region with the sail)  $C_f$  vs.  $\phi$  distribution for steady and unsteady data at all  $x/L$  locations.  $\alpha = 21.4^\circ$ ,  $t' = 7.215$ ,  $\alpha(t') = 21.4^\circ$ .

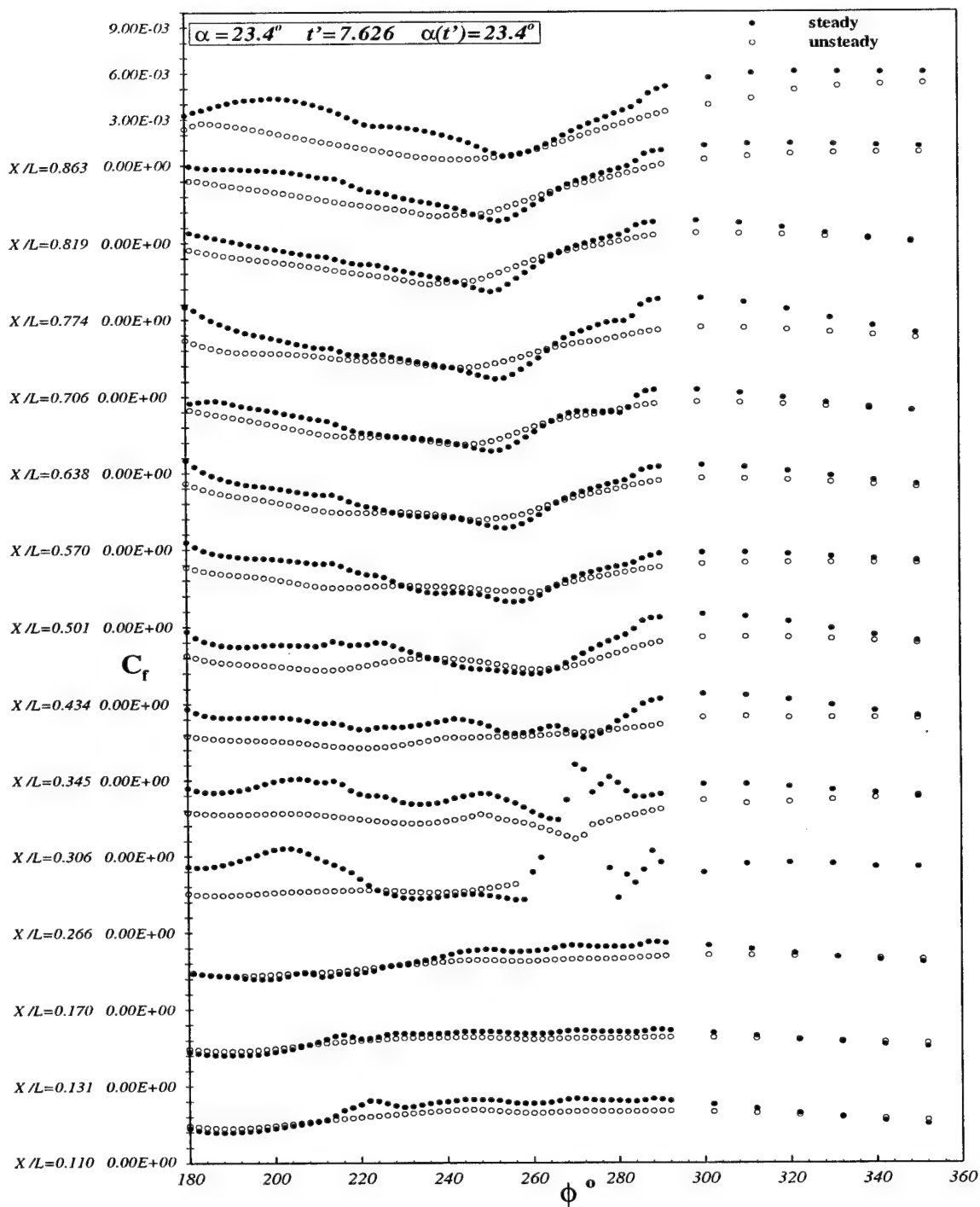


Figure 6.37: Comparison of sail-on-side (region with the sail)  $C_f$  vs.  $\phi$  distribution for steady and unsteady data at all  $x/L$  locations.  $\alpha = 23.4^\circ$ ,  $t' = 7.626$ ,  $\alpha(t') = 23.4^\circ$ .

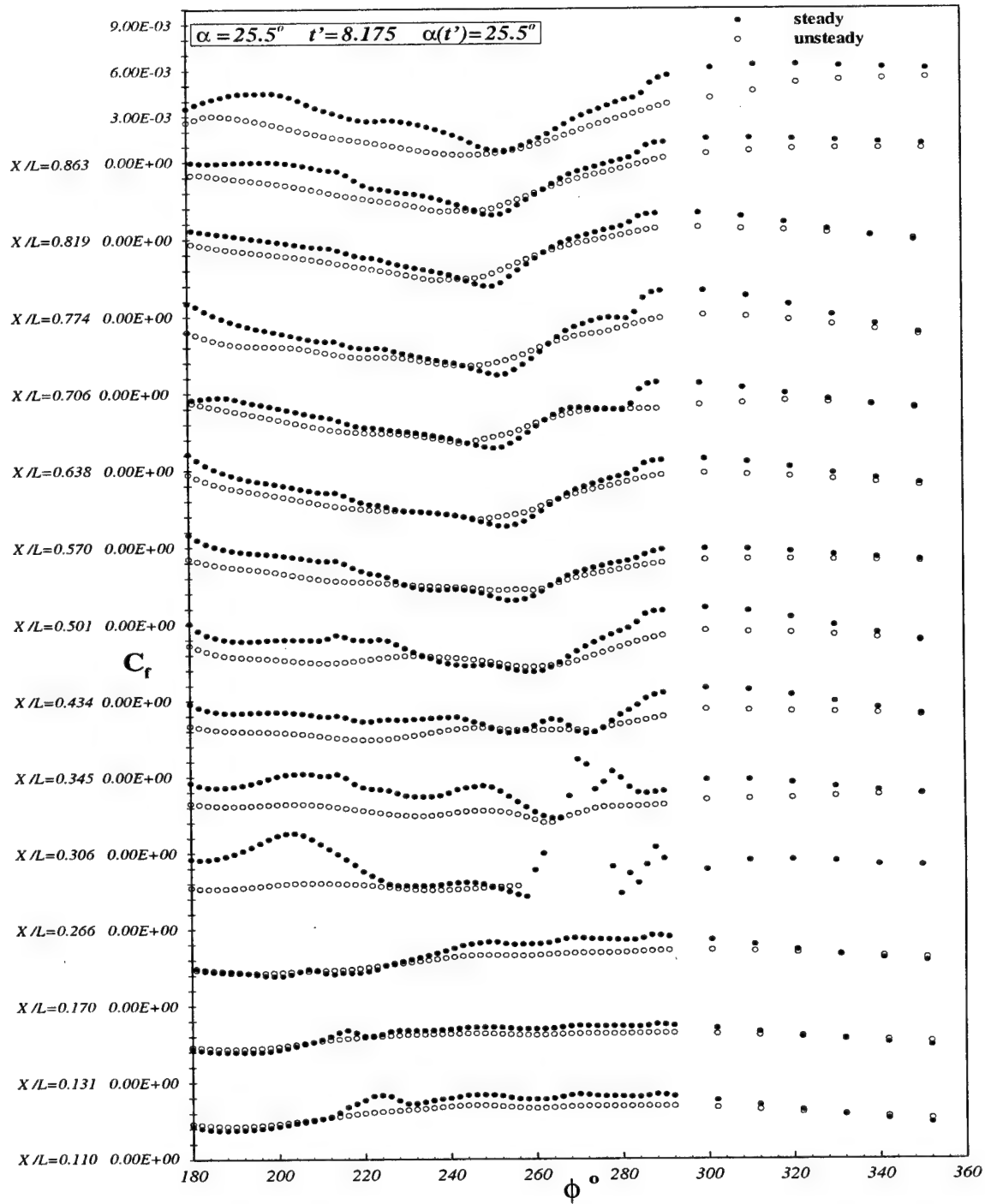


Figure 6.38: Comparison of sail-on-side (region with the sail)  $C_f$  vs.  $\phi$  distribution for steady and unsteady data at all  $x/L$  locations.  $\alpha = 25.5^\circ$ ,  $t' = 8.266$ ,  $\alpha(t') = 25.5^\circ$ .

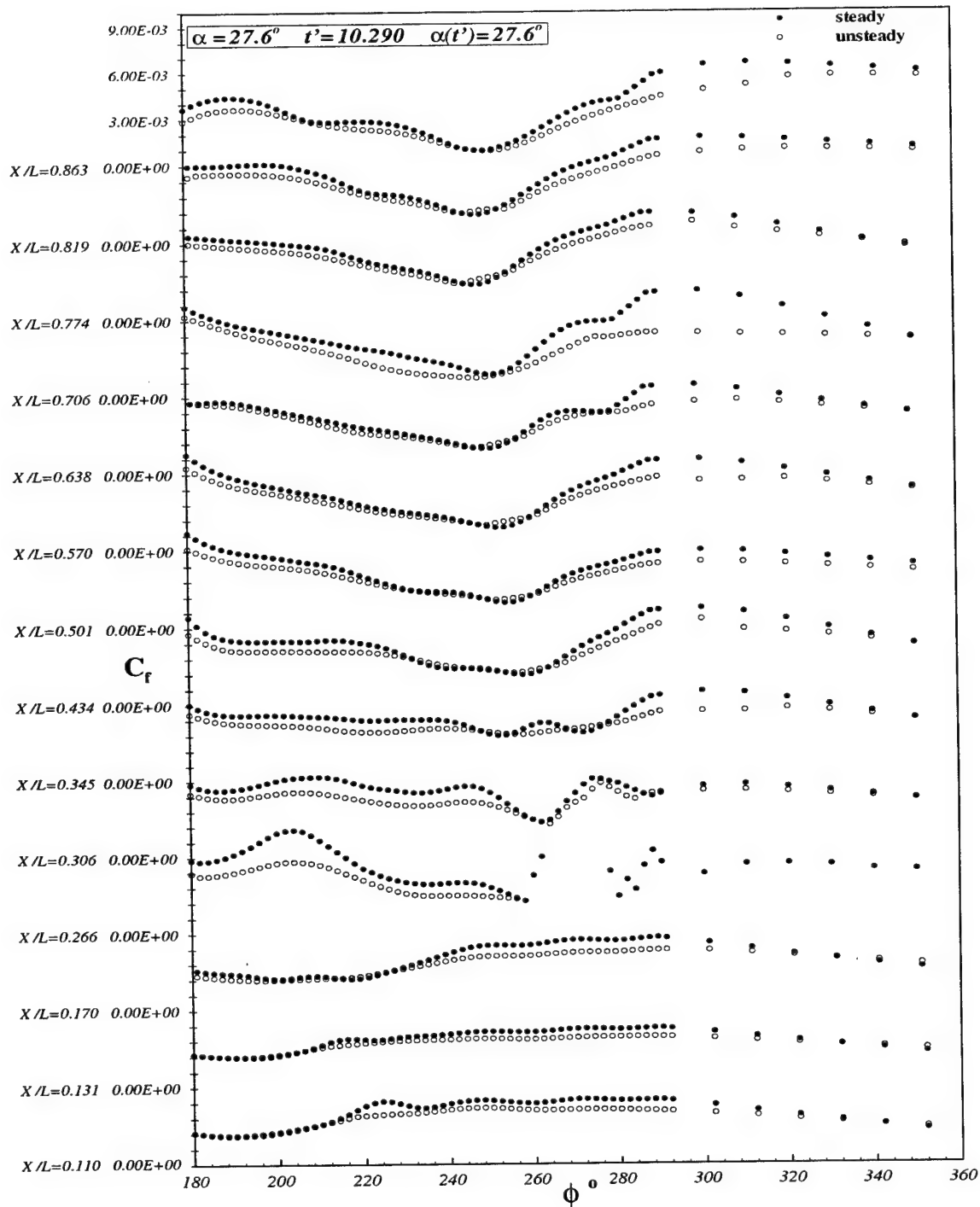


Figure 6.39: Comparison of sail-on-side (region with the sail)  $C_f$  vs.  $\phi$  distribution for steady and unsteady data at all  $x/L$  locations.  $\alpha = 27.6^\circ$ ,  $t' = 10.290$ ,  $\alpha(t') = 27.6^\circ$ .



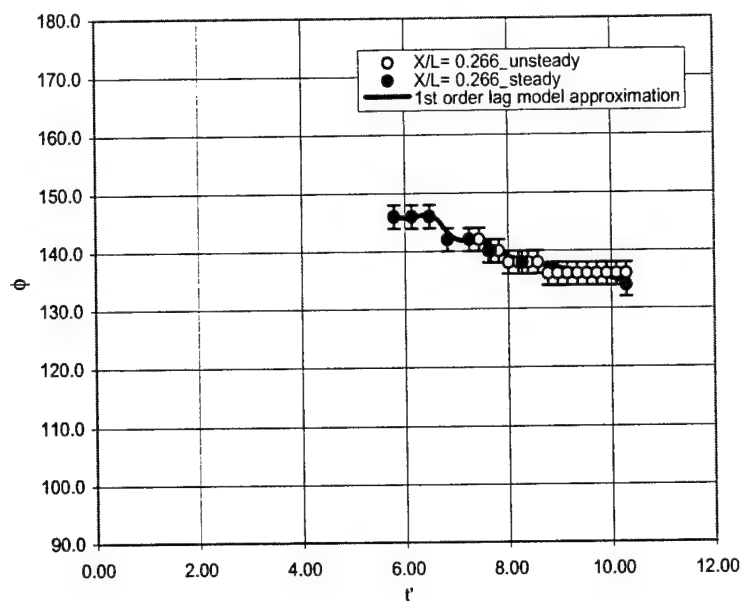


Figure 6.40: First-order differential lag approximation to the unsteady separation data at  $x/L = 0.266$  for the barebody case.

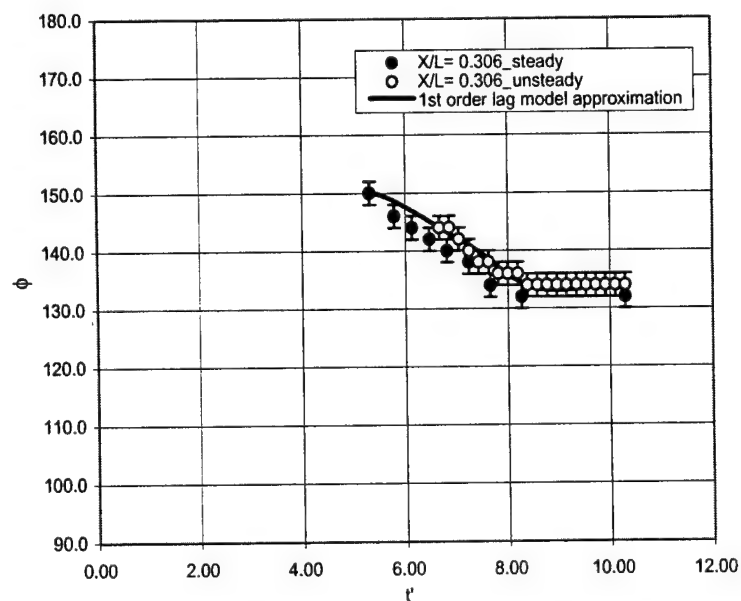


Figure 6.41: First-order differential lag approximation to the unsteady separation data at  $x/L = 0.306$  for the barebody case.

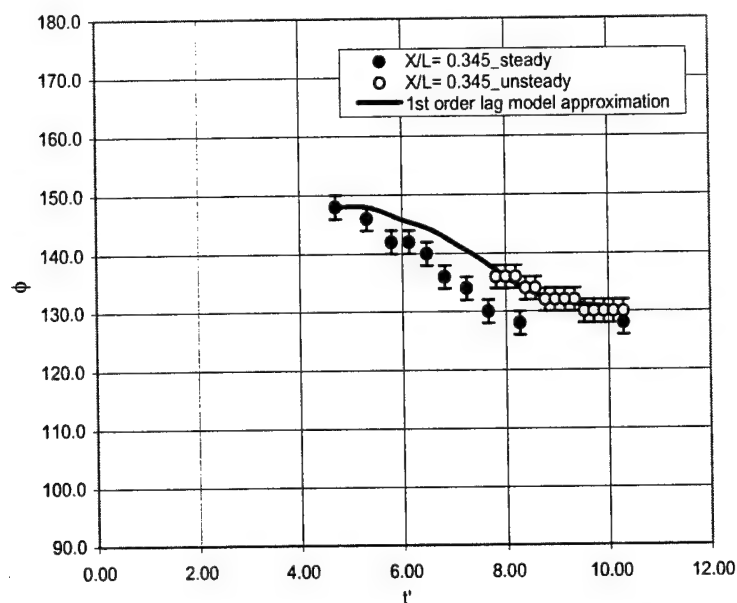


Figure 6.42: First-order differential lag approximation to the unsteady separation data at  $x/L = 0.345$  for the barebody case.

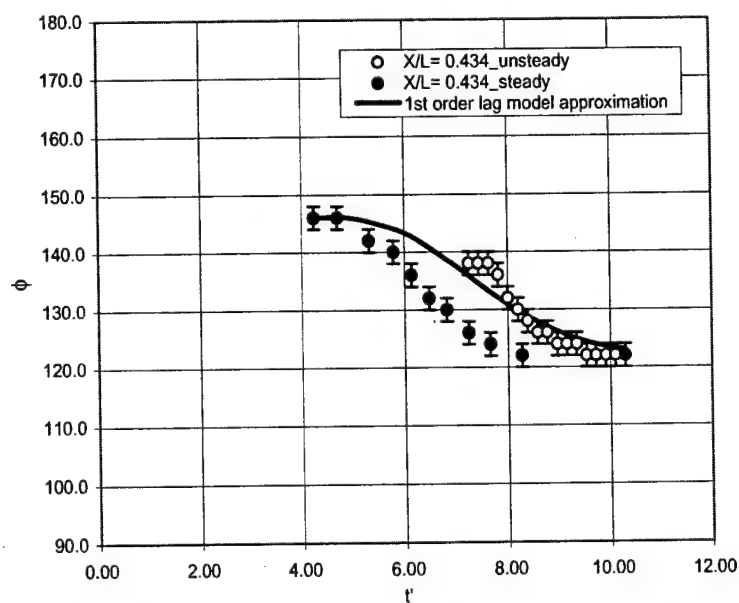


Figure 6.43: First-order differential lag approximation to the unsteady separation data at  $x/L = 0.434$  for the barebody case.

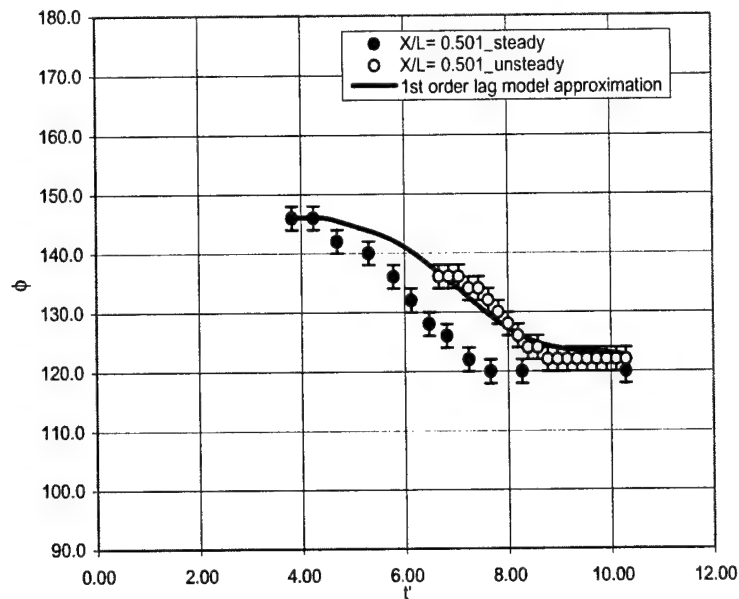


Figure 6.44: First-order differential lag approximation to the unsteady separation data at  $x/L = 0.501$  for the barebody case.

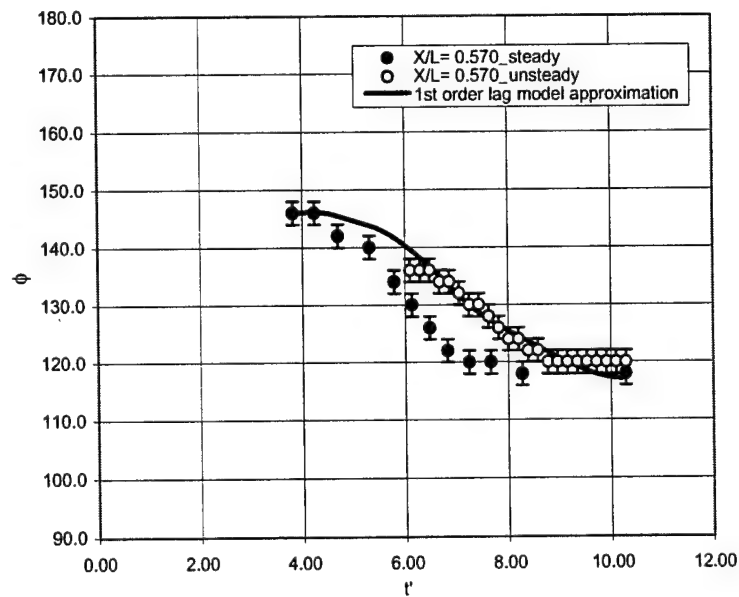


Figure 6.45: First-order differential lag approximation to the unsteady separation data at  $x/L = 0.570$  for the barebody case.

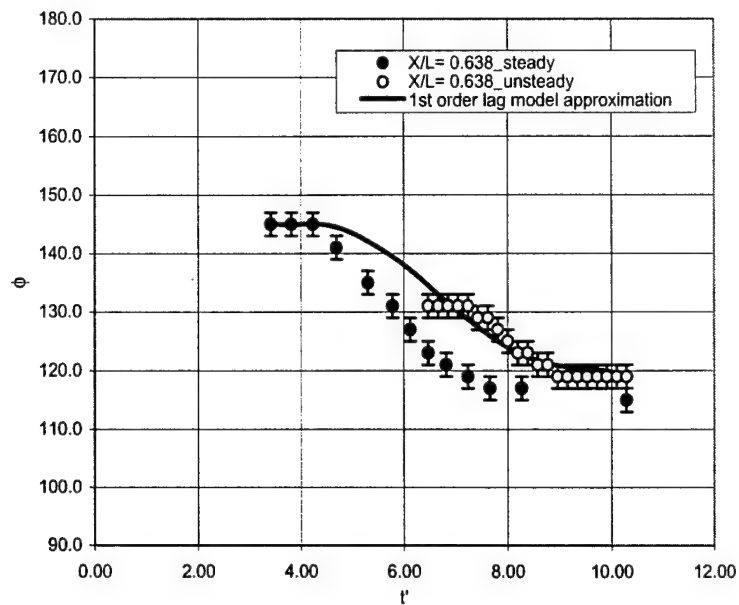


Figure 6.46: First-order differential lag approximation to the unsteady separation data at  $x/L = 0.638$  for the barebody case.

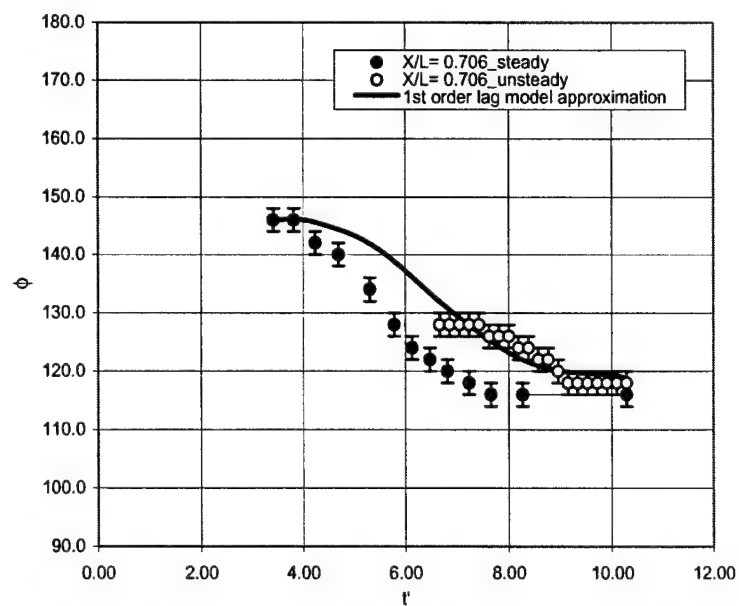


Figure 6.47: First-order differential lag approximation to the unsteady separation data at  $x/L = 0.706$  for the barebody case.

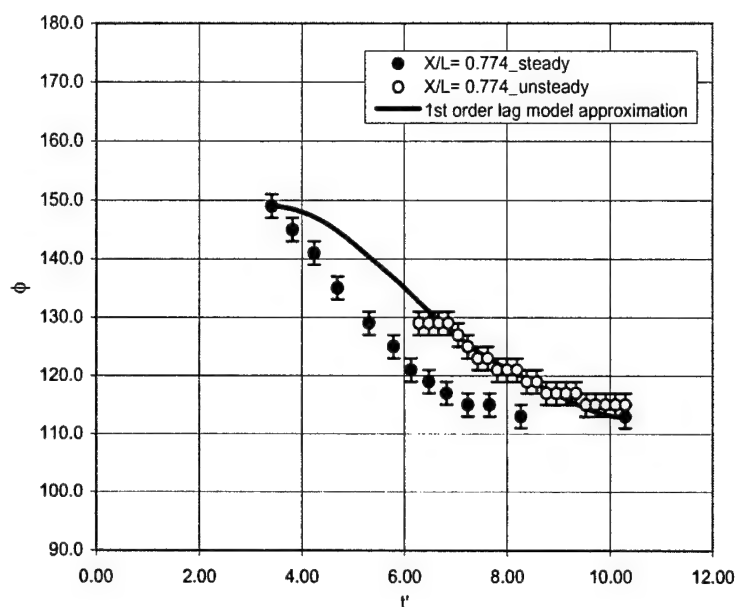


Figure 6.48: First-order differential lag approximation to the unsteady separation data at  $x/L = 0.774$  for the barebody case.

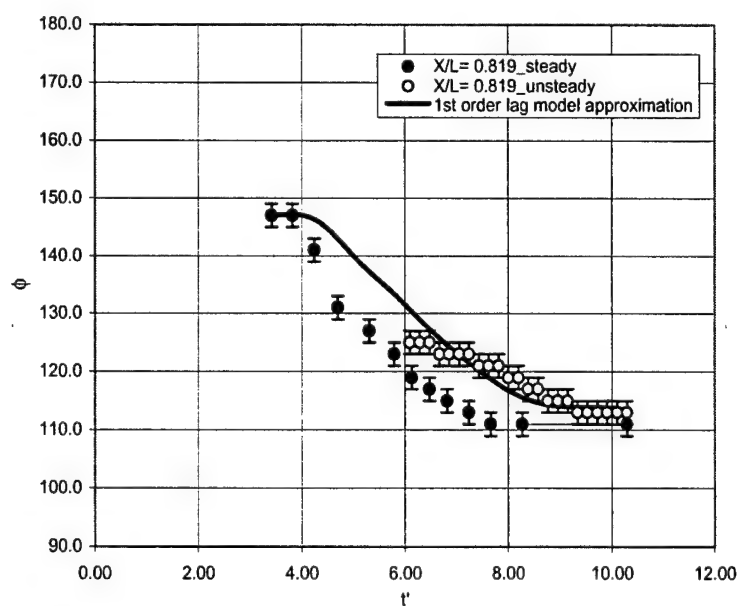


Figure 6.49: First-order differential lag approximation to the unsteady separation data at  $x/L = 0.819$  for the barebody case.

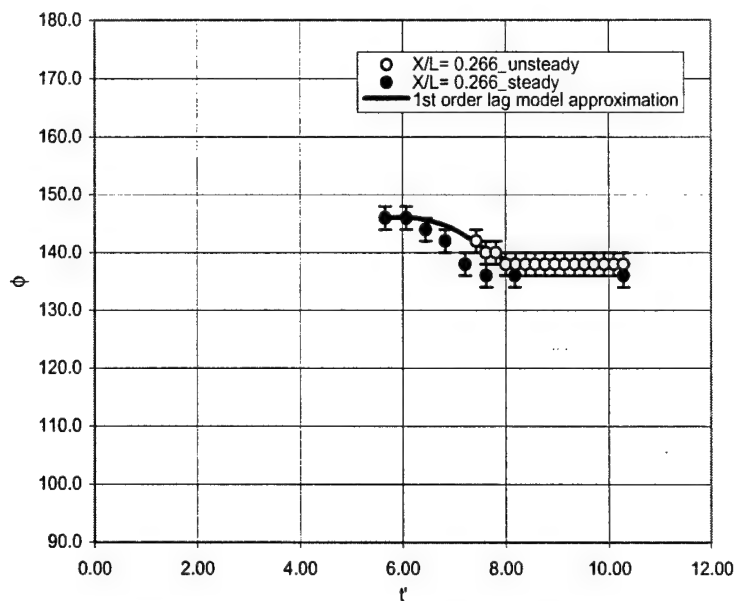


Figure 6.50: First-order differential lag approximation to the unsteady separation data at  $x/L = 0.266$  for the non-sail region of the sail-on-side case.

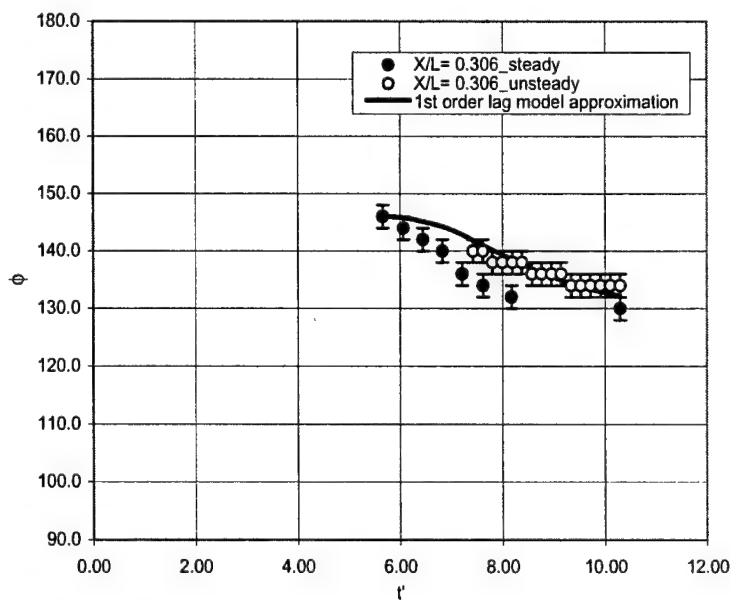


Figure 6.51: First-order differential lag approximation to the unsteady separation data at  $x/L = 0.306$  for the non-sail region of the sail-on-side case.

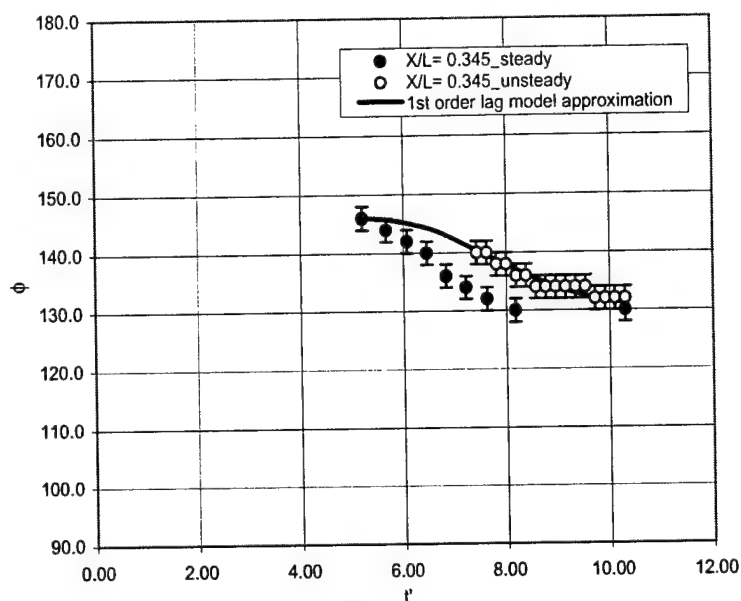


Figure 6.52: First-order differential lag approximation to the unsteady separation data at  $x/L = 0.345$  for the non-sail region of the sail-on-side case.

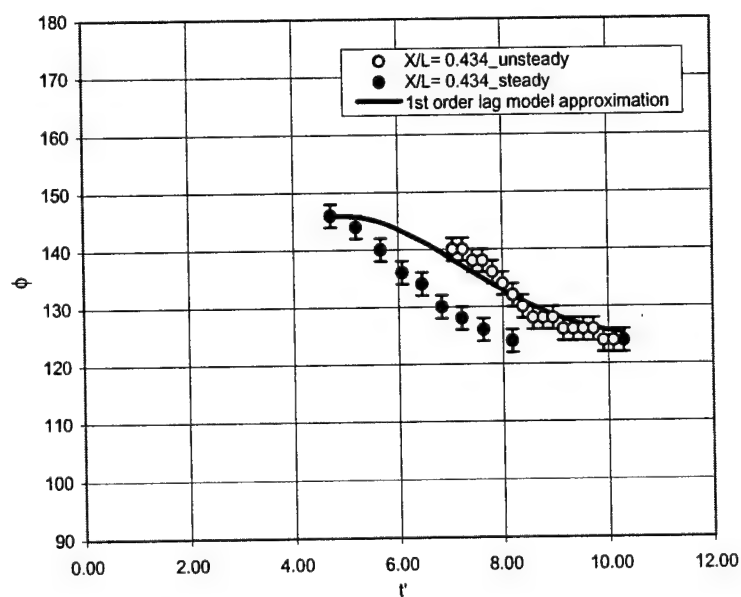


Figure 6.53: First-order differential lag approximation to the unsteady separation data at  $x/L = 0.434$  for the non-sail region of the sail-on-side case.

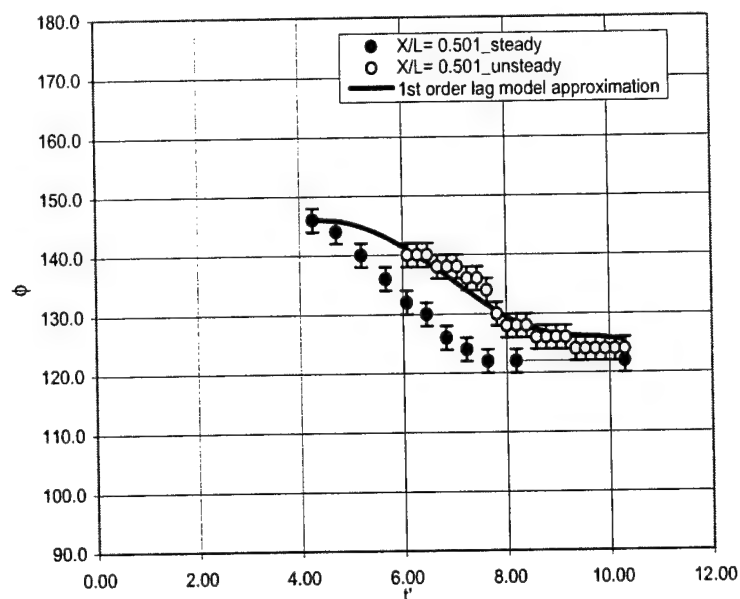


Figure 6.54: First-order differential lag approximation to the unsteady separation data at  $x/L = 0.501$  for the non-sail region of the sail-on-side case.

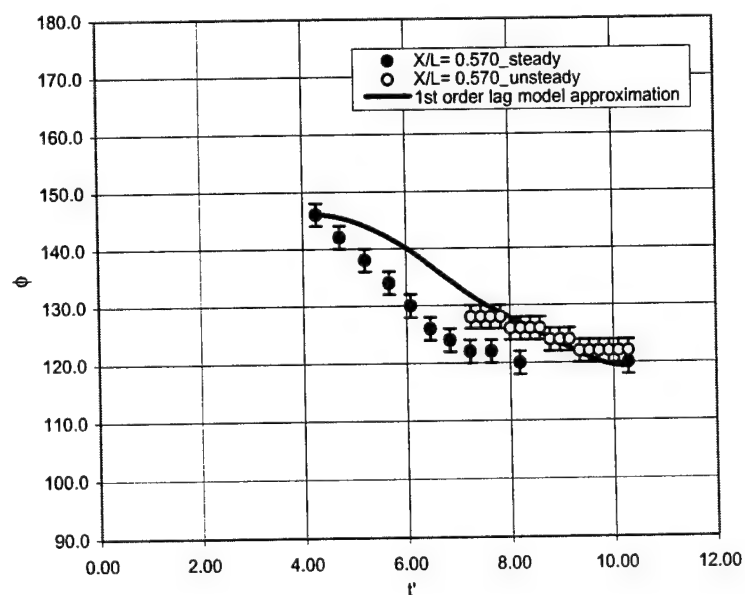


Figure 6.55: First-order differential lag approximation to the unsteady separation data at  $x/L = 0.570$  for the non-sail region of the sail-on-side case.



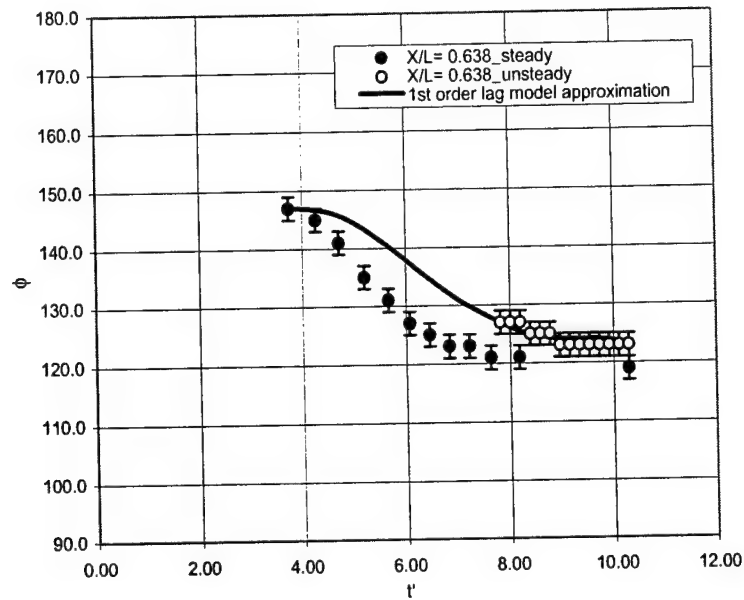


Figure 6.56: First-order differential lag approximation to the unsteady separation data at  $x/L = 0.638$  for the non-sail region of the sail-on-side case.

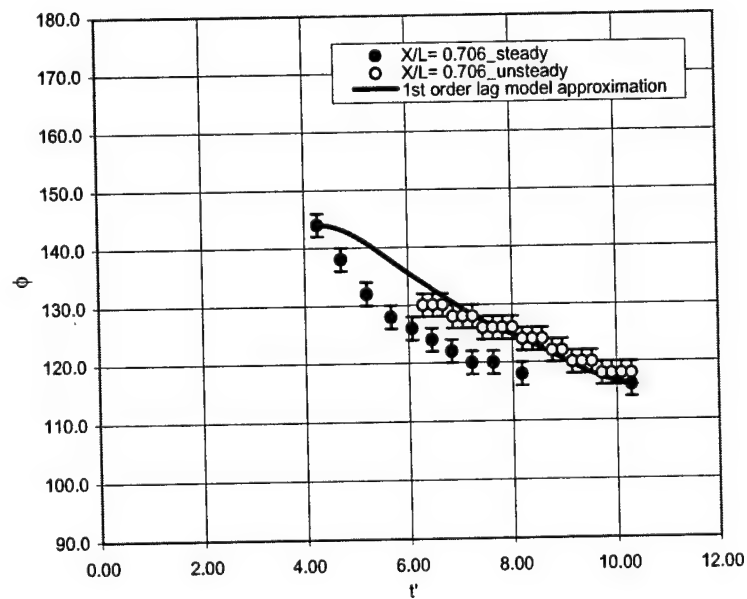


Figure 6.57: First-order differential lag approximation to the unsteady separation data at  $x/L = 0.706$  for the non-sail region of the sail-on-side case.

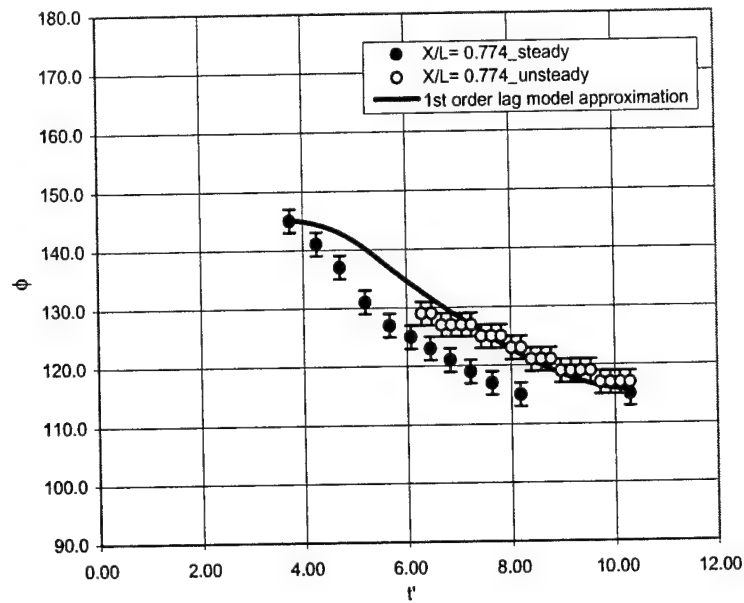


Figure 6.58: First-order differential lag approximation to the unsteady separation data at  $x/L = 0.774$  for the non-sail region of the sail-on-side case.

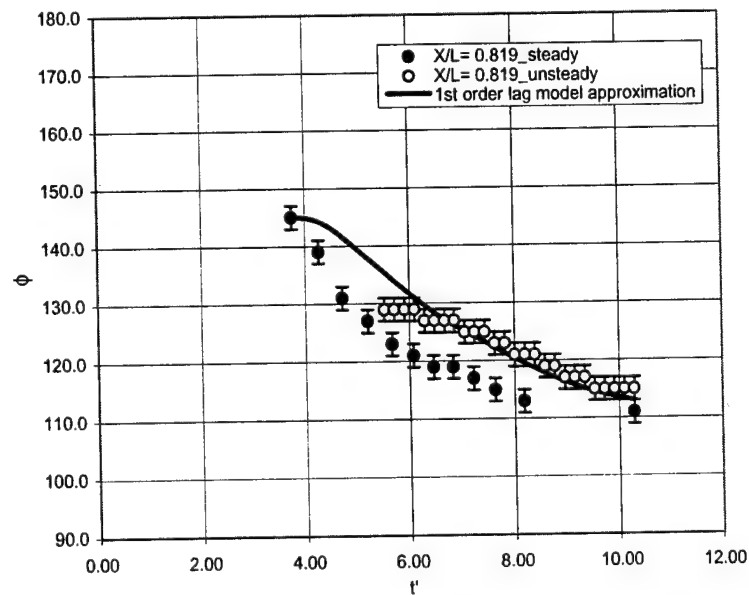


Figure 6.59: First-order differential lag approximation to the unsteady separation data at  $x/L = 0.819$  for the non-sail region of the sail-on-side case.

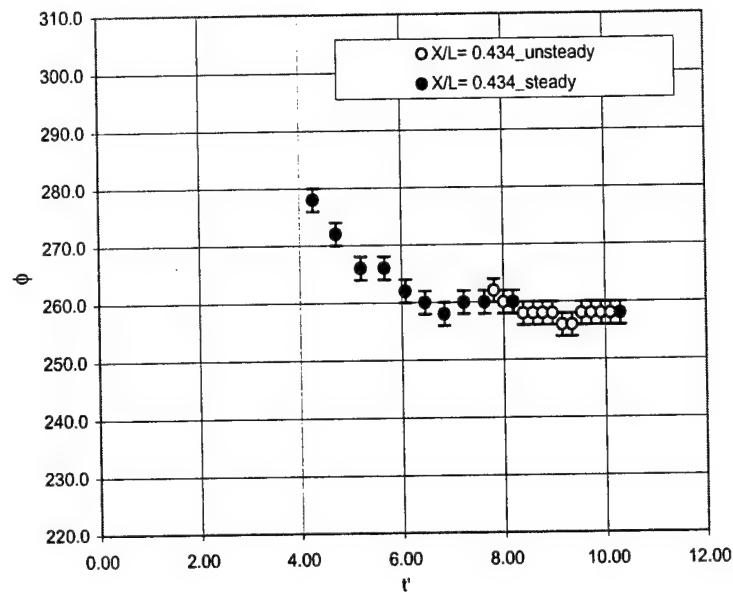


Figure 6.60: Steady and unsteady separation locations (second minima in  $C_f$  measured from  $\phi = 180^\circ$ ) vs  $t'$  at  $x/L = 0.434$  for the sail region of the sail-on-side case.

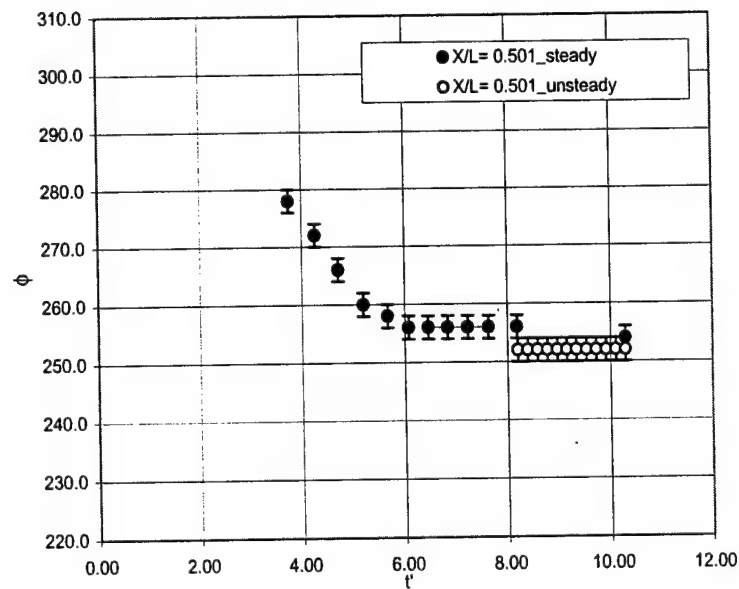


Figure 6.61: Steady and unsteady separation locations (second minima in  $C_f$  measured from  $\phi = 180^\circ$ ) vs  $t'$  at  $x/L = 0.501$  for the sail region of the sail-on-side case.

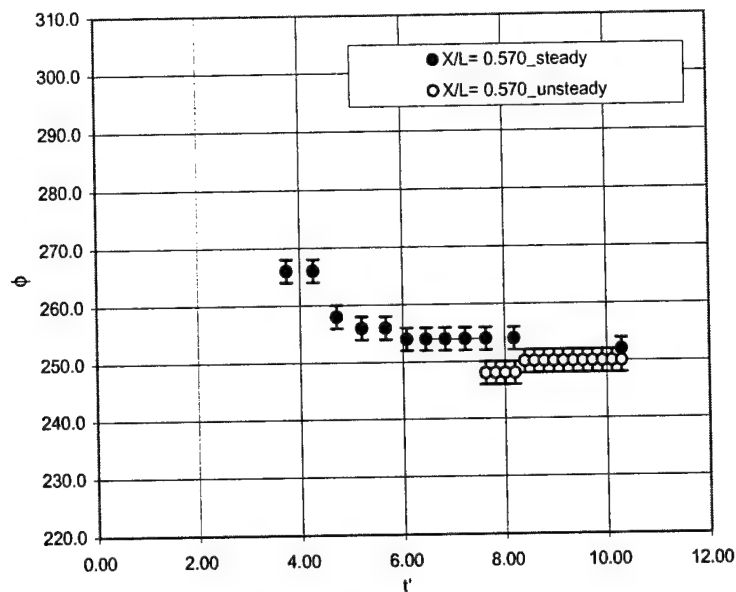


Figure 6.62: Steady and unsteady separation locations (second minima in  $C_f$  measured from  $\phi = 180^\circ$ ) vs  $t'$  at  $x/L = 0.570$  for the sail region of the sail-on-side case.

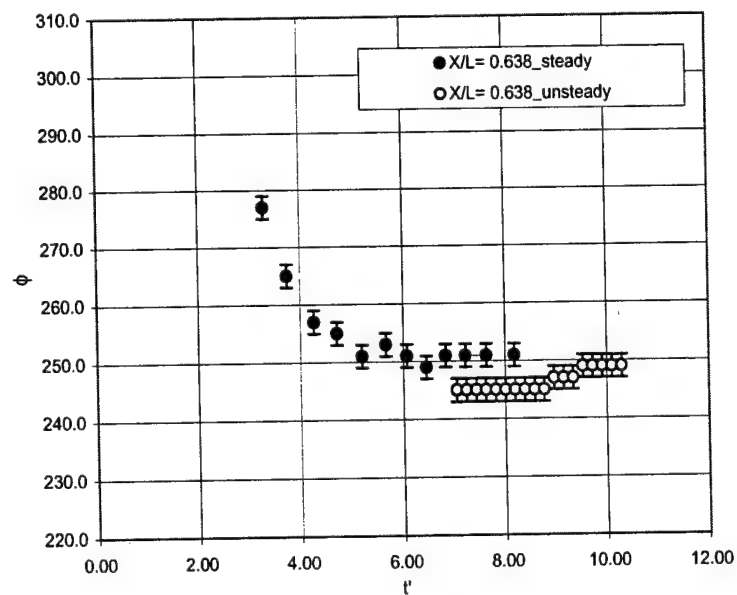


Figure 6.63: Steady and unsteady separation locations (second minima in  $C_f$  measured from  $\phi = 180^\circ$ ) vs  $t'$  at  $x/L = 0.638$  for the sail region of the sail-on-side case.

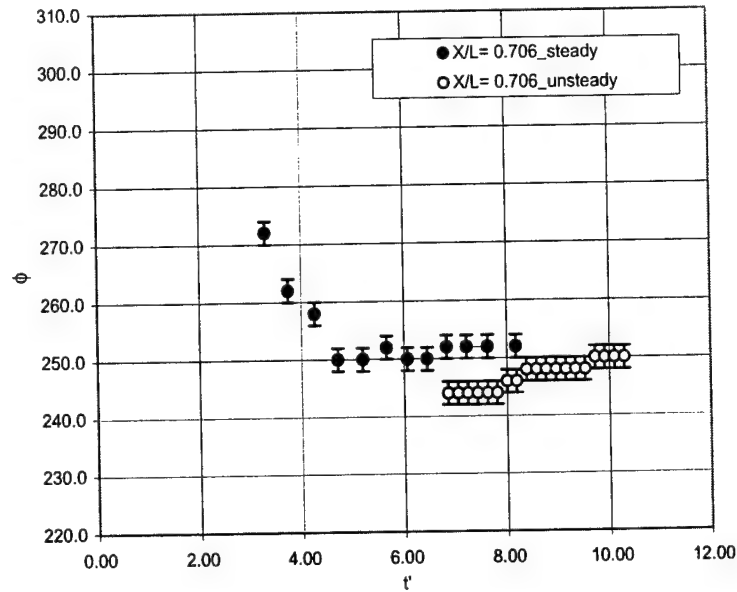


Figure 6.64: Steady and unsteady separation locations (second minima in  $C_f$  measured from  $\phi = 180^\circ$ ) vs  $t'$  at  $x/L = 0.706$  for the sail region of the sail-on-side case.

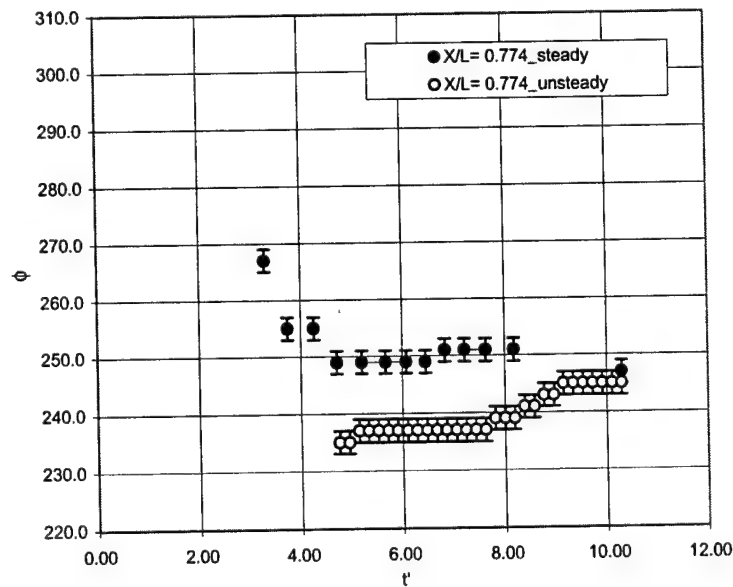


Figure 6.65: Steady and unsteady separation locations (second minima in  $C_f$  measured from  $\phi = 180^\circ$ ) vs  $t'$  at  $x/L = 0.774$  for the sail region of the sail-on-side case.

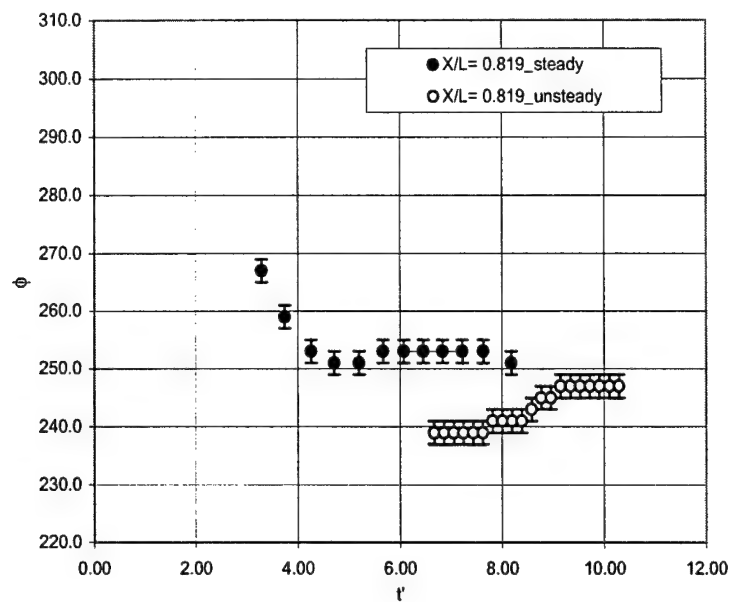


Figure 6.66: Steady and unsteady separation locations (second minima in  $C_f$  measured from  $\phi = 180^\circ$ ) vs  $t'$  at  $x/L = 0.819$  for the sail region of the sail-on-side case.

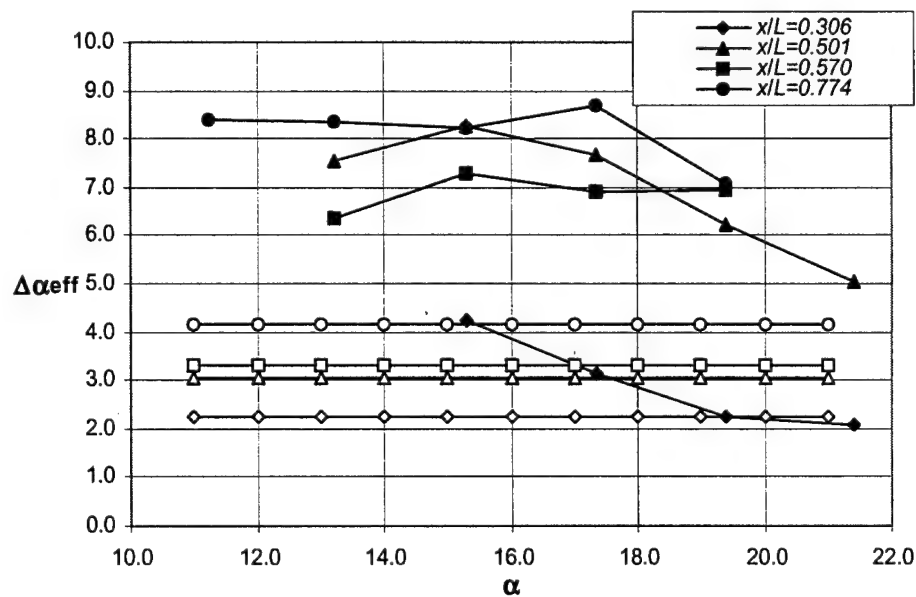


Figure 6.67: Incremental effective angle of attack  $\Delta\alpha_{eff}$  for the barebody pitch-up maneuver at four  $x/L$  stations as a function of instantaneous angle of attack  $\alpha(t')$ . Open symbols show the  $\Delta\alpha_{eff}$  given by the equation 6.17. (Both angles are in degrees)

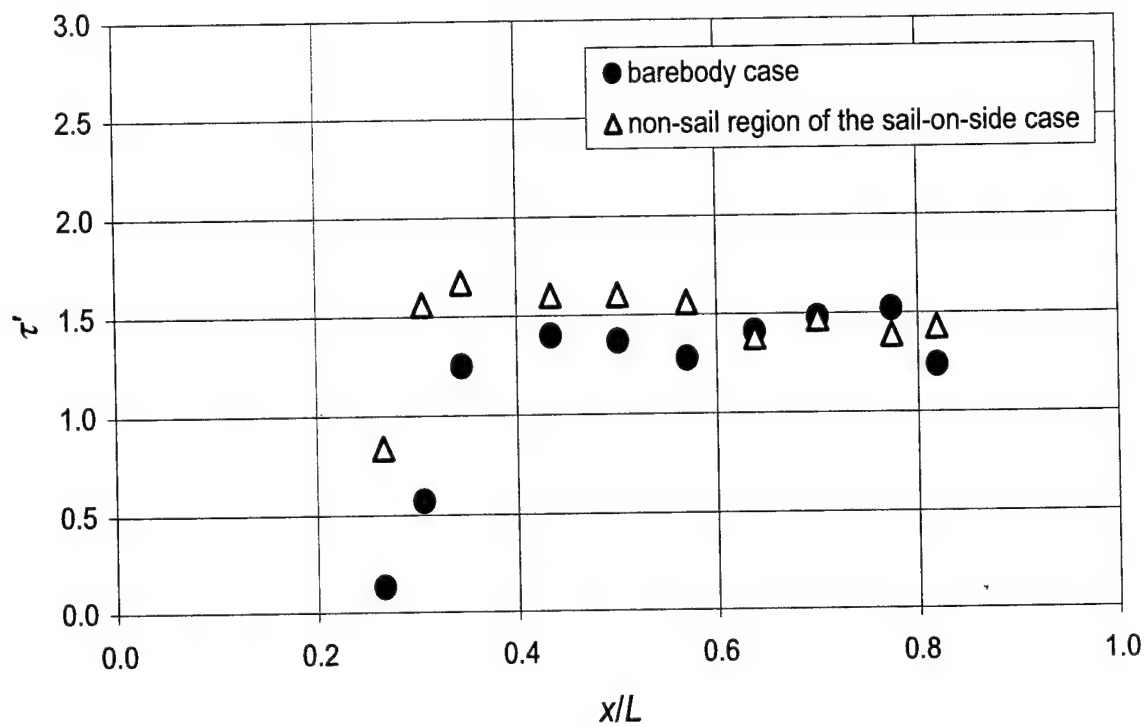


Figure 6.68: Computed time lags as a function of  $x/L$  for the barebody and the non-sail region of the sail-on-side case.

# Chapter 7

## Conclusions

Steady and the unsteady turbulent surface flow on a generic submarine model was studied. Hot-film sensors with constant temperature anemometers were used to measure the steady and the unsteady wall shear magnitudes over the model surface. Three-dimensional separation locations were determined from the minima of the skin-friction magnitudes. Steady skin-friction magnitudes were obtained at fourteen steady angles of attack. The dynamic plunge-pitch-roll model mount (DyPPiR) was used to simulate the pitchup maneuvers. The pitchup maneuver was a linear ramp from  $1^\circ$  to  $27^\circ$  in 0.33 seconds. Mean wall static pressures were measured at  $10^\circ$  and  $20^\circ$  angles of attack. Qualitative examination of the steady surface flow topology was done by using the oil-flow visualization pictures.

Two model configurations were studied in both the steady and the unsteady experiments: The barebody case and the sail-on-side case. The barebody case is the axisymmetric configuration of the model and can also be thought as a missile body or to a certain extent fuselage of an aircraft. Therefore, results obtained for the barebody case may be applied to many geometries with similar shapes. The sail-on-side measurements were performed with the sail fixed at the circumferential position  $\phi = 270^\circ$ . Pitchup maneuvers for the sail-on-side case simulate the turning maneuver of a submarine. All the tests were conducted at  $Re_L = 5.5 \times 10^6$  with a nominal wind tunnel speed of  $42.7 \pm 1\%$  m/s. For the experiments, slotted walls with an open-air-ratio of 38% are used to reduce the blockage effects. However, some steady pressure and hot-film data at certain angles of attack were also acquired with solid walls for the purpose of comparison.



For the range of conditions at which the tests are conducted, steady results over the barebody show that the flow on the leeward side of the model can be characterized by the crossflow separation. The first clear detection of the primary separation locations are at the stations downstream of  $x/L = 0.638$  at  $\alpha = 5.1^\circ$ . As the angle of attack increases, the primary separation line moves upstream and at a specific  $x/L$  location moves towards the windward side. At  $\alpha = 11.3^\circ$ , the onset of the secondary separation can be observed on the stern region. The secondary separation line migrates upstream and towards the leeward side with increasing angle of attack. The flat circumferential skin-friction profile on the stern region indicates the low speed separated flow which is also consisted with the oil-flow pattern of this region. This flat profile makes the identification of the true minimum and thus the separation location difficult for the stern region. A weak separation and reattachment of the flow on the nose region of the model can also be observed at high angles of attack.

The results of the sail-on-side case are evaluated in two separate regions, the region with no sail (between  $\phi = 0^\circ$  and  $180^\circ$ ) and the region with the sail (between  $\phi = 180^\circ$  and  $360^\circ$ ). In the first region, the origin and the variation of the primary and the secondary separation lines as a function of  $x/L$  and  $\alpha$  show the same characteristics as defined for the barebody case. This implies that the main flow feature on the non-sail region is the cross flow separation. The primary separation locations of the non-sail region start to deviate from the barebody results having an offset in the leeward direction at angles of attack starting from  $\alpha = 15.3^\circ$ . On the other hand, secondary separation locations of the non-sail region are shifted in the leeward direction compared to the secondary separation locations of the barebody case at all angles of attack.

Downstream of the sail, the flow structure on the sail side of the model is much different than the one observed for the non-sail side. The flow field in this region is strongly affected by the presence of the sail. Compared to the separation topology of the barebody and the non-sail region of the sail-on-side case, the separation location trend as a function of  $x/L$  and  $\alpha$  shows significant differences. Two minima in  $C_f$  vs.  $\phi$  distributions on the leeward side of the sail region can be observed for certain angles of attack and  $x/L$  locations. The first minima measured from  $\phi = 180^\circ$  can be observed only at a certain range of angles of attack, while second minima is detected at all angles of attack starting from  $\alpha = 5.1^\circ$ . The results on the sail side indicate that the flow field does differ from the crossflow separation structure observed for the barebody and non-sail region of the

sail-on-side case. Therefore the categorization of the separation locations as the primary or the secondary is not clear and may not reflect the real flow structure of this region. The flow in the vicinity of the sail-body junction is dominated by the horseshoe type separation.

The comparison of the barebody pressure measurements made with the solid walls and the slotted walls shows the blockage effect in the solid wall case, especially at  $\alpha = 20^\circ$ . On the leeward side of the model, the circumferential pressure gradient is found to be approximately zero over the regions of flow separation. One can think of using the flat pressure profile in regions of separation to locate the separation locations, however it is difficult to determine the exact point where this flat pressure distribution begins.

Unsteady skin-friction distributions of the barebody case and the non-sail region of the sail-on-side case show similar trends compared to the steady distributions of each. For these regions at high instantaneous angles of attack, the dominant flow feature on the leeward side of the model can again be characterized by the crossflow separation. However, the unsteady crossflow topology is different than the corresponding quasi-steady one; the primary separation formation occurs at higher angles of attack compared to the steady ones at which the onset of the first steady primary separation is observed. Also, at an instantaneous pitch angle for a specific  $x/L$  location, the primary unsteady separation starts more leeward compared with the steady case. No clear secondary separation is observed for the unsteady maneuvers. For the barebody and the non-sail region of the sail-on-side case, the difference in the separation topology originates from the fact that the unsteady separation location lags the unsteady separation.

As also seen in the steady case, the unsteady separation structure of the sail side is different from the unsteady crossflow separation topology observed on the barebody and the non-sail region of the sail-on-side case. From the results obtained for this region, it can be concluded that unsteady separation patterns do not follow the quasi-steady data with a time lag. A lag definition as described for the unsteady crossflow separation may not be appropriate for the sail side separation topology based on the results obtained in this study.

Time lag models were used to approximate the unsteady separation data of the barebody case and the non-sail region of the sail-on-side case. Algebraic time lag model results do not match with the barebody experimental results. This indicates the complex nature

of the unsteady flow separation over the Suboff model. The first-order differential time lag model of Goman and Khrabrov [35] approximates the unsteady data reasonably well and captures the time-varying nature of the unsteady crossflow separation locations. Therefore, this model may be used as part of the unsteady aerodynamic models used to describe the physics of such flows.

Time lags that are obtained by fitting the model approximation with the experimental unsteady data have a unique variation along  $x/L$  that does not match with the one obtained from the prolate spheroid study of Wetzel and Simpson [3]. In this study, time lag values are approximately constant along most part of the constant diameter region whereas in the prolate study, a linear trend increasing in the downstream direction is observed. However, the model center of rotation and the model geometry are different between two cases. This may imply the influence of these two parameters on the time lags. Further study has to be done in order to investigate the effect of these parameters.

# References

- [1] Yates, L. A. and Chapman, G. T. Streamlines, Vorticity Lines and Vortices Around Three Dimensional Bodies. *AIAA Journal*, 30(7):1819-1826, July 1992.
- [2] Wetzel, T. G. *Unsteady Flow over a 6:1 Prolate Spheroid*. PhD thesis, Department of Aerospace and Ocean Engineering, Virginia Tech, Blacksburg, VA 24061, April 1996.
- [3] Wetzel, T. G. and Simpson, R. L. Unsteady Crossflow Separation Location Measurements on a Maneuvering 6:1 Prolate Spheroid. *AIAA Journal*, 36(11):2063-2071, November 1998.
- [4] Simpson, R. L. Unsteady Aero-Hydrodynamics for Maneuvering Aircraft, Submarines and Automobiles. Report VPI-AOE 253, Department of Aerospace and Ocean Engineering, Virginia Tech, November 1997.
- [5] Etkin, B. *Dynamics of Atmospheric Flight*. Wiley, New York, 1972.
- [6] Simpson, R. L. Aspects of Turbulent Boundary-Layer Separation. *Progress in Aerospace Sciences*, 32:457-521, 1996.
- [7] Simpson, R. L., Walker, D. A., and Shinpaugh, K. A. Description of a 1000 Sensor Constant Current Anemometer System for Locating Three Dimensional Turbulent Boundary Layer Separations. Report VPI-AOE 185, Department of Aerospace and Ocean Engineering, Virginia Tech, December 1991.
- [8] Gad-el Hak, M. and Ho, C. M. Unsteady Flow Around an Ogive Cylinder. *Journal of Aircraft*, 23(6):520-528, 1986.
- [9] Montividas, R. E., Reisenthel, P., and Nagib, H. N. The scaling and Control of Vortex Geometry Behind Pitching Cylinders. *AIAA Paper 89-1003*, 1989.

- [10] Smith, L. H. and Nunn, R. H. Aerodynamic Characteristics of an Axisymmetric Body Undergoing a Uniform Pitching Motion. *Journal of Spacecraft*, 13:8-14, 1976.
- [11] Panzer, E. C., Rediniotis, O. K., and Telionis, D. P. The Hemisphere Cylinder in Dynamic Pitch-Up Motions. *AIAA-93-2963, AIAA 24<sup>th</sup> Fluid Dynamics Conference*. Orlando, FL., 1993.
- [12] Brandon, J. M. and Shah, G. H. Unsteady Aerodynamic Characteristics of a Fighter Model Undergoing Large-Amplitude Pitching Motions at High Angles of Attack. *AIAA-90-0309, AIAA 28<sup>th</sup> Aerospace Sciences Meeting*, Reno, NV., 1990.
- [13] Whitfield, C. C. Steady and Unsteady Force and Moment Data on a Darpa2 Submarine. M.S. Thesis, Department of Aerospace and Ocean Engineering, Virginia Tech, July 1999.
- [14] Willet, K. A. Design, Development and Implementation of a Low Cost Slotted Wall Test Section and Race Car Model for Use in Dynamic Wind Tunnel Testing. M.S. Thesis, Department of Aerospace and Ocean Engineering, Virginia Tech, pending.
- [15] Lofdahl, L. and Gad-el Hak, M. MEMS-based pressure and shear stress sensors for turbulent flows. *Measurement Science and Technology*, 10:665-686, February 1999.
- [16] Miller, J. A. A Simple Linearized Hot-Wire Anemometer. *Journal of Fluids Engineering*, 98(3):550-557, 1976.
- [17] Wood, N. B. A Method for Determination and the Control of the Frequency Response of the Constant Temperature Hot-Wire Anemometer. *Journal of Fluid Mechanics*, 67(4):769-786, 1975.
- [18] Suboff Darpa2 Test Model. Technical report, David Taylor Research Center, December 1988.
- [19] Olcmen, M. S., Simpson, R. L., George, J., and Whitfield, C. C. Experimental Study of High Reynolds Number ( $Re_\theta = 23000$ ) Two and Three-Dimensional Turbulent Boundary Layers. Report VPI-AOE 260, Department of Aerospace and Ocean Engineering, Virginia Tech, 1998.
- [20] Wetzel, T. G. and Simpson, R. L. Recent Steady and Unsteady Experiments for Submarine Fluid Dynamics: Unsteady Forces and Moments and Steady Oil

- Flow for the DARPA2. Report VPI-AOE 249, Department of Aerospace and Ocean Engineering, Virginia Tech, 1997.
- [21] Schoonover, S. and Simpson, R. L. Flow Improvement of the Subsonic, Three-foot, Open Throat Wind Tunnel. Technical report, Department of Aerospace and Ocean Engineering, Virginia Tech, 1993.
- [22] White, F. M. An Analysis of Axisymmetric Turbulent Flow Past a Long Cylinder. *ASME Journal of Basic Engineering*, 94:200-206, March 1972.
- [23] Coles, D. E. and Hirst, E. A. Computation of Turbulent Boundary Layers. 1968 AFORS-IFP-Stanford Conference, Vol.II 253, Stanford University, CA, 1969.
- [24] Kays, W. M. and Crawford, M. E. *Convective Heat and Mass Transfer*. McGraw-Hill, New York, 1980.
- [25] Schlichting, H. *Boundary-Layer Theory*, 7<sup>th</sup> Edition. McGraw-Hill, New York, 1979.
- [26] White, F. M. *Viscous Fluid Flow*. McGraw-Hill, New York, 1974.
- [27] Bruun, H. H. *Hot-Wire Anemometry: Principles and Signal Analysis*. Oxford University Press, New York, 1995.
- [28] Huang T. T., Liu, H., Groves N. C., Forlini, T. J., Blanton, J. N., and Gowing, S. Measurements of Flows Over an Axisymmetric Body with Various Appendages (Darpa Suboff Experiments). *Paper presented at the 9<sup>th</sup> Symposium on Naval Hydrodynamics, Seoul, Korea, August 24-28, 1992*.
- [29] Cleveland W. S. *Visualizing Data*. AT&T Bell Laboratories, Murray Hill, NJ, 1993.
- [30] Cleveland, W. S. Robust Locally Weighted Regression and Smoothing Scatterplots. *Journal of the American Statistical Association*, 74(368):829-836, 1979.
- [31] Simpson, R. L. Junction Flows. *Annual Review of Fluid Mechanics*, 33:415-443, 2001.
- [32] Wetzel, T. G., Simpson, R. L., and Chesnakas, C. J. Measurement of Three-Dimensional Crossflow Separation. *AIAA Journal*, 36(4):557-564, April 1998.

- 
- [33] Holman J. P. *Experimental Methods for Engineers*. McGraw-Hill, 6<sup>th</sup> Edition, New York, 1994.
  - [34] Ericsson, L. E. Unsteady Flows. In *Tactical Missile Aerodynamics: General Topics*, pages 490–493. edited by M. J. Hemsch, Progress in Astronautics and Aeronautics, AIAA, Washington D.C., 1992.
  - [35] Goman, M. and Khrabrov, A. State-Space Representation of Aerodynamic Characteristics of an Aircraft at High Angles of Attack. *Journal of Aircraft*, 31(5):1109–1115, 1994.
  - [36] Simpson, R. L. *The turbulent Boundary Layer on a Porous Wall*. PhD thesis, Stanford University, 1968.
  - [37] Doebelin, E. O. *Measurement Systems Application and Design* 4<sup>th</sup> Edition. McGraw-Hill, New York, 1990.

# Appendix A

## Uncertainty Analysis for the Skin-friction Measurements

### A.1 Classification of the Uncertainties

The uncertainty in the skin-friction measurements should be examined in two levels. The first part corresponds to the uncertainty in the calibration of the hot-film sensors and can be thought as a bias source of uncertainty. This uncertainty directly affects the skin-friction magnitudes, however it does not have an effect on the flow separation locations. The second one is the random relative uncertainty between the measurements made by one sensor at different circumferential locations on the model in different flow conditions. In other words, this uncertainty determines how accurately one sensor can measure the same wall shear stress  $\tau_w$  value in a given circumferential location at successive measurements. As also described in [2], this is the uncertainty that determines the accuracy of the flow separation locations.

### A.2 Uncertainty Calculations

The bias (calibration) uncertainty is mainly related to the accuracy of the wall shear stress values  $\tau_w$  used in the calibration process. As described in chapter 4, these shear stress values were calculated by using the boundary layer properties that were obtained from the boundary layer velocity profile measurements. The previous experiments that used



the same technique approximates an uncertainty of  $\pm 5\%$  in the skin friction coefficient  $C_f$  (Simpson [36]). Since the uncertainty in the determination of the free-stream velocity  $\delta U_\infty$  was less than 1% during the measurements, the uncertainty of the wall shear stress  $\delta \tau_w$  can also be thought as  $\pm 5\%$ . Thus, this value may be taken as the bias uncertainty in the calibration process.

In order to calculate the relative uncertainty in the actual measurements, we should again consider the King's equation written for the constant-temperature hot-film anemometers (CTA):

$$\tau_w^{1/3} = \bar{A} \frac{E^2}{\theta} + \bar{B} \quad (\text{A.1})$$

where  $\theta$  is the difference between the sensor operating temperature (which is constant for CTA) and the free-stream temperature:

$$\theta = T_w - T_\infty \quad (\text{A.2})$$

The relative uncertainty of  $\tau_w$  measured by each sensor will be due to the random uncertainties of the measured sensor voltage  $\delta E$  and the temperature difference  $\delta \theta$ . Note that the calibration constants  $\bar{A}$  and  $\bar{B}$  are not considered here, since they don't have a random variation. These coefficients have the same value between each calibration run as described in chapter 4. The overall relative uncertainty in  $\tau_w$  can be determined by using the *Kline and McClintock method* given in Doebelin [37]:

$$\delta W = \sqrt{\left(\frac{\partial W}{\partial x_1} \delta x_1\right)^2 + \left(\frac{\partial W}{\partial x_2} \delta x_2\right)^2 + \dots + \left(\frac{\partial W}{\partial x_n} \delta x_n\right)^2} \quad (\text{A.3})$$

In the above equation,  $W = W(x_1, x_2, \dots, x_n)$  represents the measured variable;  $\delta W$ , the uncertainty of the measured variable;  $x_i$ , each variable that effect the measured quantity; and  $\delta x_i$ , the uncertainty in each of these variables. The partial derivatives are the sensitivities of  $W$  with respect to each  $x_i$ . In order to use this method, each  $\delta x_i$  should be random and uncorrelated and have the same confidence level (e.g. 20:1 odds). Then the overall random uncertainty in  $W$  will also have the same odds.

By using equation A.3,  $\delta \tau_w^{1/3}$  can be approximated by:

$$\frac{\delta \tau_w^{1/3}}{\tau_w^{1/3}} = \frac{\tau_w^{1/3} - \bar{B}}{\tau_w^{1/3}} \sqrt{\left(\frac{\delta \theta}{\theta}\right)^2 + \left(\frac{\delta E^2}{E^2}\right)^2} \quad (\text{A.4})$$

Since the sensor temperature  $T_w$  is constant, temperature difference uncertainty will be equal to the uncertainty of the free-stream temperature which was at most  $\pm 0.5^\circ\text{C}$

between each calibration run in the experiments. By using the nominal 1.1 value of the overheat ratio,

$$\frac{\delta\theta}{\theta} = \pm 0.013 \quad (\text{A.5})$$

can be obtained. In order to get statistically meaningful uncertainty results, equation A.4 has been calculated for each steady and unsteady skin-friction value in the corresponding steady and the unsteady data reduction programs. The value of each  $\delta E^2$  has been obtained by using the voltage standard deviation info calculated in the same programs. At the last step, the overall random uncertainty of  $\tau_w$  was obtained by considering:

$$\frac{\delta\tau_w}{\tau_w} = 3.0 \frac{\delta\tau_w^{1/3}}{\tau_w^{1/3}} \quad (\text{A.6})$$

Note that the uncertainty in the skin-friction  $\delta C_f$  is equal to the wall shear stress uncertainty  $\delta\tau_w$ , since the uncertainty of the free-stream velocity is negligible. As the final results, the random uncertainties in  $C_f$  with 20:1 odds were obtained as:

$$\begin{array}{ll} \text{for the steady measurements} & \delta C_f = 6\% \text{ of } C_f \\ \text{for the unsteady measurements} & \delta C_f = 8\% \text{ of } C_f \end{array}$$

The higher uncertainty in the unsteady measurements come from the relatively higher unsteady voltage uncertainties. Above values lead to an uncertainty of  $\pm 2^\circ$  in the determination of the separation locations.

## Appendix B

# Robust Locally Weighted Regression and Smoothing *LOESS*

Robust locally weighted regression technique (Loess) is a smoothing method which uses the pre-determined windows of the original data in the regression process. Within each individual window, the data points near to the location where the smoothed value of the dependent variable is sought are given higher weights. Outliers in the data set are detected during the fitting process in an iterative manner and not used in the regression. These features of Loess technique enable to smooth the data without changing the original pattern.

### B.1 Mathematical Description

Mathematical details of the Loess method are described in Cleveland [29] and [30]. The theory behind the smoothing process can be summarized as follows: Let  $(x, y)$  be the point where we seek for the smoothed value  $\hat{g}(x)$ . Here  $x$  corresponds to the independent and  $y$  to the dependent variable in our data set. Two parameters are needed to be chosen to fit a loess curve. The first parameter,  $\alpha$ , is a smoothing parameter; it can be any positive number but typical values are 0.25 to 1.0. As  $\alpha$  increases, the curve becomes smoother. The second parameter,  $\lambda$ , is the degree of the certain polynomials that are fitted by the method;  $\lambda$  can be 1 or 2. Suppose first that  $\alpha \leq 1.0$ . Let  $q$  be  $\alpha n$  truncated to an integer where  $n$  is the total number of the data points. We assume that  $\alpha$  is large enough so that  $q$  is at least 1, although  $q$  is much larger than 1 in most of the

applications.

Let  $\Delta_i(x) = |x_i - x|$  be the distance from  $x$  to  $x_i$ , and  $\Delta_{(i)}(x)$  be these distances ordered from the smallest to the largest.  $T(u)$ , the *tricube weight function* is defined as:

$$T(u) = \begin{cases} (1 - |u|^3)^3 & \text{for } |u| \leq 1.0 \\ 0.0 & \text{otherwise} \end{cases} \quad (\text{B.1})$$

Then the neighborhood weight given to the observation  $(x_i, y_i)$  for the fit at  $x$  is

$$w_i(x) = T\left(\frac{\Delta_i(x)}{\Delta_{(q)}(x)}\right) \quad (\text{B.2})$$

For  $x_i$  such that  $\Delta_i(x) < \Delta_{(q)}(x)$ , the weights are positive and decrease as  $\Delta_i(x)$  increases. For  $\Delta_i(x) > \Delta_{(q)}(x)$ , the weights are zero. If  $\alpha > 1$ , the  $w_i(x)$  are defined in the same manner, but  $\Delta_{(q)}(x)$  is replaced by  $\Delta_{(n)}(x)\alpha$ .

If  $\lambda = 1$ , a line is fitted to the local data using weighted least squares with weight  $w_i(x)$  at  $(x_i, y_i)$ ; and the values of  $a$  and  $b$  are found that minimize:

$$\sum_{i=1}^n w_i(x) (y_i - a - bx_i)^2 \quad (\text{B.3})$$

Let  $\hat{a}$  and  $\hat{b}$  the minimizing values, then the fit at  $x$  is

$$\hat{g}(x) = \hat{a} + \hat{b}x \quad (\text{B.4})$$

For  $\lambda = 2$ , a quadratic polynomial is fitted to the local data using weighted least squares; values of  $a$ ,  $b$ , and,  $c$  are found that minimize

$$\sum_{i=1}^n w_i(x) (y_i - a - bx_i - cx_i^2)^2 \quad (\text{B.5})$$

If  $\hat{a}$ ,  $\hat{b}$ , and  $\hat{c}$  are the minimizing values, then the fit at  $x$  is

$$\hat{g}(x) = \hat{a} + \hat{b}x + \hat{c}x^2 \quad (\text{B.6})$$

## B.2 Selection of the Loess Parameters

In the previous section, two important parameters  $\alpha$  and  $\lambda$  that must be chosen in the smoothing process are defined. As described in Cleveland [29], in any specific application

of the loess method, the choice of these two parameters must be based on a combination of judgment and of trial and error. As  $\alpha$  increases, the loess fit becomes smoother. However after a certain value of  $\alpha$ , a lack of fit may be observed as the peaks and valleys in the data are missed because of the large value of  $\alpha$ . For small values of  $\alpha$ , the underlying pattern is tracked, but the local wiggles do not appear to be supported by the data. *The goal in choosing  $\alpha$  is to produce a fit as smooth as possible without unduly distorting the underlying pattern in the data.* Cleveland [29] also shows that a locally quadratic fit ( $\lambda = 2$ ) may be superior to the linear fit ( $\lambda = 1$ ) in terms of picking the local minima and maxima in certain data sets.

In this study, the loess method is used in smoothing some  $C_f$  vs  $\phi$  distributions, and the optimum combination of the parameters for each configuration and test condition have been found to be as follows:

Unsteady, barebody	$\alpha = 0.25$ and $\lambda = 1$
Steady, sail-on-side	$\alpha = 0.10$ and $\lambda = 1$
Unsteady, sail-on-side (sail region)	$\alpha = 0.20$ and $\lambda = 1$
Unsteady, sail-on-side (non-sail region)	$\alpha = 0.25$ and $\lambda = 1$

Figures B.1 and B.2 show the loess fits to the barebody unsteady  $C_f$  vs.  $\phi$  data at  $\alpha(t') = 11.3^\circ$  and  $x/L = 0.819$ , and at  $\alpha(t') = 21.5^\circ$  and  $x/L = 0.638$  respectively. As can be seen from these figures, by using the loess parameters  $\lambda = 1$  and  $\alpha = 0.25$ , a desirable level of smoothing is achieved without changing the general trend and the local minima of the data.

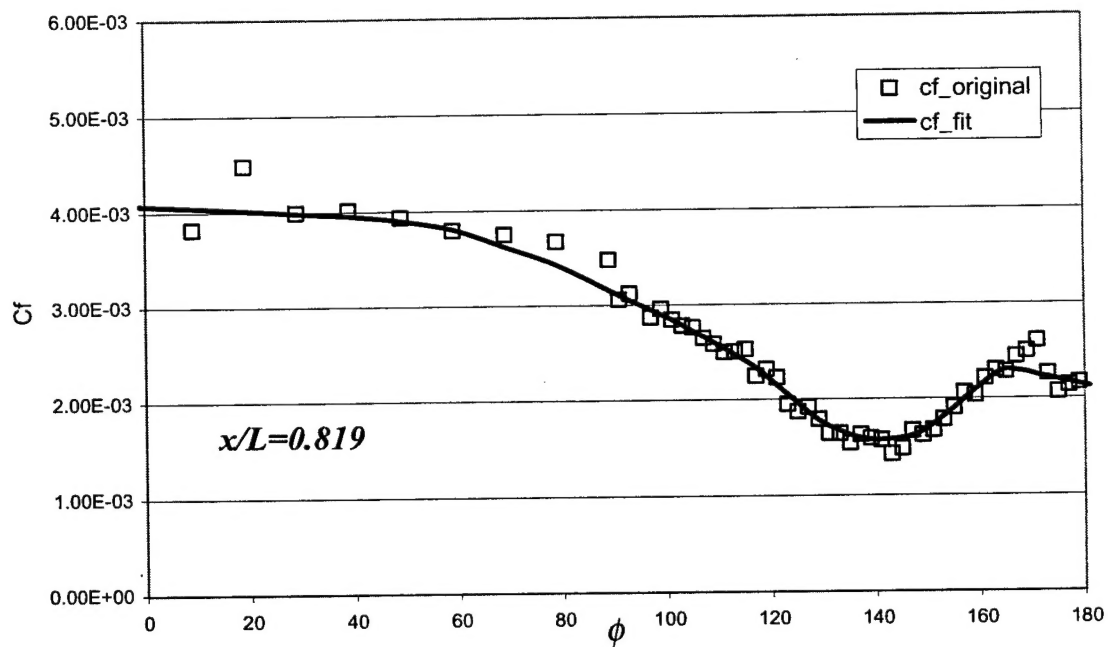


Figure B.1: Loess smoothing for unsteady barebody data at  $\alpha(t') = 11.3^\circ$  and  $x/L = 0.819$ .

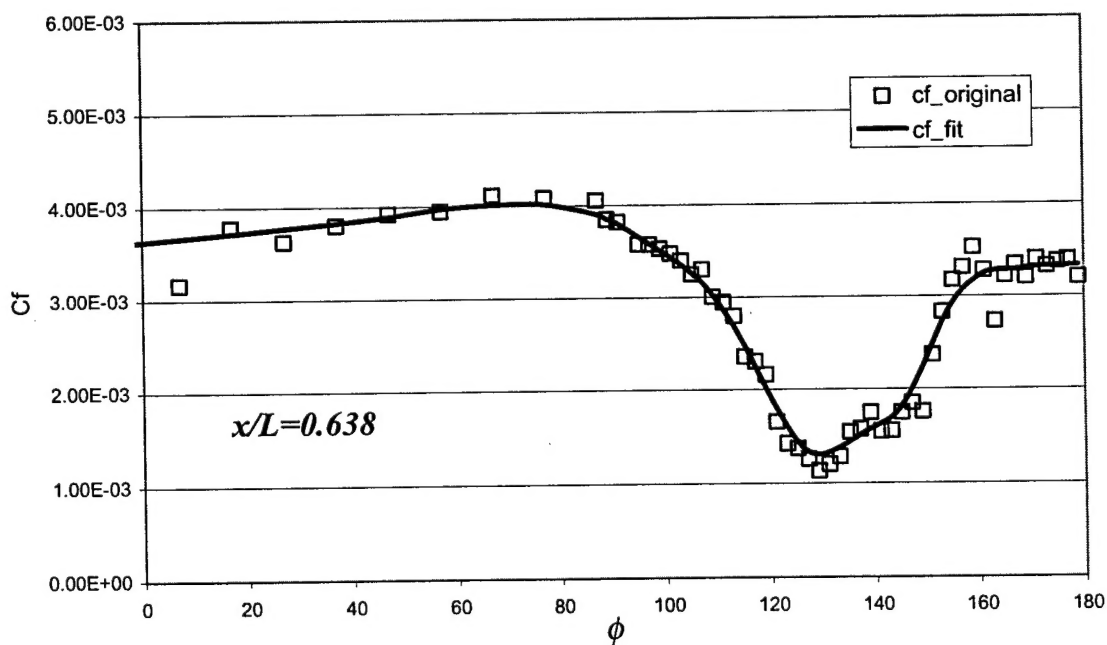


Figure B.2: Loess smoothing for unsteady barebody data at  $\alpha(t') = 21.5^\circ$  and  $x/L = 0.638$ .